Polymer-stabilized Transition Metal Nanocatalysts: Synthesis, Characterization, and Applications

by

Olivier Jérémie Nguon

A thesis
presented to the University of Waterloo
in fulfillment of the
thesis requirement for the degree of
Doctor of Philosophy
in
Chemistry

Waterloo, Ontario, Canada, 2014

AUTHOR'S DECLARATION

I hereby declare that I am the sole author of this thesis. This is a true copy of the thesis, including any required final revisions, as accepted by my examiners.

I understand that my thesis may be made electronically available to the public.

Abstract

Novel polymeric architectures and analytical methods were designed for the synthesis, characterization, and applications of metallic nanocatalysts. Four main research areas were investigated, namely: i) palladium nanocatalysts, ii) metal content analysis by a novel microplasma-based technique, iii) polyion complex micelle-metal hybrid structures, and iv) nickel nanocatalysts.

The solution and solid-state properties of dendrigraft (arborescent) polystyrene-*graft*-poly(2-vinylpyridine) copolymers were studied by dynamic light scattering (DLS) and atomic force microscopy (AFM). The unimolecular micelles exhibited good colloidal stability and narrow size distributions in organic solvents, and a *fried egg* morphology when deposited onto mica substrates. The preparation of stable colloidal Pd nanoparticles within the dendritic templates was reported for the first time. The diameter of the nanoparticles varied from 0.7 to 3.4 nm depending on the loading level, reduction time, and arborescent copolymer generation used. The catalytic activity of the colloidal Pd nanoparticles was evaluated in the Suzuki-Miyaura (SM) cross-coupling reaction under *green* conditions. Good catalytic activity and a positive dendritic effect were evidenced, although air-sensitivity and flocculation limited the activity and recyclability of the catalysts. To determine the concentration of Pd in the copolymers, a novel microplasma-based technique was applied in organic solvents for the first time. Metal quantification by microplasma-optical emission spectrometry revealed stoichiometric complexation of the Pd salt by the pyridine groups, and kinetic aggregation studies highlighted the benefits of the polymer for colloidal stability.

To obtain Pd nanoparticles dispersible in high water content solutions, polyion complex micelles were synthesized from arborescent copolymers and double-hydrophilic block copolymers. The latter, viz. poly(acrylic acid)-*block*-poly(2-hydroxyethyl acrylate), were obtained by hydrolysis of poly(*tert*-butyl acrylate)-*block*-poly(2-trimethylsilyloxyethyl acrylate), synthesized by atom transfer radical polymerization. The self-assembled complexes formed supramolecular aggregates with hydrodynamic diameters of 132 to 354 nm and narrow size distributions. The assemblies exhibited thermo-responsive properties in ethanol, dissociating above ca. 35 °C and reforming upon cooling. The polyion complexes, with hydrodynamic diameters ranging from 110 to 306 nm, were stable in water and were used for the solubilization of Pd nanocatalysts for aqueous Suzuki-Miyaura reactions.

Lastly, the properties of nickel nanoparticles prepared at Vale-Inco by a novel thermal decomposition method were investigated. The specific surface area of the bare nanopowders ranged from 6.4 to 97.2 $m^2 \cdot g^{-1}$, and their catalytic activity in the hydrogenation of adiponitrile and mesityl oxide was higher than for commercial catalysts in some cases. Treatment of the nanoparticles with diethylenetriamine further improved their catalytic activity. Polymeric stabilizers were designed to maximize the dispersibility and catalytic activity of the nanopowders. The structures investigated included triblock copolymers of polystyrene with poly(ethylene oxide) or poly(2-vinylpyridine), and telechelic poly(ethylene glycol). Application of the polymer-stabilized nickel catalysts in hydrogenation yielded up to 15-fold increases in specific catalytic activity as compared to the bare particles. The polymer was also effective at preventing oxidation by air under storage.

Acknowledgements

I would like to express my profound gratitude to the many individuals who have offered their precious support, and encouragements throughout this journey. My special appreciation goes to my supervisor, Prof. Mario Gauthier, whose knowledge, wisdom, support and guidance have been cardinal to the accomplishment of this research. I am also thankful to my co-supervisor Prof. Flora T.T. Ng, my supervisory committee members, Prof. Jean Duhamel, Prof. Éric Fillion, and Prof. Garry Rempel who have provided me with their help and guidance throughout.

I am indebted to Prof. Vassili Karanassios, who has been a unique mentor. I truly enjoyed our discussions, and his profound wisdom. I would also like to thank my collaborators at Vale-Inco, Dr. Vladimir Paserin and Steven Baksa, and at the Université de Bordeaux, Prof. Olivier Sandre and Emmanuel Ibarbour.

I wish to express my warm and sincere thanks to my colleagues and friends, who have made my experience in the lab so much more valuable: Mosa Alsehli, Ala Alturk, Yahya Alzahrany, Ryan Amos, Dr. Toufic Aridi, Jennipher Aumis, Dr. Lorena Eugenia Cadena-Sánchez, Dr. Jason Dockendorff, Joanne Fernandez, Dr. Eda Güngör, Timothy Hall, Lisa Hutfluss, Dr. Jonathan Juger, Dr. Hemali Lad, Wai Yau Lin, Dr. Firmin Moingeon, Dr. Abdul Munam, Mehdi Neqal, An Nguyen, Rama Selvarajah, William Szolga, Dr. Deepak Vishnu, Coline Voirin, Dr. Champa Wellappili, Dr. Greg Whitton, Aklilu Worku, and Yan Rong Wu.

Also a sincere thank you to all the members of Prof. Duhamel's group who have been eminently helpful and welcoming, as well as to my friends and to the staff of the Chemistry Department who are exceptional individuals.

I wish to thank the following groups and agencies for financial support: The Natural Sciences and Engineering Research Council (NSERC), the University of Waterloo, GreenCenter Canada, the Ontario Centres of Excellence, and Vale-Inco.

Last but not least, I would like to thank my parents, family, and Derya Demirtaş for their unwavering support, patience, encouragements and love.

Dedication

I dedicate this work to my grandmother, Madeleine Corbin-Gouyette, who is a constant inspiration of courage, strength, and generosity.

Je tiens à dédier ce travail à ma Mamie, Madeleine Corbin-Gouyette, qui m'inspire chaque jour par son courage, sa grandeur, et sa générosité.

"*Dans la nature rien ne se crée, rien ne se perd, tout change.*
In nature nothing is created, nothing is lost, everything changes."

— Antoine Lavoisier, *Traité Élémentaire de Chimie*

Table of Contents

List of Figures

List of Tables

List of Schemes

List of Abbreviations and Symbols

2VP	2-Vinylpyridine
A	Hamaker constant (for colloidal stability) or frequency factor (in Arrhenius equation)
AA	Acrylic acid
ac	Alternating current
ACF	Autocorrelation function
ACP	Arborescent copolymer
ADN	Adiponitrile (hexanedinitrile)
AES	Atomic emission spectroscopy
AFM	Atomic force microscopy
AGP	Arborescent graft polymer
AIBN	Azobisisobutyronitrile [2,2′-azobis(2-methylpropionitrile)]
Arb	Arborescent
atm	Standard atmosphere
ATRP	Atom transfer radical polymerization
b	Broad signal (NMR)
b	Block or length of a freely-jointed chain element
BA	4-Bromoanisole
BCP	Block copolymer
BET	Brunauer, Emmett and Teller
BHT	Butylated hydroxytoluene (2,6-di-*tert*-butyl-4-methylphenol)
bp	Boiling point
BP	1-1’-Biphenyl
c	Concentration or constant
cat	Catalyst
CMC	Critical micelle concentration

CMDP	Critical molecular design parameter
compl	Complex
COSY	Correlation spectroscopy
CSC	Core-shell-corona
CVD	Chemical vapor deposition
d	Doublet (NMR)
d	Deuterated, diameter or distance
d_{TEM}	Diameter measured by TEM
$Đ$	Dispersity
$Đ_M$	Molar-mass dispersity (also known as polydispersity index)
$Đ_p$	Particle-size dispersity (also known as polydispersity index)
D_h	Hydrodynamic diameter
D_t	Translational diffusion coefficient
dc	Direct current
DEN	Dendrimer-encapsulated nanoparticle
DETA	Diethylenetriamine [*N*-(2-aminoethyl)-1,2-ethanediamine]
DHBC	Double-hydrophilic block copolymer
DLS	Dynamic light scattering
DLVO	Derjaguin, Landau, Verwey and Overbeek
DMF	*N*,*N*-Dimethylformamide
DMSO	Dimethyl sulfoxide
d*n*/d*c*	Refractive index increment
DNA	Deoxyribonucleic acid
DPE	1,1-Diphenylethylene
DRI	Differential refractive index
DSN	Dendrimer-stabilized nanoparticle
DVB	Divinylbenzene
e	Electron charge or Euler's number
E_a	Activation energy

$E(h)$	Interaction energy
EO	Ethylene oxide
Equiv	Equivalent
EtOH	Ethanol
f	Branching functionality
fcc	Face-centered cubic
FID	Free-induction decay or flame ionization detector
FTIR	Fourier transform infrared
funct.	Functionalized
g	Graft
$g^{(2)}(t)$	Second-order autocorrelation function
G	Gibbs free energy
GC	Gas chromatography
Gn	Generation number
h	Hour(s), interparticle distance or length
H	Enthalpy
HEA	2-Hydroxyethyl acrylate
HEA-TMS	2-Trimethylsilyloxyethyl acrylate
HMD	1,6-Hexamethylenediamine (hexane-1,6-diamine)
hybr	Hyperbranched
ICP	Inductively coupled plasma
IMO	Isomesityl oxide (4-methylpent-4-en-2-one)
IPA	Isopropanol (2-propanol)
IR	Infrared
k	Rate constant or slope
k_B	Boltzmann constant
kc	Kilocounts
l	Segment or monomer length
L-N_2	Liquid nitrogen

LALS	Low angle light scattering
LDPE	Low density polyethylene
LOD	Limit of detection
m	Number of shells or degree of polymerization
$\bar{M}_n$	Number-average molar mass
$\bar{M}_w$	Weight-average molar mass
MAA	Methacrylic acid
MALLS	Multi-angle laser light scattering
MBP	4-Methoxy-1,1'-biphenyl
MIBC	Methyl isobutyl carbinol (4-methyl-2-pentanol)
MIBK	Methyl isobutyl ketone (4-methylpentane-2-one)
MLCT	Metal-ligand charge transfer
MO	Mesityl oxide (4-methylpent-3-en-2-one)
mol %	Mole percent
MPD	Microplasma device
MWCO	Molecular weight cutoff
n	Refractive index of solution or degree of polymerization
n_o	Refractive index of solvent
n/a	Not applicable or not available
N_A	Avogadro constant
net	Network
NMP	Nitroxide-mediated polymerization
NMR	Nuclear magnetic resonance
NNLS	Non-negatively constrained least-squares
NP	Nanoparticle
OES	Optical emission spectrometry
p	Extent of reaction conversion
P	Pressure or product
P2VP	Poly(2-vinylpyridine)

P4VP	Poly(4-vinylpyridine)
PAA	Poly(acrylic acid)
PAMAM	Poly(amidoamine)
PBA	Phenylboronic acid
$Pd(OAc)_2$	Palladium acetate
PEG	Poly(ethylene glycol)
PEI	Polyethyleneimine
PEO	Poly(ethylene oxide)
PFS	Poly(ferrocenyldimethylsilane)
Ph	Phenyl
PHEA	Poly(2-hydroxyethyl acrylate)
P(HEA-TMS)	Poly(2-trimethylsilyloxyethyl acrylate)
PIC	Polyion complex
PIP	Polyisoprene
PMAA	Poly(methacrylic acid)
PMDETA	*N*,*N*,*N′*,*N″*,*N″*-Pentamethyldiethylenetriamine
PMMA	Poly(methyl methacrylate)
PMT	Photomultiplier tube
PNIPAM	Poly(*N*-isopropylacrylamide)
ppb	Parts per billion
ppm	Parts per million
PS	Polystyrene
psig	Pounds per square inch gage
P*t*BA	Poly(*tert*-butyl acrylate)
PTFE	Polytetrafluoroethylene
PVPy	Poly(*N*-vinyl-2-pyrrolidone)
q	Scattering vector (light scattering)
QSI	QuantumSphere Inc.
r	Radius or reaction rate

$\langle r^2 \rangle_0^{1/2}$	Root-mean-square end-to-end distance
r_b	Bulk polymer radius
r_m	Specific rate
r_{sa}	Areal rate
R	Ideal gas constant
R_g	Radius of gyration
R_h	Hydrodynamic radius
RaNi	Raney® nickel
RALS	Right-angle light scattering
rbf	Round-bottomed flask
RI	Refractive index
rpm	Revolutions per minute
RU	Repeating unit
s	Singlet (NMR)
S	Saturation ratio or entropy
SANS	Small-angle neutron scattering
SEC	Size-exclusion chromatography
SEM	Scanning electron microscopy
SM	Suzuki-Miyaura
SSA	Specific surface area
SWB	Spectral bandwidth
t	Triplet (NMR)
T	Temperature
T_c	Critical temperature
TEA	Triethylamine
TEM	Transmission electron microscopy
TFA	Trifluoroacetic acid
THF	Tetrahydrofuran
TMEDA	*N*,*N*,*N*′,*N*′,-Tetramethylethylenediamine

TMS	Trimethylsilyl
TMS-Cl	Trimethylsilyl chloride
TOF	Turnover frequency
TON	Turnover number
UV-vis	Ultraviolet-visible
V	Potential energy, molecular volume or volume
VITSL	Vale-Inco Technical Services Limited
wt %	Weight percent
x	Mole fraction
XPS	X-ray photoelectron spectroscopy
$\bar{X}_n$	Number-average degree of polymerization
$\bar{X}_w$	Weight-average degree of polymerization
γ	Surface free energy
Γ	Autocorrelation function decay constant
δ	Hildebrand or Hansen solubility parameter, or chemical shift
Δ	Difference operator
ε	Dielectric constant or binding energy
ζ	Zeta potential
η	Viscosity
θ	Scattering angle, or bond angle
κ	Debye-Hückel reciprocal length
λ	Wavelength
μ	Decay moment
μ_2	Second moment (cumulants analysis)
ν	Scaling parameter
ρ	Density
σ	Standard deviation or steric factor (chain flexibility)
σ_c	Collision diameter
τ	Decay rate

φ	Volume fraction
χ	Flory-Huggins interaction parameter
ω	Rotational speed of the stirrer
%RSD	Percent relative standard deviation

Chapter 1

Foreword

1.1 Opening remarks

The unique size-dependent properties exhibited by nanosized materials have led to the thriving advances recently seen in nanotechnology. Although heterogeneous catalysis has long been concerned with the preparation and applications of metallic nanostructures, the controlled supramolecular assembly of nanomaterials, coupled with the use of novel characterization methods, have set apart nanocatalysis as a new field of research.[1,2] To maintain their small size and high catalytic activity nanoparticles must be stabilized, and polymers have emerged as extremely successful and versatile candidates for that purpose. Moreover, the role of the polymeric matrix is not limited to providing colloidal stability but is central to the synthesis, solubilization, catalytic performance, recovery and recycling of the metallic species.[3,4]

Several polymeric structures ranging from linear homopolymers, block copolymers, and more recently dendritic structures have been employed for the preparation and stabilization of metallic nanoparticles.[3] Dendrimers in particular have shown great promise in nanocatalysis, but other dendritic architectures remain largely unexplored. Palladium has been one of the most studied highly performant catalysts for hydrogenation, oxidation, and carbon-carbon forming reactions among others.[5] Magnetic nanomaterials have also garnered great interest in catalysis, since recovery of the metallic species by subjecting them to a magnetic field is of particular interest. Among ferromagnetic materials nickel has been rather exiguously investigated, even though this metal exhibits a high catalytic performance for many reactions including hydrogenation, oxidation, carbonylation, and cross-coupling reactions.[6]

Further understanding and control of structure formation, morphological diversity, and self-assembly dynamics are critical to the implementation of nanocatalysts in a wide range of technological applications, and nanocatalysis will likely remain an active field of research in the future.[7,8]

1.2 Research objectives and thesis outline

The research presented in this Thesis focuses on the synthesis, characterization, and applications of polymeric stabilizers for the preparation of metallic nanocatalysts. In particular, different polymeric architectures and a novel characterization technique were investigated to further expand fundamental understanding in this field of research.

This dissertation is organized into seven chapters. Following this Foreword, a detailed review of the relevant literature on nanocatalysis is presented in Chapter 2. This background information highlights the fundamental properties of nanosized catalysts, the utilization of polymers as stabilizers, and the application of these materials in carbon-carbon bond-forming reactions. To the best of our knowledge, this review is the first one to summarize extensively the preparation of polymer-stabilized Pd nanoparticles. Arborescent (dendrigraft) copolymers exhibit a cascade-branched architecture akin to that of dendrimers, but their synthesis protocol – based on the utilization of polymeric moieties – allows a rapid increase in molar mass while maintaining a low molar-mass dispersity. In Chapter 3, after studying the properties of arborescent amphiphilic structures, we investigated the formation of Pd nanoparticles within these templates. We also demonstrated their use as catalysts in the Suzuki-Miyaura reaction. The determination of the metal content of nanocatalytic systems largely relies on inductively coupled plasma (ICP) measurements. Unfortunately, this

characterization technique is marred by several important limitations. In Chapter 4, we demonstrated for the first time the application of a microplasma-based technique for the direct determination of the concentration of Pd in arborescent polymer-stabilized nanoparticle systems in organic solvents. These results are published as References 9 and 10 in this Chapter. The preparation of polyion complex micelles from arborescent copolymers and double-hydrophilic block copolymers is reported in Chapter 5. In addition to exhibiting interesting thermo-responsive properties in ethanol, the self-assembled supramolecular structures formed by these polymers can serve for the preparation of water-dispersible Pd catalysts for application in aqueous Suzuki-Miyaura reactions. A fundamental study on the properties of nickel nanoparticles prepared by a novel thermal decomposition method developed at Vale-Inco is reported in Chapter 6. The influence of polymeric stabilizers on the catalytic activity of the particles is emphasized. The overarching conclusions from the Thesis are presented in Chapter 7, which provides an overall summary of the body of research completed, the original contributions to knowledge, and suggestions for future work.

In agreement with the University of Waterloo Thesis regulations, the format of each chapter is organized as a manuscript for publication in scientific journals. Each chapter therefore includes an introductory section providing relevant background information on the subject matter, experimental methods, results and discussion, and conclusions. Additionally, an overall abstract for the complete Thesis is provided in the preliminary pages of this dissertation, and a single list of references at the very end of the document is organized and numbered according to each individual chapter.

Chapter 2

Polymer-stabilized Pd Nanocatalysts: Theory, Synthesis, and Applications

2.1 Nanoscience and nanotechnology

The formidable potential offered by the production, control and manipulation of structures down to the molecular level has led, over the past 30 years, to major developments in the fields of nanoscience and nanotechnology.[1] As emboldened in 1959 by Nobel laureate Richard Feynman, in his visionary lecture entitled "*There is plenty of room at the bottom*",[2] the dynamic body of research in these areas has paved the way to exciting novel technological applications.

At the core of nanoscience and nanotechnology are the significant changes in the properties exhibited by materials as their size is decreased from the macroscopic to the atomic or molecular level. In an intermediate region where at least one dimension is in the nanometer range (1–100 nm) unique properties emerge, different from those of the bulk or atoms, and which can vary significantly with the size, shape and structure of the nanoscale materials.[3] At the lower end of this size range, both surface and quantum effects become important and can lead to unique chemical, electronic, magnetic, mechanical, optical, photonic, thermal, thermodynamic and catalytic properties among others.[4–7]

The effect on catalytic properties, in particular, has shown such promise that Somorjai[*] was led to qualify catalysis as the central field of nanoscience and nanotechnology.[8] As a matter of fact nanocatalysis has emerged as a research field in its own right,[9,10] and has attracted steadily rising interest from the research community (Figure 2.1) with several books already dedicated to this subject.[6,11–18]

[*] G. A. Somorjai is regarded as one the fathers of modern surface chemistry.

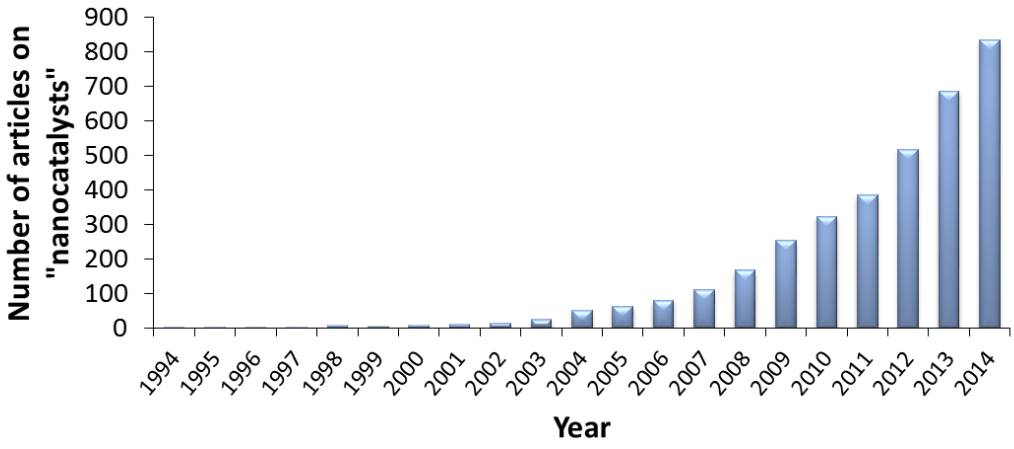

Figure 2.1 Number of published articles including the topic "nanocatalysts or nanocatalysis" (from Web of Science™ statistics).

Atoms at the surface of a solid often exhibit a high chemical reactivity because of their unsatisfied coordination and as the size diminishes, the fraction of surface atoms rises rapidly. The electronic and chemical properties are greatly affected by the particle size reduction, and these have been shown to even depend on the exact number of atoms present.[19] It is, however, the intrinsic changes in the chemical and catalytic reactivity in the nanometer size range, non-scalable from the bulk properties, that distinguish nanocatalysts from other large surface-area catalysts.[20] Nanocatalysis, as a consequence, is concerned with understanding the inner workings of a catalyst at the molecular level, and the rational production of catalysts with a well-defined size, morphology, composition, and structure in order to control its properties.[21–23]

Changes in the optical properties represent another important surface-sensitive size effect that is beautifully illustrated by the deep coloration of coinage metal nanoparticle

colloids. In the lower size range, the absorbance of light in the ultraviolet-visible (UV-vis) region becomes important for these nanoparticles. Mie provided in 1908 a solution to Maxwell's equations to account for the absorbance spectra of spherical particles.[24] This effect, known as surface plasmon resonance, stems from coherent oscillation of the valence electrons of the atoms in the particles upon interacting with electromagnetic waves in the UV-vis region. Since then, important applications such as bio-sensing devices[25] have been developed for these materials.

Furthermore, when the size of a material becomes comparable to the associated wavelength of charge carriers (typically in the nanometer range[†]), restriction in the motion of the electrons known as quantum confinement[26] results in discrete energy levels. This electronic structure differs significantly from the continuum of energy states displayed by bulk materials. Important applications have emanated from the idiosyncratic electrical and optical properties displayed by such nanoparticles. In the information technology and telecommunications industries for instance, semiconductor nanoparticles (quantum dots) are promising as single electron transistors and in the elaboration of quantum computers.[26]

Since many nanomaterial properties exhibit a non-monotonic size dependency, important efforts have been devoted to the development of synthetic strategies offering control over the size but also over the structure, composition and shape of nanoparticles. A variety of materials – ranging from three-dimensional to zero-dimensional structures – are

[†] The electron wavelength stems from the particle-wave duality of any particle, as enunciated by De Broglie in 1924.[353,354]

now obtainable including nanocrystals; monolayer films and nanosheets; carbon nanotubes, nanorods and nanowires; nanoparticles and quantum dots.[26,27]

Transition metal nanostructures are of particular importance in catalysis, and have by far attracted the most interest. These nanosized materials have emerged as an alternative to the classical division between homogeneous and heterogeneous catalysts, and stand in the continuum in size that exists between molecular organometallic compounds, metal clusters, nanoparticles (and colloids or sols), and solid state metals. An abundant body of research exists on synthetic strategies devised for the preparation of well-defined nanoparticles, as outlined in several reviews.[23,28–59]

After highlighting the relevance of metal nanoparticles to catalysis, we will review the different synthetic strategies used to prepare efficient nanocatalysts. In particular, we will see that *wet chemistry* methods arose as the most popular route. Colloidal stability of metal nanoparticles is essential however, and polymers have emerged as very successful candidates to provide steric and/or electrostatic stabilization. In this Chapter, we will particularly focus on the more recent utilization of dendritic polymers and highlight their interesting characteristics. We will also review some of their important applications in the Suzuki-Miyaura cross-coupling reaction, which employs primarily Pd catalysts. As the most extensively studied catalyst,[60] this noble metal shows great promise for the advent of more sustainable processes (i.e., green chemistry) with important industrial and economical applications.

2.2 Catalysis

2.2.1 Definitions

Catalysts are ubiquitous in modern societies and central to the production of chemicals, lubricants, refrigerants, polymers, pharmaceuticals and transportation fuels among many others.[10] In fact, it is estimated that more than 95% by volume of all the products are synthesized using catalysts, the latter amounting to a $13-billion market in the world economy.[61] Catalysts are also of prime importance to life, with enzymes accounting for most of the processes on the planet and in the human body.

The word catalysis, derived from the Greek κατα and λνσιζ meaning 'wholly loosening', was coined by Berzelius in 1835 to describe the "decomposition of bodies" under a certain "catalytic force".[62] Although definitions may vary,[63] it is usually agreed that the role of a catalyst is to increase the rate at which the equilibrium of a reaction is approached without itself becoming permanently involved in the reaction.[64] Even though a catalyst is not consumed during the reaction and can be reused, deactivation by poisoning, fouling, material loss through leaching, and/or structural reorganization/degradation typically limit its lifetime.[65,66] It is not surprising that catalysts have been employed extensively in industry since they can lower production costs by decreasing the energy requirements while being reusable. Selectivity is another important parameter for a catalyst which can favor the formation of a particular reaction product. In practice, selectivity augments the production yield and simplifies recovery procedures. It is also of importance in the production of drugs for instance, where safety can be improved by preventing the formation of harmful side

products.[67] The relevance of selectivity is perhaps best illustrated by the challenge set by Somorjai for catalysts of the 21st century to reach 100% selectivity.[68]

2.2.2 Role of a catalyst

The effect of a catalyst is to reduce the activation energy (E_a) of a reaction, by favoring the formation of a transition state (activated complex) with a lower potential energy. As illustrated in Figure 2.2, the reactants form preferably the "desired" products, characterized by a lower activation energy (E_{cat}). The non-catalyzed reaction proceeds through the formation of an activated complex with a much greater activation energy (E_{uncat}).

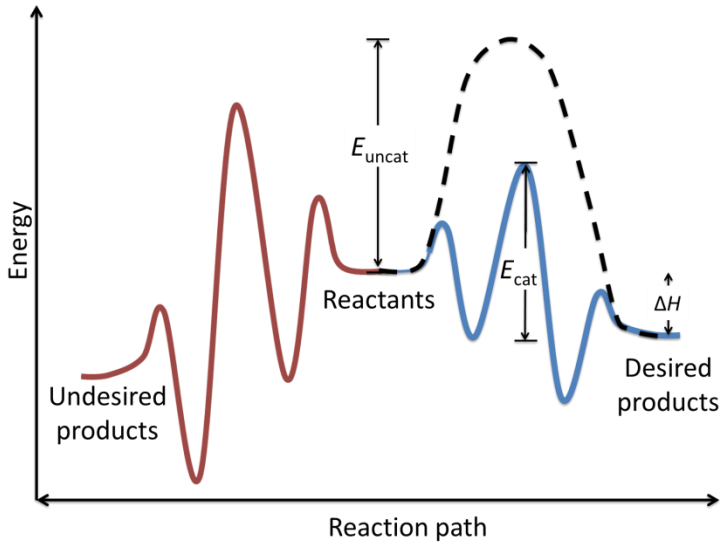

Figure 2.2 Potential energy diagram for catalyzed (solid line) and non-catalyzed reactions (dashed line). A selective catalyst can favor the desired catalyzed reaction (right) with a lower activation energy over the undesired reaction (left). Adapted with permission from Reference 69. Copyright 2012 John Wiley & Sons.

Selectivity can be achieved by favoring the formation of the species with the lowest E_{cat}. It should be noted that catalysis is fundamentally a kinetic phenomenon, as opposed to a thermodynamic one, so the change in enthalpy of the reaction (ΔH) is not affected.[69] The Arrhenius equation links the rate constant k for a reaction to the activation energy E_{cat} as:

$$k = Ae^{-\frac{E_{cat}}{RT}} \tag{2.1}$$

The parameters involved are the pre-exponential factor A (a frequency factor for an elementary process, related to the number of collisions per unit time between the reactants having the adequate orientation to yield the products), the gas constant R, and the absolute temperature T.[70] A decrease in E_{cat} leads to an increase in the rate of the reaction as described by Equation 2.1.

2.2.3 Classification of catalysts

Traditionally, catalysts have been divided based on their physical state and that of the reactants (substrates) between two main groups, namely homogeneous and heterogeneous. Homogeneous catalysts are in the same phase as the reactants, which usually is the liquid state. In heterogeneous systems the catalyst and reactants are in different phases, although most commonly, the catalyst is in the solid state and the reactants are liquids or gases.[71] A third intermediate group includes enzymes serving as biocatalysts, and is attracting growing interest due to mounting regulatory demands for the chemical industry to develop processes that are energy-efficient and respectful of the health and environment.

Homogeneous catalysts are characterized by greater performance (i.e., activity and selectivity) over heterogeneous systems. However, industrial applications favor the usage of

the latter because of their greater stability and easier recovery. Indeed, heterogeneous catalysts are involved in about 80% of all industrial catalytic processes. Enzymatic catalysts, while representing only about 5% of all catalytic processes, have a well-defined structure, high activity and selectivity, and show promise in various applications.[61]

Recently, nanocatalysts have challenged this classification and have been referred to variously as homogeneous,[72] heterogeneous,[72,73] quasi-homogeneous,[40,54] quasi-heterogeneous,[74] semi-heterogeneous,[75,76] heterogeneous in solution,[77] soluble heterogeneous, soluble hybrid heterogeneous-homogeneous, soluble near-homogeneous,[78] or homogenous cluster catalysts.[79] The different terminologies used reflect the uncertainty about the nature of the active species in solution and the onset of a heterogeneous phase.[80] For instance, atoms leaching from finely dispersed heterogeneous particles,[46] or metal particles formed by the decomposition of soluble complexes[81–83] may also participate in catalytic processes. These difficulties have long been recognized, and criteria have been proposed to help differentiate the occurrence of homogeneous versus heterogeneous catalysis.[79,80,84,85] Since such distinction may remain *in principle* unfeasible within a narrow intermediate size range, and to avoid confusion in terminology, Crabtree rather proposed to distinguish between homotopic and heterotopic catalysts to highlight the participation of single or multiple sites in the catalytic mechanism, respectively.[80]

2.3 Nanocatalysis

2.3.1 Definitions

The continuum in size that exists between organometallic compounds, clusters, and nanoparticles or colloids can render difficult the assignment of a specific size range to each species, and various definitions have been used by different authors. We will attempt to clarify the understanding of each term by reporting the definitions given by authorities in the field. For instance, Rösch and Pacchioni have defined clusters as "aggregates of atoms, not necessarily of the same element, which do not exist in measurable quantities in an equilibrium vapor".[86] This definition allows one, for instance, to distinguish fullerenes and a tetrahedron of phosphorous atoms (P_4) (both considered molecules) from sodium aggregates (Na_n) and some transition metal carbonyls such as $[Ni_5(CO)_{12}]^{2-}$ (considered clusters[‡]). Bradley, in the same book, restricted the term colloids[§] "to metallic elements, principally transition metals", with a size range which "reflects the current interest among chemists and

[‡] This definition is different from the one used by Blackman and Binns, who do not distinguish between clusters and nanoparticles, and include fullerenes in the cluster classification.[355] Pomogailo, on the other hand, regards clusters as "particles with ordered structures (their size ranging from 1 to 10 nm) composed as a rule of 38–40 (sometimes more) metal atoms" and nanoparticles as "disordered structures, having a size of 10–50 nm and including in most cases 10^5–10^6 atoms.[29]

[§] This definition is different from the original term introduced by Graham in 1861 to describe the "glue-like" properties of aqueous solutions of silver chloride or gold (i.e., a slow diffusion rate and non-crystallizability).[356] In this context, colloids described a suspension of a liquid or solid phase in another liquid phase. IUPAC defines colloidal systems as particles having at least one dimension within the size range of 1 nm to 1 μm.[357]

physicists in exploring those special properties which are expected to be exhibited by small particles of solid inorganic materials, including metals, as their size approaches that of molecular clusters".[28] More practically perhaps, he noted a lower limit ranging from 1 to 20 nm while stressing the flexibility of the upper bound. In the current literature, however, the term 'nanoparticle' has usually been substituted to the term 'colloid'[87] (or ultrafine particles[88]) and principally refers to isolated particles with diameters ranging from 1 to 100 nm.[89,90] We will follow the definition provided by Bönnemann and Serp among others, and regard colloids (or sols) as nanoparticles stabilized by a protective shell in a liquid phase.[39,91] It should be noted, however, that some authors make a clear distinction between colloids and nanoparticles (nanoclusters).[**] In this context, nanoclusters correspond to particles "at or below the 1-nm end of the size range", as noted by Crabtree.[80] More recently, the term *superatom* has been used to describe sub-nanoparticles with only a few tens of metal atoms, exhibiting unique properties that depend on the exact number of atoms.[92] These particles exhibit chemical behaviors reminiscent of the properties of the elements.

The characterization of the size distribution of nanoparticles differs from that of polymeric molecules for instance, and a population with a standard deviation of less than 10% (dispersity of 1.1) from the mean particle size is commonly described as

[**] For instance, Finke et al. restricted the term nanoclusters to particles displaying a narrow size distribution, a diameter between 1 and 10 nm, and that are isolable, and of well-defined composition.[78,358] This is in contrast with colloids, considered to be larger than 10 nm, with a broader size distribution, and generally in aqueous media. Furthermore, Wang and Ostafin also agreed on the upper bound of 100 nm but preferred to set the lower limit at a few hundred atoms for nanoparticles.[42]

monodispersed.[45,93] We will, however, heed the advice of Aiken and Finke and prefer to employ the term 'near monodispersed'.[78] Furthermore, standard deviations up to 20% (dispersity of 1.2) from the average particle size are generally accepted as representative of narrow size distributions.[45,54]

2.3.2 Size effects

Heterogeneous catalysis is foremost a surface process where the catalyst mediates the interactions between the substrate molecules;[94,95] therefore both the nature and texture of the catalyst are of importance for its activity. The nature of the catalyst determines its ability for chemisorption and complex formation with the substrate molecules (ligand effect).[96] The texture, characterized by properties such as the porosity and particle size distribution, directly influence the surface area available to the substrate molecules.[97]

As the particle size decreases, the surface-to-volume ratio of a material increases ($\propto r^{-1}$), thus imparting nanosized materials a large specific surface area.[95] From a topological viewpoint, the catalytic reaction is facilitated by open structures with low-coordinating, highly reactive surface sites located at surface imperfections such as edges, steps, kinks, and F-centers (oxygen vacancies).[98,99] A reduction in particle size is generally associated with important structural changes and a greater number of crystallographic defects promoting the catalytic activity of a material.[100–103] Pd nanoparticles, for instance, often adopt a cuboctahedral morphology for which the number of terrace, edge, and corner atoms on the surface can be calculated.[100,104–106] As shown in Figure 2.3, the fraction of highly reactive edge and corner atoms increases more rapidly than the corresponding fraction of terrace

atoms as the size is reduced.[107] Indeed, the excess energy of superficial atoms has often prompted the qualification "energy-saturated systems" to describe nanoparticles.[29]

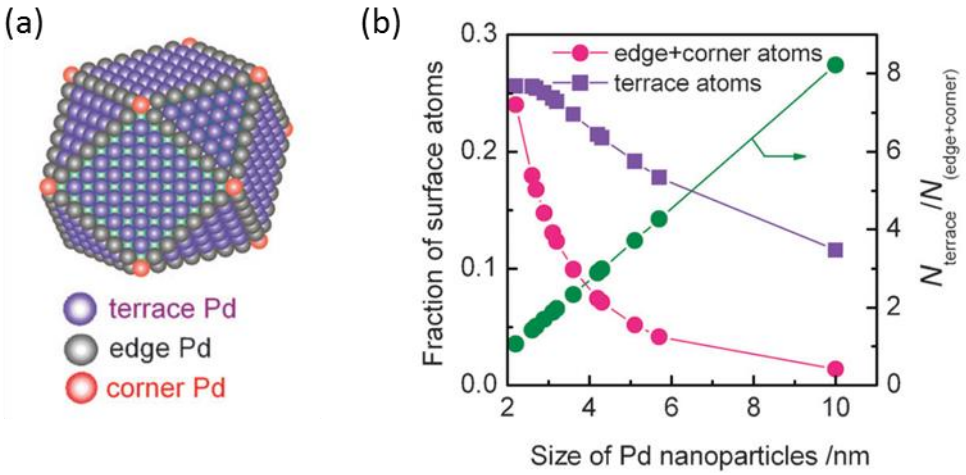

Figure 2.3 (a) Structure of the cuboctahedral model showing the different types of surface atoms used in the calculation of (b) the fraction of surface atoms, and the ratio of terrace atoms to edge and corner atoms ($N_{terrace}/N_{(edge+corner)}$) as a function of the nanoparticle size. Reprinted with permission from Reference 107. Copyright 2011 The Royal Society of Chemistry.

In addition to geometric effects, important changes in the intrinsic properties of materials – known as quantum size effects – are observed as the size diminishes.[20] Bulk metals display energy band structures that enable the delocalization and transport of electrons. As the size approaches the nanometer range, discreet energy levels with a size-dependent spacing replace the band structure (quantum confinement), and confer to the material properties approaching those of molecules or atoms (Figure 2.4).[20,102,108–111]

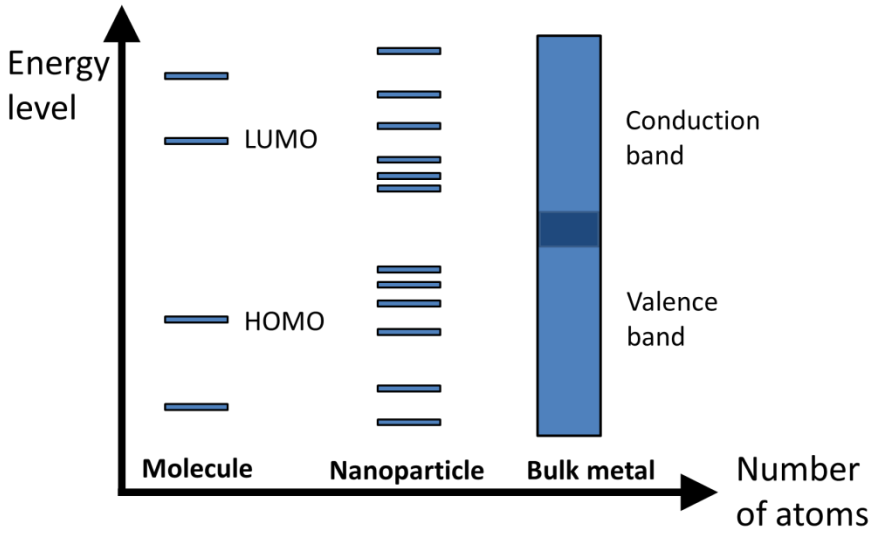

Figure 2.4 Illustration of the electronic energy levels in molecules, nanoparticles and bulk metals. Adapted from Reference 111. Copyright 2002 Taylor & Francis.

The influence of particle size on catalytic activity has long been an important discussion topic.[112] Following the definition of structure sensitivity given by Boudart,[113,114] reactions have been classified into three different categories:[99,115] i) Negative (antipathetic, class Ia) or positive (sympathetic, class II) structure-sensitive (demanding) reactions, ii) reactions with a local maximum (class Ib), and iii) structure-insensitive (facile, class III) reactions, as depicted in Figure 2.5. The first two categories correspond to reactions for which the turnover frequency (TOF, number of molecules reacting per number of active site per unit time) increases and decreases, respectively, with decreasing particle size. The reactions in class Ib exhibit a maximum in TOF as the particle size is varied. All structure-sensitive reactions require the presence of specific catalytic sites with particular geometric requirements (ensemble size effects). The last class corresponds to reactions unaffected by

particle size, for which typically all the atoms at the surface are available for reaction.[116,117] It should be noted that size variations are often accompanied by structural changes, and that the origin of the effect observed is not always clearly identified.[94,103]

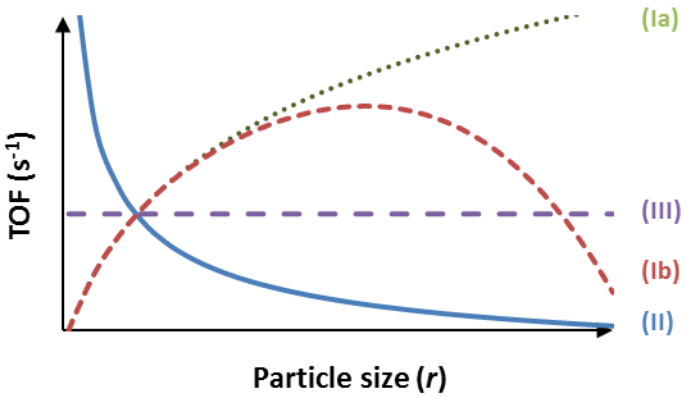

Figure 2.5 Schematic illustration of the dependence of the turnover frequency (TOF) on the size of nanocatalysts for major classes of reactions: (Ia) negative and (II) positive structure-sensitive reactions, (Ib) reactions with a mix of positive and negative structure sensitivity, and (III) structure-insensitive reactions. Adapted with permission from Reference 20. Copyright 2013 Wiley-VCH.

2.3.3 Shape, composition, and support effects

Additional parameters are found to have important effects on the catalytic performance of nanoparticles. For structure-sensitive reactions, the shape of a catalyst governs the type of surface facets, as well as the proportion of atoms at corners, edges, and planes; it thereby plays a significant role in controlling the activity and selectivity of nanocatalysts.[118] A variety of strategies devised for the preparation of shape-controlled noble metal nanocrystals with interesting catalytic activity have been reviewed recently in several publications.[44,50,102,118–126] As illustrated in Figure 2.6, Pd NPs of various shapes have been

prepared such as cubes, cuboctahedra, octahedra,[127,128] concave tetrahedra, concave trigonal bipyramids,[129] decahedra, icosahedra,[127,130] rhombic dodecahedra,[131] trapezohedra, hexoctahedra,[132] bars, rods,[127] five-fold twinned rods[133] and plates.[134]

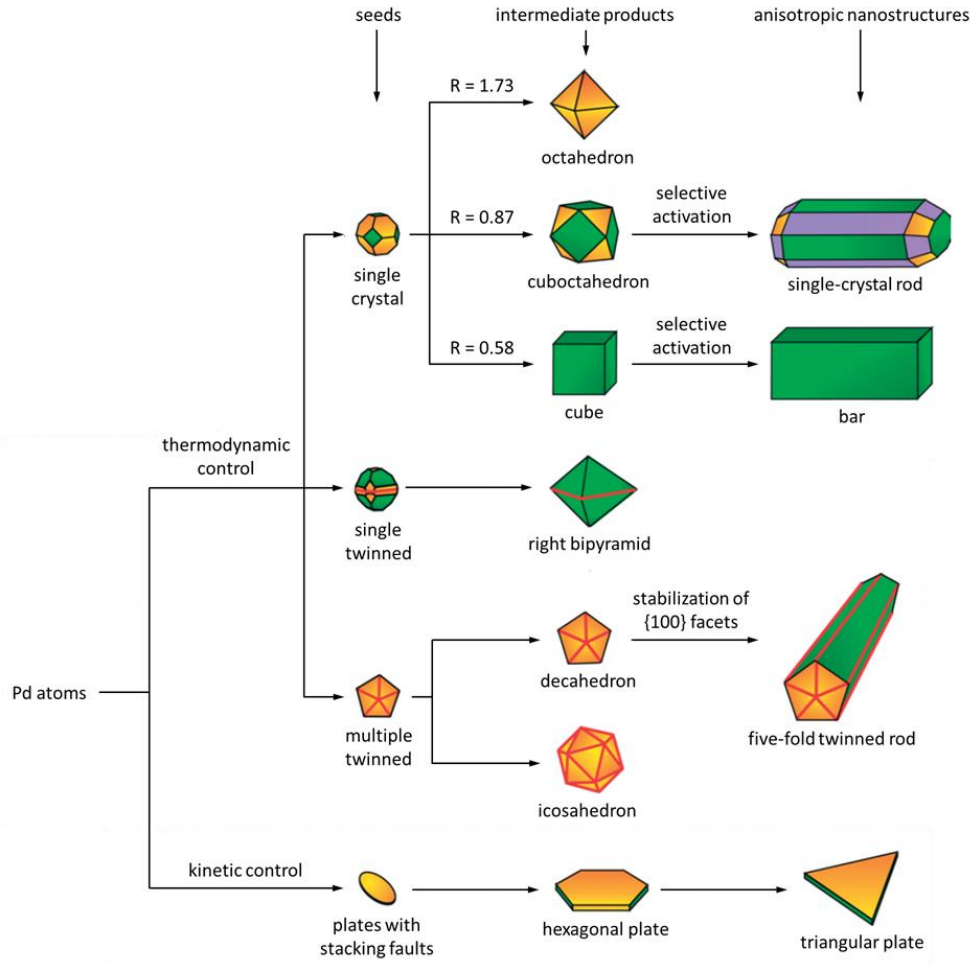

Figure 2.6 Schematic illustration of the preparation of Pd nanostructures with different shapes by reduction of a Pd precursor. The green, orange, and purple colors represent the {100}, {111}, and {110} facets, respectively. The ratio *R* of the growth rate along the <100> and <111> axes determine the evolution of the single-crystal seeds into particles of different shapes. Reprinted with permission from Reference 119. Copyright 2007 Wiley-VCH.

In their seminal work, Narayanan and El-Sayed compared the catalytic activity of tetrahedral, near spherical, and cubic Pt nanoparticles in the electron transfer reaction between hexacyanoferrate(III) and thiosulfate ions.[135] By determining the activation energy and the average rate constant of the reactions, they found a correlation between the fraction of atoms located on the corners and edges of the particles and the catalytic activity – which varied as tetrahedral > near spherical > cubic. The same authors reported a decrease in the rate of the Suzuki-Miyaura (SM) cross-coupling reaction between phenylboronic acid and iodobenzene as the shape of the Pt NPs rearranged from tetrahedral to near spherical during the reaction.[136] Comparison of the catalytic activity of Pd concave nanocubes, displaying high-index facets {730}, with conventional nanocubes in the SM coupling reaction revealed a TOF 3.5 times higher when using the former catalyst.[137] Nanorods and branched nanocrystals, synthesized by a seed-mediated growth approach, likewise displayed a high catalytic activity in the SM coupling reaction.[138]

The intrinsic composition of nanoparticles also greatly influences the performance of a catalyst. In particular, bimetallic and multimetallic structures have displayed synergetic effects between the different metal elements, with enhanced catalytic performance as compared to their monometallic counterparts. A variety of bimetallic nanocatalysts have been prepared with core-shell, cluster-in-cluster, hetero- and alloyed structures, and employed in several reactions such as hydrogenation, hydration, electro-oxidation, oxidation, reduction, aromatization, combustion, and cross-coupling reactions.[139] The enhanced performance of bimetallic catalysts is often interpreted in terms of ensemble and/or electronic (ligand) effects. For instance, Scott et al. reported higher TOFs for bimetallic Au-Pd nanoparticles

than for Pd NPs in the oxidation of alcohols and in hydrogenation reactions.[140] Using trimetallic Au-Ag-Pd nanoparticles, Venkatesan and Santhanalakshmi obtained a higher catalytic activity in SM cross-coupling reactions than for monometallic Pd nanoparticles.[141] Choi et al., using ZnO-supported bimetallic nanoparticles of Pd and Ag, Ni or Cu prepared by γ-irradiation,[142] or Pd-Cu supported on carbon,[143] also achieved better catalytic activity than for their monometallic counterparts in SM reactions.

In heterogeneous catalysis, nanoparticles are typically deposited onto a solid support that provides advantages in terms of particle dispersion, stability, recovery, handling, and recycling.[144] For instance, a variety of supports have been applied to the preparation of Pd NPs for cross-coupling reactions including metal oxides (alumina, silica, zeolites, etc.),[145–147] carbonaceous materials (activated carbon,[147] graphene,[148] nanotubes[149]), polymers,[150–153] dendrimers,[154] and more recently biomaterials.[155–157] For small particle sizes, interactions with the support can affect the electronic properties of the surface atoms and dramatically alter their catalytic activity.[102,158–161] For instance, while carrying out theoretical and experimental studies on Pd nanoclusters, Pacchioni et al. uncovered the special role of point defects (particularly F-centers) on the surface of MgO supports for the catalytic activation of Pd in the cyclization reaction of acetylene.[162] Another important example of support effect was illustrated in the seminal studies by Haruta et al. on the catalyzed oxidation of CO by O_2 on oxide-supported Au nanoparticles.[163–164]

2.4 Nanoparticle synthesis and aggregation

2.4.1 Nanoparticle synthesis

Since the first description by Faraday in 1857 of the synthesis of colloidal gold NPs,[165] a variety of methods have been devised for the preparation of nanoparticles for all the transition metal elements.[166] While these have been traditionally divided between top-down and bottom-up approaches, the advancement of nanosciences has largely favored the latter approach which generally provides better control over the size, structure, shape and composition of the particles.[36,167]

The top-down approaches proceed by size reduction of bulk metals down to the nanometer size range, and subsequent stabilization of the particles. Some limitations of these techniques include the level of impurities and surface imperfection of the particles.[168] Size reduction of the bulk metal can be performed by several physical methods such as mechanical grinding[42] (ball milling,[169] attrition[170]), controlled vapor deposition (chemical[171] or physical[172]), pulsed laser deposition,[173,174] arc melting,[175] flame combustion,[176] microwave plasma discharge,[177] and various lithographic techniques (e.g., electron beam lithography,[174,178] focused ion beam irradiation etching[179] and sputtering,[180,181] X-ray interference lithography,[182] UV lithography,[183] laser interference lithography[184]).

In the case of bottom-up strategies, the nanoparticles are synthesized by the controlled decomposition or reduction of a metal precursor in the presence of a stabilizer. Three main *wet chemical* strategies have been employed in this regard, namely i) metal salt reduction, either chemically or electrochemically, ii) thermolysis via photolytic, radiolytic or sonochemical pathways, and iii) controlled decomposition of organometallic compounds.[36,47]

Lithographic techniques may be regarded as hybrid, since etching is associated with top-down approaches while nanolithography and the growth of thin films are usually linked to bottom-up schemes.[168] Comprehensive reviews have treated both the size reduction[35,42,44,57–59] and the molecular self-assembly strategies.[23,28–56]

2.4.2 Metal salt reduction

Among the synthetic *wet chemistry* methods, the reduction of metal salts has become the most common route for the preparation of transition metal nanoparticles due to its simplicity and advantages.[36,39] The reduction of a metal salt to yield zerovalent metal atoms proceeds as expressed by Equation 2.2.[55] The concomitant oxidation of species *X* is also shown in Equation 2.3. The formation of metal atoms in the embryonic stage of nucleation is controlled by the difference in redox potentials between the metal salt and the reducing agent, and can lead to the formation of metal *seeds* with a size well below 1 nm (vide infra).[39]

$$M^{n+} + ne^- \rightarrow M^0 \tag{2.2}$$

$$X^m - ne^- \rightarrow X^{m-n} \tag{2.3}$$

A wide variety of metal salts and reducing agents have been employed for this purpose. Some representative examples for the preparation of Pd NPs are provided in Table 2.1. Metal salt precursors are typically palladium chloride and carboxylate derivatives, and the reducing agents employed include hydrogen, carbon monoxide, hydrides, carboxylic acids, salts, oxidizable solvents, and polymers.[36] Invariably, a stabilizer is used in the synthetic protocol to confer colloidal stability and to control the size, size distribution and

shape of the nanoparticles. The different types of stabilization mechanisms and stabilizers employed are reviewed in Section 2.4.5.

Table 2.1 Precursors and reducing agents used for the preparation of polymer-stabilized Pd nanoparticles.

Compound	Formula	Reference
Precursor		
Palladium chloride	$PdCl_2$	Nord et al.[185]
Palladium acetylacetonate	$Pd(acac)_2$	Hashimoto et al.[186]
Palladium bis(dibenzylideneacetone)	$Pd(dba)_2$	Bradley et al.[187]
Palladium acetate	$Pd(OAc)_2$	Astruc et al.[188]
Ammonium tetrachloropalladate	$(NH_4)_2PdCl_4$	Mayer,[189] Zhou et al.[190]
Sodium tetrachloropalladate	Na_2PdCl_4	Antonietti et al.[191]
Potassium tetrachloropalladate	K_2PdCl_4	El-Sayed et al.[192]
Reducing agent		
Carbon monoxide	CO	Chaudret et al.[193]
Hydrazine	N_2H_2	Antonietti et al.[194]
Hydrogen	H_2	Mecking et al.[195]
Ascorbic acid	$C_6H_8O_6$	Adschiri et al.[196]
Ammonia-borane	H_3NBH_3	Metin et al.[197]
Sodium borohydride	$NaBH_4$	Antonietti et al.[194]
Potassium borohydride	KBH_4	Mayer et al.[198]
Lithium triethylhydroborate	$LiBEt_3H$	Toshima et al.[199]
Sodium triethylhydroborate	$NaBEt_3H$	Biffis et al.[150]
Sodium carbonate	$NaCO_3$	Nord et al.[185]
Triethylsilane	Et_3SiH	Shifrina et al.[200]
Acyl tetraethylammonium pentacarbonyltungstate (Fischer carbene complex)	$(CO)_5W{=}C(Me)ONEt_4$	Sarkar et al.[201]
Methanol	MeOH	Miyake et al.[202]
Ethanol	EtOH	Hirai et al.,[203]
1-Propanol	*n*-PrOH	Miyake et al.[202]
1-Butanol	*n*-BuOH	Hirai et al.[203]
Polysilane		Sanji et al.[204]
Poly(ethylene oxide) (in pluronic copolymer)	PEO	Hyeon et al.[205]
Hydrosilane (in polymethylhydrosilane)	PMHS	Chauhan et al.[206]
hybr-Poly(glycerol)/heat		Mecking et al.[195]

2.4.3 Particle nucleation

Although still under debate,[207] metal nanoparticle formation is generally understood as a stepwise process proceeding through the nucleation, growth and agglomeration of nanoclusters. The reduction of a metal salt precursor produces zerovalent species that can collide in solution with other ionic species, reduced metal atoms, and/or small clusters of atoms to yield stable nuclei (seeds).[47,207] An illustration of a nucleation and growth mechanism proposed by Bönnemann et al. is shown in Figure 2.7. Alternately, nucleation may occur via the reduction of dimeric and trimeric species formed by the metal precursors, as demonstrated for the reduction of Pt complexes.[47,123]

During decomposition of the metal precursor, the concentration of metal atoms (atomic concentration) increases with time in solution (Figure 2.8). Above a critical concentration $C_{\min}^{\mathrm{nu}}$, the atoms aggregate into small clusters which can further grow to yield nanocrystals. As the clusters are formed, the concentration of metal atoms in solution can decrease below $C_{\min}^{\mathrm{nu}}$ at which stage no further nucleation events take place and only growth of the nuclei is promoted.

According to classical nucleation theory,[208] the overall change in free energy ΔG during the nucleation process can be expressed as the sum of the free energy contributions of the volume and the surface created;[44,122] which for spherical particles can be written as:

$$\Delta G = -\frac{4}{3V}\pi r^3 k_{\mathrm{B}} T ln(S) + 4\pi r^2 \gamma \tag{2.4}$$

where V is the molecular volume of the bulk crystal, r is the radius of the clusters, k_{B} is the Boltzmann constant, T is the solution temperature, S is the saturation ratio between the solute

concentration at saturation $[A]_s$ and at equilibrium $[A]_{eq}$ ($S = [A]_s/[A]_{eq}$), and γ is the surface free energy per unit surface area.

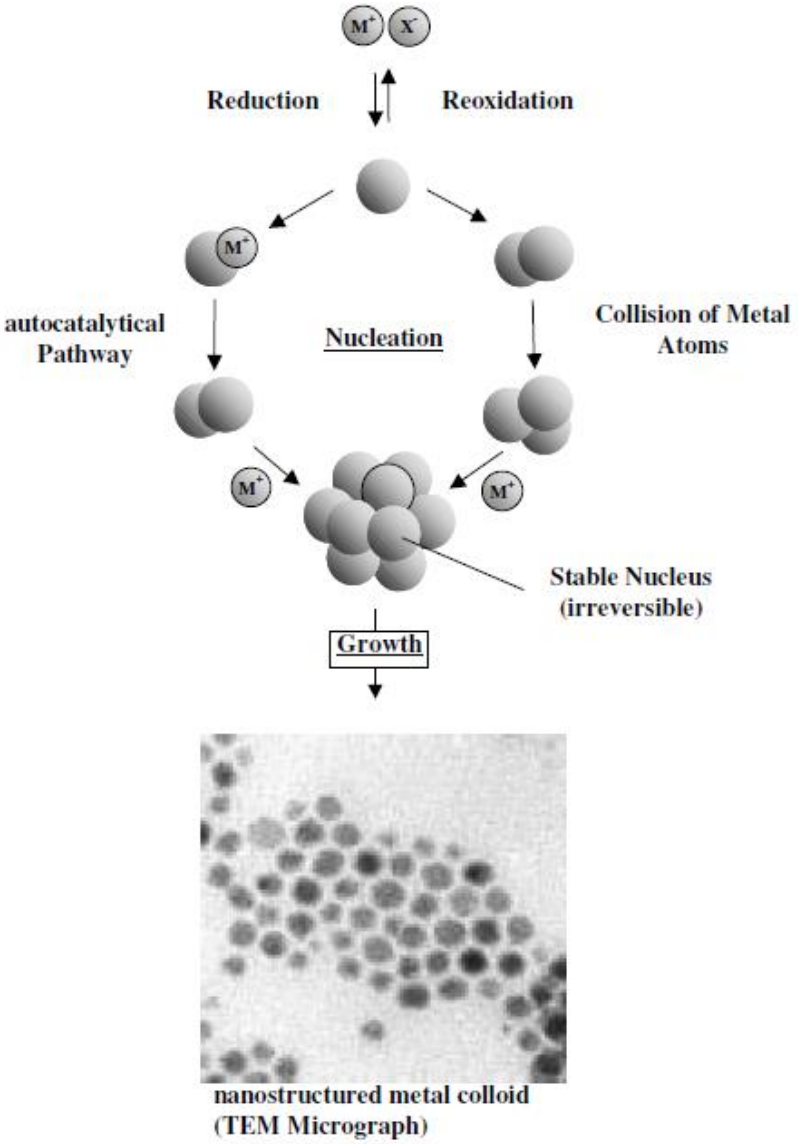

Figure 2.7 Schematic illustration of the formation of Pd colloidal nanostructures by reduction of a salt precursor. Reprinted with permission from Reference 39. Copyright 2004 Kluwer Academics.

The critical nucleus size r^*, obtained by solving the equation $d\Delta G/dr = 0$, is

$$r^* = -\frac{2\gamma V}{k_B T ln(S)} y \tag{2.5}$$

In supersaturated conditions (i.e., $S > 1$), ΔG displays a maximum at the critical nucleus size r^* and becomes negative for cluster sizes greater than r^*. Therefore, for a given S, the nuclei formed above a critical size become stable and grow to yield larger particles (Figure 2.8). Growth is promoted by the diffusion and adsorption of the soluble species onto the particle surface, or by aggregation with other particles (secondary growth).[123,209]

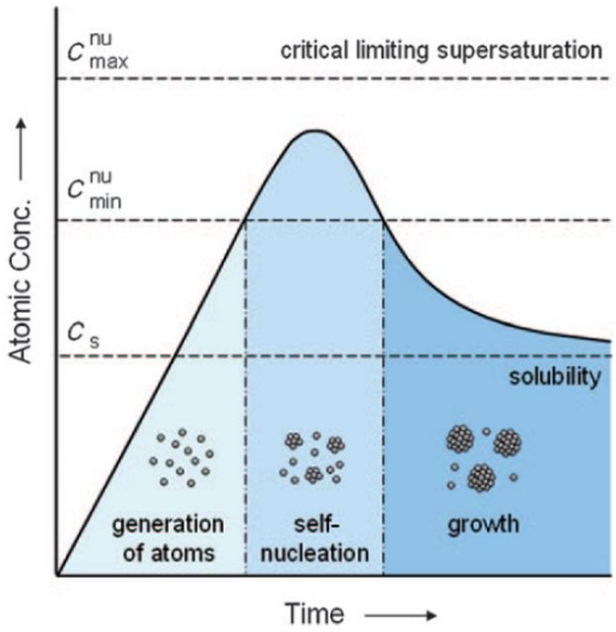

Figure 2.8 Schematic representation of the evolution of the atomic concentration with time in the decomposition of a metal precursor. Above a critical concentration C^{nu}_{min}, atoms start to aggregate into small clusters via self-nucleation. As the atomic concentration decreases below C^{nu}_{min}, no further nucleation takes place and only particle growth occurs. Reprinted with permission from Reference 123. Copyright 2009 Wiley-VCH.

At a specific reactant composition, the relative rates of the nucleation and growth steps govern the size of the particles formed.[207] The preparation of nanoparticles with a narrow size distribution necessitates a short nucleation event (burst nucleation) followed by a slower growth period. Broader size distributions are expected when the nucleation and growth steps overlap, as different growth periods will take place for the particles.[47] However, as the solute is consumed during the growth period, the critical nucleus size increases (since the saturation ratio *S* diminishes). As a result, the growth of larger nanocrystals takes place at the expense of smaller nanoclusters in a defocusing process known as Ostwald ripening.[44] Broad size distributions, with a bimodal distribution of larger and smaller particles, are characteristic for defocusing events. The total disappearance of smaller particles may eventually occur if the process is allowed to proceed to completion.

2.4.4 Colloidal interactions

Particles in solution are subject to various interaction forces, the balance of which can result in particle aggregation or stabilization. The interaction potential of colloidal dispersions has been explained on the basis of the DLVO theory, enunciated independently by Derjaguin and Landau,[210] and Verwey and Overbeek,[211] as well as on the basis of structural forces such as steric repulsion.[212]

The DLVO theory invokes contributions from attractive van der Waals forces (with potential energy V_A), repulsive electrical double layer interactions (with potential energy V_R), and short-range Born repulsions (with potential energy V_B). Assuming the additivity of the different contributions, the total potential energy of interaction V_T is given by Equation 2.6.

$$V_T = V_A + V_R + V_B \tag{2.6}$$

Each interaction potential is expressed in terms of the interparticle distance h. For instance the interaction energy V_A at close approach, for two spheres of radius r, can be evaluated using Equation 2.7, where A is the Hamaker constant for the particles (for metals,[213] $A \approx 4\times10^{-19}$ J).[214]

$$V_A \approx \frac{-Ar}{12h} \tag{2.7}$$

The sphere-sphere double layer interaction can be calculated as a function of the zeta potential ζ using Equation 2.8, where e is the electron charge and κ is the Debye-Hückel reciprocal length.

$$V_R = 2\pi er\zeta^2 e^{-\kappa h} \tag{2.8}$$

Lastly, an estimation of the Born repulsions for sphere-plate interactions is given by Equation 2.9, where σ_c is the collision diameter (typically ca. 0.5 nm); a more general equation in the case of sphere-sphere interactions was given by Feke et al.[215]

$$V_B = \frac{A\sigma_c^6 + h}{7560}\left(\frac{8r + h}{(2r + h)^7} + \frac{6r - h}{h^7}\right) \tag{2.9}$$

A characteristic interaction profile V_T describing the evolution of the potential energy as a function of the interparticle distance is represented in Figure 2.9. It is seen that a secondary minimum exists in the potential energy curve, which promotes the formation of weak aggregates as the particles approach each other. The colliding particles must overcome a potential energy barrier to come into close contact. The magnitude of the activation energy (potential energy maximum) will directly influence the ability for the particles to form

aggregates held together by strong van der Waals interactions in the low energy primary minimum.

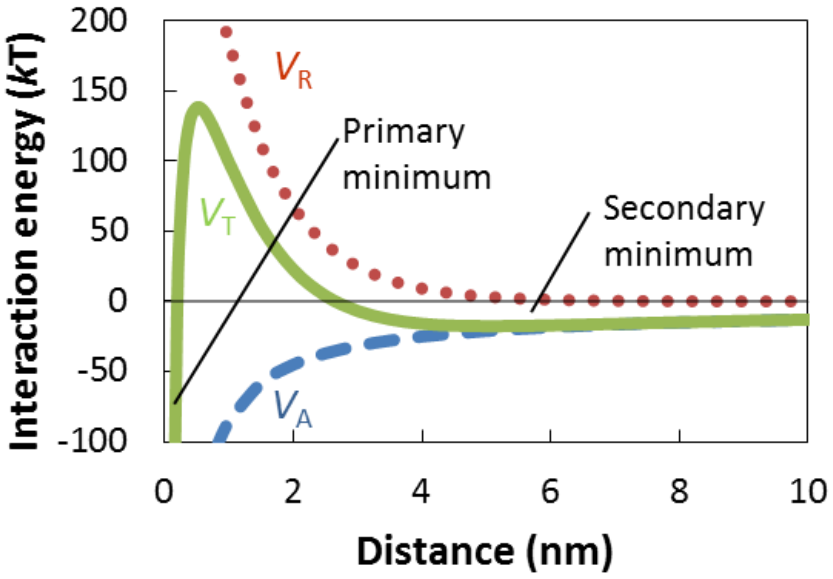

Figure 2.9 Schematic representation of the van der Waals (V_A), electric double layer (V_R), and total interaction (V_T) energy as a function of the interparticle distance. Adapted with permission from Reference 122. Copyright 2008 Elsevier.

2.4.5 Particle stabilization

As previously mentioned, a stabilizer plays an essential role in controlling the nucleation and growth of nanoparticles, but also in preventing their agglomeration. Being only kinetically stable, the nanoparticles will tend to aggregate to reach a thermodynamic minimum favoring a low surface-to-volume ratio and bulk metal formation.[216] Stabilization can be accomplished by various means: electrostatically, sterically (with polymers or ligands), electrosterically (with both steric and electrostatic contributions), with solvent molecules, and via depletion stabilization (Figure 2.10).[47,57]

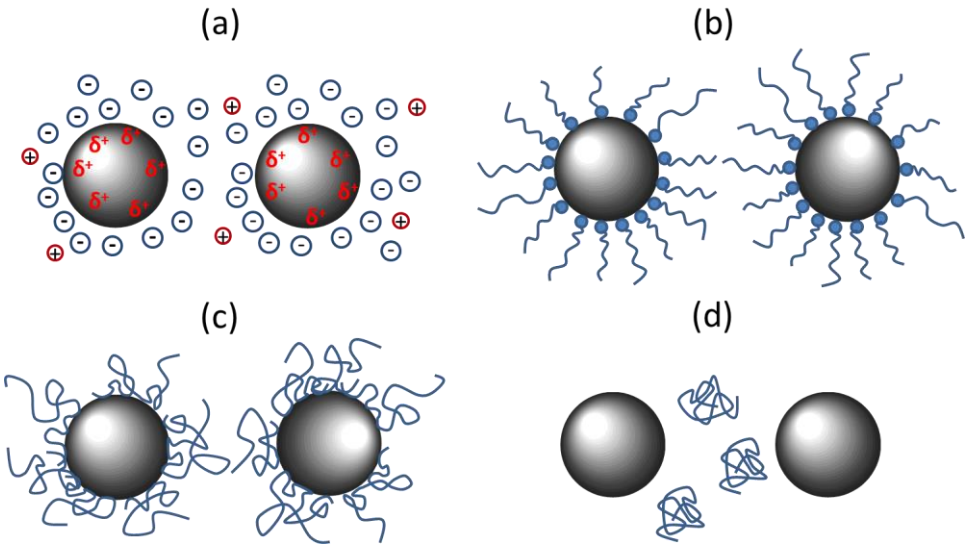

Figure 2.10 Schematic illustration of the stabilization of metal nanoparticles: (a) electrostatically, (b) sterically with low molar mass ligand molecules, (c) sterically with polymers, and (d) by a depletion mechanism.

Electrostatic stabilization takes place when van der Waals interactions are counterbalanced by an electrical double layer formed by the accumulation of anions and cations at the particle surface. A partial positive charge can be induced upon adsorption of anions on the surface of the coordinatively unsaturated metal surface as an *electrostatic charge mirror*.[78] Steric stabilization is promoted by large organic molecules adsorbed at the surface of the dispersed particles, which induce repulsive contributions between the colloidal particles (vide infra). A combination of electrostatic and steric stabilization mechanisms, known as electrosteric stabilization, results from the presence of charged species on bulky molecules such as polyelectrolytes or surfactants. Even solvent molecules have been shown to promote colloidal stability at low particle concentrations. In some instances the presence

of polymeric chains that are not attached to the nanoparticle surface can also favor stabilization, by introducing repulsive osmotic forces between the particles (depletion stabilization).[217]

2.5 Steric stabilization

More efficient colloidal stabilization is generally achieved with polymeric stabilizers. Macromolecular chains adsorbed at the surface of the particles induce steric stabilization by preventing their close approach, to a range where van der Waals interactions become significant. The affinity of polymeric moieties for the particle surface results in their adsorption at several anchoring sites, while the non-interacting portions of the chains (adopting various conformations such as *trains*, *loops* and *tails*) promote steric stabilization.[218] The two main effects favoring stabilization are entropic and osmotic in origin. The first effect stems from the reduced configurational freedom of the polymer chains when the particles approach each other, while the second contribution is spawned by the solvation of domains displaying a higher local thermodynamic activity (effective concentration).[219–221] Due to numerous interactions between the monomeric units and the particle surface, even relatively weak interactions can result in overall strong and irreversible adsorption.[222] In the particular case of block copolymers, the lyophilic block – non-interacting with the particle surface – provides additional steric stabilization to the colloidal dispersion.

Since the Hamaker constant is generally low for macromolecules,[212] the tendency for aggregation through the adsorbed layer is minimal. As a matter of fact, desolvation of the

hydrophilic segments and/or entropically unfavorable confinement[218] of the chains upon close approach result in an increase in the free energy of the system and repulsion between the particles. The repulsive energy per molecule $E(h)$ between two polymer chains end-grafted onto a flat surface in the so-called "mushroom" regime (i.e., at a relatively low surface coverage), as proposed by Li and Pincet, is given by Equation 2.10, where k_B is the Boltzmann constant and R_g the radius of gyration of the polymer chains.[223]

$$E(h) = 36k_BTe^{-\frac{\sqrt{3}h}{2R_g}} \tag{2.10}$$

For weakly bound polymers, the description is more complicated because of the dynamic nature of the interactions upon approach of the particles. In this situation, both the amount of polymer adsorbed and the number of binding sites may change over time as the two surfaces approach each other.[218]

2.5.1 Gold number and protective value

A parameter characterizing the ability of a polymer to impart colloidal stability was proposed by Zsigmondy as the *gold number*.[224] This value was defined as the number of milligrams of stabilizer which is just *insufficient* to prevent a change in color for 10 mL of a red gold sol to violet when 1 mL of 10% NaCl solution is added to it. Another measure, later proposed by Thiele and coined the *protective value*, was defined as the number of grams of gold in a red gold sol which could be protected by 1 gram of the protective agent against flocculation upon addition of a 1% NaCl solution.[225] The gold number and protective value of a series of polymers, as reported by Thiele and von Levern, are compared in Table 2.2.[225]

Table 2.2 Protective value and gold number of polymeric stabilizers by Thiele and von Levern. Adapted with permission from Reference 225. Copyright 1965 Elsevier.

Protective agent	Protective value	Gold number
Natural		
Hemacel®	100	0.004
Gelatin	90	0.005
Chondroitin sulfate	4	0.1
Heparin	0.2	2
Algin acid amide	0.2	2
Ox albumin povite	0.09	5
Na-alginate	0.04	10
Pepsin, trypsin	0.04	10
Synthetic		
Poly(acrylic acid hydrazide)	400	0.001
Poly(*N*-vinyl-5-methoxazolidone)	70	0.006
Poly(*N*-vinyl-2-pyrrolidone)	50	0.009
N-Alkyl polyimine	40	0.02
Albatex® PO	20	0.02
Poly(vinyl alcohol)	5	0.09
N-Acetyl polyimine	2	0.2
Polyacrylamide	1.3	0.3
Poly-*L*-lysine hydrobromide	1	0.4
Polyacrolein	0.4	1
Poly(acrylic acid)	0.07	6
Polyethylenimine	0.04	10
Poly(4-vinylpyridine-*co*-methyl vinyl ketone)	0.005	90

2.5.2 Control of nanoparticle synthesis

In practice, metal salt reduction can precede or follow the polymer coordination process. In the former case, the structure of the nanoparticles is governed solely by the synthetic protocol. Steric stabilization occurs subsequently through the formation of a polymer-metal *atom* complex. Coordination of the metal ions prior to salt reduction is usually favored however, since the interactions with the polymer chains affect the nucleation and

growth processes, and offers control over the size and structure of the nanoclusters. This protocol can also yield greater steric stabilization by promoting interactions between the reduced metal species and the polymeric stabilizer (Figure 2.11).[31] In both instances, the polymer can be used to modulate the dispersibility of the nanoparticles in polar or non-polar solvents.[226]

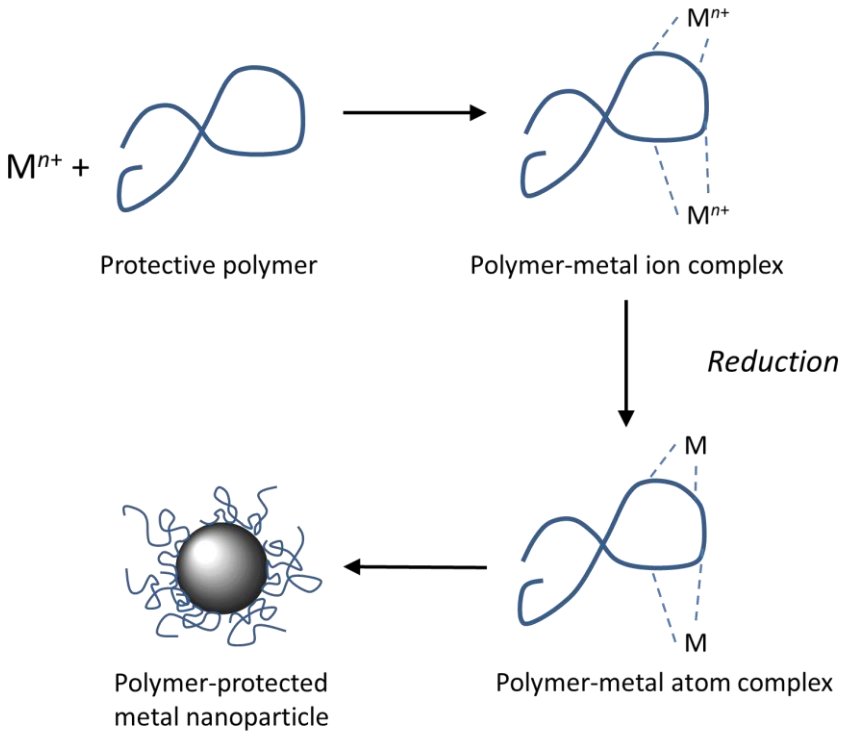

Figure 2.11 Schematic representation of the reduction of a metal salt in the presence of a polymeric stabilizer. Adapted with permission from Reference 31. Copyright 1998 The Royal Society of Chemistry.

The influence of the polymer in the reduction of metal ions has been studied in detail by Hirai et al. in the case of the alcohol reduction of Rh salts in presence of poly(vinyl alcohol), poly(vinyl methyl ether), and poly(*N*-vinyl-2-pyrrolidone).[227–231] The model

proposed relied upon complexation of the metal salt by the polymer via electrostatic interactions, physical adsorption or coordination, followed by reduction with methanol to Rh(0).[29] The polymer covering the metal particles was found to mediate nanoparticle growth and prevent further aggregation. The attractive forces between metallic rhodium and the polymer chains were assumed to be governed by hydrophobic interactions.

In the preparation of colloidal Pd from $PdCl_2$, Nord et al. highlighted a different mechanism where poly(vinyl alcohol) could also act as reducing agent in the formation Pd(0).[232] Later Smith and Wychick, while studying the thermal decomposition of $Fe(CO)_5$ in the presence of polymers, differentiated between *active* and *passive* polymers to rationalize the formation of nanoparticles according to a *locus control formalism*.[233] In this description, a functional polymer binds with a metal precursor and serves as functional locus for the decomposition of the metallic species by creating discrete domains. The nucleation and growth of the nanoparticles occur within the polymeric domains, which determine the number of particles formed (Figure 2.12). In this formalism, active polymers participate catalytically in the decomposition of the metal precursor while passive polymers do not influence the decomposition rate of the organometallic compound.

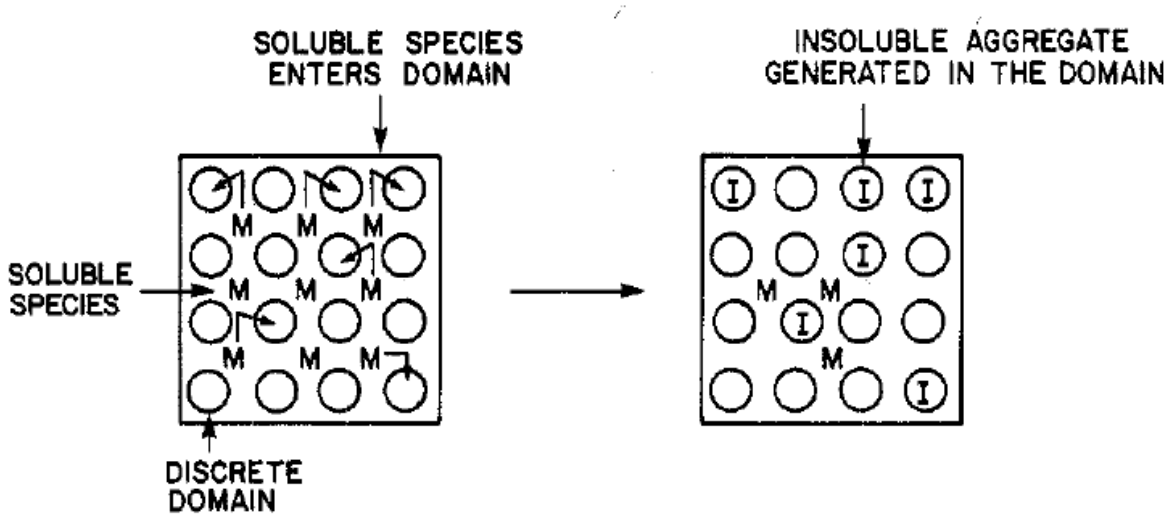

Figure 2.12 Schematic illustration of the *locus control formalism* proposed by Smith and Wychik. The molecular species *M* undergoes reduction within polymeric domains (circles) dispersed in a continuous medium, which determines the number of particles formed. Reprinted with permission from Reference 233. Copyright 1980 American Chemical Society.

2.5.3 Polymer bridging

In some instances, individual polymer chains may rather induce flocculation by adsorbing on the surface of multiple particles as illustrated in Figure 2.13. This phenomenon, known as bridging, is favored for high molar mass polymers, particularly at low particle surface coverage.[212] The attractive energy per bridging molecule between two surfaces is expressed as a function of the binding energy ε per segment by Equation 2.11, where n is the number of monomers in the polymer chain and l is the monomer length.[218]

$$E_{bridging}(h) = -\frac{\varepsilon(nl - h)}{l} \tag{2.11}$$

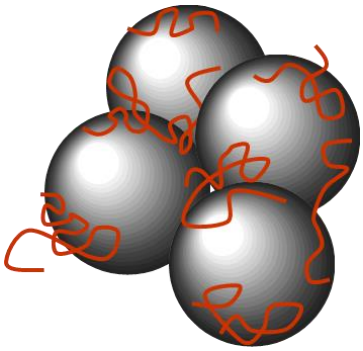

Figure 2.13 Schematic illustration of bridging flocculation promoted by low surface coverage and high molar mass polymers. Adapted from Reference 234. Copyright 1995 Butterworth-Heinemann.

2.5.4 Effect of polymers on catalytic activity

For a polymer-inorganic system, a high protective value is beneficial in terms of colloidal stability; however, strong interactions between the polymer and the particle surface can also hinder access of the substrate molecules to the catalytically active sites. Polymers with weak local coordination between the monomeric units and the metallic surface may therefore be preferable, as they can still provide strong colloidal stabilization through the involvement of multiple binding sites (Figure 2.14). Local displacement of the bonds between the polymer and the surface takes place upon approach of a substrate molecule, while stabilization is promoted by the remaining multiple interactions.[235] This contrasts, for instance, with the stabilization of nanoparticles by small molecules, which typically requires strong interactions with the metallic surface and results in lower catalytic activity.[37,236]

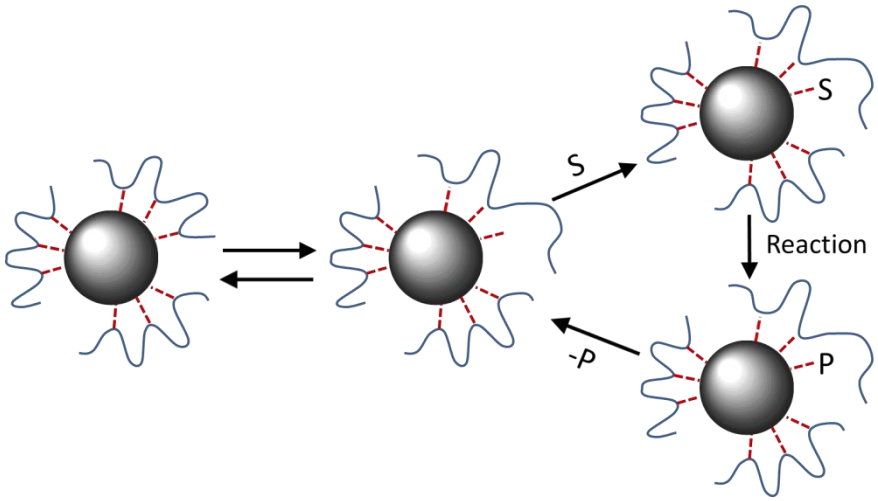

Figure 2.14 Schematic illustration of a weakly coordinating polymer attached to a metal catalyst surface. The substrate molecule *S* can replace a coordinating site of the polymer chain to form product *P* of the catalyzed reaction. Adapted with permission from Reference 37. Copyright 2003 Kluwer Academic.

Long polymer chains surrounding a metal catalyst may also affect negatively the activity of a catalytic system by sterically hindering the approach of a substrate. This phenomenon was observed by Klingelhöfer et al. while using Pd NPs stabilized by PS-*b*-P4VP micelles as catalysts in the Heck reaction:[237] The yield of the reaction between styrene and 4-bromoacetophenone in toluene was found to decrease by 1/3 when the molar mass of the stabilizing PS block was increased from 5,000 to 15,000 g·mol^{-1}.

The polymer may furthermore modify the catalytic activity and selectivity of a nanocatalyst by influencing the environment of the particles; this effect is known as the *polymer field* or *reaction field*.[13] For instance, specific interactions between the substrate molecules or a promoter[238] and the polymer chains may increase the local concentration of

the former in the vicinity of the catalyst. This was observed for instance by Toshima et al. in comparing the performance of polymer-stabilized Rh nanoparticles either in solution or supported on *N*-(2-aminoethyl)-substituted polyacrylamide gels.[239] Despite increased steric hindrance, the hydrophilic and basic polymer support increased the catalytic activity and selectivity in the hydrogenation of olefins, by increasing the concentration of hydrophilic and acidic substrates near the catalyst.

2.6 Polymer stabilization of Pd nanoparticles

2.6.1 Nanoparticle-polymer interactions

Palladium, often regarded as one of the most efficient metals in catalysis, has been the subject of numerous studies and applications.[144,240,241] More recently Pd nanoparticles have attracted lots of attention because of the unique properties displayed by nanosized materials, and have been applied to a broad range of catalytic reactions including hydrogenation,[242–244] oxidation,[245] dehalogenation,[246] carbonylation,[247] and carbon-carbon bond formation.[192,248–251] The latter reaction, in particular, represents one of their most important applications.[252] We will particularly focus on the Suzuki-Miyaura (SM) carbon-carbon cross coupling reaction in this review, as it has showed great promise for green chemistry applications.[253] One should also add that Pd NPs have found other important applications including hydrogen storage[254] and sensing.[255]

Polymers have been widely employed to impart colloidal stability to Pd nanoparticles, especially for applications in catalysis. Macromolecules generally provide greater colloidal stability to Pd NPs as compared to lower molar mass stabilizers such as ligands, surfactants,

or coordinating solvents, particularly under the demanding conditions of many catalytic reactions.[199,256] The Pd NPs can complex with a wide range of functional groups bearing P, N, O, and S atoms, and different types of polymers have been used ranging from natural (e.g., gelatin, agar), biological (proteins, DNA, etc.), to linear, block and dendritic (co)polymers.[29,257] Representative examples of polymers used for the preparation of Pd NPs are provided in Table 2.3 to Table 2.7. Polymer-supported Pd nanocatalysts have also been used successfully and have been the topic of reviews.[34,258] Recent developments in this area include the use of porous organic polymers[259–262] and insoluble biopolymers (e.g., DNA,[263,264] fibroin,[265] plant materials[266]) as supports. These systems will not be covered in the present chapter however, which will focus on colloidal systems. It should be noted that insoluble polymeric supports and colloidal stabilizers can feature comparable properties. For instance, dispersible cross-linked polymers (microgels, Table 2.7) have been prepared for the stabilization of Pd NPs and employed as catalysts for the Heck and Suzuki reactions and for the selective oxidation of alcohols.[150,267–269]

Table 2.3 Homopolymer stabilizers for the preparation of colloidal Pd NPs.

Polymer	NP diameter (nm)	Reference
Neutral homopolymers		
Poly(*N*,*N'*-dialkylcarbodiimide)	3	Liu et al.[270]
Poly(2-ethyl-2-oxazoline)	1.6 ± 0.7	Mayer et al.[243]
Poly(ethylene glycol)	7.3–9.8	Sawoo et al.[201]
Poly(2-hydroxyethyl methacrylate)	21.5 ± 8.4 23.2 ± 6.8	Mayer et al.[271]
Poly(2-hydroxypropyl methacrylate)	9.1 ± 5.6	Mayer et al.[271]
Poly(*N*-isopropylacrylamide), thiol-terminated	2.8	Wei et al.[272,273]
Poly(methyl acrylate)	n/a	Nord et al.[185]
Poly(methyl methacrylate)	n/a	Nord et al.[185]
Poly(methyl vinyl ether)	5.4	Telkar et al.[274]
Poly(vinyl acetate) and derivatives (formvar, butvar, alvar)	n/a	Nord et al.[275]
Poly(vinyl alcohol)	5.7	Nord et al.[185,232] Hirai et al.[230] Chaudhari et al.[274]
Poly(*N*-vinyl-2-pyrrolidone)	6.0	Hirai[229]
Anionic polyelectrolytes		
Poly(acrylic acid)	5.0 ± 1.5	Coulter et al.[276]
Poly(2-acrylamido-2-methyl-1-propane sulfonic acid)	5.1 ± 2.3	Mayer et al.[243]
Poly(itaconic acid)	3.1 ± 4.1	Mayer et al.[243]
Poly(methacrylic acid)	6.8 ± 1.8	Mayer et al.[243]
Poly(styrenesulfonic acid)	4.0 ± 1.6	Mayer et al.[243]
Poly(vinylphosphonic acid)	n/a	Mayer et al.[243]
Poly(R-triazolylmethyl)styrene R = phenyl, ferrocenyl, sodium sulfonate	1.0 ± 0.2 to 25.2 ± 6.0	Astruc et al.[277]
Cationic polyelectrolytes		
Poly(3-chloro-2-hydroxypropyl-2-methacryloxyethyldimethylammonium chloride)	3.5 ± 0.98	Mayer et al.[278]
Poly(diallyldimethylammonium chloride)	6.1 ± 1.2	Mayer et al.[278]
Poly(2-hydroxy-3-methacryloxypropyltrimethyl-ammonium chloride)	5.7 ± 1.5	Mayer et al.[278]
Poly(methacrylamidopropyltrimethylammonium chloride)	5.0 ± 1.2	Mayer et al.[278]

Table 2.4 Block and star copolymer stabilizers for the preparation of colloidal Pd NPs.

Polymer	NP diameter (nm)	Reference
Linear copolymers		
Poly(butadiene-*co*-maleic acid)	2.7 ± 0.7	Mayer et al.[243]
Poly(butyl acrylate-*co*-acrylic acid)	7–20[b]	Mayer et al.[243]
Poly(4-styrenesulfonic acid-*co*-maleic acid)	3.5 ± 1.2	Metin[197]
Poly(methyl vinyl ether-*co*-maleic anhydride)	39.7 ± 11.0	Mayer et al.[278]
Poly(*N*-vinyl-2-pyrrolidone-*co*-acrylic acid)	2.6 ± 1.2	Mayer et al.[278]
Poly(*N*-vinyl-2-pyrrolidone-*co*-vinyl acetate)	3.0 ± 1.5	Mayer et al.[278]
Poly(ethylene oxide)-*block*-poly(ethylene imine)	n/a	Bronstein et al.[194]
Polystyrene-*block*-poly(ethylene oxide)	3.4–6.8	Mayer et al.[198]; Bronstein et al.[279]
Polystyrene-*block*-poly(methacrylic acid)	2.1–7.8	Mayer et al.[198]
Polystyrene-*block*-poly(sodium acrylate)	3.0 ± 0.7	El-Sayed et al.[192]
Polystyrene-*block*-poly(4-vinylpyridine)	9.8 ± 0.9	Antonietti et al.[191]
Poly(2-vinylpyridine)-*block*-polyisoprene	4–5	Hashimoto et al.[186,280]
Poly(2-vinylpyridine)-*block*-poly(ethylene oxide)	1.0–1.5 7	Bronstein et al.[281]
Polyion complex micelles		
Poly(acrylic acid)-*compl*-poly(ethylene imine)	6.0	Hirai et al.[229,282]
[Polystyrene-*co*-poly(ethylene oxide)]-*compl*-(cetylpyridinium chloride)	4–6	Bronstein et al.[279]
Triblock copolymers		
Poly(ethylene oxide)-*block*-poly(propylene oxide)-*block*-poly(ethylene oxide)	4.8 ± 0.5 to 27	Hyeon et al.[205]
Poly(methyl vinyl ether-*co*-maleic anhydride) *funct.*[a] (*R*)-2-aminobutanol	22	Favier et al.[283]
Polystyrene-*block*-polybutadiene *funct.*[a] *p*-chlorodiphenylphosphine	n/a	Antonietti et al.[284]
Star copolymers		
star-[Polystyrene-*block*-poly(2-vinylpyridine)]	2–3	Hawker et al.[285]
5-Arm *star*-[poly(ethylene oxide)-*block*-poly(ε-caprolactone)]	3.6 ± 0.2 to 4.7 ± 0.3	Schubert et al.[250]

[a] Functionalized; [b] precipitation after 1 day.

Table 2.5 Dendritic stabilizers for the preparation of colloidal Pd NPs.

Polymer	NP diameter (nm)	Reference
Hyperbranched and arborescent polymers		
hybr-Polyglycerol	2.1 ± 0.6 5.2 ± 1.8	Mecking et al.[195]
hybr-Poly(ethylene imine), alkylated	2–4	Neumann et al.[76]
Arb-Polystyrene-*graft*-poly(2-vinylpyridine)	n/a[a]	Dockendorff et al.[286]
Arb-Polystyrene-*graft*-[poly(2-vinylpyridine)-*block*-polystyrene]	n/a	Dockendorff et al.[287]
Dendrimers		
Poly(amidoamine), -OH, -NH_2	1.3 ± 0.3	Crooks et al.[244]
Poly(propylene imine)	2.2 ± 0.3 2.1 ± 0.3	Crooks et al.[249]
Poly(phenylene-pyridyl)	2.1 ± 0.3	Muellen et al.[200]
Poly(1,2,3-triazolylferrocenyl)	1.2 ± 0.2 to 2.8 ± 0.3	Astruc et al.[188]
Fréchet-type polyaryl ether dendrons	3.2 ± 0.5 to 5.0 ± 0.4	Fox et al.;[288] Fan et al.[289]

[a] Not reduced.

Table 2.6 Natural polymeric stabilizers for the preparation of colloidal Pd NPs.

Polymer	NP diameter (nm)	References
Gum arabic	n/a[a]	Nord et al.[232]
Gum tragacanth	n/a	Nord et al.[185]
Nitrocellulose	3.5	Chaudret et al.[193]
Cellulose acetate	3.5	Chaudret et al.[193]
i-motif DNA	1.02 ± 0.20 to 2.61 ± 1.15	Li et al.[295]
Pluricaria glutinosa	20–25	Siddiqui et al.[296]
Fish sperm	7–8	Wang et al.[297]
Calf thymus	5–8	Hori et al.[263]
λ-DNA	4.6 ± 1.3 to 20.1 ± 8.3	Adschiri et al.[196]
Peptide	1.9 ± 0.3 to 3.7 ± 0.9	Knecht et al.[298]
G-/C-rich oligonucleotides	1.3 ± 0.3 to 3.3 ± 1.3	Zhang et al.[299]

[a] Not reduced.

Table 2.7 Brush and microgel stabilizers for the preparation of colloidal Pd NPs.

Polymer	NP diameter (nm)	References
Brushes		
net-Polystyrene-*graft*-[poly(2-methylpropenoyloxyethyl) trimethylammonium chloride]	2.4 ± 0.5	Ballauff et al.[290]
net-Poly(*tert*-butyl acrylate)-*graft*-poly[methoxytri(ethylene glycol) methacrylate]	8.6 ± 3.0	Zhao et al.[291]
Microgels		
net-Poly(methacryloyloxyethyltrimethylammonium chloride)	3–50	Antonietti et al.[267]
net-Polymethylhydrosiloxane	6 ± 1	Chauhan et al.[206,292]
net-Polystyrenesulfonate	9–25	Antonietti et al.[267]
net-Poly(*N*,*N*-dimethylacrylamide-*co*-ethylene dimethacrylate-*co*-*N*,*N*-dimethylamino-ethyl methacrylate)	2.3 ± 0.8	Biffis et al.[150]
[*net*-Poly(methacrylic acid)]-*block*-poly(1,1-dimethyl-2,2-dihexyldisilene)	20 ± 10.7	Sakurai et al.[204]
(*net*-Polystyrene)-*co*-[*net*-(*N*-isopropylacrylamide)]	3.8 ± 0.6	Ballauff et al.[290]
Hydroxylated polyisoprene-[*net*-(poly(2-cinnamoyloxyethyl methacrylate)]-*block*-poly(*tert*-butyl acrylate)	<15	Underhill et al.[293,294]
net-[Poly(sulfoethyl methacrylate-*co*-methyl methacrylate-*co*-ethylene dimethacrylate)]	10–20	Biffis[268]

2.6.2 Linear polymers

As early as 1941, Rampino and Nord reported the preparation of Pd NPs by reduction of $PdCl_2$ with hydrogen in water and water/alcohol mixtures while using poly(vinyl alcohol) as stabilizer.[185,300] They thus obtained a catalytic performance superior to Pd/C for various hydrogenation reactions. Interestingly, they also noted a positive structure-sensitive behavior (activity increase for smaller particle sizes) for this catalyst in the hydrogenation of nitrobenzene.[232] Twenty-five years later, Hirai et al. extended the salt reduction method by

using alcohols as both solvents and reducing agents.[227] They also used a styrene-divinylbenzene copolymer functionalized with iminodiacetic acid groups as support, and the catalyst was active for the selective hydrogenation of diolefins to mono-olefins.[301] The same group further reported the use of poly(*N*-vinyl-2-pyrrolidone),[229] and a polyion complex of poly(acrylic acid) with poly(ethylene imine) (PEI) for the stabilization of Pd NPs, which were selective for the hydrogenation of diolefins.[282] The former polymer, in particular, proved to be a very efficient colloidal stabilizer for a variety of nanocatalysts, and it has even been qualified as a "magic polymer".[139] Among water-soluble polymers, colloidal stability was generally improved when the polymer backbone had hydrophobic character. Polymers with an oxygen-containing backbone such as poly(ethylene oxide) were rather poor steric stabilizers for Pd NPs.[278] Interestingly, the stable complexes formed between the metallic precursor and polymer functional groups such as amines were particularly difficult to reduce.[243] Hu et al. rather used the hydrophilic backbone of poly(*N*,*N'*-dihexylcarbodiimide) for the complexation of Pd(II).[270] This polymer had a rigid helical conformation resembling a cylindrical unimolecular micelle (Scheme 2.1),[302] providing remarkable stability to the reduced Pd NPs that were about 3 nm in diameter.

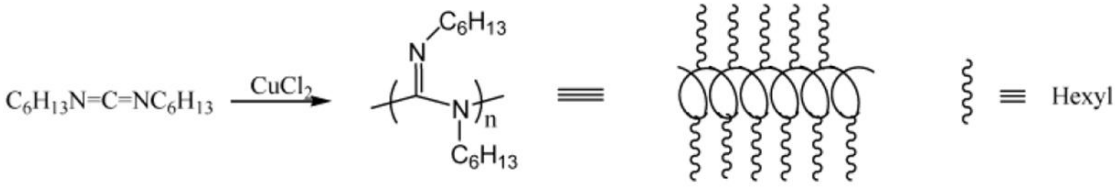

Scheme 2.1 Cu-catalyzed synthesis of poly(*N*,*N'*-dihexylcarbodiimide). Reprinted with permission from Reference 302. Copyright 2002 American Chemical Society.

Small-size (1.1–1.4 nm) Pd nanoparticles were obtained when using positively charged polymers such as poly(diallyldimethylammonium chloride)[303] and other polymeric quaternary ammonium chlorides.[278] This type of macromolecule provides both steric and electrostatic (i.e., electrosteric) contributions to the colloidal systems that can improve their stability. However the catalytic activity with these stabilizers was lower than for non-ionic polymers in the hydrogenation of cyclohexene.[243,278] Additionally, less stable dispersions were obtained when using polyacids as stabilizers.[243] Repulsion between the anionic precursors and the negatively charged polymer side groups were thought to be responsible for the poor interactions and stability.

2.6.3 Block and star copolymers

The utilization of block copolymers (BCPs) in the preparation of colloidal nanoclusters was introduced at the beginning of the 1990s.[304] The amphiphilic properties of BCPs promote the formation of micelles that can accommodate a metal precursor in their interior and act as nanoreactors. Block copolymers can afford control over the particle size and size distribution as well as over catalytic activity and selectivity. A wide range of BCPs have been used for the preparation of Pd nanoparticles in both organic and aqueous media (Table 2.4). For instance Antonietti et al., when using PS-*b*-P4VP as a stabilizer for the preparation of Pd NPs, demonstrated good catalytic activity for the selective hydrogenation of 1,3-cyclohexadiene to cyclohexene.[191] By adjusting the strength of the reducing agent, the morphology of the metal colloids could be varied from *cherry*- to *raspberry*-type structures (Figure 2.15).

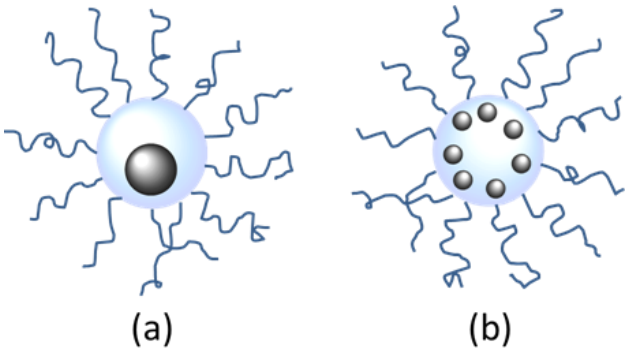

Figure 2.15 Schematic illustration of *cherry*- and *raspberry*-type morphologies for block copolymer-stabilized metal nanoparticles. The morphology obtained depends on the strength of the reducing agent used. Adapted with permission from Reference 191. Copyright 1995 VCH.

The group of Antonietti also prepared a series of amphiphilic block copolymers by epoxidation and ring opening of polystyrene-*block*-polybutadiene. Phosphine functionalities were introduced by reacting the epoxidized copolymer with *P*-chlorodiphenylphosphine, and complexed with Pd(II) in toluene. After reduction of the metal precursor, colloidal stabilization was promoted by the diphenylphosphine-functionalized copolymer.[284] Extending their work to the utilization of double-hydrophilic block copolymers, the same group reported the preparation of Pd colloids from PEO-*b*-PEI in aqueous media.[194] It is noteworthy that the addition of PEI alone resulted in precipitation of the metal-containing polymer, thus highlighting the role of the non-interacting PEO moiety to provide colloidal stability. Mayer and Mark rather used polystyrene-*block*-poly(methacrylic acid) and polystyrene-*block*-poly(ethylene oxide) as nanoreactors for the synthesis of Pd NPs with

sizes ranging from 1.3 to 7.8 nm. These systems were catalytically active in the reduction of cyclohexene, with full conversion obtained.[198]

Unimolecular micelles present an interesting alternative to BCPs, since their structure is independent of their concentration (they do not display a critical micelle concentration). A strategy for the preparation of amphiphilic star polymers by nitroxide-mediated radical polymerization was presented by Hawker et al. for PS-*b*-P2VP star copolymers.[285] After complexation of the polymeric templates with $Pd(OAc)_2$ and alcohol reduction, Pd NPs with a diameter of 2–3 nm were obtained. These catalytic systems were effective in the hydrogenation of cyclohexene (TOF = 138 h^{-1} atm $(H_2)^{-1}$) and in the Heck reaction between 1-bromo-4-nitrobenzene and *n*-butyl acrylate (TOF = 95 h^{-1}). No formation of Pd black was noted and the catalyst was reused five times without decrease in performance.

Using an automated synthesizer, Schubert et al. prepared star-shaped block copolymers with a poly(ethylene glycol) core by the controlled ring-opening polymerization of ε-caprolactone from a poly(ethylene glycol) macroinitiator (Figure 2.16).[305] Loading of the star copolymers with $Pd(OAc)_2$ in DMF and their subsequent reduction with $NaBH_4$ led to the formation of nanoparticles with a size ranging from 3.6 ± 0.2 to 4.1 ± 0.1 nm.[250] Broader size distributions were noted for short poly(ε-caprolactone) segments (degree of polymerization $\leq$ 6), as insufficient steric stabilization was imparted by these chains. The colloidal species were stable for at least 3 months, and only minor aggregation occurred after heating the solutions to 100 °C for three days. The Pd NPs were also active as catalysts in the Heck reaction between 4-bromoacetophenone and styrene, a reaction likewise performed in an automated fashion with a robotic synthesizer.

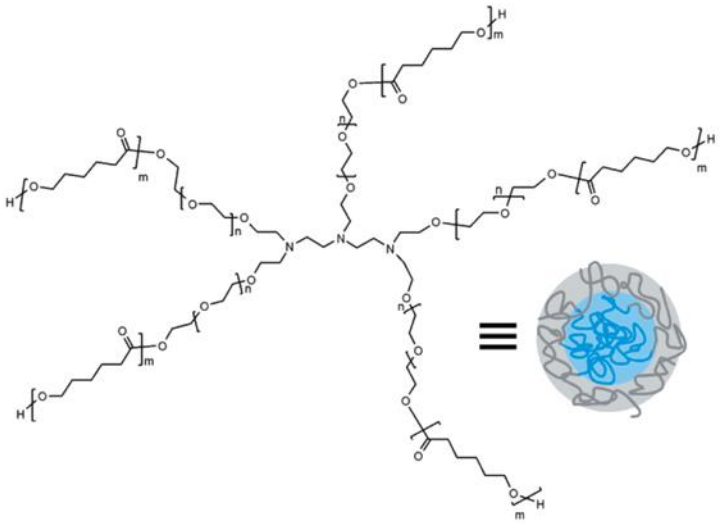

Figure 2.16 Structure and schematic representation of a star-shaped block copolymer with a poly(ethylene glycol) core and a poly(*ε*-caprolactone) shell. Reprinted with permission from Reference 305. Copyright 2004 American Chemical Society.

2.6.4 Dendrimers

The stabilization of metal nanoparticles by dendrimers was introduced in the seminal studies by Crooks et al.[306] and Balogh and Tomalia[307] in 1998, and has found widespread interest. These systems were described in several reviews.[154,308–320] The group of Crooks utilized amine- and hydroxyl-terminated poly(amidoamine) (PAMAM) dendrimers as templates and stabilizers for Pd NPs in water (Figure 2.17).[244,312,321] The dendrimer-encapsulated nanoparticles (DEN) had a relatively narrow size distribution (d_{TEM} = 1.3 ± 0.3 (*G*4-OH) to 1.7 ± 0.5 nm (*G*4-NH_2)) and a high catalytic activity for the hydrogenation of alkenes in water. A negative dendritic effect on catalytic activity was reported as the dendrimer generation increased, which was attributed to greater steric hindrance within the

larger dendrimer cores. The maximum Pd loading achieved correlated with a 1:1 stoichiometric ratio for the number of interior amine groups.

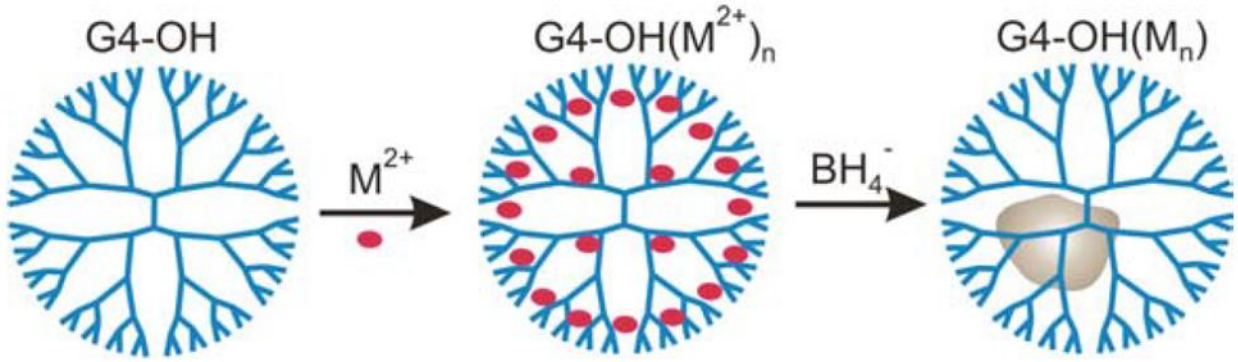

Figure 2.17 Schematic representation of the synthesis of dendrimer-encapsulated Pd nanoparticles. The metal ions complex with the tertiary amines inside the dendrimers and are reduced to Pd(0) nanoparticles. Reprinted with permission from Reference 312. Copyright 2003 Académie des sciences.

Yeung and Crooks subsequently reported the preparation of poly(propylene imine) dendrimers functionalized on their periphery with perfluorinated polyether chains.[249] The uniformly distributed Pd NPs (d_{TEM} = 2.1 ± 0.3 nm) obtained with this template were active in Heck coupling reactions for unactivated aryl halides in fluorous/organic biphasic solvents in pure liquid or supercritical CO_2, and without added base.[322] The group of Astruc later reported the synthesis of poly(1,2,3-triazolylferrocenyl) dendrimers by *click* chemistry, that were efficient ligands for Pd(II) species and useful for application in catalysis (Section 2.7.3.4).[188] Reduction of the metallic salt resulted in the formation of dendrimer-encapsulated Pd nanoparticles with a size dependent on the dendrimer generation, the metal loading, and

the power of the reducing agent (Figure 2.18a). The size ranged from 1.3 ± 0.2 to 1.6 ± 0.3 nm for the *G*1 and *G*2 polymers, respectively. The small size and open structure of the *G*0 dendrimer did not allow encapsulation however, and colloidal stability was rather promoted by a multimolecular association mechanism as illustrated in Figure 2.18b. Larger Pd NPs (d_{TEM} = 2.8 ± 0.3 nm) were obtained in this case.

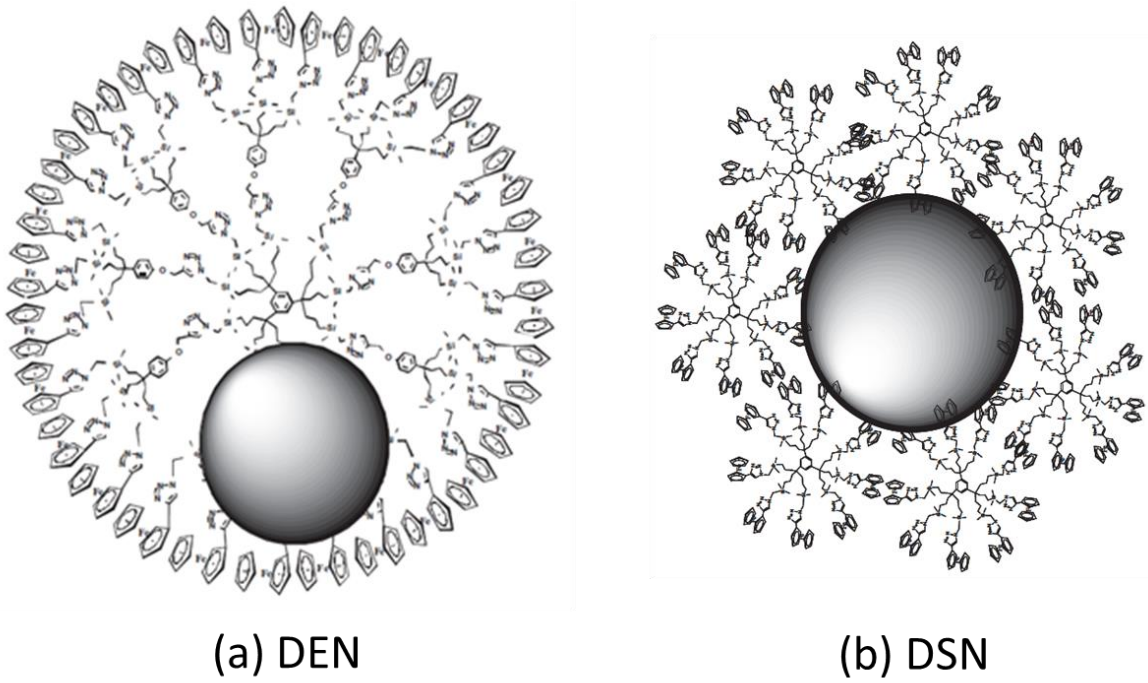

Figure 2.18 Schematic illustration of (a) dendrimer-encapsulated (DEN) and (b) dendrimer-stabilized (DSN) nanoparticles prepared from *G*1 and *G*0 poly(1,2,3-triazolylferrocenyl) dendrimers, respectively. Reprinted with permission from Reference 188. Copyright 2007 The Royal Society of Chemistry.

2.6.5 Other dendritic polymers

In addition to dendrimers, hyperbranched and dendrigraft (arborescent) polymers have also been investigated for the complexation of Pd salts and the preparation of nanoparticles. These macromolecules belong to the same architectural class as dendrimers, characterized by a cascade-branched structure. In contrast to dendrimers, synthesized using strictly controlled cycles of protection, condensation, and deprotection of AB_n-type monomers; also displaying a well-defined architecture and a narrow molar-mass dispersity ($\bar{M}_w \cdot \bar{M}_n^{-1} < 1.01$), hyperbranched and dendrigraft polymers possess a randomly branched architecture. Hyperbranched macromolecules are typically obtained in one-pot procedures by the self-condensation of AB_n-type monomers without protecting groups. The statistical condensation reactions result in many structural flaws and generally broad molar-mass dispersity ($\bar{M}_w \cdot \bar{M}_n^{-1} > 2$), however.[323] The synthesis of dendrigraft polymers proceeds in a step-wise fashion akin to dendrimers, but using polymeric chains as building blocks rather than small molecules. This semi-controlled synthesis results in a rapid increase in molar mass per generation, while maintaining a relatively narrow molar-mass dispersity ($\bar{M}_w \cdot \bar{M}_n^{-1} < 1.1–1.2$).[324]

Sunder et al. thus synthesized hyperbranched amphiphilic polyglycerol by the ring-opening multibranching polymerization of glycidol, with subsequent partial esterification of the OH groups with an alkylcarboxylic acid chloride (Scheme 2.2).[325] These unimolecular micelles served for the preparation of Pd NPs by complexation of $Pd(OAc)_2$ and further reduction with hydrogen, or by simply heating toluene dispersions to 60 °C for several hours.[195] The size of the NPs could be varied from 5.1 ± 1.8 nm to 2.1 ± 0.6 nm by

decreasing the size of the hyperbranched polymer, and even below 1 nm by further lowering the metal loading. The weakly coordinating hydroxyl groups were deemed advantageous in terms of catalytic activity, as they caused limited hindrance of the active sites. These systems were active in the hydrogenation of cyclohexene, with a TOF of 700 h^{-1} atm $(H_2)^{-1}$.

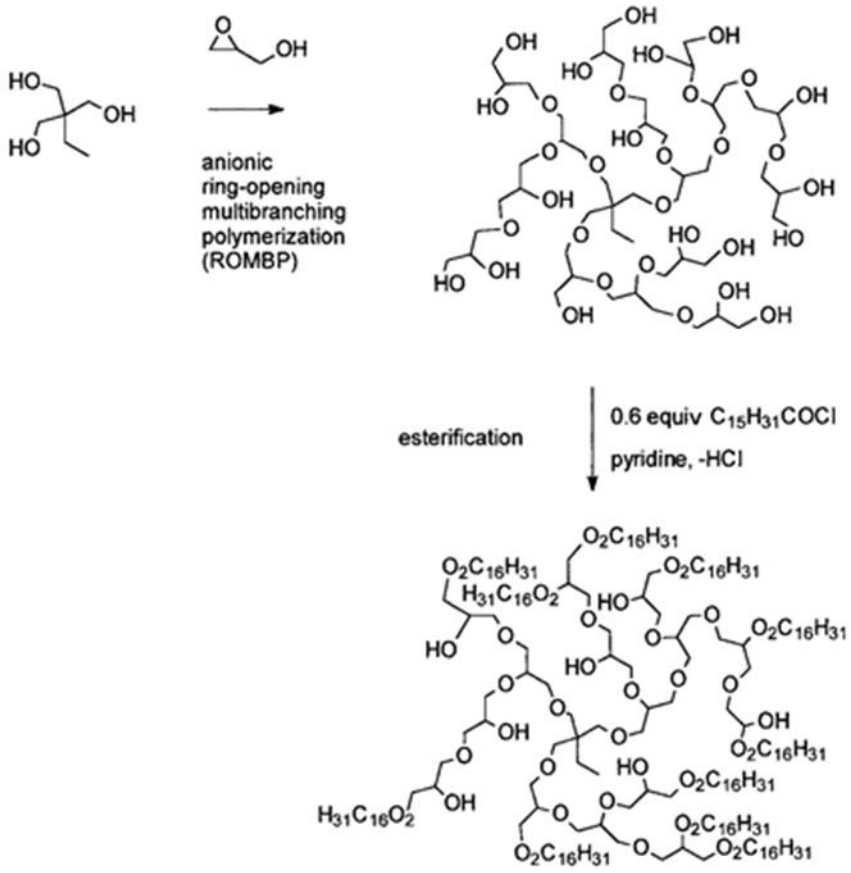

Scheme 2.2 Synthesis of amphiphilic hyperbranched polyglycerol by ring-opening polymerization of glycerol and partial esterification with hexadecanoyl chloride. Reprinted with permission from Reference 325. Copyright 1999 Wiley-VCH.

Vasylyev et al. rather used hyperbranched PEI for the synthesis and stabilization of Pd NPs with sizes ranging from 2 to 4 nm. After alkylation of the polymer, greater catalytic activity was noted for the biphasic hydrogenation of hydrophobic alkenes. Interestingly, the catalyst was selective for less hindered alkenes and could be recycled at least five times without activity loss.[76]

Arborescent copolymers synthesized by Dockendorff et al. were also used for loading with metal salts, although their catalytic properties were not investigated. Using amphiphilic arborescent copolymers composed of a dendritic PS core of generation *n* (*Gn*), grafted with an outer layer of P2VP side chains (*Gn*PS-*g*-P2VP)[326] or P2VP-*b*-PS side chains (*Gn*PS-*g*-[P2VP-*b*-PS])[327] (Scheme 2.3), colloidal dispersions of Au(III)[328], Pd(II), or bimetallic Au(III)-Pd(II) were obtained.[286,287]

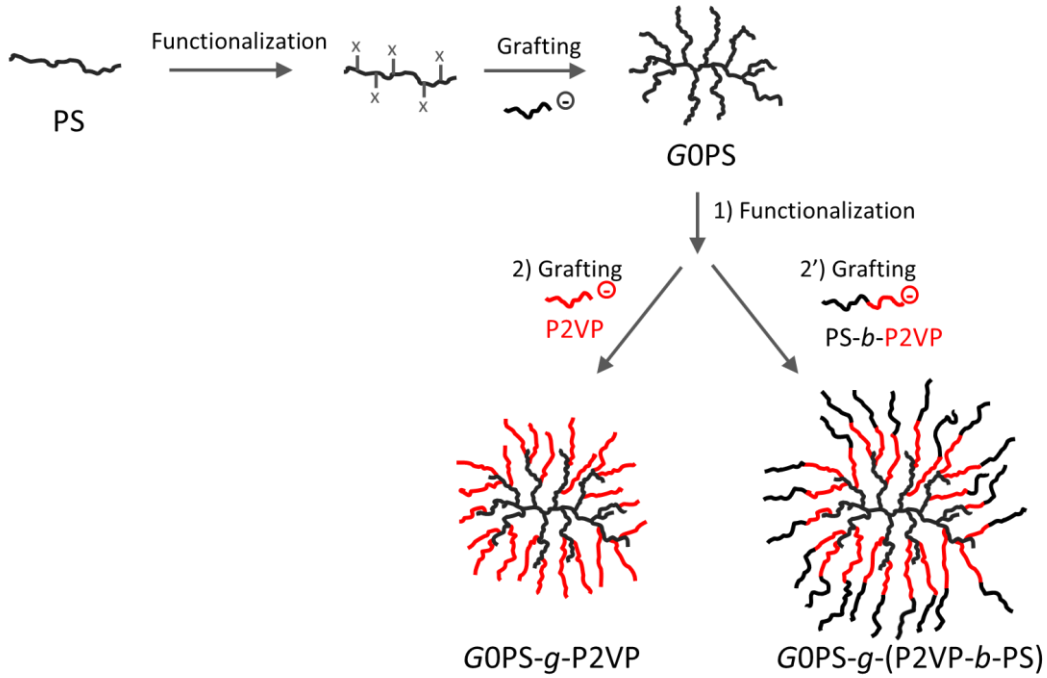

Scheme 2.3 Synthesis of arborescent *G*0PS-*g*-P2VP and *G*0PS-*g*-(P2VP-*b*-PS) by anionic polymerization and successive cycles of functionalization and grafting.

In THF the complexation of Pd(II) by *Gn*PS-*g*-P2VP was observed within a few minutes, but sedimentation was noted after one week.[286] Imaging by TEM of the *G1*PS-*g*-P2VP/Pd complex revealed spheres lightly aggregated into pearl-necklace-like ribbons, while the *G*0PS-*g*-P2VP/Pd hybrid formed a less defined aggregated network (Figure 2.19). Greater stability was achieved for the *Gn*PS-*g*-(P2VP-*b*-PS) copolymers in toluene, as the outer PS shell promoted steric repulsions and prevented bridging by the metallic species. As shown in Figure 2.20, toroidal and raspberry-type morphologies were imaged by TEM for the Pd(II)-loaded *G*1PS-*g*-(P2VP-*b*-PS) and *G*2PS-*g*-(P2VP-*b*-PS) copolymers, respectively. Aggregated networks were observed on micrographs for films of *G*3PS-*g*-(P2VP-*b*-PS) complexed with Pd(II).[287] In these studies, no attempt was made to reduce the Pd(II) species to Pd(0) nanoparticles however.

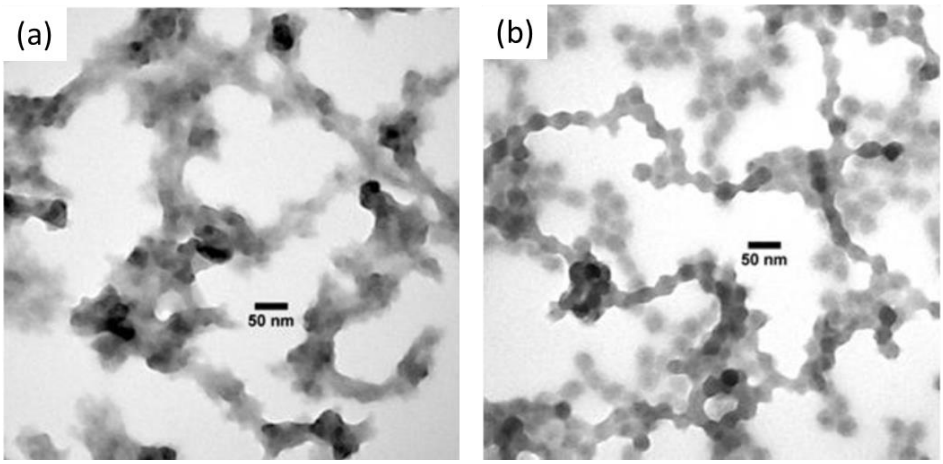

Figure 2.19 Transmission electron micrographs for palladium(II) acetate loaded in (a) *G*0PS-*g*-P2VP and (b) *G*1PS-*g*-P2VP. Reprinted with permission from Reference 286. Copyright 2011 J.M. Dockendorff.

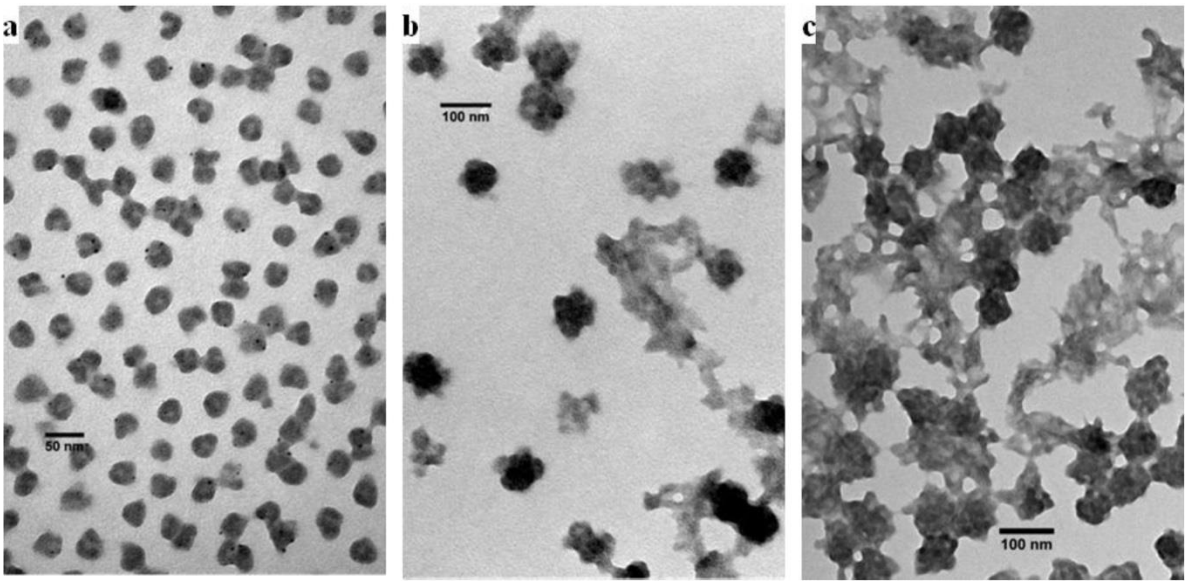

Figure 2.20 Transmission electron micrographs for (a) *G*1PS-*g*-(P2VP-*b*-PS), (b) *G*2PS-*g*-(P2VP-*b*-PS), and (c) *G*3PS-*g*-(P2VP-*b*-PS) after loading with 0.5 equiv of palladium(II) acetate in toluene. Reprinted with permission from Reference 287. Copyright 2011 J.M. Dockendorff.

2.7 Application of Pd nanoparticles to the Suzuki-Miyaura cross-coupling reaction

2.7.1 Suzuki-Miyaura cross-coupling

The formation of C-C bonds is one of the most important transformations in organic synthesis.[329] It represents a key step in building complex molecules from simple precursors. Different palladium-catalyzed cross-coupling reactions have been developped over the last 40 years including the Suzuki-Miyaura (SM), Mizoroki-Heck, Negishi, Sonogashira-Hagihara, Migita-Kosugi-Stille, Tsuji-Trost, Kumada-Corriu, and Hiyama reactions (Scheme

2.4).[85,252,330,331] As one the most versatile, robust and environmentally friendly reactions, the SM reaction has attracted an extraordinary amount of interest from researchers.

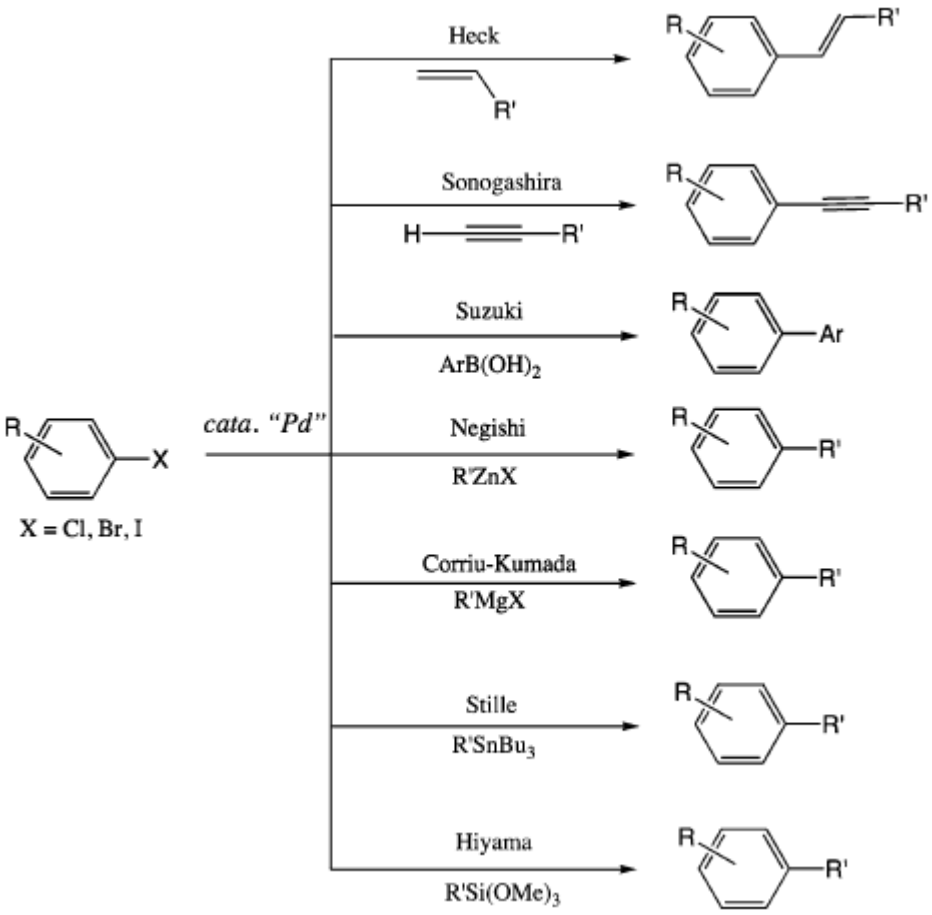

Scheme 2.4 Main Pd-catalyzed carbon-carbon cross-coupling reactions. Reprinted with permission from Reference 331. Copyright 2013 American Chemical Society.

Before the advent of the SM cross-coupling reaction, discovered by the Nobel laureate Akira Suzuki in 1979, no simple methods were available for the generation of carbon-carbon linkages between unsaturated species such as vinyl or aryl compounds. Stereo- and regioselective synthetic procedures for the formation of conjugated alkadienes

had been devised using organometallic compounds but were marred with severe limitations. Organometallic compounds (such as Grignard reagents) are sensitive to reactive functional groups and the presence of protic impurities or protic solvents. This limits greatly their synthetic scope, and stringent conditions of temperature and pressure, along with toxic organic solvents, are also often required. Tin compounds have greater stability, but their toxicity and the difficulties associated with their separation remains a significant drawback.[332]

The SM reaction allows coupling between an aryl- or vinylboronic acid with an aryl or vinyl halide (or triflate) using a palladium catalyst.[333] This powerful cross-coupling method can be used for the synthesis of conjugated olefins, styrene derivatives, biphenyls, and even polymers.[334] SM reactions have recently attracted tremendous interest owing to some of their advantages. First, the reagents can tolerate a wide range of substrates and functional groups, and mild conditions can be used. This is particularly interesting for the synthesis of complex drug molecules and biochemicals. Second, the boronic acid starting materials are readily available, and stable in air or aqueous environments. A generic reaction scheme for the SM reaction is shown in Scheme 2.4.

A soluble palladium complex containing various ligands (typically tetrakis(triphenylphosphine)palladium(0), $Pd(PPh_3)_4$) in organic solvents is generally used for these reactions.[334] These homogenous catalysts are selected for their high activity and selectivity, but they are difficult to separate from the reaction products. With increasing demand for environmentally acceptable processes and the recent developments in green chemistry,[335] recovery and reusability of the catalysts have become important issues. From an

economical and industrial viewpoint, the recovery and recycling of catalysts is also generally preferred over using more active but difficult to recover catalysts.[329]

2.7.2 Catalysts

Important efforts have been devoted by the scientific community to 'heterogenize' the Pd catalyst in SM reactions. The various supports considered include high surface area solids (silica, alumina, carbon, zeolites, etc.), carbon nanotubes, cross-linked polymers, and magnetic nanoparticles.[252,329,330,336,337] Although it may facilitate the separation of the catalyst after the reaction, the support has been shown to limit the access of the substrate molecules to the active sites present on the surface of the catalysts on many occasions.[329] Polymeric supports were also found to be sensitive to the reaction conditions and to degrade at high temperatures.[338] As a consequence, when compared to their homogeneous counterparts, a decrease in overall catalytic activity and efficiency is often observed for the polymer-supported systems. Leaching of the metal from the support is also an important limitation that affects catalyst recyclability as well as the purity of the products, in the SM reaction as in other catalytic processes in general.[85,339]

2.7.3 Polymer-stabilized catalysts

2.7.3.1 Homopolymers

An interesting approach combining the high activity of homogeneous catalysts with the recyclability of heterogeneous catalysts relies upon the use of polymeric stabilizers. For instance, Reetz et al. reported the utilization of poly(*N*-vinyl-2-pyrrolidone) (PVPy) as

stabilizer for Pd nanoparticles, and demonstrated the catalytic activity of the system in the SM reaction in *N*,*N*-dimethylacetamide.[340] El-Sayed et al. extended the application of this system to aqueous solutions, by showing that the catalyst was active in SM reactions under reflux conditions; however, precipitation of the catalyst was noted during the reaction. The catalytic activity level depended on the amount of stabilizer present:[341] Increasing the amount of PVPy led to decreased catalytic activity, presumably because of the polymer limiting the access to the active sites. It is noteworthy that Ostwald ripening of the particles was observed by the same authors during the catalytic process, but the polymer was found to mitigate this process. In contrast, the helical structure of poly(*N*,*N'*-dihexylcarbodiimide) allowed the formation of particularly stable Pd NPs.[270] Relatively weak coordination of the polymer with the NP surface was thought to account for the good catalytic activity of these catalysts in the SM reaction (turnover number [TON, mol substrate/mol of Pd] ca. 1600), and the catalyst could be recycled five times with no significant aggregation.

2.7.3.2 Copolymers

Beletskaya *et al*. employed a polystyrene-*co*-poly(ethylene oxide) copolymer as stabilizer in water. Excellent catalytic activity and good recyclability were achieved for these systems.[338] A water-dispersible catalytic system was also obtained by Zhang *et al*. using poly(*N*-isopropylacrylamide) (PNIPAM) as a stabilizer (Figure 2.21).[273] Both hydrophilic and hydrophobic reactants could penetrate in this 'nanoreactor', and recyclability was expected (although not tested).

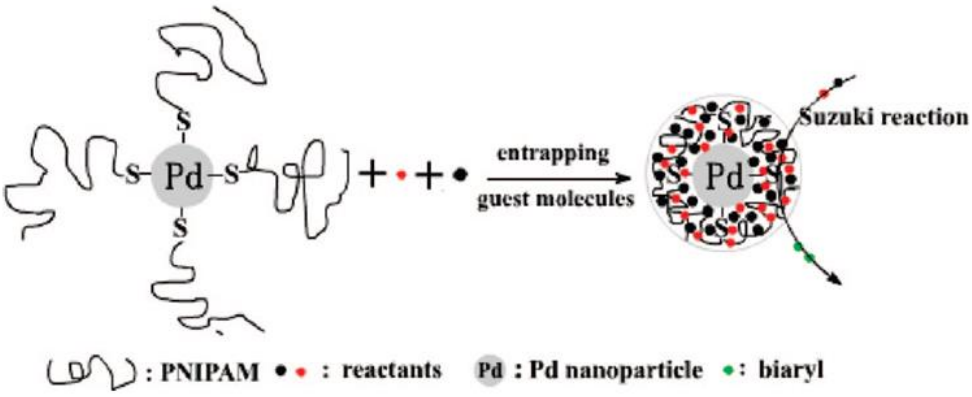

Figure 2.21 Schematic illustration of poly(*N*-isopropylacrylamide)-stabilized Pd nanoparticles, and entrapment of the reactants for the Suzuki-Miyaura reaction. Reprinted with permission from Reference 273. Copyright 2008 American Chemical Society.

In a similar fashion, Ohtaka *et al*. prepared polyion complex-stabilized Pd nanoparticles by the complexation of poly{4-chloromethylstyrene-*co*-(4-vinylbenzyl) tributylammonium chloride} with poly(acrylic acid). They reported high yields for Suzuki coupling reactions with various aryl bromides and arylboronic acids in water with this catalytic system.[342]

2.7.3.3 Dendritic polymers

Investigating the use of dendritic structures, El-Sayed *et al*. stabilized Pd nanoparticles with hydroxyl-terminated PAMAM dendrimers of different generations and demonstrated their excellent activity for the SM reaction in ethanol.[192,343] They found that for larger dendrimers (*G*4), however, extensive encapsulation of the catalyst resulted in loss of

catalytic activity. The dendrimers were nevertheless found to be more robust than PVPy for the colloidal stabilization of Pd NPs. Unfortunately, their activity in water was deemed unsatisfactory. A similar study by Christensen *et al*. showed that the *G*4 dendrimers were inactive for the more demanding aryl chlorides.[344] Using a Fréchet-type dendrimer based on polyaryl-ether dendrons to stabilize Pd nanoparticles, Fan and co-workers reported good catalytic activity in SM reactions and could re-use the catalyst four times by precipitation while maintaining a high performance (Scheme 2.5).[289,345]

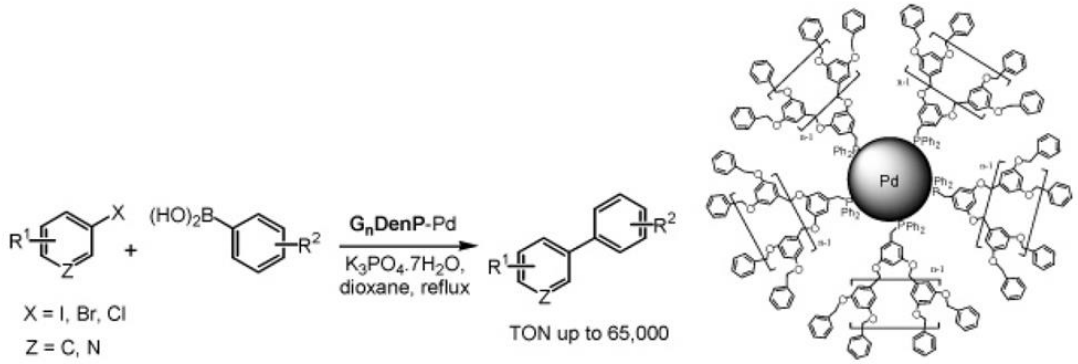

Scheme 2.5 Suzuki-Miyaura reaction catalyzed by Pd nanoparticles stabilized by phosphine-functionalized polyaryl ether dendrons. Reprinted with permission from Reference 289. Copyright 2006 American Chemical Society.

2.7.3.4 Homeopathic catalysis

The very low amounts (0.01–0.1 mol % or lower) of Pd NPs required for some catalytic reactions has spurred the term *homeopathic* doses to refer to these conditions.[346,347] Although ligand-free and homeopathic Pd loadings have been successfully used in SM reactions without stabilizer, the precipitation of Pd was noted before full conversion could be attained.[348]

Astruc and co-workers compared the activity of dendrimer-encapsulated and dendrimer-stabilized Pd nanoparticles at metal concentrations ranging from 1 to 0.0001 mol %, using 1,2,3-triazole-linked dendrimers with ferrocenyl termini (*G*0-*G*2, Figure 2.18).[349] They found no difference in catalytic efficiency for dendrimers of different generations, and thus concluded on the non-involvement of the dendrimers in the catalytic process. Interestingly, the TON of the coupling reaction between iodobenzene and phenylboronic acid in chloroform/methanol (2:1 v/v) increased at lower catalyst concentrations: A TON of 540,000 was obtained for as little as 1 ppm (part per million) of Pd NPs in *G*0 dendrimers. Reduced deactivation of the catalyst at 1 ppm argued in favor of Pd-atoms leaching as proposed by Hu et al., whereby extremely active Pd atoms dissociate from the catalyst surface during the oxidative insertion of the arylhalide. Rapid quenching of the discrete species subsequently takes place on the nanoparticles surface and is therefore more efficient at higher Pd concentrations.[350] Functionalization of the triazole-containing dendrimers with sulfonate groups led to the formation of water-soluble dendrimers that, when loaded with Pd, were catalytically active for the SM reaction in aqueous media.[351] Using as little as 0.01 mol % of Pd in aqueous solution, TONs up to 10,000 were obtained when coupling phenylboronic acid with bromobenzene in water/ethanol (1:1 v/v) solutions at 100 °C. At 25 °C, a TON of up to 9400 and a TOF ca. 1500 mol PhI (mol Pd^{-1}) h^{-1} were reached when iodobenzene served as substrate. The dendritic catalyst was highly stable in air and moisture, and its activity was notably greater than when using the triazol-containing linear polymer analogue.[277] By functionalization of the dendrimers with tri(ethylene glycol) termini, Pd NPs with diameters of 1.4 ± 0.7 nm (*G*0) or 2.1 ± 1 nm (*G*1) were stabilized in water (Figure

2.22).[352] In this case stabilization resulted from the formation of supramolecular assemblies by several dendrimers rather than by the individual molecules. Using only 3 ppm of Pd, the system displayed a particularly high catalytic activity in the SM reaction between bromoarenes and phenylboronic acid (TON up to 2.7×10^6, TOF of 4.5×10^4 h^{-1}). Loose intra-dendritic stabilization coupled with the small size of the particles favoring actuation of the leaching mechanism was thought to be responsible for the high performance of these catalysts (vide supra).

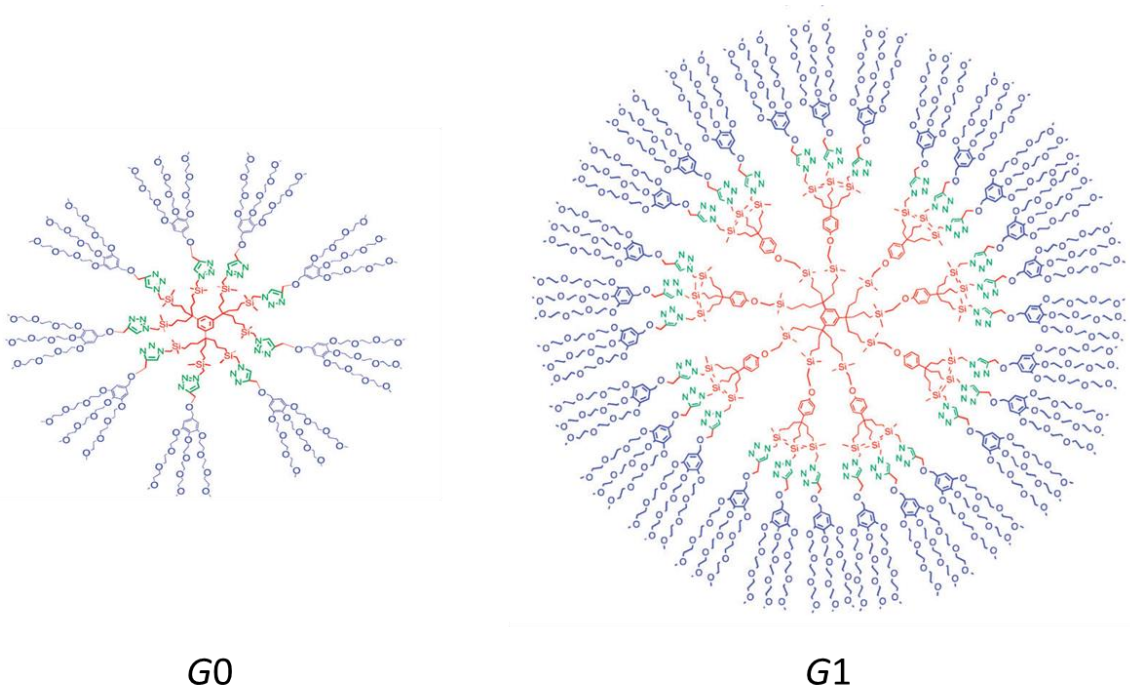

Figure 2.22 Structure of *G*0 and *G*1 poly(1,2,3-triazolylferrocenyl) dendrimers functionalized with triethylene glycol termini, used for the preparation of Pd NPs. The catalytic systems were highly active in the Suzuki-Miyaura reaction in water-ethanol mixtures for homeopathic doses (sub-ppm) of Pd catalyst. Reprinted with permission from Reference 352. Copyright 2013 The Royal Society of Chemistry.

2.8 Conclusions

Nanoparticles have emerged as promising materials for a variety of applications, notably in catalysis, thanks to their unique size-dependent properties. Transition metal nanoparticles in particular show great promise as high performance catalysts, as they exhibit a large specific surface area and are highly reactive because of the prominence of low coordination surface defects. Intrinsic changes in the electronic properties of nanoclusters also have important effects on the interactions between the surface and the substrate molecules. In liquid media, nanoparticles require a stabilizer to prevent their aggregation and the concomitant decrease in their surface area under the influence of van der Waals interactions. Polymers are successful candidates for the steric and/or electrostatic stabilization of colloidal metal particles. Polymer-stabilized nanoparticles are a class of catalysts that exhibit the advantages of homogeneous systems in terms of catalytic activity and selectivity, while allowing the recovery and recycling of the metal particles similarly to heterogeneous systems.

The reduction of a metal salt in solution and in the presence of a polymer is one of the most widely employed synthetic strategies because of its simplicity, and the control it offers over the size, composition, and structure of the nanoparticles formed. The polymer plays an active role in the synthesis as it can i) govern the nucleation and growth of the nanoclusters, ii) prevent their aggregation, iii) control their shape, and iv) modulate their dispersibility in polar or non-polar solvents. Additionally, the polymer can affect the performance of the metal catalyst by interacting with the substrates molecules (polymeric field), and either increase their local concentration or screen their access to the active sites.

Palladium is one of the most efficient catalysts available, and Pd nanoparticles are particularly active for hydrogenation, oxidation, and carbon-carbon bond-forming reactions. A wide range of polymers have been used for the preparation of colloidal Pd nanocatalysts including natural, biological, linear, block and dendritic (co)polymers. The latter category is noteworthy for the preparation of high performance catalysts, as small Pd nanoparticles with narrow size distributions can be obtained with these systems. They exhibit robust colloidal stability, while separation and recovery of the catalyst can be achieved by nanofiltration or precipitation. Among the dendritic architectures dendrimers have been by far the most frequently studied materials, but their synthesis remains a tedious process. More recently, hyperbranched and dendrigraft structures have appeared as promising candidates for the preparation of colloidal metallic species. The application of polymer-stabilized Pd nanoparticles in the Suzuki-Miyaura reaction has been an important area of research, and extremely active catalysts have been obtained by using even very low amounts (homeopathic doses) of catalysts in dendrimers.

The concept of polymer stabilization to increase catalyst activity and stability appears to be highly pervasive, as it is applicable to a wide range of metals and chemical transformations of industrial significance. The development of new polymeric materials providing control over the size, stability, performance and recyclability of the nanoparticles will be important to realize the full potential of nanocatalysts. These materials could help meet the challenges of current and future industrial applications, as well as further advance the scientific understanding of nanocatalysts.

Chapter 3

Arborescent Polymer-stabilized Palladium Nanoparticles as Green Catalysts for the Suzuki-Miyaura Reaction

3.1 Overview

The application of arborescent copolymers of generations *G*0–*G*3 to the preparation of palladium nanoparticle (Pd NP) catalysts is reported. The copolymers used, incorporating a polystyrene (PS) core and a corona of poly(2-vinylpyridine) (P2VP) chains, displayed good colloidal stability in ethanol. Nanomorphologies stemming from phase segregation of the PS and P2VP blocks were observed by atomic force microscopy (AFM). These copolymers, when used as templates for the loading of Pd(II) in ethanol, displayed greater colloidal stability for the higher generation polymers. After reduction of the metallic salt, imaging by transmission electron microscopy (TEM) revealed the formation of raspberry-type nanomorphologies, with Pd nanoparticles of 0.7–3.4 nm diameter and a uniform size encapsulated within the polymer matrix. The size of the particles obtained depended upon the loading level, the reduction time, and the copolymer generation used. Metal quantification by microplasma-optical emission spectrometry confirmed the formation of a 1:1 complex between Pd and the pyridine pendants, and the presence of Pd(0). The catalytic activity of the nanoparticles was evaluated in the Suzuki-Miyaura cross-coupling reaction between phenylboronic acid and 4-bromoanisole in situ using ^{1}H NMR spectroscopy in ethanol/D_2O (85/15 v/v). Good catalytic activity and a positive dendritic effect were evidenced, although air-sensitivity and flocculation affected the activity and recyclability of the catalyst.

3.2 Introduction

The important changes observed in the properties of materials as their size is decreased from the macroscopic to the atomic or molecular level have attracted considerable interest. The change in surface reactivity of metals, in particular, has led to the development of nanocatalysis as a major field of research in nanoscience and nanotechnology.[1] Atoms at the surface of a solid often exhibit high chemical reactivity because of their unsatisfied coordination. As the size of a material diminishes, a rapid increase in the fraction of surface atoms can promote greater catalytic activity.[2] However additional intrinsic changes in the low nanometer size range, non-scalable from the bulk properties, also distinguish nanocatalysts from other large surface-area catalysts.[3,4]

Transition metals such as palladium have attracted by far the most interest in catalysis, and significant efforts have been devoted to the development of synthetic strategies offering control over the size but also over the structure, composition and shape of the nanoparticles (NPs) obtained. The most commonly employed method consists in the reduction of a metallic salt in solution in the presence of a stabilizer. Various stabilizing agents have been used including ions, ligands, surfactants, linear polymers, and dendritic polymers.[3]

Dendrimers, hyperbranched and star polymers have attracted much interest over the last 20 years, owing to the unique properties displayed by these materials.[1,5–11] In particular, their typically well-defined, three-dimensional branched structure affords tunable templates for the formation of monodispersed nanoparticles. Furthermore, the branches of dendritic polymers can screen the access of substrate molecules to the metal active centers, while

providing dispersibility in the reaction medium.[8] Ease of separation from the reaction products is another advantage of these macromolecules, as they can be easily recovered by precipitation[12] or ultrafiltration.[13]

While various dendritic structures have been used in the preparation of Pd NPs,[14–21] to the best of our knowledge no report has demonstrated the utilization of arborescent graft (dendrigraft) polymers as stabilizers and their application to catalysis. These dendritic macromolecules were reported simultaneously in 1991 by Gauthier and Möller,[22] and by Tomalia et al.[23] Arborescent graft polymers (AGPs) combine features of both dendrimers and hyperbranched polymers.[24] Their synthesis proceeds through generation-based functionalization and grafting cycles, leading to the formation of multiple branching levels and a cascade-branched structure. In contrast to their dendritic counterparts, however, polymeric chains rather than small molecule monomers serve as building blocks. This allows a rapid increase in molar mass while maintaining a low molar-mass dispersity ($Đ \leq 1.1$). Because the synthetic scheme relies on anionic or controlled radical[25] polymerization, and predetermined substrate functionalization levels, good control is achieved over the so-called critical molecular design parameters (CMDPs).[26] In particular, the length of the chains and the grafting density can be adjusted, and the number of grafting cycles (generations) employed determines the overall branching functionality and the size of the molecules. The synthesis of arborescent copolymers (ACPs) with core-shell and core-shell-corona (CSC) architectures, based upon a PS core/corona and a P2VP shell, was also reported by Gauthier et al.[27–30] The unimolecular micelle character of these molecules allowed the solubilization of polycyclic aromatic hydrocarbons in aqueous solutions.[31] The large number of 2-

vinylpyridine units in these molecules also enabled the coordination of metallic compounds such as Au and Pd salts in organic solvents.[27,32]

The control achieved in the synthetic protocol over the CMDPs (structure, shape, composition, size, flexibility, surface chemistry) of these macromolecules affords versatile templates with tunable density, solubility, and polymeric field, making them promising materials for applications in catalysis and microencapsulation. For instance, their open structure should not lead to steric crowding of the type observed with dendrimers; and thanks to their large size, they are easily recovered after the reaction through ultrafiltration.

Pd catalysts have been used in many reactions,[33–35] but carbon-carbon coupling represents one of their most important applications in organic synthesis.[36] Among the Pd-catalyzed cross-coupling reactions, the Suzuki-Miyaura (SM) reaction allows cross-coupling between an aryl- or vinylboronic acid with an aryl or vinyl halide (or triflate), as illustrated in Scheme 3.1. This powerful coupling method is particularly interesting for the synthesis of complex drug molecules and other bioactive chemicals, owing to the mild and 'green' conditions that can be employed.[1]

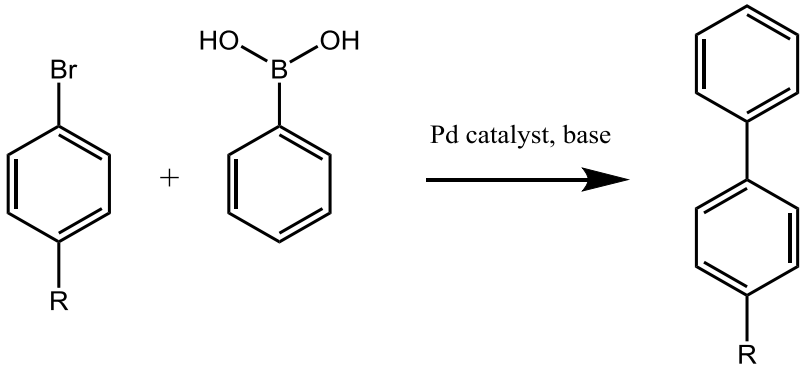

Scheme 3.1 Suzuki-Miyaura cross-coupling reaction.

After investigating the solution and solid state properties of ACPs, we will demonstrate their utilization in the preparation of stabilized Pd NPs. The influence of the polymer generation on catalytic activity in the SM cross-coupling reaction will also be examined. Characterization of the catalytic systems was performed using dynamic light scattering (DLS) measurements, atomic force microscopy (AFM), UV-visible (UV-vis) spectrophotometry, transmission electron microscopy (TEM), as well as microplasma-optical emission spectrometry (microplasma-OES).

3.3 Experimental procedures

3.3.1 Materials

Ethanol (undenatured grade, anhydrous, Commercial Alcohols Inc., Brampton, ON, Canada) used for the microplasma-OES measurements was distilled in a polytetrafluoroethylene (PTFE) apparatus. Palladium(II) acetate ($Pd(OAc)_2$, min. 98%, Strem Chemicals Inc., Newburyport, MA, USA), deuterium oxide (D_2O, Cambridge Isotopes Laboratories Inc., D, 99.8%, Tewksbury, MA, USA), 4-bromoanisole (≥99.0%, Sigma-Aldrich, Oakville, ON, Canada), phenylboronic acid (≥97.0%, Fluka, Milwaukee, WI, USA), potassium carbonate (≥99.0%, ACS reagent, Sigma-Aldrich), acetone (ACS reagent, ≥99.5%, Sigma-Aldrich), chloroform ($CHCl_3$, ACS reagent, ≥99.8%, containing 0.5–1.0% ethanol, Sigma-Aldrich), *N*,*N*-dimethylformamide (DMF, ACS reagent ≥99.8%, Sigma-Aldrich), tetrahydrofuran (THF, ReagentPlus®, ≥99.0%, containing 250 ppm BHT, Sigma-Aldrich), deuterated chloroform ($CDCl_3$, Cambridge Isotopes Laboratories Inc., 99.8% D), and

deuterated dimethyl sulfoxide (DMSO-d_6, Cambridge Isotopes Laboratories Inc., 99.9% D + 1% v/v TMS) were used without further purification.

3.3.2 Arborescent copolymers

The arborescent copolymers used in this study were synthesized by Munam and Gauthier by anionic polymerization and grafting according to a reported procedure.[28] The polymers consisted of different generations of arborescent polystyrene (PS) substrates grafted with poly(2-vinylpyridine) (P2VP) chains at their periphery. The characteristics of the copolymers used are summarized in Table 3.1 and Table 3.2, and their synthesis is depicted in Scheme 3.2. Briefly, linear polystyrene was synthesized by anionic polymerization using *sec*-butyllithium as initiator in toluene and THF. Friedel-Crafts acylation of the polymer was carried out with acetyl chloride and anhydrous $AlCl_3$ in nitrobenzene. The functionalized polystyrene substrate was then coupled with living polystyryl anions to yield a comb-branched polymer. Higher generation PS substrates were obtained by repeating cycles of functionalization and grafting. Synthesis of the arborescent copolymers proceeded by coupling living poly-2-vinylpyridinyl anions, obtained by polymerization of 2-vinylpyridine in THF with *sec*-butyllithium. The red-colored solution was titrated with the PS substrate to obtain the copolymer.

3.3.3 Palladium loading

An arborescent copolymer was first dissolved overnight in ethanol (0.4 mg·mL^{-1}) in a vial. The required amount of $Pd(OAc)_2$ (0.25 to 2.5 equiv per 2VP unit) was then added and the solution was diluted with ethanol to the desired concentration (0.3×10^{-3}–1.0 mg·mL^{-1}).

After sonication for about 5 min, the solution turned yellow or translucent brown. The ethanol solution was heated at 60 °C for at least 3 h and turned dark brown. Dialysis of the polymer-catalyst complex was performed against ethanol (10:1 volume ratio of ethanol per volume of solution) with a 1,000 molecular weight cut-off, regenerated cellulose Spectra/Por® 7 membrane. The solution was recovered after changing the solvent five times over 2 days.

3.3.4 Suzuki-Miyaura reactions

The Suzuki-Miyaura (SM) cross-coupling reactions were conducted by dissolving 4-bromoanisole (100 mg, 0.53 mmol, 1 equiv), phenylboronic acid (98 mg, 0.8 mmol, 1.5 equiv), and K_2CO_3 (148 mg, 1.1 mmol, 2 equiv) in 9 mL of a mixture of ethanol/D_2O (85/15 v/v) containing acetone (40 µL, 0.5 mmol, 1 equiv) as an internal standard. The polymer-stabilized Pd catalyst (0.15 mg polymer/mL, Pd/2VP = 0.25–1.0) was then added to the solution to obtain a Pd content of 1 mol % (concentration ca. 0.3 mmol·L^{-1}). The solution was transferred to an NMR tube, sealed and mechanically stirred at room temperature.

3.3.5 Size-exclusion chromatography (SEC)

The arborescent copolymers used in the investigation were analyzed by size-exclusion chromatography (SEC) on a Viscotek GPCmax instrument (VE2001) equipped with a TDA 305 triple detector array consisting of refractive index (RI), light scattering at low and right angles (LALS and RALS, respectively) and viscometer detectors, as well as a UV detector (Viscotek 2600). Three Polyanalytik SupeRes™ Series 300 mm × 8 mm linear mixed bed columns having linear polystyrene molar mass ranges of 10^3 to 10^6 were used in

the analysis. The mobile phase was THF at a flow rate of 1.0 $mL \cdot min^{-1}$ and a temperature of 35 ºC. Analysis of the chromatograms was performed with the OmniSEC 4.6.1 software package.

3.3.6 Transmission electron microscopy (TEM)

Imaging by TEM was performed in the bright-field mode on a Philips CM10 electron microscope operated at 60–80 kV accelerating voltage. The samples were prepared by depositing two drops of solution (0.07 $mg \cdot mL^{-1}$) onto a 300 mesh Formvar® carbon-coated copper TEM grid (Electron Microscopy Sciences, FCF300-Cu) placed onto a filter paper serving as wicking medium. After deposition of the solution, the grid was transferred onto a new piece of filter paper in a Petri dish and dried overnight at room temperature. The images were recorded with an Advance Microscopy Techniques 11 megapixel digital camera and the Image Capture Software Engine version 5.42.558. The feature sizes and size distributions were measured with the open source processing program ImageJ (version 1.46r).[37] Depending on the contrast and the resolution of the images, either automatic analysis or manual selection of the features was used. In either case, at least 50 measurements were made. Contrast adjustment was also performed on some of the micrographs to improve visualization and help with measurement of the features.

3.3.7 Atomic force microscopy (AFM)

Muscovite mica discs (9.9 mm diameter, NanoAndMore GmbH) were adhered onto stainless steel discs with a double-sided adhesive tape (NanoAndMore GmbH), and a fresh surface was exposed by cleaving with a strip of tape (Scotch® MultiTask tape). Polymer

solutions were prepared either in THF or chloroform at concentrations ranging from 0.2 to 0.05 mg·mL^{-1}. The solutions were deposited on the mica substrates with a Pasteur pipet and spin-coated at about 3000 revolutions per minute (rpm) for 60 s under ambient conditions. After solvent evaporation, AFM imaging was carried out on a Nanoscope IIIa instrument (Digital Instruments, model MMAFM-2, scan stage J) set in the tapping mode to acquire simultaneously height and phase data. The instrument was housed in a NanoCube acoustic isolation cabinet and mounted on a Halcyonics Micro 40 vibration isolation table. The cantilever probes used were VistaProbes, T300 silicon tip (spring constant 40 N·m^{-1}, resonant frequency 300 kHz), with the following characteristics: length 125 μm, width 40 μm, tip height 14 μm, and tip radius < 10 nm. NanoScope Analysis v1.40 software was used for the image analysis. The scan rate was typically set between 0.7 and 1 Hz, at a scan angle of 0°, acquiring with 512 samples/line. The drive amplitude was varied between 30 and 50 mV, and the amplitude set-point between 0.50 and 0.85 V to adjust the force applied on the surface. The feedback loop sensitivity was controlled by adjusting the integral gain to 0.5, and the proportional gain to 6.0 typically.

3.3.8 Dynamic light scattering (DLS)

Light scattering measurements were performed on a Brookhaven BI-200 SM goniometer equipped with a Thorn EMI B2F.BK/RFI photomultiplier tube and a BI-2030AT 201-channel correlator operated in the exponential sampling mode. The light source was a 500 mW Claire Quiet-Power-660 laser operating at 660.0 nm. The ACPs were dissolved in ethanol, DMF, THF, or chloroform at least 24 h before analysis. The concentration of the

solutions was 3 mg·mL^{-1}, 1 mg·mL^{-1}, and 0.2 mg·mL^{-1} for the *G*0, *G*1 and *G*2–*G*3 copolymers, respectively. In this concentration range the solutions of the *G*0–*G*2 copolymers were clear, while the *G*3 solution was faintly opalescent. All the solutions were filtered at least 3 times with a PTFE membrane filter with a nominal pore size of 0.45 μm prior to the measurements, and transferred to a flamed and acetone-washed cylindrical cuvette. The scattered light intensity was measured at 25 °C and an angle of 90°, using a 200–400 μm aperture. A minimum of 5 analyses were performed for a duration of 300 s each. The decay rate Γ was calculated from cumulants analysis of the intensity-weighted autocorrelation function $g^{(2)}(t)$ (ACF),[38] after ensuring that the measured and calculated baselines differed by less than 0.1%. The z-average translational diffusion coefficient (D_t) was obtained from $\Gamma = D_t\boldsymbol{q}^2$, where the magnitude of the scattering vector $q = (4\pi\tilde{n}_0/\lambda_0)\sin(\theta/2)$ and $\tilde{n}_0$, θ, and λ_0 represent the refractive index of the medium, the scattering angle, and the wavelength of the incident light, respectively. The hydrodynamic diameter (D_h) was then obtained using the Stokes-Einstein equation, $D_t = k_B T/(3\pi\eta D_h)$ where k_B is the Boltzmann constant, T the absolute temperature and η the viscosity of the medium. Size distributions were obtained by the Laplace transform inversion of the decay rate distribution function using the CONTIN method.[39,40]

3.3.9 Nuclear magnetic resonance (NMR) spectroscopy

^{1}H NMR spectra were recorded on a Bruker Avance-300 (300 MHz) nuclear magnetic spectrometer equipped with a z-gradient QNP 5 mm sample probe, in $CDCl_3$ or DMSO-d_6 as solvent. Two-dimensional [^{1}H ^{1}H] correlation spectroscopy (COSY) spectra were recorded on a Bruker Avance-500 (500 MHz). The chemical shift of the lock solvent

was used as the reference frequency.

3.3.10 UV-visible spectrophotometry

UV-visible (UV-vis) spectra were recorded on a Cary 100 Bio UV-Vis spectrophotometer with a spectral bandwidth (SWB) of 2 nm, operated with the Cary Varian UV Scan Application (v3.001339). The polymer solutions were added to a quartz cell with a 1 cm path length. Absorbance measurements at a Pd concentration of 6.0 $\mu g \cdot mL^{-1}$ were performed in the 200–800 nm range at a scan rate of 600 $nm \cdot min^{-1}$ and 1 nm intervals. Baseline correction was also applied for water or ethanol.

3.4 Results and discussion

3.4.1 Characterization of the ACP substrates – Solutions properties

3.4.1.1 Copolymer characteristics

The ACPs used as templates in this study incorporated a PS core of generation *n* (*Gn*; $n = [-1,2]$, $n \in \mathbb{N}$) and a shell of grafted P2VP chains.[28] Within this notation *G*(-1) corresponds to a linear polymer, and *G*0 to a comb-branched polymer. The overall generation is denoted as *G*[*n*+1]. The sample nomenclature employed (*Gn*PS-*g*-P2VP) indicates the generation number of the PS substrate as well as the composition of the polymer segments grafted last (P2VP). The characteristics of the PS homopolymers and the copolymers derived from these substrates are reported in terms of absolute number-average molar mass ($\bar{M}_n$), molar-mass dispersity ($Đ_M = \bar{M}_w \cdot \bar{M}_n^{-1}$), branching functionality (*f*), and composition in Table 3.1 and Table 3.2, respectively. The molar mass of the generation *n* ACPs is expected to

increase according to Equation 3.1,

$$\bar{M}_{\mathrm{n}}(n) = \sum_{i=0}^{n+1} \bar{M}_{\mathrm{n,br}}(i) \left[\prod_{j=0}^{i} f(j) \right] \tag{3.1}$$

where $\bar{M}_{\mathrm{n,br}}$ is the number-average molar mass of the side chains (branches), and the branching functionality (*f*) is defined as:

$$f(j) = \frac{\bar{M}_{\mathrm{n}}(j) - \bar{M}_{\mathrm{n}}(j-1)}{\bar{M}_{\mathrm{n,br}}(j)} \tag{3.2}$$

If $\bar{M}_{\mathrm{n,br}}$ and f remain constant for each grafting cycle, then $\bar{M}_{\mathrm{n}}$ can be expressed as a geometric series, such as:

$$\bar{M}_{\mathrm{n}}(n) = \sum_{n=0}^{n+1} \bar{M}_{\mathrm{br}} f^{n} = \bar{M}_{\mathrm{br}} \left(\frac{f^{n+2} - 1}{f - 1} \right) \tag{3.3}$$

The short P2VP chains (5,000 g·mol^{-1}) attached onto the relatively larger PS cores confers a spherical shape and micellar characteristics to the AGP molecules, which compare to the crew-cut micelle topology (Scheme 3.2).[41] Small-angle neutron scattering (SANS) measurements on these molecules highlighted a non-uniform segmental density consistent with a hard core–soft shell morphology.[42] These results were also confirmed with fluorescence quenching measurements.[43] Such a morphology is also reminiscent of poly(amidoamine) (PAMAM) dendrimer structures, characterized by a dense core with internal cavities and a more flexible shell (up to *G*6, after which back-folding of the chains pervades the cavities).[44]

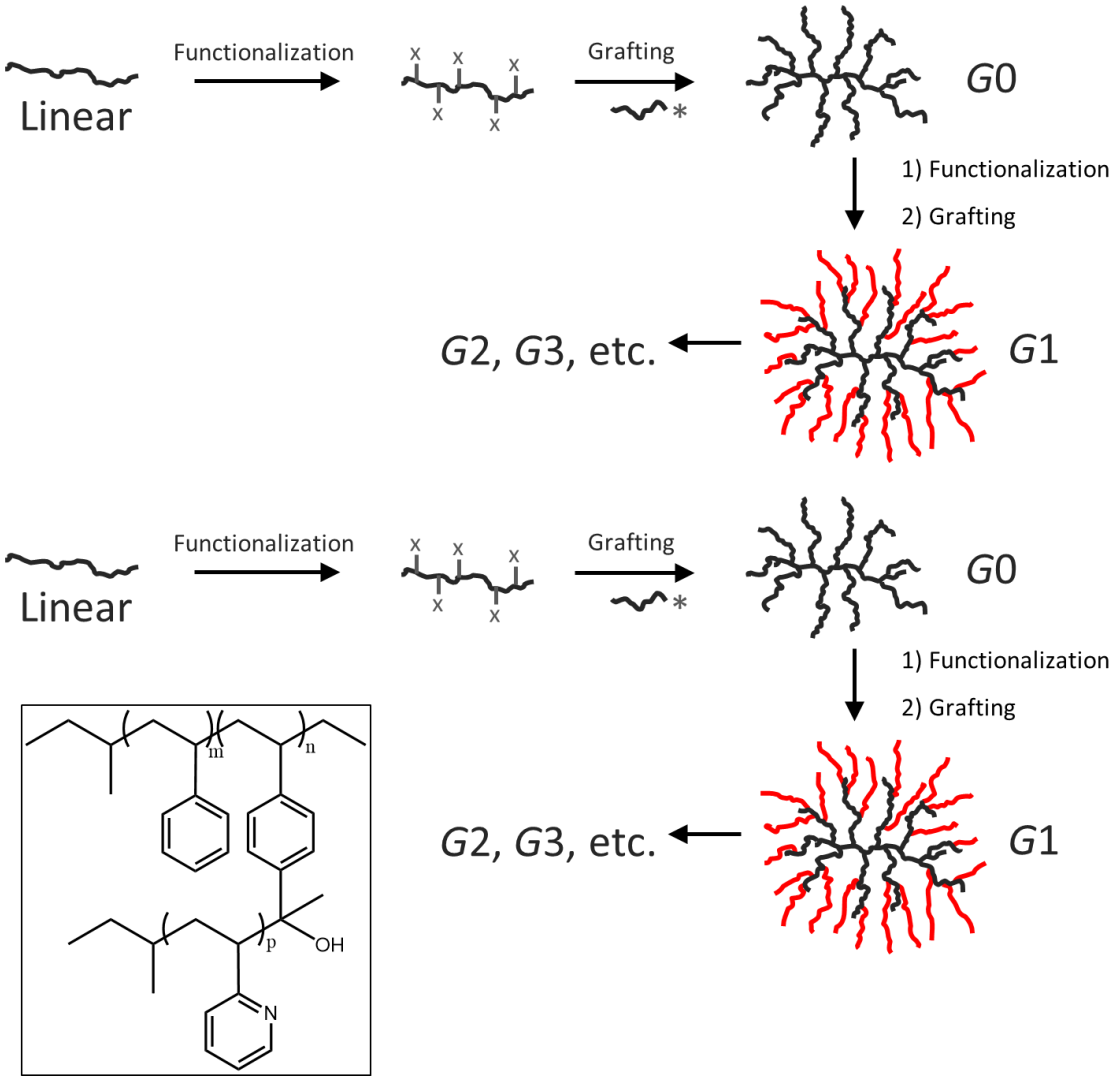

Scheme 3.2 Synthesis of arborescent polymers of different generations (*Gn*). Inset: Structure of the polystyrene-*graft*-poly(2-vinylpyridine) copolymer.

Table 3.1 Characteristics of the PS substrates and side chains used in the preparation of arborescent copolymers. Adapted from Reference 28. Copyright 2012 The Royal Society of Chemistry.

Polymer	Side chains		Substrate		
	$\bar{M}_n$ (g/mol)[a]	$\bar{M}_w/\bar{M}_n$[a]	$\bar{M}_n$ (10^3 g/mol)[b]	$\bar{M}_w/\bar{M}_n$[b]	f_n[c]
Linear PS	n/a	n/a	5.2	1.06	-
*G*0PS	5,500	1.06	97	1.03	17
*G*1PS	4,900	1.07	1,100	1.03	205
*G*2PS	4,300	1.25	5,300	1.09	1013

[a] Absolute values determined from SEC and polystyrene standards calibration curve. [b] Absolute values from SEC-multi-angle laser light scattering (MALLS) analysis. [c] Branching functionality: Number of branches grafted in the last cycle per molecule.

Table 3.2 Characteristics of the arborescent copolymers templates. Adapted with permission from Reference 28. Copyright 2012 The Royal Society of Chemistry.

Polymer	P2VP side chains		Graft copolymer				
	$\bar{M}_n$ (10^3 g/mol)[a]	$\bar{M}_w/\bar{M}_n$	$\bar{M}_n$ (10^3 g/mol)[a]	$\bar{M}_w/\bar{M}_n$	f_n[b]	2VP (mol %)[c]	2VP groups[d]
PS-*g*-P2VP	5.1	1.15	74	1.08	13	96	900
*G*0PS-*g*-P2VP	5.5	1.15	1,100	1.08	182	95	9,600
*G*1PS-*g*-P2VP	6.2	1.10	8,400	1.09	1177	91	66,500
*G*2PS-*g*-P2VP	4.1	1.14	20,400[e]	n/a[e]	3693	91	144,000

[a] Absolute values from SEC-MALLS and light scattering measurements. [b] Branching functionality: Number of branches grafted in the last cycle per molecule. [c] From ^{1}H NMR analysis. [d] From $\bar{M}_n$ and f_n. [e] Interaction of the *G*3 copolymer with the SEC column prevented elution. Estimated values obtained from the absolute $\bar{M}_n$ of the substrate and the composition measured by ^{1}H NMR.

3.4.1.2 SEC analysis

Characterization of the copolymers by SEC in THF confirmed the low molar-mass dispersity of the samples ($Đ_M \leq 1.1$, Table 3.2). However, it has been reported that poor elution of the larger generation polymer (*G*3) from the SEC column in THF hampered the analysis.[28,29,45] Similar difficulties were reported even for linear block copolymers, and were attributed to interactions of the P2VP component with the SEC stationary phase.[46]

3.4.1.3 ^{1}H NMR analysis and solubility

The 2VP units within the shell of the *Gn*PS-*g*-P2VP copolymers account for more than 90% of the repeating units in the ACPs, as revealed by ^{1}H NMR spectroscopy, and provide good solubility to the copolymers in ethanol (Table 3.2). The molar fraction of styrene increases with the generation number to reach 9 mol % for the *G*3 molecules. The glass transition temperature (T_g) of the PS homopolymer AGPs with branches of about 5000 g·mol^{-1}, measured previously by differential scanning calorimetry (DSC), was found to range from 87–103 °C.[47] It can thus be inferred that in ethanol at room temperature, the collapsed PS core should form a compact glassy domain within the unimolecular micelle. However, SANS characterization of the ACPs in methanol-d_4 suggested that partial mixing of the P2VP chains at the core-shell interface of the molecules hinders the complete collapse of the PS core within the micelles.[48] The solubility characteristics and size determined from DLS analysis (Section 3.4.1.4) present circumstantial evidence that a similar behavior is observed in ethanol.

Good solubility of the ACPs is observed in DMF (a good solvent for both blocks), although this polar aprotic solvent is better at solubilizing the P2VP than the PS moieties.[46]

On the other hand THF, also a good solvent for both moieties, displays a preference for the PS segments and could lead to a low level of aggregation.[46] Differences in solvent quality were indeed invoked when accounting for polymer adsorption onto the stationary phase in SEC analysis, particularly for the larger *G*3 copolymers.[29]

3.4.1.4 DLS analysis

Cumulants analysis of the ACF obtained from DLS measurements in DMF revealed a relatively low particle-size dispersity ($Đ_p = \mu_2/\Gamma^2$), below 0.16 for all the structures investigated (Table 3.3, column 1). Low dispersities were also observed for ACPs of generations *G*1 and above in ethanol, which is a non-solvent for the PS block but a good solvent for the P2VP block (Table 3.3, column 2). The comb-branched copolymer (*G*0) had a larger size dispersity in ethanol ($Đ_p = 0.26$), presumably due to a low level of aggregation of the flexible, open structure of these copolymers. In less polar solvents, viz. THF and $CHCl_3$, broader size distributions were observed for all the copolymers ($Đ_p \approx 0.20$), with a size dispersity decreasing as the size of the macromolecules increased (Table 3.3, column 3 and 4). It can be concluded that the lower solubility of the P2VP segments in these solvents induces a low level of aggregation, and therefore broadens their size distribution.

CONTIN analysis of the ACFs supported the results obtained in both THF and $CHCl_3$ for the *G*0 copolymer; a broader size distribution was also noted in DMF (Figure 3.1). Monomodal and uniform size distributions were nevertheless observed for all the upper generation copolymers (*G*1 and above) in the solvents investigated (Figure 3.1). In ethanol even the *G*0 copolymer displayed a narrow size distribution, in contrast to the $Đ_p$ determined from cumulants analysis (Table 3.3). This discrepancy likely stems from the known

sensitivity of these methods to noise levels in the baseline and to dust contamination. These issues are particularly pronounced for small particles, as the signal-to-noise ratio decreases and leads to broader size distributions.[49,50]

Table 3.3 Hydrodynamic diameter and size dispersity of arborescent *Gn*PS-*g*-P2VP from dynamic light scattering measurements in different solvents.[a]

Sample	DMF		Ethanol		THF		$CHCl_3$	
	Diameter (nm)	$Đ_p$	Diameter (nm)	$Đ_p$	Diameter (nm)	$Đ_p$	Diameter (nm)	$Đ_p$
PS-*g*-P2VP	10.9 ± 0.2	0.08	10.0 ± 0.1	0.26	9.4 ± 0.1	0.24	8.1 ± 0.3	0.19
*G*0PS-*g*-P2VP	23.8 ± 0.1	0.02	28.3 ± 0.2	0.07	22.8 ± 0.6	0.26	24.0 ± 0.1	0.29
*G*1PS-*g*-P2VP	50.1 ± 0.2	0.16	55.8 ± 0.2	0.10	53.0 ± 0.7	0.20	61.6 ± 0.6	0.22
*G*2PS-*g*-P2VP	98.2 ± 0.7	0.06	107.5 ± 0.6	0.08	109.1 ± 1.1	0.11	117.9 ± 0.6	0.18

[a] Z-average diameter and size dispersity ($Đ_p$) obtained from cumulants analysis. Standard deviation obtained from a series of at least 5 measurements.

In conclusion, the copolymers exist as well-dispersed colloidal species in both DMF and ethanol; a low level of aggregation was only observed for the relatively open comb-branched structures. In less polar solvents, decreased solubility of the P2VP segments leads to broadening of the size distribution. Interestingly, a similar aggregation phenomenon was reported for comb-branched PS-*g*-P2VP copolymers in methanol[27] and in aqueous HCl

solutions, where the P2VP segments acquire polyelectrolyte character.[29] The upper generation copolymers, characterized by a higher branching functionality, formed more uniform dispersions with low size dispersities.

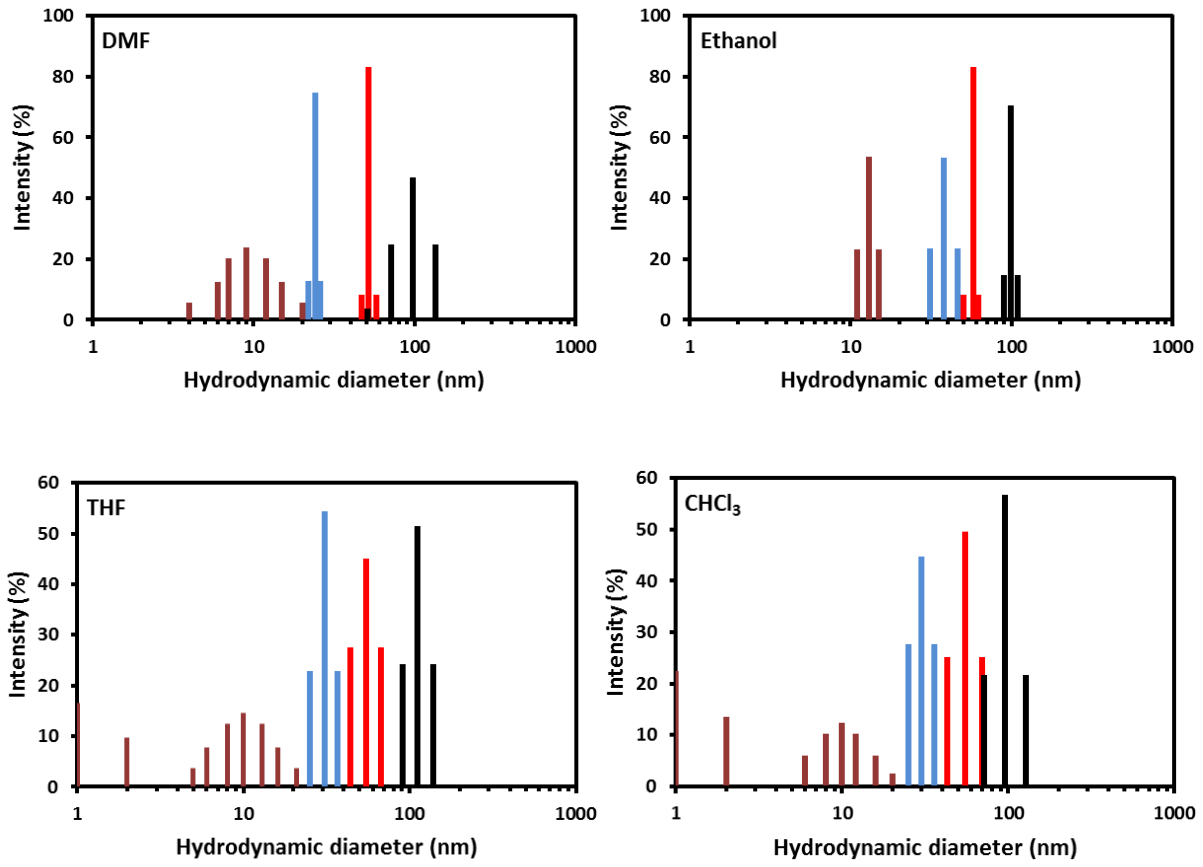

Figure 3.1 Intensity-weighted size distributions from DLS analysis of different generations (*Gn*) of PS-*g*-P2VP. From left to right: *n* = 0 (purple), *n* = 1 (blue), *n* = 2 (red), and *n* = 3 (black).

The hydrodynamic diameter (D_h) increased with the generation number of the copolymers as expected, varying from 28 to 108 nm for molar masses ranging from 1×10^6 to 2×10^7 g·mol^{-1} (Table 3.3). D_h was slightly larger in ethanol than in DMF, pointing to greater solvation of the P2VP chains due to hydrogen bonding with the solvent molecules.

The molar mass of the *G*1 copolymer was around 10^6 g·mol^{-1}; for comparison, a PAMAM dendrimer equates this molar mass only after generation 10, requiring 20 reaction steps for its synthesis.[26] The theoretical number of nitrogen atoms in a *G*10 PAMAM is 16,378,[44] while a *G*2PS-*g*-P2VP molecule contains almost 12 times this amount (Figure 3.2). In terms of the number of grafted P2VP chains in the shell, the *G*3 copolymer also has about 300 times more side chains than the *G*0 molecules (Table 3.2). These data clearly illustrate the very rapid growth of arborescent polymers over successive generations in comparison to dendrimers, as a result of both a high branching multiplicity (ca. 10-15 branching sites per side chains) and the use of polymeric segments rather than small molecule monomers as building blocks.

The amphipolar character of arborescent PS-*g*-P2VP molecules, reminiscent of unimolecular micelles in both polar and relatively non-polar solvents, pave the way to applications in areas such as catalysis, drug delivery, and environmental remediation. Previous solubilization studies using polycyclic aromatic hydrocarbons already highlighted the ability of these copolymers to solubilize hydrophobic compounds in aqueous solutions.[31] Sustained release was also demonstrated for bioactive molecules, the release rate being controlled by both the polymer generation and the loading level employed.[51]

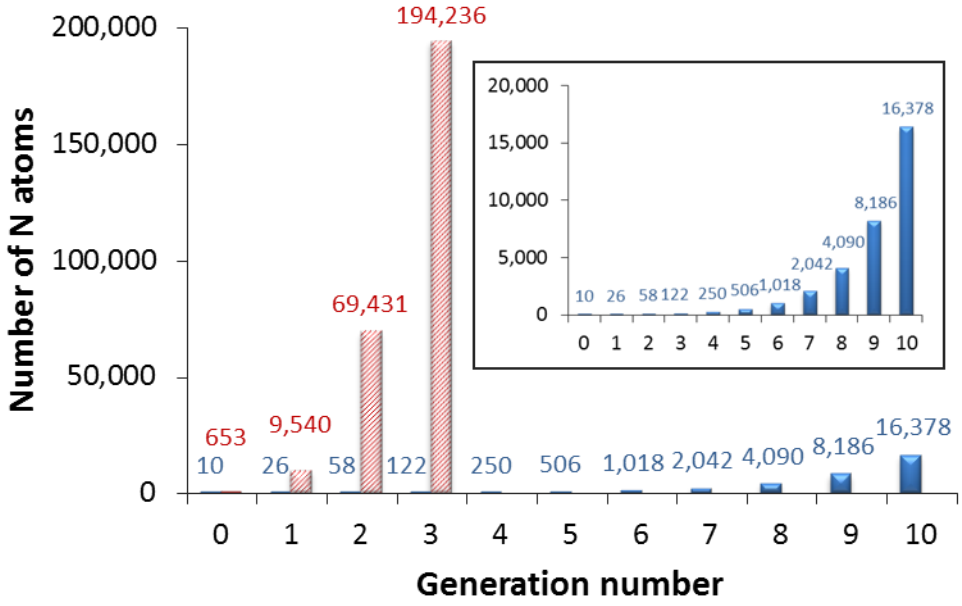

Figure 3.2 Comparison of the total number of N atoms in PAMAM dendrimers (left, blue; and inset) and ACPs (right, red stripes) as a function of the generation number.

3.4.2 Characterization of the ACP substrates – Solid state properties

The molecular organization and size of the ACPs was visualized by AFM in the tapping mode, after casting a monolayer of copolymer onto a mica substrate. All the particles displayed equiaxial (spherical) morphologies, but the extent of phase segregation observed between the different blocks depended on the generation number and the type of solvent used. A geometric increase in the molecular volume of the copolymers was observed up to *G*2 as expected, but the increase was more modest for the *G*3 copolymer.

3.4.2.1 Influence of the casting solvent

Among the different solvents considered the less polar and more volatile solvents, viz. chloroform and THF, were favored since they led to the formation of better resolved

monolayers. In ethanol for instance, aggregation of the molecules was observed as well as poor adhesion on the mica substrate upon spin-casting. Solvent removal was an issue for DMF. While chloroform and THF are both good solvents for the PS and P2VP moieties, the former is slightly better for P2VP than for PS. This was observed by Kiriy et al. in the analysis by AFM of PS-P2VP heteroarm star copolymers, which exhibited intramolecular phase segregation when deposited from chloroform solutions, while the PS and P2VP arms of these copolymers were randomly distributed when deposited from THF.[52] These experimental observations were supported by solubility parameters calculations in these solvents. Figure 3.3 compares *G*0PS-*g*-P2VP copolymers deposited from chloroform and THF solutions. The structures observed for the latter solvent clearly display lower contrast and less defined phase boundaries. This is consistent with better mixing of the PS and P2VP segments in THF. On the other hand, smoother and more uniform boundaries are observed when the micelles are deposited from chloroform (Figure 3.3, left). Upon deposition, strong interactions between the hydrophilic mica surface and the P2VP chains lead to flattening of the structures, while the PS core located at the center forms spherical humps. To enhance the phase difference, chloroform was therefore preferred for AFM sample preparation.

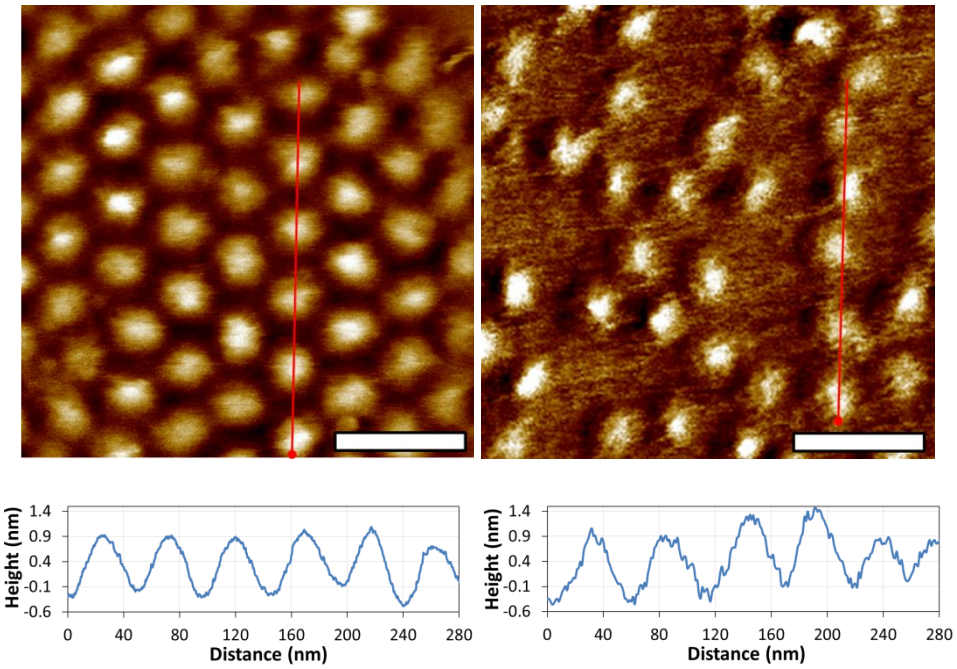

Figure 3.3 AFM imaging in the phase contrast mode for *G*0PS-*g*-P2VP in $CHCl_3$ (top, left) and THF (top, right), and corresponding height section profiles (bottom). The scale bars represent 100 nm; the whole picture is 350 × 350 nm^2.

Micrographs obtained for the *Gn*PS-*g*-P2VP sample series in the height mode are represented in Figure 3.4, along with the height profiles derived from section analysis of the images. The corresponding phase images are provided in Figure 3.5. The overall dimensions of the polymers measured in the height mode are summarized in Table 3.4, and the core-shell features measured in the height and phase modes are provided in Table 3.5.

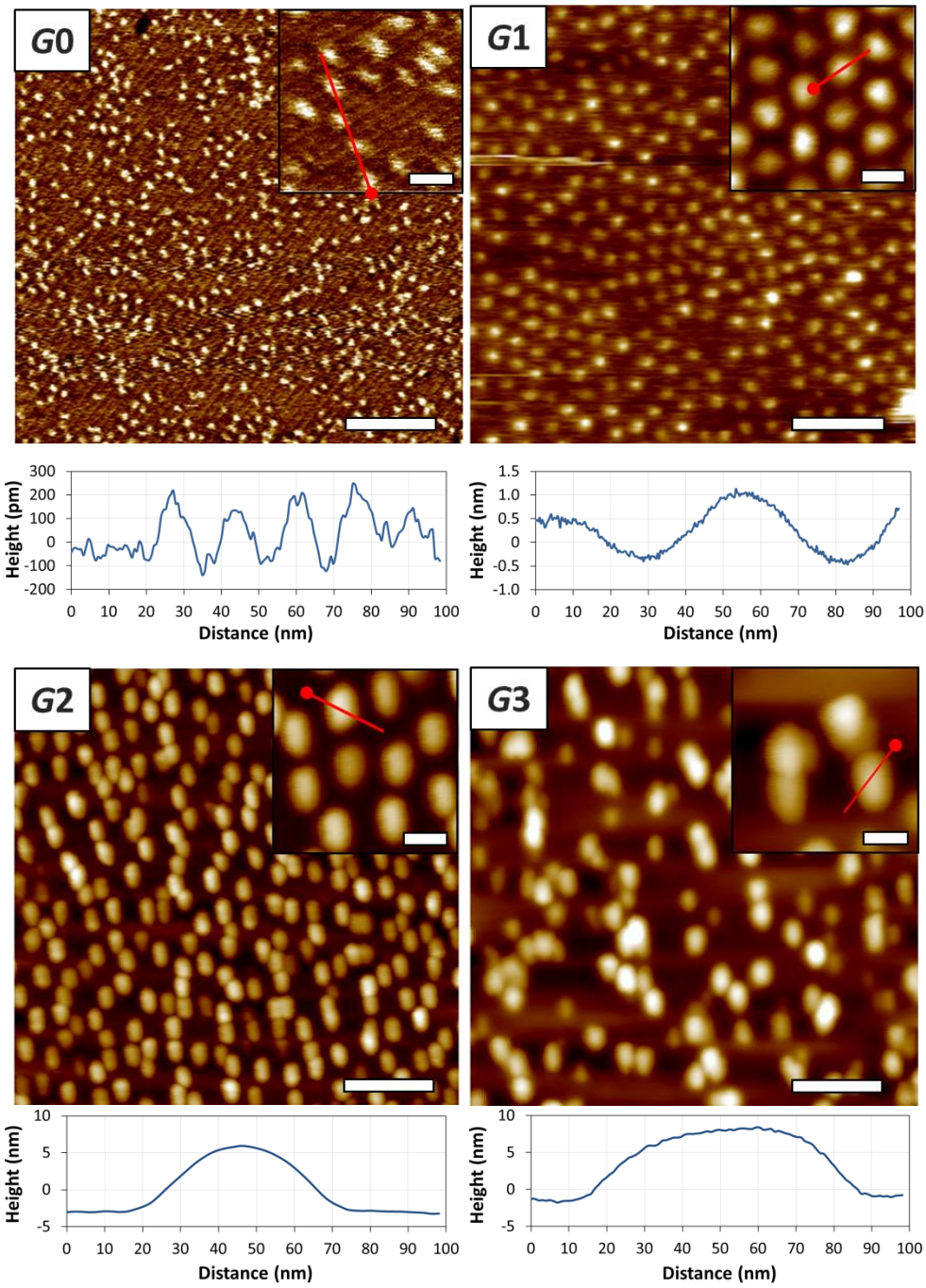

Figure 3.4 AFM imaging of the arborescent copolymer templates in the height mode (top), and corresponding height profiles (bottom). The scale bars are, for *G*0: 100 nm, inset 20 nm; and for *G*1-*G*3: 200 nm, inset 50 nm. The picture size for *G*0 is 500 × 500 nm^2, inset 80 x 80 nm^2; the picture size for *G*1-*G*3 is 1 × 1 µm^2, inset 250 × 250 nm^2.

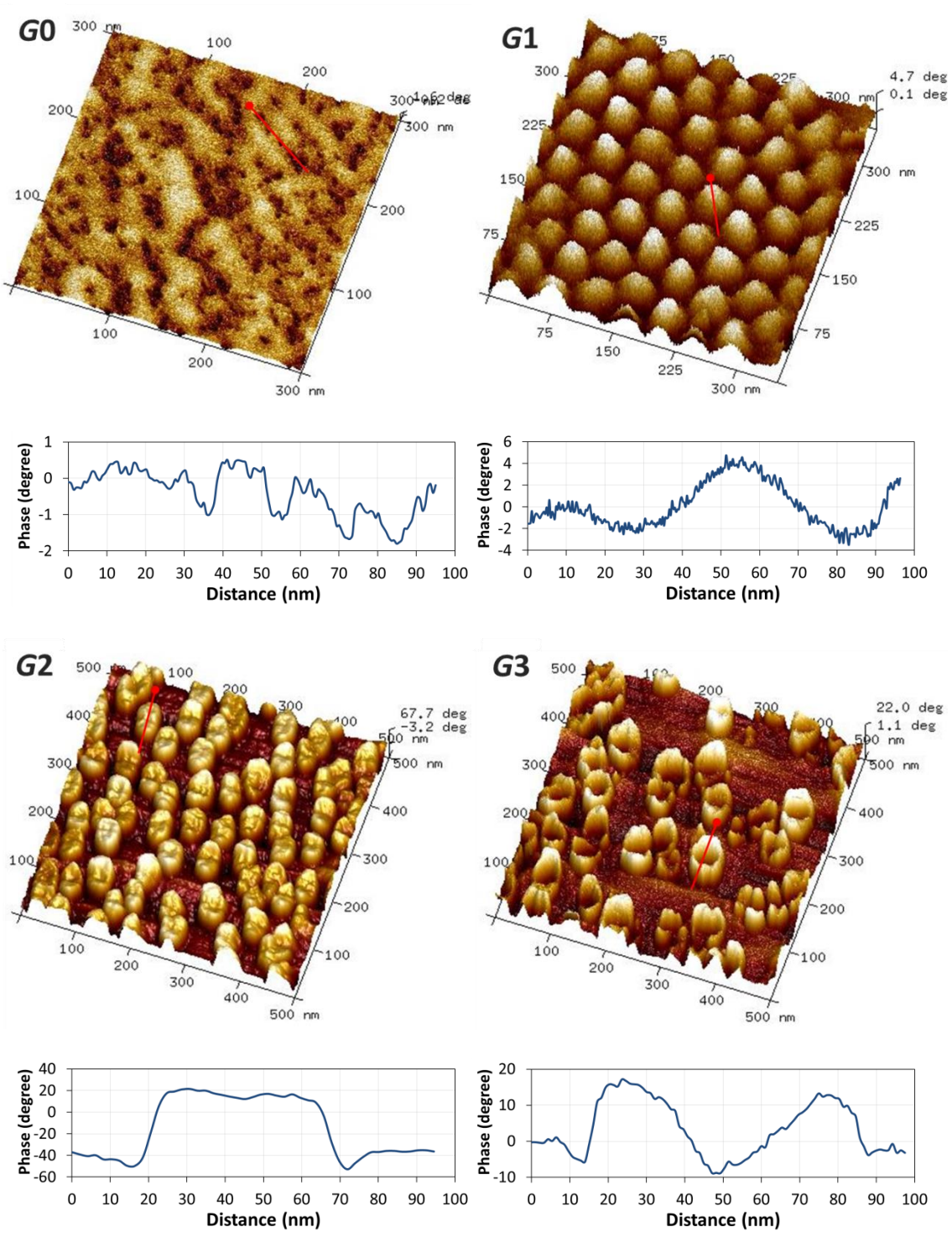

Figure 3.5 AFM imaging of the arborescent copolymer templates (*G*0–*G*3) in the phase contrast mode (top) and the corresponding phase profiles (bottom).

Table 3.4 Size of arborescent copolymers measured by AFM in the height mode.

Sample	Width, *d* (nm)	Height, *h* (nm)	Volume (nm^3)	Equivalent sphere diameter (nm)	Bulk diameter (nm)
PS-*g*-P2VP	14.2 ± 3.5	0.43 ± 0.03	48 ± 25	4.4 ± 0.8	5.9 ± 0.8
*G*0PS-*g*-P2VP	52.8 ± 2.2	1.4 ± 0.2	2000 ± 390	15.6 ± 1.1	14.5 ± 2.0
*G*1PS-*g*-P2VP	67.9 ± 7.7	10.5 ± 1.4	25600 ± 6300	36.4 ± 2.9	28.6 ± 4.2
*G*2PS-*g*-P2VP	77.1 ± 4.1	10.4 ± 3.1	33000 ± 12000	39.2 ± 4.8	40.5[a]

[a] The molar-mass dispersity of the *G*3 copolymer could not be obtained by SEC (column interactions).

Table 3.5 Dimensions of the core-shell arborescent copolymers measured by AFM in the height and phase modes.

	Height mode			Phase mode		
Sample	Core (nm)	Shell (nm)	Overall diameter (nm)	Core (nm)	Shell (nm)	Overall diameter (nm)
PS-*g*-P2VP	6.1 ± 1.0	4.3 ± 1.6	14.2 ± 3.5	4.6 ± 0.9	7.4 ± 1.3	12.0 ± 1.3
*G*0PS-*g*-P2VP	22.6 ± 4.1	14.4 ± 2.5	52.8 ± 2.2	21.8 ± 3.4	14.8 ± 2.0	51.3 ± 4.5
*G*1PS-*g*-P2VP	n/a	n/a	67.9 ± 7.7	57.1 ± 4.5	5.2 ± 3.9	67.4 ± 4.0
*G*2PS-*g*-P2VP	n/a	n/a	77.1 ± 4.1	72.9 ± 6.3	6.8 ± 4.1	86.4 ± 3.7

3.4.2.2 Comb-branched (*G*0) copolymer

Individual molecules of the comb-branched copolymer deposited from chloroform were imaged by AFM in the height mode and are represented at different magnifications in

Figure 3.4. The isolated molecules formed irregular disk-like structures with a protruding central globule and a seemingly shallower corona. The cross-sectional profile reveals a very flat topology with a maximum height of 0.43 ± 0.03 nm and a diameter of 6.1 ± 1.0 nm, while the corona, appearing as a shallow layer, has a diameter of 14.2 ± 3.5 nm (Table 3.4). The P2VP chains within the corona therefore extend about 4.3 ± 1.6 nm from the core, with a thickness below 0.22 ± 0.06 nm (Table 3.5). The protrusion presumably corresponds to the rigid PS core, while the surrounding P2VP chains form a flat corona with dimensions lower than the end-to-end distance (r_s) calculated for a fully elongated P2VP chain (13.2 ± 7.2 nm).[*] Measurements by AFM and X-ray photoelectron spectroscopy (XPS) previously confirmed that P2VP has strong polar interactions with mica, forcing the chains to adopt a highly stretched conformation. It was estimated that every second to third 2VP unit was chemisorbed on the mica surface, as illustrated in Scheme 3.3.[53] It was proposed that phase segregation was favored by the selectivity of chloroform for the P2VP chains, as well as the unfavorable interactions between the P2VP and PS chains,[54] although van der Waals interactions originating from the substrate were also invoked.[53]

The phase lag measured on the AFM instrument in the phase mode, presented in Figure 3.5, confirms the presence of spheroidal nodules and more diffuse areas. While AFM alone cannot be used to assign clearly a domain to a specific component,[55] knowledge of the copolymer structure can be used to attribute the nodular regions to the spherical PS core and the compliant, adhesive component to the P2VP chains surrounding the core. In comparison

[*] $r_s = 2nb \sin(\theta/2)$, where the number-average degree of polymerization, $n = 52$ ($\bar{M}_n = 5500$ g.mol^{-1}, $Đ_M = 1.15$), the C–C bond distance $b = 0.154$ nm, and the bond angle $\theta = \cos^{-1}(-1/3)$.

to the height measurements, the core of the sample was found to be slightly smaller (4.6 ± 0.9 nm diameter) while the outer layer, spanning 7.4 ± 1.3 nm, was slightly larger (the differences are however insignificant when considering the error limits on the measurements).

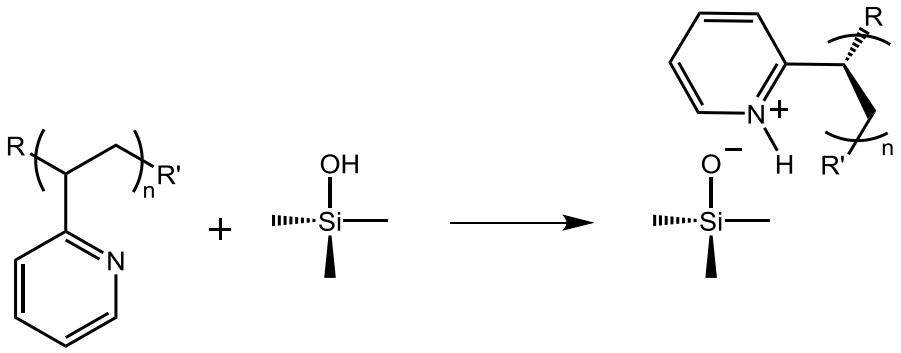

Scheme 3.3 Polar interactions between the 2VP units of the ACPs and the mica surface. Adapted with permission from Reference 53. Copyright 1997 American Chemical Society.

3.4.2.3 First generation (*G*1) copolymer

A monolayer film of *G*0PS-*g*-P2VP, obtained by spin-casting of the copolymer from a chloroform solution, is shown in Figure 3.4 at two different magnifications. Similarly to the *G*0 copolymer, the *G*1 sample displays disk-like structures, but better resolved and larger in size. The protruding globule, presumably formed by the PS core, and the flat P2VP shell are reminiscent of a *fried-egg* morphology.[56] From the cross-sectional profile measurements shown in Figure 3.4, the overall diameter of the molecules is about 52.8 ± 2.2 nm. The protruding core extends to a height of 1.4 ± 0.2 nm and a diameter of 22.6 ± 4.1 nm (Table 3.4 and Table 3.5). The thickness of the adsorbed P2VP layer was 0.85 ± 0.23 nm, extending

14.4 ± 2.5 nm from the core. Interestingly, this distance is comparable to the end-to-end distance (r_s) calculated for the fully elongated P2VP chains (13.2 ± 7.2 nm). These results corroborate the favorable interactions of the P2VP chains with the polar mica substrates noted earlier, causing the ACP molecules to spread as a monolayer composed of "pancake-like" macromolecules. The narrow size distribution of the molecules promotes the formation of hexagonal packing with a lattice parameter of 50.5 ± 3.8 nm (section profile in Figure 3.4). The distance measured between the particles was below 2.0 ± 0.4 nm. The close packing is consistent with the narrow size distribution of the macromolecules, the inherent molar-mass dispersity of the molecules being responsible for long-range defects such as dislocation and point defects. Such molecular organization could be interesting for applications requiring nanoscale patterning of surfaces.[57]

Phase mode imaging of the *G*1 molecules, shown in Figure 3.5, delineates a relatively rigid core and a more deformable corona. Phase segregation was already noted between the P2VP and PS domains from the height profile corresponding to a *fried-egg* morphology. Phase imaging revealed a difference in terms of adhesive properties between the non-polar PS and the polar P2VP fractions of the copolymer. Determination of the size of the core and the corona in the *G*1 molecules, using this imaging mode, indicated dimensions comparable to the ones measured in the height mode (Table 3.4).

3.4.2.4 Second generation (*G*2) copolymer

Deposition of the *G*1PS-*g*-P2VP copolymer solutions also led to the formation of a monolayer (Figure 3.4), where some local ordering into a hexagonal lattice could be

observed by AFM near the center of the image. The insets in Figure 3.4 represent the *G*2 and *G*1 molecules at the same magnification. As expected, the *G*2 copolymer molecules are larger than their lower generation counterpart. The cross-sectional profile displayed in Figure 3.4 reveals spheroidal structures extending to a height of about 10.5 ± 1.4 nm, and a diameter of about 67.9 ± 7.7 nm. It is noteworthy that the large *G*2 copolymers display a more uniform oblate topology rather than the *fried-egg* topology observed for the smaller copolymers.

Phase imaging revealed a broad inner domain with a large positive phase shift, slightly depressed at the center of the domain (Figure 3.5). Interestingly, a large phase lag is noted at the periphery of the structures, revealing a secondary domain. The domain separation, reminiscent of the *G*1 copolymer structures, is attributed to a hard PS core surrounded by a more adhesive P2VP corona. As expected, the *G*1 PS core is larger than for the lower generation copolymers (Figure 3.5). The overall size measured in phase mode imaging is comparable to the size obtained from the height mode (Table 3.5). The former mode, which discriminates between the different phases, allows size estimations for the PS core (57.1 ± 4.5 nm) and the P2VP corona (5.2 ± 3.9 nm). The core size, corresponding to a *G*1 PS molecule, is larger than the *G*0 PS core; however, the corona has a span almost 3 times smaller. The rigid PS core presumably prevents stretching of the P2VP chains, which are forced to form more compact domains at the core periphery.

3.4.2.5 Third generation (*G*3) copolymer

The structures observed for the *G*3 (largest) copolymers are spheroidal and analogous to the *G*2 molecules (Figure 3.4; the magnification is the same as for the *G*1-*G*3 copolymers).

From the cross-sectional profile of Figure 3.4, the overall diameter is 77.1 ± 4.1 nm (Table 3.4). However the maximum height is comparable to the *G*2 copolymer at 10.4 ± 3.1 nm. Partial flattening of the molecules could be a consequence of the strong interactions of the P2VP shell with the mica surface. Also apparent in the AFM image are a few smaller particles, which could be *G*1 and/or *G*2 copolymer contaminants. These species could not be removed even after 4 successive cycles of precipitation fractionation from THF/methanol (4/1 v/v) mixtures and *n*-hexane. From the particle count on the AFM image, the contaminants correspond to a number fraction of 23% of the macromolecules present. Given their smaller size, their corresponding weight fraction would be much smaller however.

Phase mode imaging of the structures reveals a rigid ring-like domain circumscribed by a more adhesive domain. It is proposed that in this system, the outer P2VP shell near the mica surface can phase-separate and adsorb on the surface, as for the *G*1 and *G*2 copolymers. The P2VP chains covering the PS core are not able to interact with the mica surface, however, and may also phase separate in the interior of the structure. The feature sizes measured in this imaging mode are larger than in the height mode (Table 3.5). Better resolution of the outer P2VP domain could account for the discrepancy. The core diameter thus obtained was 72.9 ± 6.3 nm, while the thickness of the P2VP shell (6.8 ± 4.1 nm) was comparable to the *G*2 copolymer (Table 3.5).

3.4.2.6 Phase segregation

The phase segregation observed between the PS and P2VP segments is in agreement with the well-documented phase behavior of diblock copolymers (DBCs). Phase separation

depends on the number of monomer units in the different blocks A and B (N_A, N_B) and on the Flory-Huggins segment-segment interaction parameter ($\chi_{A\text{-}B}$). In the case of DBCs phase segregation occurs above the *weak segregation limit* ($\chi_{A\text{-}B}N \geq 10$), while entropy-driven phase mixing is favored below this limit.[58,59] Although structurally different, ACPs are expected to qualitatively display comparable phase behavior;[59] that is an increase in the molar mass of the chemically distinct polymer segments should promote microphase segregation.

3.4.2.7 Bulk dimensions

The dimensions of the ACP macromolecules as measured by AFM can be compared with their theoretical bulk dimensions. The unimolecular micelles of generations *G*0 to *G*3 exhibited very flat morphologies, with heights of 0.4 to 11 nm and widths ranging from 14 to 77 nm. The polymers can thus be approximated by hemi-oblate spheroids with a width, *d* (length of the major axis) and a height, *h* (length of the semi-minor axis) determined from the analysis of the cross-sectional profiles of the AFM images acquired in height mode, and reported in Table 3.4. The volume (*V*) of the structures was calculated from:

$$V = \frac{\pi}{6} d^2 h \tag{3.4}$$

The diameter (d_{eq}) of an equivalent sphere having the same volume as the hemi-oblate macromolecules was then obtained from:

$$d_{eq} = 2\left(\frac{3V}{4\pi}\right)^{\frac{1}{3}} = (d^2 h)^{\frac{1}{3}} \tag{3.5}$$

The results obtained are summarized in Table 3.4, with statistical deviations determined by analysis of the full images. As expected from Equation 3.3, the volume initially increases in a geometric fashion within the copolymers series but tapers off after the second generation.

The theoretical bulk diameters were calculated using Equation 3.6, where N_A represents Avogadro's constant, ρ the average bulk density, and $\bar{M}_n$ the number-average molar mass of the copolymer. The average density was determined from the molar composition of the copolymers (where x_{P2VP} represents the molar fraction of 2VP), and the density of the PS (ρ_{PS} = 1.04 g.cm^{-3})[60] and P2VP moieties (ρ_{P2VP} = 1.153 g·cm^{-3})[60] according to Equation 3.7. Of course in this particular case, the molar fraction of PS, $x_{PS} = 1 - x_{P2VP}$.

$$d_{bulk} = 2 \times \left(\frac{3}{4\pi} \frac{\bar{M}_n}{N_A \rho} \right)^{\frac{1}{3}} \tag{3.6}$$

$$\rho = x_{P2VP}(\rho_{P2VP} - \rho_{PS}) + \rho_{PS} \tag{3.7}$$

As can be seen in Table 3.5, the bulk diameter and the equivalent-sphere diameter were in good agreement, clearly indicating the presence of single macromolecules deposited onto the mica surface. The size uncertainties were evaluated from the molar-mass dispersity of the copolymers, since:[61]

$$\frac{\bar{M}_w}{\bar{M}_n} = 1 + \frac{\sigma^2}{\bar{M}_n^2} \tag{3.8}$$

Unfortunately, poor elution of the *G*3 copolymer from the SEC column (Section 3.4.1.2) forbade such estimates for the largest macromolecules.

3.4.3 Loading of the arborescent copolymers with Pd in ethanol

3.4.3.1 Metal loading and reduction

Loading of the arborescent copolymers was achieved by co-dissolution of the macromolecules with the Pd(II) salt in ethanol. As noted previously, ethanol can act both as solvent and reducing agent for $Pd(OAc)_2$. As a matter of fact, the reduction of $Pd(OAc)_2$ to Pd(0) according to Scheme 3.4[62] was observed in the absence of a polymeric stabilizer and led to the deposition of Pd black at the bottom of the vial within 2 h at room temperature (Figure 3.6a).[63] In presence of the ACP, however, the ethanolic solutions remained translucent yellow (Figure 3.6b and Figure 3.6c) or dark brown (Figure 3.6d and Figure 3.6e) for a period of at least 5 months. To investigate the role of the polymer and its interactions with the Pd species, characterization of the colloidal solutions was performed by DLS, TEM, and UV-vis analysis. Determination of the Pd loading in the copolymers was also achieved by a novel technique based on microplasma-optical emission spectrometry (OES – Chapter 4).

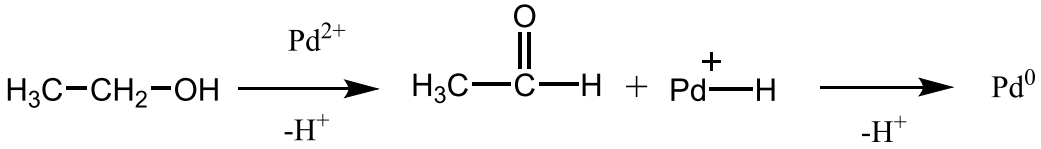

Scheme 3.4 Reduction of $Pd(OAc)_2$ to Pd(0) in ethanol. Reprinted with permission from Reference 62. Copyright 2004 Springer.

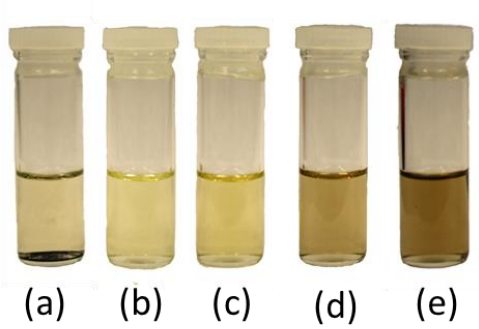

Figure 3.6 Solutions of (a) $Pd(OAc)_2$ in ethanol after 2 h, and *G*0PS-*g*-P2VP (*G*1) in ethanol after 1 week with the following molar equivalents of $Pd(OAc)_2$: (b) 0.25 equiv, (c) 0.5 equiv, (d) 1.0 equiv, and (e) 1.5 equiv.

3.4.3.2 DLS analysis

The solution properties of the arborescent copolymers in ethanol, after addition of 0.5 molar equiv of Pd(II) per 2VP unit, were investigated by DLS and analysis of the autocorrelation function by the cumulants and CONTIN methods. The sizes and size distributions obtained from cumulants analysis are summarized in Table 3.6 for the metal-polymer complexes. Up to the second generation, the copolymers with Pd displayed somewhat broader size distributions ($Đ_p \approx 0.2$) than the bare copolymers ($Đ_p \approx 0.1$, Table 3.3). Since the analysis of non-monomodal distributions by the method of cumulants may lead to significant errors in the calculated hydrodynamic diameters,[50] values are not reported in this case. Clearly, the addition of Pd induced some level of aggregation, even though all the organic–inorganic hybrids remained dispersible in ethanol. The Pd-loaded *G*3 copolymer, on the other hand, had a low size dispersity and its hydrodynamic diameter was comparable to that of the native copolymer (Table 3.3). The large arborescent copolymer therefore seems to provide enhanced steric stabilization for the Pd species in ethanol.

Table 3.6 Size and size distributions obtained from DLS and TEM analysis of arborescent *Gn*PS-*g*-P2VP loaded with 0.5 molar equiv of $Pd(OAc)_2$ in ethanol (see text for details).[a]

Description	$D_{h,z}$ (nm)[a]	$Đ_p$ [a]	$D_{h,c}$ (nm)[b]	D_{TEM} (nm)	$D_{h,c}$ polymer (nm)[c]
PS-*g*-P2VP-Pd(II)	n/a	0.18	12.8 ± 1.7	3.2 ± 0.8	10.0 ± 0.1
*G*0PS-*g*-P2VP-Pd(II)	n/a	0.23	68.7 ± 27.9	21.2 ± 2.4	28.3 ± 0.2
*G*1PS-*g*-P2VP-Pd(II)	n/a	0.20	80.9 ± 22.2	36.1 ± 3.2	55.8 ± 0.2
*G*2PS-*g*-P2VP-Pd(II)	104.9 ± 0.5	0.10	108.9 ± 14.2	50.8 ± 5.9	107.5 ± 0.6

[a] Z-average diameter and size dispersity ($Đ_p$) from cumulants analysis. Standard deviations estimated from a series of 5 measurements. Average diameters cannot be calculated for bimodal distributions of *G*0-*G*2 polymer by cumulants analysis. [b] Hydrodynamic diameter from CONTIN analysis. [c] Data reported in Table 3.3, hydrodynamic diameter from cumulants analysis for the polymer alone, included for convenience.

Size distributions were also obtained from CONTIN analysis and are shown in Figure 3.7. The results are in agreement with the cumulants analysis, with broader and bimodal size distributions for generations below *G*3 in presence of Pd. Small particles, with a diameter below 8 nm, were also detected in the *G*1-Pd solutions. This suggests that the *G*1 copolymer provided relatively poor steric stabilization, and that unbound Pd could have resulted in the formation of free nanoparticles in solution. The intensity-weighted size distribution of both the *G*0-Pd and *G*2-Pd samples show a small amount of large aggregates (>100 nm), that would be insignificant on a number basis however. In both systems, bridging between the micelles through intermolecular bonding of the Pd species could favor aggregate formation.

The larger *G*2 copolymers appear to provide better steric stabilization than the *G*1 copolymers, since no small particle contaminant was evidenced. CONTIN analysis of the *G*3-Pd solutions yielded a narrow size distribution, similarly to cumulants analysis (Table 3.6). The larger copolymer therefore likewise provided greater steric stabilization for the Pd NPs in ethanol than the smaller ACPs.

Interestingly, a similar trend was reported for Pd-loaded PAMAM dendrimers: Lower generation (*G*2) dendrimers were found ineffective for the steric stabilization of Pd NPs in ethanolic aqueous mixtures, while good stabilization was achieved with *G*3 and *G*4 dendrimers.[16] As the generation number of the dendrimers increased, the more compact and closed structure of the macromolecules was thought to provide greater protection against aggregation of the Pd NPs. In another study using DLS measurements, the size of hydroxyl-terminated PAMAM dendrimers at neutral pH was found to double after the encapsulation of Pt NPs. Although the mechanism at play was not fully understood, electrostatic interactions involving the metallic NPs were thought to induce aggregation.[64]

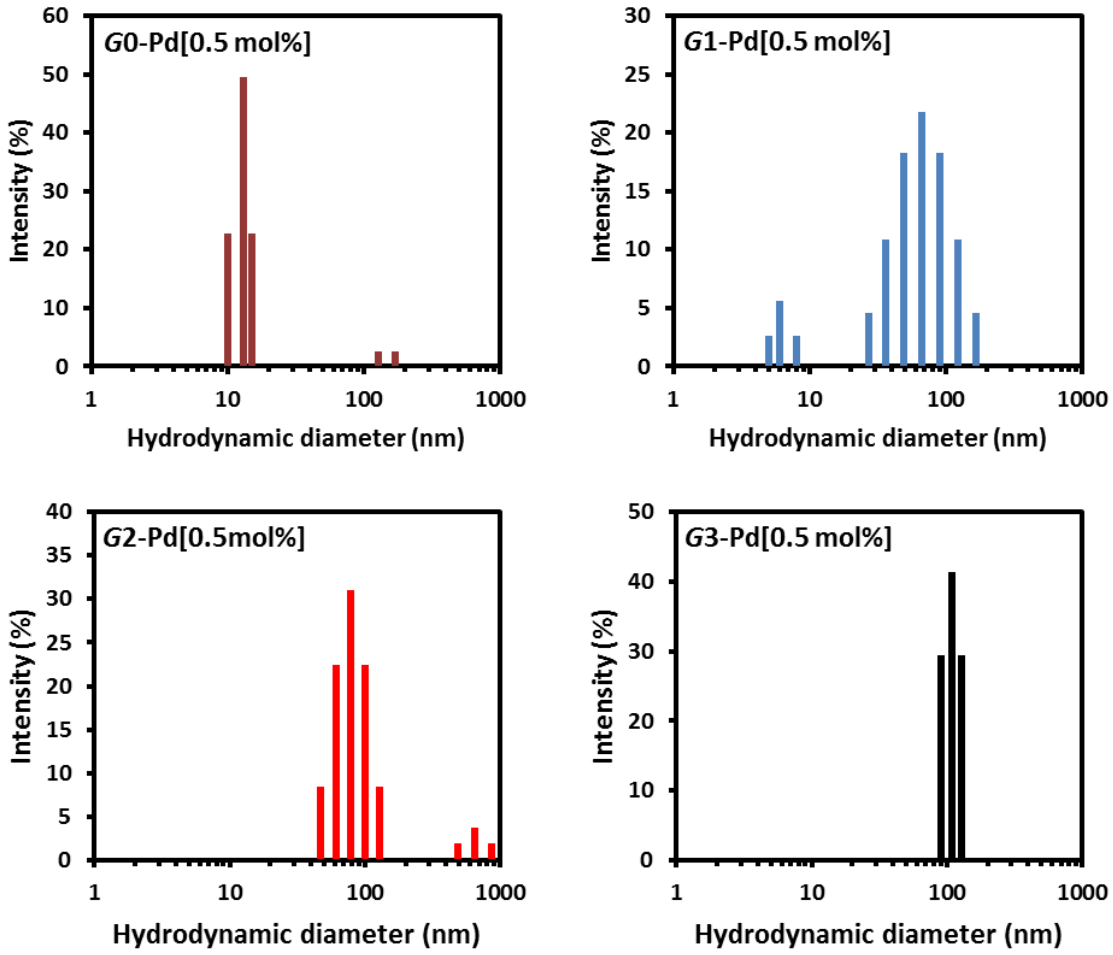

Figure 3.7 Intensity-weighted DLS size distributions for different generations (*Gn*) of PS-*g*-P2VP loaded with 0.5 molar equiv of $Pd(OAc)_2$ in ethanol.

3.4.3.3 TEM analysis

Imaging by TEM of the *Gn*-Pd composites confirmed the presence of Pd within the copolymer templates, as can be seen from the contrast caused by differences in electron density between the Pd-rich regions and Pd-poor regions on the electron micrographs of Figure 3.8–Figure 3.11. The Pd-loaded micelles are spherical particles with overall diameters ranging from 3.2 ± 0.8 nm to 50.8 ± 5.9 nm, from *G*0-Pd to *G*3-Pd, respectively (Table 3.6).

The diameters determined from the electron micrographs are smaller than the hydrodynamic diameters measured by DLS in solution (Table 3.6). Individual micelles were observed for all the samples except for *G*3-Pd, suggesting aggregation as noted by DLS (Section 3.4.3.2).

To investigate the influence of the Pd content on NP formation, the amount of metal added was varied from 0.25 to 1.0 molar equiv per 2VP unit (Pd/2VP). The image contrast of the particles increased with the amount of Pd added as expected. For Pd/2VP $\geq$ 0.5, the formation of small NPs occurred within the micelles, the number of which increased with the loading level.

Reduction of the Pd(II) species was achieved by heating the polymer-metal composites in ethanol at 60 °C for at least 3 h.[65] Reduction of the Pd ions led to the formation of a larger number of Pd NPs (Figure 3.8–Figure 3.11) clearly confined within the *G*1-*G*3 micelles, confirming their stabilization within the copolymers. Only *G*0-Pd had larger Pd NPs in solution, presumably formed by aggregated Pd(0). Interestingly, the size of the Pd NPs formed from the *G*0 samples was largest at Pd/2VP = 0.5, with a diameter of 14.5 ± 1.9 nm (Figure 3.12, and Appendix A3.1). Loading of the micelles with 1.0 equiv of Pd led to the formation of smaller Pd NPs, 3.0 ± 1.1 nm in diameter. The stabilization mechanism in these systems may be akin to the *inter*micellar stabilization observed for small *G*0 PAMAM dendrimers, with several dendritic polymers stabilizing the NPs on their surface.[66] Alternatively, a depletion stabilization mechanism between the polymer and the metal species may be at play.[67]

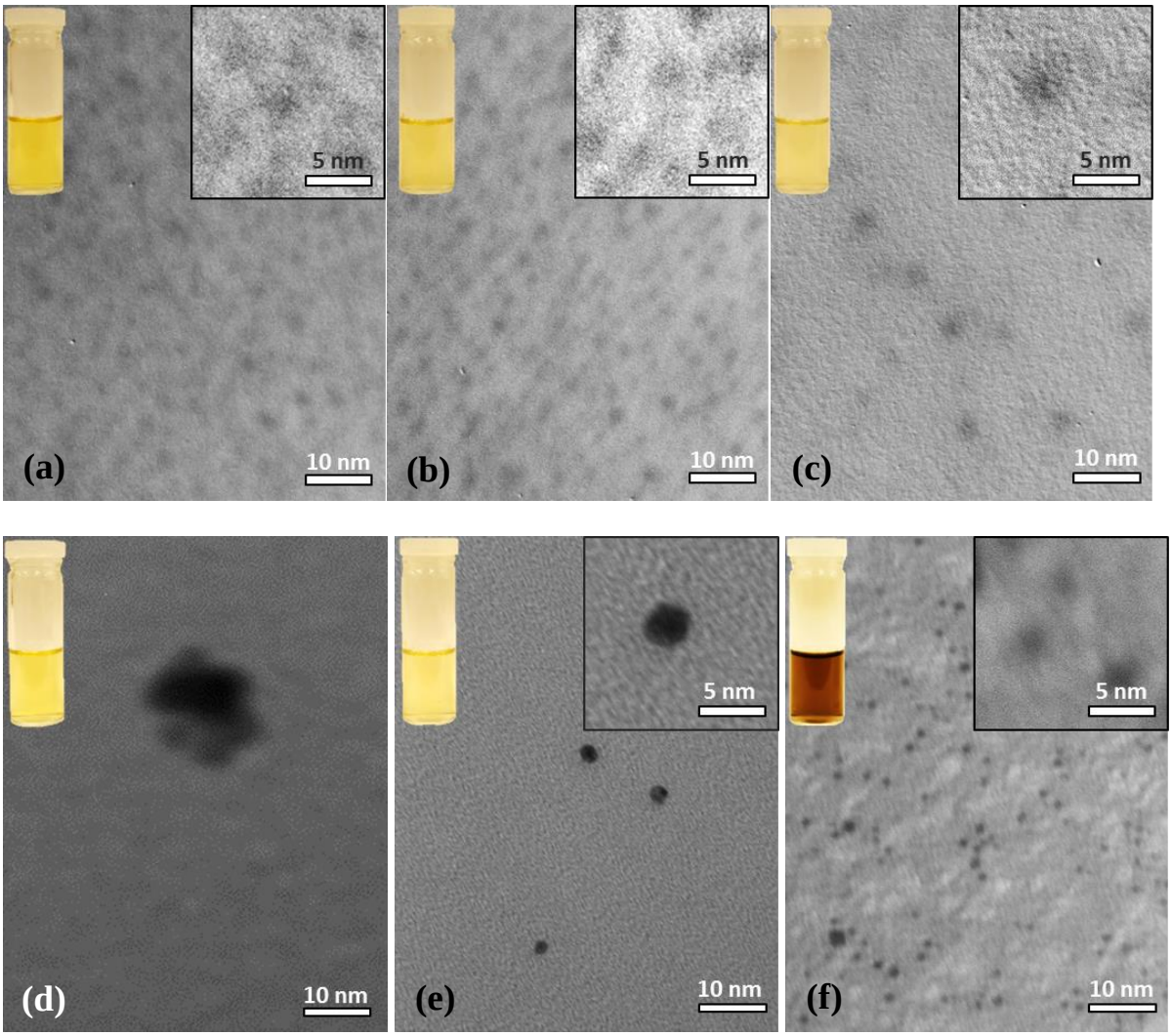

Figure 3.8 Transmission electron micrographs for PS-*g*-P2VP (*G*0-Pd) from ethanolic solutions and in the presence of different molar equivalents of $Pd(OAc)_2$: (a) 0.25 equiv, (b) 0.5 equiv, and (c) 1.0 equiv. The same samples are shown after heating for 3 h at 60 °C in (d)-(f), respectively. Inset: Magnification of individual micelles.

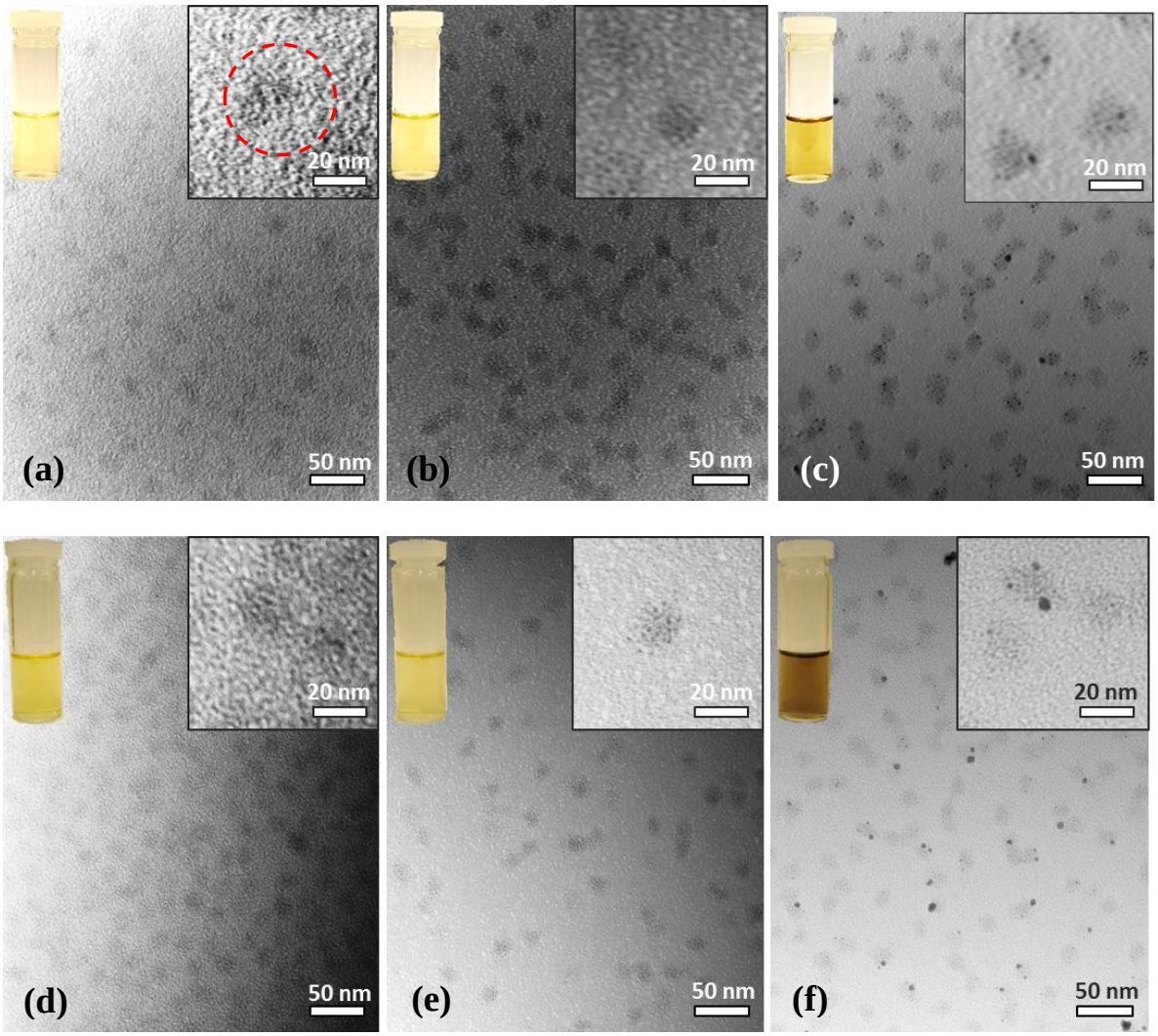

Figure 3.9 Transmission electron micrographs for *G*0PS-*g*-P2VP (*G*1-Pd) from ethanolic solutions and in the presence of different molar equivalents of $Pd(OAc)_2$: (a) 0.25 equiv, (b) 0.5 equiv, and (c) 1.0 equiv. The same samples are shown after heating for 3 h at 60 °C in (d)-(f), respectively. Inset: Magnification of individual micelles.

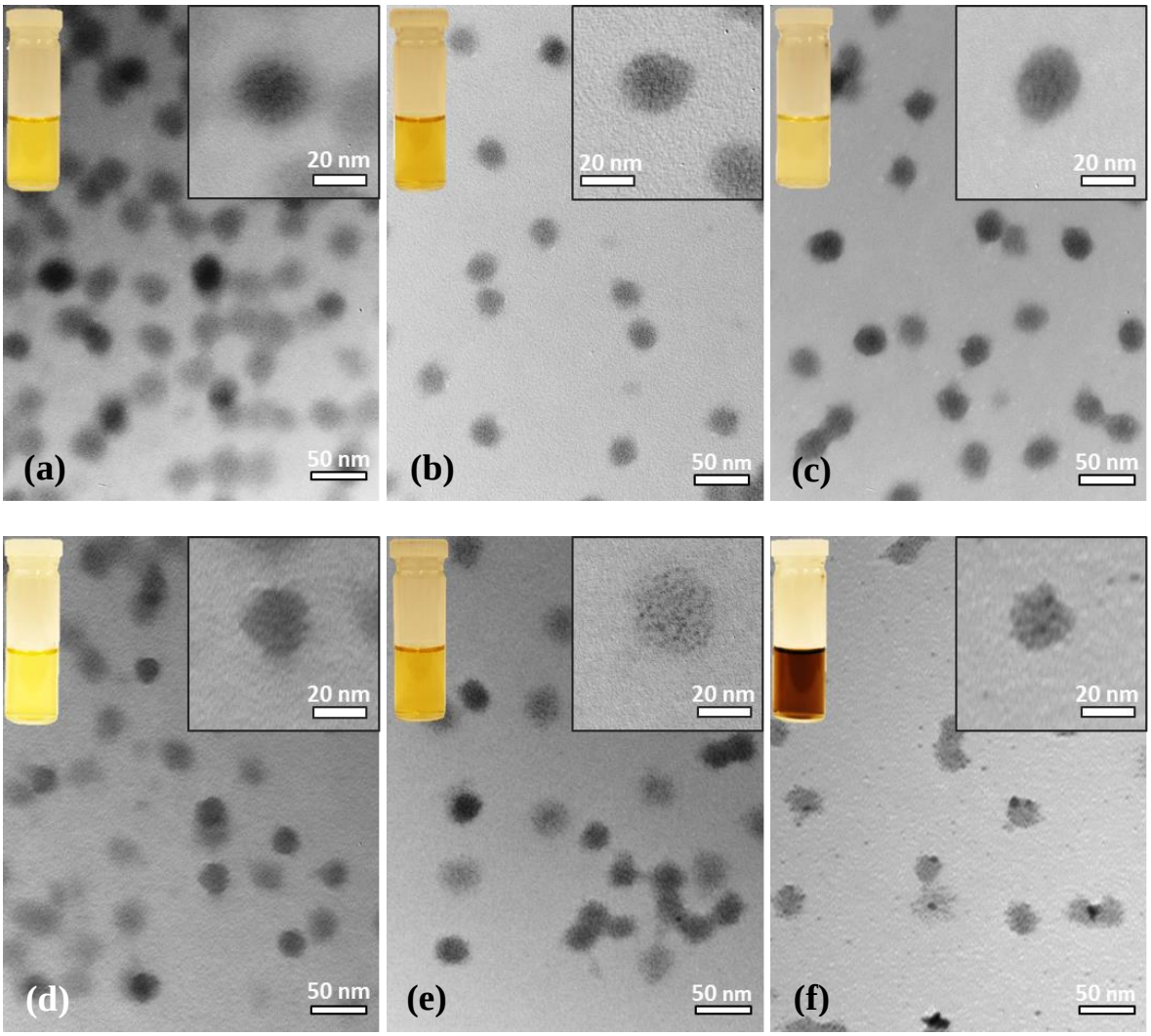

Figure 3.10 Transmission electron micrographs for *G*1PS-*g*-P2VP (*G*2-Pd) from ethanolic solutions and in the presence of different molar equivalents of $Pd(OAc)_2$: (a) 0.25 equiv, (b) 0.5 equiv, and (c) 1.0 equiv. The same samples are shown after heating for 3 h at 60 °C in (d)-(f), respectively. Inset: Magnification of individual micelles.

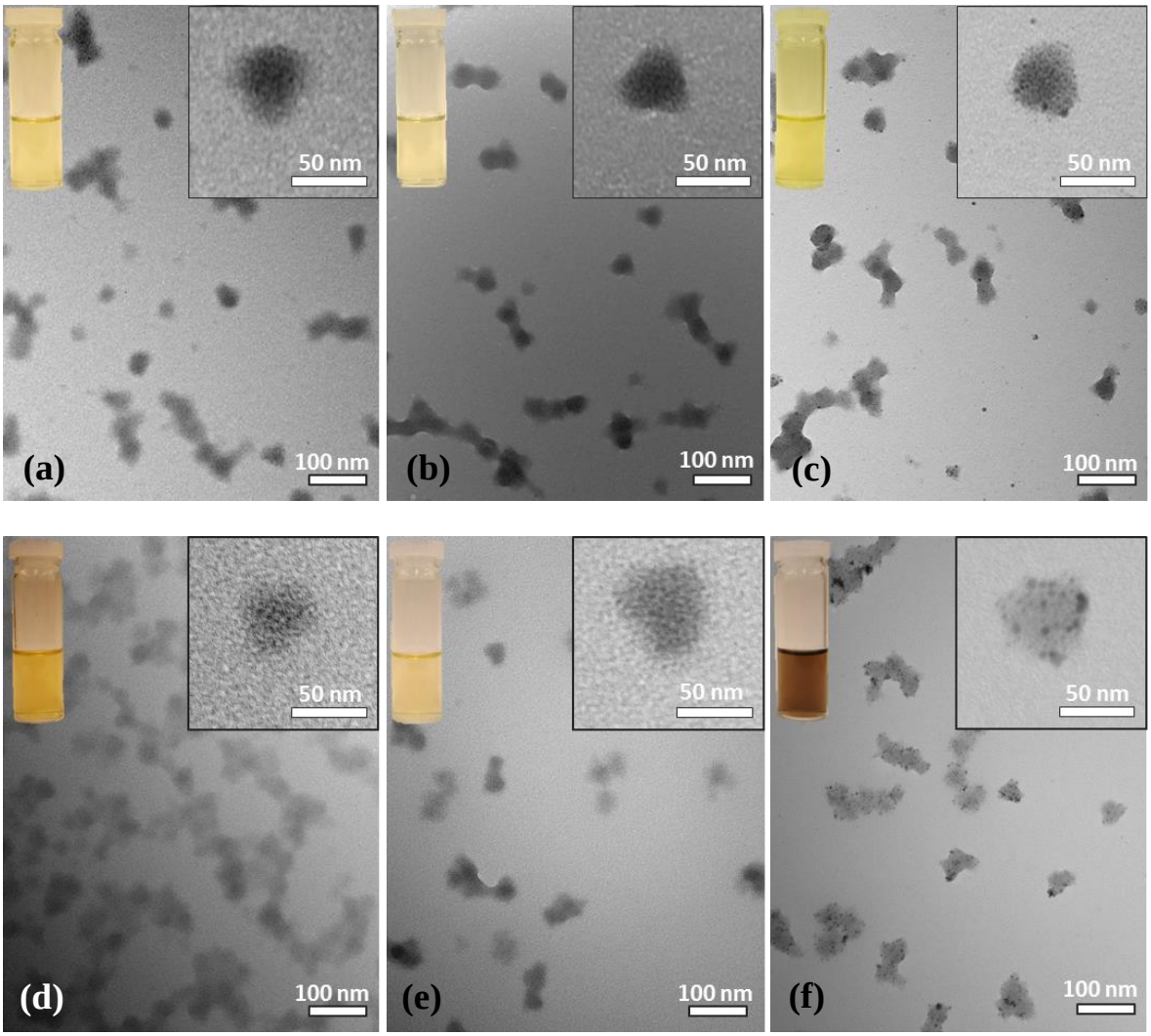

Figure 3.11 Transmission electron micrographs for *G*2PS-*g*-P2VP (*G*3-Pd) from ethanolic solutions and in the presence of different molar equivalents of $Pd(OAc)_2$: (a) 0.25 equiv, (b) 0.5 equiv, and (c) 1.0 equiv. The same samples are shown after heating for 3 h at 60 °C in (d)-(f), respectively. Inset: Magnification of individual micelles.

In the larger copolymers with 0.25–1.0 equiv of Pd per 2VP, small-size NPs ranging from 0.7 ± 0.04 to 3.4 ± 1.0 nm in diameter can be observed (Figure 3.12). As expected, increasing the Pd content led to the formation of larger NPs, these being located primarily at the periphery of the micelles. At 1.0 Pd equiv, the size of the Pd NPs increased with the

copolymer generation, but at lower Pd loadings the particle size varied as *G*1 < *G*3 < *G*2, which may suggest lower chain mobility in the larger *G*3 ACP hindering particle growth. The detailed size and size distribution data for the Pd NPs are reported in Appendix A3.1

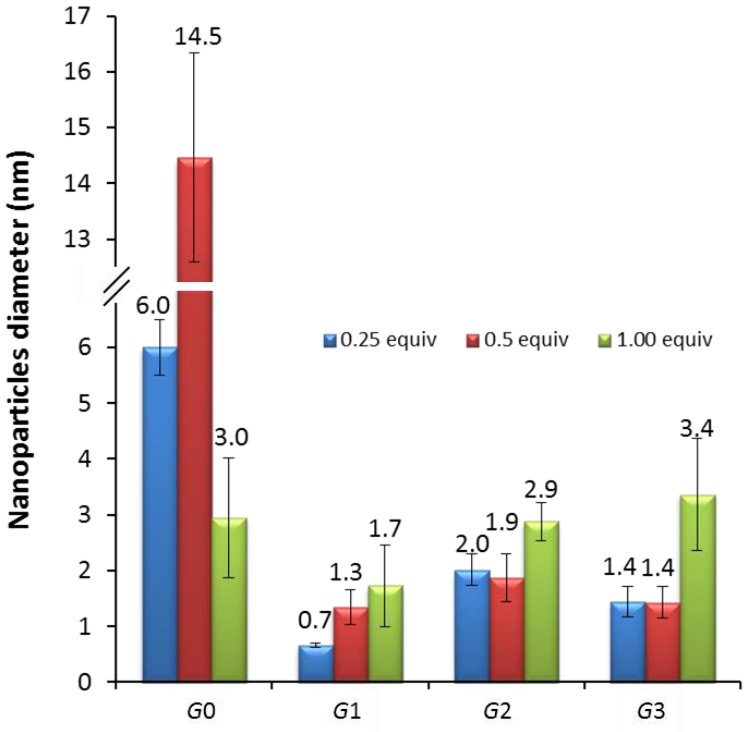

Figure 3.12 Size of the Pd NPs formed within the copolymer templates.

While various topologies have been observed for Pd NPs,[65] the solution-phase synthesis of small particles (<5 nm) typically results in the formation of cuboctahedral shapes.[68,69] If the commonly observed face-centered cubic (fcc) structure for equidimensional particles imaged by TEM[70,71] is assumed, the number of atoms in each complete shell *m* beyond the first atom in a cuboctahedron (*m*+1) is given by the progression 10 m^2 + 2, and the total number of atom (N_{tot}) is given by ⅓(2*m* - 1)(5m^2 - 5*m* + 3).[72,73] If one considers the

atomic volume of a Pd atom (V_{Pd}) in such structures to be 14.7 Å^3,[70,74] then the total number of Pd atoms can be obtained from Equations 3.9 and 3.10, where V_{tot} represents the volume of a single NP. The number of shells can be obtained by solving a cubic equation (Equation 3.11).

$$V_{\text{tot}} = N_{\text{tot}} \times V_{\text{Pd}} \tag{3.9}$$

$$V_{\text{tot}} = \frac{4}{3}\pi\left(\frac{d}{2}\right)^2 \tag{3.10}$$

$$\frac{\frac{4}{3}\pi\left(\frac{d}{2}\right)^2}{V_{\text{Pd}}} = \frac{1}{3}(2m-1)(5m^2-5m+3) \tag{3.11}$$

Table 3.7 provides the average number of shells calculated for the Pd NPs formed within the arborescent templates, if the presence of organic material (2VP units) within the nanoparticles is ignored. The number of shells was found to increase with micelle loading, and ranged from 1 to 7 for copolymers of generations $G \geq 1$. The maximum number of NPs that can be encapsulated within an arborescent structure was estimated from the measured NPs diameter and the number of 2VP units (Table 3.7). The *G*3 polymer with 0.5 equiv Pd was found to encapsulate the maximum number of NPs, with up to 1190 ± 920 NPs per micelle, while the *G*2 with 0.25 equiv Pd was lowest with 67 ± 38 NPs per micelle. The large standard deviations in the number of particles arise from the uncertainties on the measured diameters which approach the resolution limit of the TEM instrument (ca. 1 nm).

Table 3.7 Calculated number of NPs per micelle and shells per NP, assuming a cuboctahedral shape and an fcc structure.

Generation/	Number of NPs per micelle			Number of shells		
Loading	0.25	0.5	1.0	0.25	0.5	1.0
*G*0	0.02 ± 0.008	0.03 ± 0.002	2 ± 2	13	31	6
*G*1	240 ± 60	80 ± 70	140 ± 180	1	2	3
*G*2	70 ± 40	200 ± 170	90 ± 40	4	4	6
*G*3	570 ± 400	1200 ± 900	240 ± 250	3	3	7

3.4.3.4 Phase segregation

The distribution of small particles within the arborescent PS-*g*-P2VP micelles is reminiscent of the *sphere-on-sphere* morphology (also known as *raspberry*,[75] *football*,[76] or *red currant* morphology, Figure 3.13).[77] Within polymeric materials, the raspberry morphology is commonly observed for multicompartment micelles[78] assembled from linear triblock terpolymers[79–82] or miktoarm star terpolymers.[83–85] While analytical theories describing the self-assembly of these macromolecular structures are far less developed than for diblock copolymers[86] their qualitative description involves the interplay of factors including the incompatibility of the polymeric blocks; electrostatic, hydrophobic, and/or van der Waals interactions; constraints imposed by the covalent connectivity of the blocks; and the non-ergodicity of these systems.[84] Similar morphologies were also observed for various hybrid metal-containing polymer systems. For instance, small gold NPs were synthesized within inverse micelles of linear PS-*b*-P2VP in toluene by Spatz et al.[87] Interactions between

the metal species and the 2VP units were shown to enhance the segregation parameter ($\chi_{core\text{-}shell}$) and to promote the formation of micellar structures. The presence of metallic species generally promotes microdomain formation by directing the behavior of the system into the superstrong segregation regime.[87]

Using PS-*b*-P2VP with various metals including Pd, the strength of the reducing agent was shown to be an important parameter influencing the nucleation step. Stronger reducing agents favored rapid nucleation (seed formation) at several sites and the formation of raspberry-like morphologies.[88,89] Raspberry structures were also obtained by Jiang et al. by the complexation of PS-*b*-P4VP onto microspheres of polystyrene-*co*-poly(methacrylic acid) and subsequent Pd loading.[90]

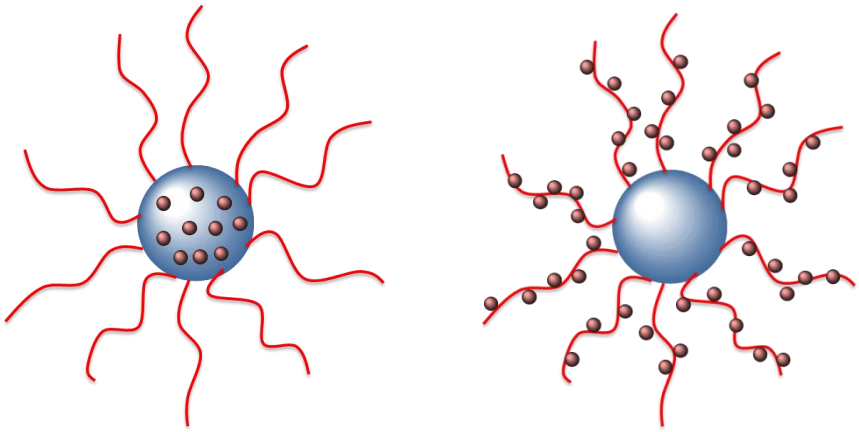

(a) **(b)**

Figure 3.13 (a) Raspberry and (b) red currant morphologies of metal-amphiphilic copolymer systems. Adapted with permission from Reference 77. Copyright 1998 Elsevier.

3.4.3.5 Nanoparticle formation mechanism

Nanoparticle formation generally follows a stepwise process of nucleation, growth and agglomeration.[91] The balance between the rate of nucleation and growth is particularly important for the resulting size and size distribution of the NPs.[92] Fast nucleation, leading to a high seed concentration, accompanied by a rapid reduction rate, promotes the formation of small NPs. In the present case, the nucleation of a large number of particles was evidenced by TEM. Particle growth is expected to follow an Ostwald ripening process, where the growth of larger clusters occurs at the expense of the smaller ones. The Pd atoms migrate from the high energy surface of small clusters to the lower energy surface of growing NPs.[19] In this case the diffusion length of the Pd atoms is limited by interactions with the polymeric chains, thereby providing some control over the growth process and the cluster size. Moreover, Ostwald ripening is typically accompanied by narrowing of the particle size distribution.

Even though transmission electron micrographs provide useful information about the structure and composition of the hybrid micelles, it is understood that the equilibrium structures observed on the deposited films may differ from the thermodynamically stable configurations in dilute solutions. It is likely that rearrangements can take place after transfer of the polymer-Pd nanocomposites from the solution to the bulk phase.[87] Furthermore, reduction of the Pd(II) species to Pd(0) has been reported to occur upon irradiation with the electron beam during the TEM measurements.[93,94] It is therefore useful to measure solution-state properties by UV-visible spectroscopy to characterize the formation of the NPs within the copolymers templates.

3.4.3.6 UV-visible spectrophotometry

UV-visible absorbance spectra for dilute solutions of the copolymers in ethanol displayed absorption maxima at 263 and 203 nm, as shown in the inset of Figure 3.14. Both bands correspond to $\pi \rightarrow \pi^*$ transitions of isolated phenyl groups of the PS chain[95,96] and of the pyridine pendant groups of P2VP.[97,98] The transitions have been assigned to the vibronic transition bands $^1A_{1g} \rightarrow {}^1B_{2u}$ and $^1A_{1g} \rightarrow {}^1B_{1u}$ at the longer and lower wavelengths, respectively.[99,100]

Absorbance spectra for Pd(II) acetate in ethanol were acquired at concentrations ranging from 0.02 to 0.3 mg·mL^{-1} and are displayed in Figure 3.14. The characteristic absorbance at 400 nm has been attributed to a charge transfer-band,[101] but also more recently to the formation of interatomic chemical bonds between neighboring Pd atoms.[102]

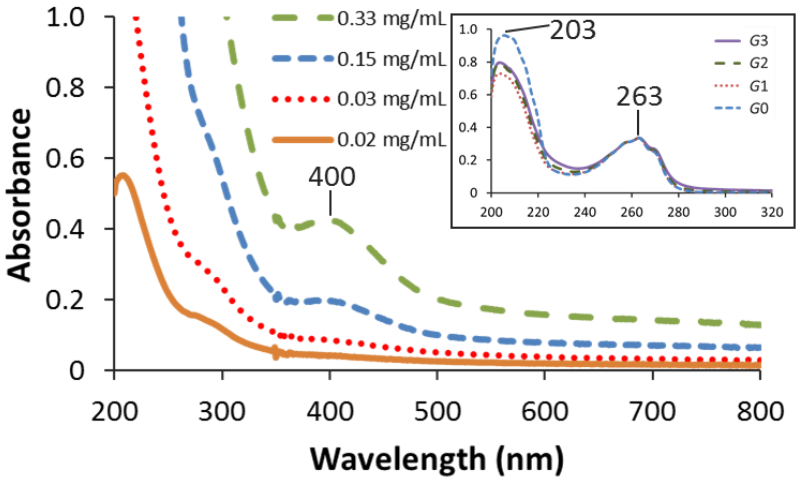

Figure 3.14 UV-visible absorbance spectra for $Pd(OAc)_2$ in ethanol at different concentrations. Inset: Absorbance spectra of *Gn*PS-*g*-P2VP (*n* = -1, 0, 1, 2) in ethanol (15 µg·mL^{-1}), normalized at 263 nm.

3.4.3.7 Pd(II) reduction in ethanol

The trimer formed by palladium acetate has been reported to dissociate in methanol (or water) upon dechelation of one or more acetate anion;[66] a similar mechanism is expected to favor metal reduction and complexation in ethanol. In the absence of polymer, the Pd(II) species in ethanol were indeed reduced to Pd(0) within 1 hour according to Scheme 3.4, resulting in the deposition of Pd black at the bottom of the vial. This was evidenced spectrophotometrically by the disappearance of the absorption band at 400 nm and a hyperchromic shift (at longer wavelengths; Figure 3.15). The broad and featureless absorption at long wavelengths is characteristic for Pd(0) metal clusters, which do not display pronounced surface plasmon resonance due to considerable *d–d* interband transitions.[103] Differential spectroscopy can be used to quantify the formation of Pd(0) clusters, by subtracting the influence of the baseline shift;[104] however, the weak absorbance of the metal-to-ligand charge transfer (MLCT) at the concentrations employed in the current work and scattering from the NPs resulted in large signal-to-noise ratios. Alternatively, the variation in absorbance with the wavelength has been shown to be sensitive to particle size for Pt colloids below 4 nm.[105,106] A decrease in the slope k (with $k = -\,\mathrm{d}\log A/\mathrm{d}\log \lambda$) was shown to be indicative of an increase in particle size. The slope k obtained from the log–log plot of the absorbance spectra of $Pd(OAc)_2$ in ethanol at different times is shown in the inset of Figure 3.15. The gradual decrease in k with time confirms the reduction of $Pd(OAc)_2$, and the concomitant nucleation and growth of Pd NPs.

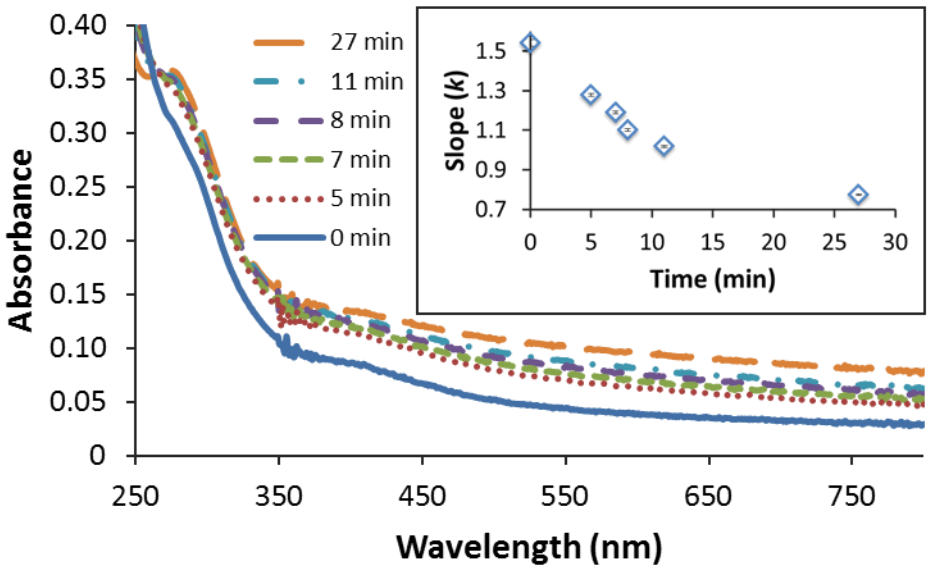

Figure 3.15 UV-visible absorbance spectra for $Pd(OAc)_2$ in ethanol (0.03 mg·mL^{-1}) after different times. Inset: Slope (k = –dlog A/dlog λ) of the absorption spectra from 400–800 nm for the same samples. Changes in k are indicative of particle size variations.

3.4.3.8 Polymer-stabilized Pd

After the addition of Pd(II), complexation by the 2VP units within the corona of the molecules was evidenced by UV-visible spectrophotometry: The absorption band for Pd(II) was red-shifted and appeared as a shoulder at 432 nm (Figure 3.16). The bathochromic shift is characteristic for complex formation between the Pd(II) species and the 2VP units of polymers.[107,108] In analogy to complexes formed by 2-methylpyridine and $PdCl_2$, the absorption band can tentatively be attributed to dπ-π* transitions from metal-to-ligand charge transfer.[107] The complexes formed were stable for an extended period of time. For instance, the absorption spectrum for *G*0PS-*g*-P2VP with 0.25 equiv Pd was unchanged after 2 days.

Complex formation between Pd and the ACPs was further investigated for 3 different

Pd loadings, namely 0.25, 0.5, and 1.0 Pd/2VP molar ratios. The MLCT absorption band was observed for all the nanocomposites but was less pronounced at higher loadings (Figure 3.16). The increase in long wavelength absorbance at higher Pd contents indicates the presence of a greater amount of Pd(0) species within the micelles. It is expected that the ability of the polymer template to stabilize the Pd(II) species should decrease as the Pd concentration is increased. Additionally, there is evidence that nucleated Pd(0) species acting as seeds can promote further reduction of the ionic species and the concomitant NPs formation via an autocatalytic pathway.[91] Such a mechanism would be favored at higher Pd concentrations. These results are also in agreement with the TEM data discussed above. Nonetheless, all the solutions remained yellow and translucent for several months without indication of Pd black formation.

After reduction of the Pd(II) species at 60 °C, a gradual change in coloration from bright yellow to orange was observed for solutions with lower Pd loadings (Pd/2VP = 0.25–0.5), while samples with an equimolar amount of Pd per 2VP units turned brown (Figure 3.8–Figure 3.11). Reduction was confirmed by UV-visible spectrophotometry and the disappearance of the MLCT absorption band. The brown copolymer samples displayed a significant baseline shift revealing the presence of larger Pd(0) clusters (Figure 3.16).

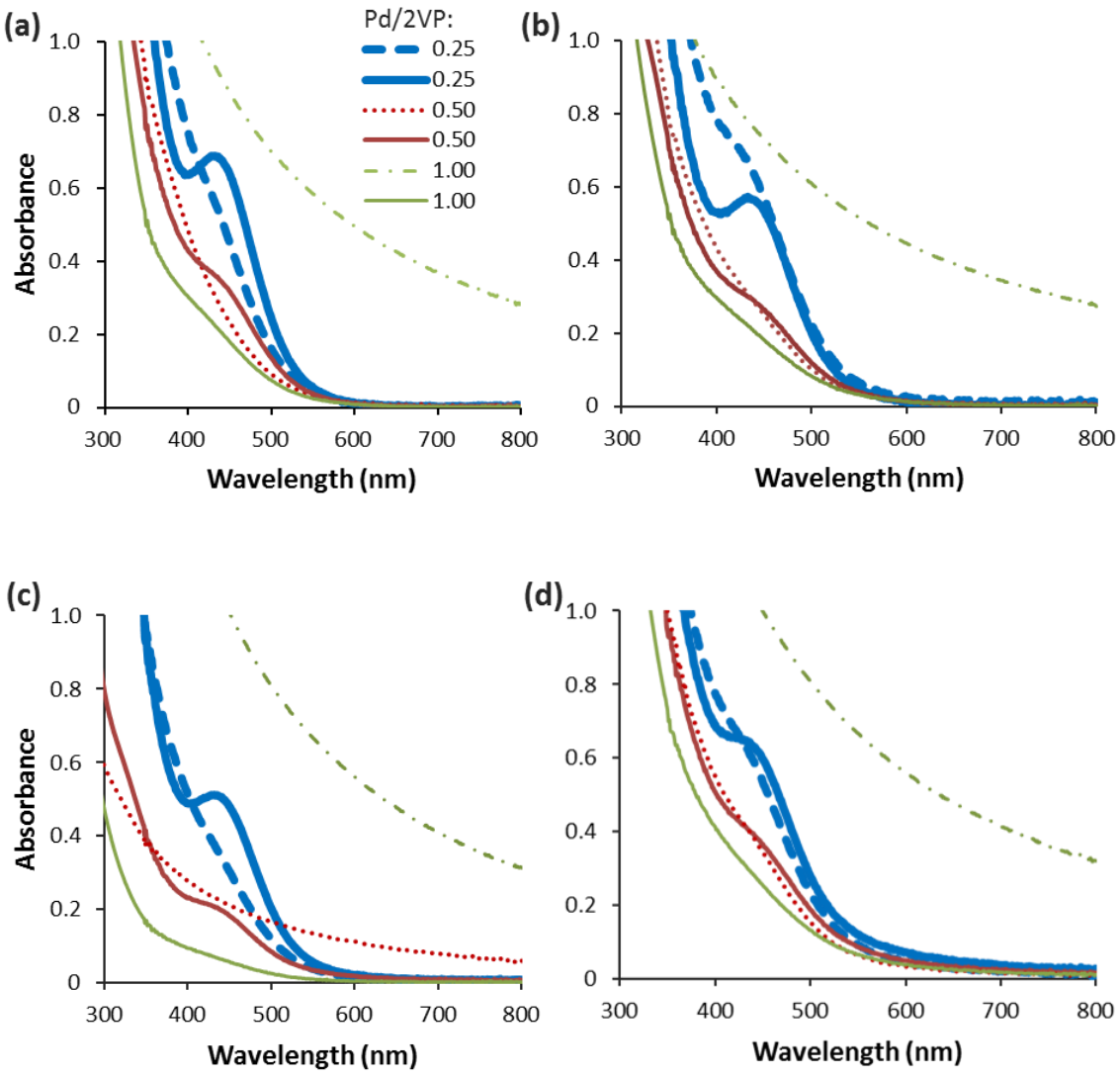

Figure 3.16 UV-visible absorbance spectra for *Gn*PS-*g*-P2VP with (a) *n* = -1, (b) *n* = 0, (c) *n* = 1, (d) *n* = 2, in ethanol with different Pd/2VP ratios ([Pd] = 0.07 mg·mL^{-1}). Samples freshly prepared (solid lines) and after 3 h at 60 °C (dashed/dotted lines).

The size of the NPs increased with the loading level of the copolymers. For instance, spectrophotometric analysis of the *G*0PS-*g*-P2VP template revealed a linear decrease in the size-dependent parameter *k* as the loading level increased from 0.25 to 1.0 Pd equivalent

(Figure 3.17). These results further substantiate the reduced stability at higher loading levels and the formation of larger nanoclusters. A plateau was reached above 1.0 Pd equiv, however, suggesting the presence of a limiting NP size when the unimolecular micelles were fully loaded. The variation in size of the NPs was corroborated by TEM measurements, as shown in Section 3.4.3.3.

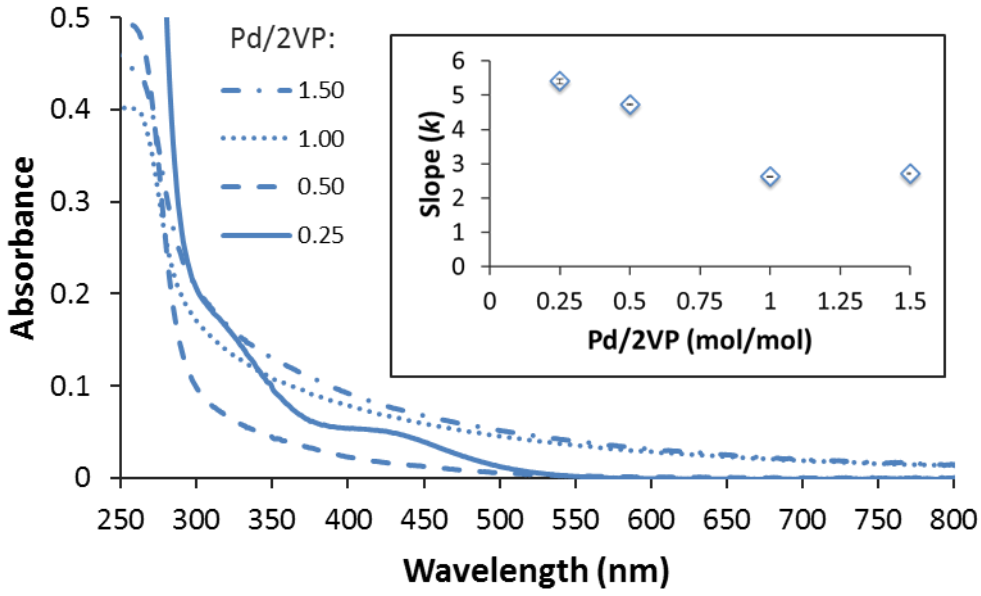

Figure 3.17 UV-visible absorbance spectra for *G*0PS-*g*-P2VP (*G*1) with various Pd/2VP ratios in ethanol. Inset: Variation of the slope ($k = -\text{dlog } A/\text{dlog } \lambda$) with the Pd content loaded in the *G*0PS-*g*-P2VP (*G*1) in ethanol.

Aside from the loading level, the growth of Pd clusters could be controlled by adjusting the duration of the reduction step. For instance, since the *G*3 copolymers provided the greatest stabilization for the Pd(II) species, longer reduction times were required for the solution to turn orange or brown. Figure 3.18 provides UV-visible absorption spectra for

*G*2PS-*g*-P2VP with 0.5 molar equiv of Pd at different reduction times. Analysis of the slope *k* showed a gradual increase until a maximum was reached after 12 h (Figure 3.19). This change is related to the reduction of Pd(II) and the concomitant formation of small NPs, as observed in the TEM images. At longer reaction times the small Pd(0) clusters aggregated into larger NPs, as seen from the baseline shift in the absorption spectra. The electron micrographs also revealed the formation of larger NPs, and the solution turned brown after 58 h (Figure 3.19). For comparison, the solutions prepared from lower generation copolymers and 0.5 equiv Pd turned brown after only 12 h of reduction time. It is worth noting that no Pd black deposition was observed in any of these samples even after several months.

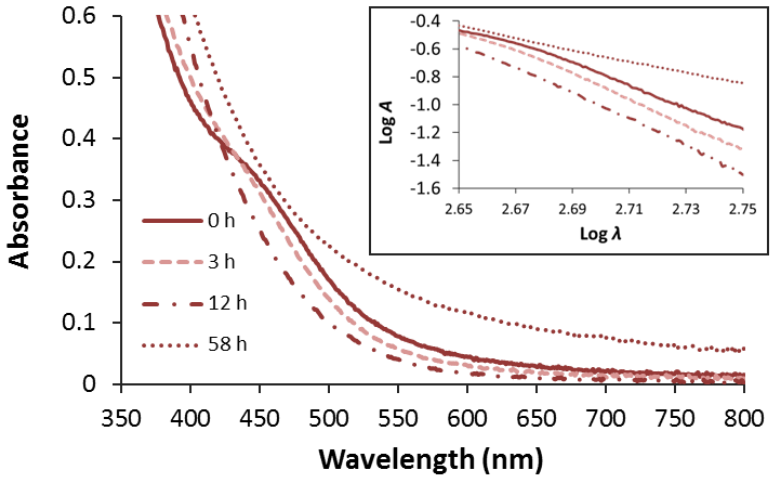

Figure 3.18 UV-visible absorbance spectra for *G*2PS-*g*-P2VP (*G*3) with 0.5 equiv of Pd/2VP in ethanol at various reduction times. Inset: Plots of log *A* against log *λ* for the same solutions from 450-560 nm.

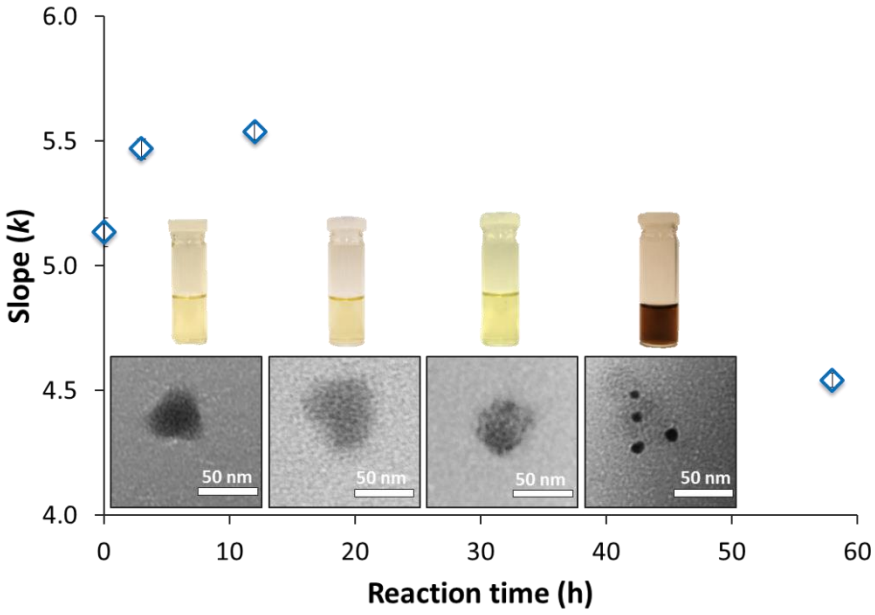

Figure 3.19 Particle size variation characterized by the slope (k = –dlog A/dlog λ) at different reduction times for *G*2PS-*g*-P2VP (*G*3) in ethanol at a molar ratio Pd/2VP = 0.5. The corresponding transmission electron micrographs and sample appearance are also provided.

3.4.3.9 Pd content determination

Quantification of the Pd content in the arborescent copolymers was performed by a novel characterization technique based on microplasma-atomic emission spectrometry. Details on this characterization technique and the experimental procedure employed are provided in Chapter 4. In this study, measurements with *G*1PS-*g*-P2VP revealed that the pyridine units can complex up to one equiv of Pd(II) in ethanol (Figure 3.20). Furthermore, when loading the copolymer template with 0.25 equiv of Pd/2VP unit, 92.8 ± 1.1 mol % of the Pd remained bound within the macromolecules (Figure 3.20).

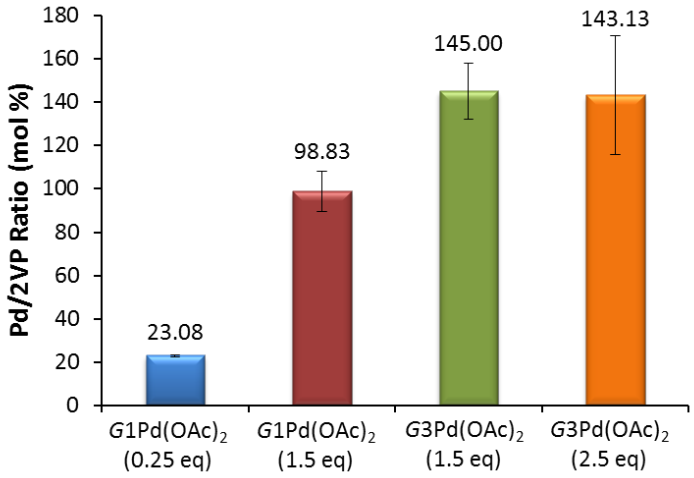

Figure 3.20 Pd loading capacity of copolymers *G*0PS-*g*-P2VP (*G*1) and *G*2PS-*g*-P2VP (*G*3) in ethanol measured by microplasma-OES.

The maximum loading capacity for *G*2PS-*g*-P2VP with $Pd(OAc)_2$ in ethanol was also determined by the same technique and is reported in Figure 3.20. A maximum loading capacity of 1.44 ± 0.30 mol % Pd/2VP was measured when using both 1.5 and 2.5 Pd equiv. In contrast to the *G*1 copolymer, the Pd loading capacity of the *G*3 copolymer is greater than the number of 2VP units present.

The higher chain segment density, closer to that of brushes, may account for the excess of Pd present with respect to the complexing species. A similar excess of Pd was noted by Fernandes et al. for polymer brushes containing dipyridylamine ligands.[109] However, the presence of zerovalent species was proposed to account for the excess of metal atoms loaded within the polymeric support. Analogous behavior could be expected for the arborescent systems where the reduction of Pd(II) is promoted by ethanol, as well as other ligands,[110] and where Pd(0) species could act as nucleation sites for the formation of

nanoparticles. Indeed, the presence of reduced Pd was detected within the arborescent systems at the highest loading levels (Pd/2VP = 1) by spectrophotometry (vide supra). Moreover, XPS analysis by Fernandes et al. revealed that Pd(0) species may also be present in the $Pd(OAc)_2$ precursor, up to 33 mol % of Pd(0) being reported for some commercial $Pd(OAc)_2$ samples.[109] The formation of NPs was likewise found in other Pd precursors.[111]

3.4.4 Catalytic activity

3.4.4.1 Conversion and turnover frequency

The activity of the *Gn*PS-*g*-P2VP-stabilized Pd(0) catalysts was investigated in the SM cross-coupling reaction between phenylboronic acid (PBA) and 4-bromoanisole (BA) in a mixture of ethanol/D_2O (85/15 v/v) as shown in Scheme 3.5, and compared with a linear P2VP-Pd sample ($\bar{M}_n$ = 5000 g·mol^{-1}, $Đ_M$ = 1.4). The Pd/2VP ratio was maintained constant at 0.5 and the reaction was performed at room temperature. The conversion of the reagents to 4-methoxy-1,1'-biphenyl (MBP) was monitored in situ by ^{1}H NMR spectroscopy, as illustrated with a representative set of spectra in Figure 3.21. A 2D [^{1}H ^{1}H] COSY spectrum is also displayed in Appendix A3.2 for that reaction.

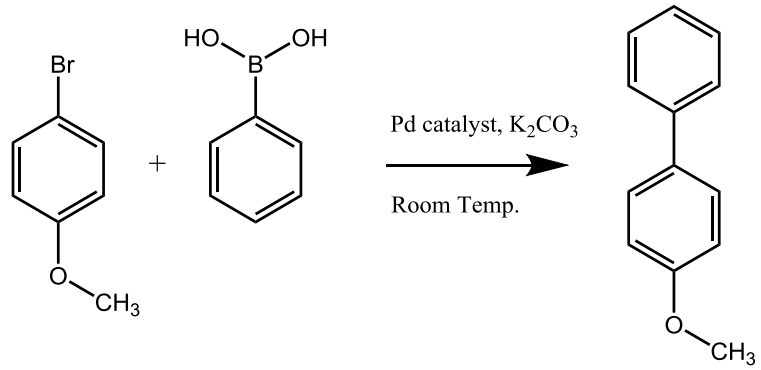

Scheme 3.5 Suzuki-Miyaura cross-coupling reaction between 4-bromoanisole and phenylboronic acid with 1 mol % of Pd catalyst in a mixture of ethanol/D_2O (85/15 v/v).

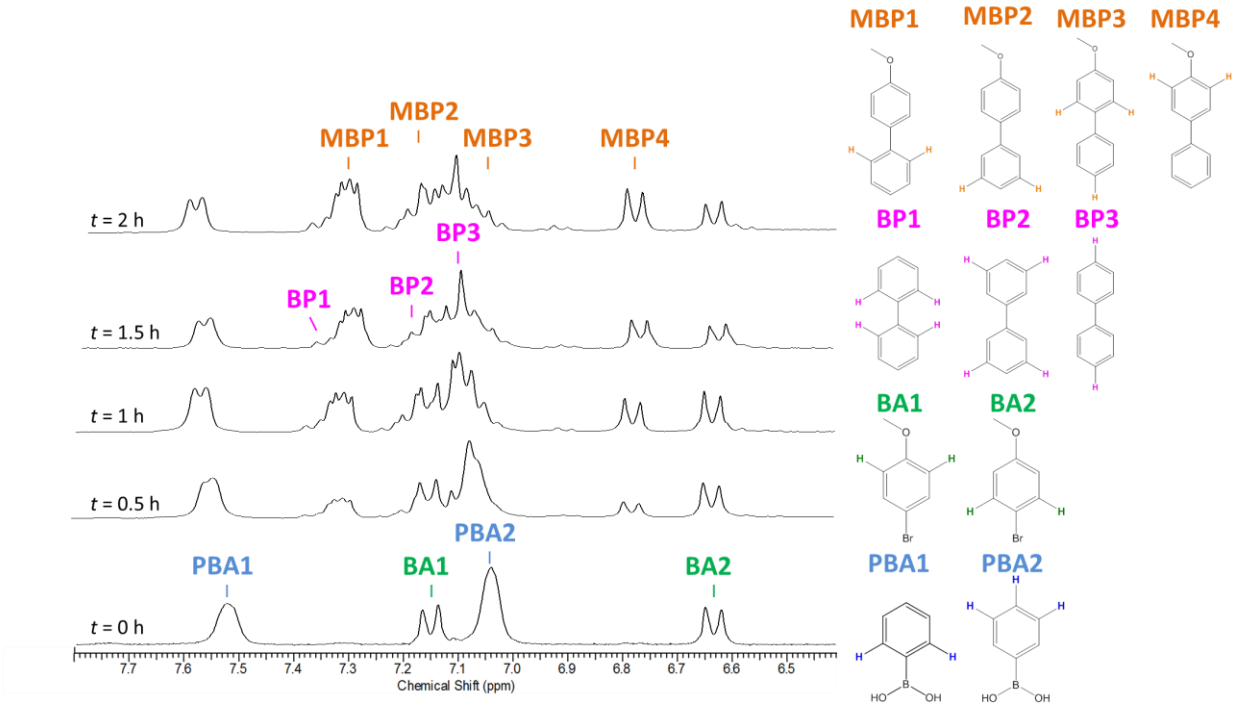

Figure 3.21 Time-dependent ^{1}H NMR spectra for the Suzuki-Miyaura reaction catalyzed with *G*1PS-*g*-P2VP-Pd[0.5 eq]. The peak assignments are indicated for each signal.

When using the catalyst precursor $Pd(OAc)_2$ without a stabilizer, a substrate conversion of 51% was attained within 1 h before reaching a plateau (Figure 3.22). At longer reaction times, deactivation occurred as the catalyst precipitated as Pd black. Using G*n*PS-*g*-P2VP as stabilizer, conversions over 50% were observed in less than 2 h in all cases. Pd black formation was only observed for the *G*0 copolymer. The conversions displayed asymptotic profiles and the maximum conversion reached varied in the order *G*0 ≈ *G*1 < *G*2 < *G*3, suggesting a positive dendritic effect (Figure 3.22a). These results suggest that deactivation of the catalyst occurs during the reaction. Indeed, similar trends were observed for dendrimer-encapsulated (DEN) and dendrimer-stabilized (DSN) Pd NPs.[112] The loss of activity was found to occur through leaching of the Pd catalyst from the polymer stabilizer, and the concomitant formation of Pd black. Much lower conversions were attained when using the P2VP homopolymer stabilizer (<40 mol % after 7 h) and Pd black formation was observed, which highlights its lower stabilizing effect.

The mechanism for the SM reaction catalyzed by NPs has been postulated to proceed via leaching of Pd species after oxidative addition of the aryl halide onto the NP surface. Following transmetalation and reductive elimination, discrete Pd(0) species were proposed to rapidly redeposit onto the NP surface.[7] The reaction rate constants (k_{SM}) were determined by assuming a pseudo-first order reaction rate (r) for the MBP product formation, such that:

$$r = -\frac{d[\mathrm{MBP}]}{dt} = k_{\mathrm{SM}}[\mathrm{MBP}] \tag{3.12}$$

and therefore,

$$\ln\left(\frac{[1-\mathrm{MBP}]}{1-[\mathrm{MBP}]_0}\right) = k_{\mathrm{SM}}t \tag{3.13}$$

where $[MBP]_0$, and [MBP] correspond to the initial MBP concentration and the concentration at time *t*, respectively. The reaction rate constants were determined from the linear portion of the semi-logarithmic plots. The turnover frequencies (TOF), obtained as k_{SM} × (mole of BA / mole of Pd catalyst), are summarized in Figure 3.22b. The TOF of the arborescent copolymer-stabilized catalyst ranged from 34 to 59 h^{-1}, and increased with the generation number of the copolymers. The TOF was lowest (11 h^{-1}) for the P2VP-Pd catalyst, while it was highest for the Pd precursor alone (124 h^{-1}).

Neither linear P2VP nor the *G*0 copolymer provided sufficient steric stabilization for the Pd(0) species, and aggregation to Pd black was observed during the reaction. The small hydrodynamic diameter of the linear polymer (D_h = 2.2 ± 0.1 nm by DLS) and of the *G*0 copolymer (D_h = 10.0 ± 0.1 nm) proved insufficient for the steric stabilization of the metallic species in the SM reaction. For the larger copolymers (*G*1–*G*3), there was no evidence for Pd black formation and higher conversions and TOFs were obtained. It should be pointed out that no catalytic activity was displayed by the copolymers alone, and similar profiles were obtained using a Pd/2VP ratio of 0.25.

The selectivity of the different catalytic systems was compared regarding the formation of 1-1'-biphenyl (BP) as a side product (Figure 3.21) after 3 h of reaction. In all the cases, less than 4 mol % of side product formed in the reaction.

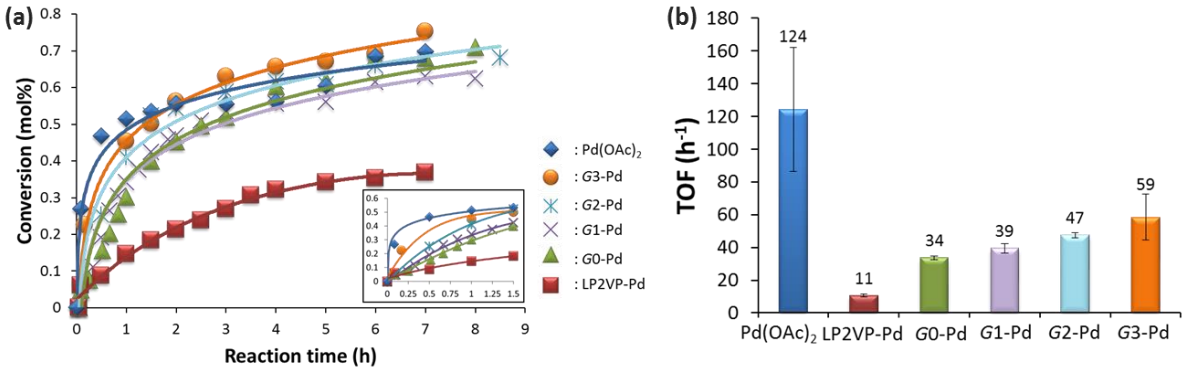

Figure 3.22 (a) 4-Methoxy-1,1'-biphenyl formation in the Suzuki-Miyaura cross-coupling reaction between phenylboronic acid and 4-bromoanisole in ethanol/D_2O (85/15 v/v), with 1 mol % Pd, in the presence of arborescent polymers (*G*0-*G*3), linear P2VP (LP2VP) and without stabilizer ($Pd(OAc)_2$). (b) Turnover frequency (TOF) obtained from k_{SM} × (mole of BA / mole of Pd catalyst).

3.4.4.2 Oxidation state

The activity of the polymer-stabilized catalysts in their different oxidation states was also compared. For instance, the *G*2PS-*g*-P2VP-stabilized Pd was tested before and after reduction in ethanol at 60 °C. The conversion attained before reduction was lower than when using the reduced catalyst, as shown in Figure 3.23. While both reactions displayed comparable asymptotic profiles, an induction time was noticeable for the pristine catalyst; suggesting the forgoing reduction of the catalyst to Pd(0), then operating as the catalytically active species.

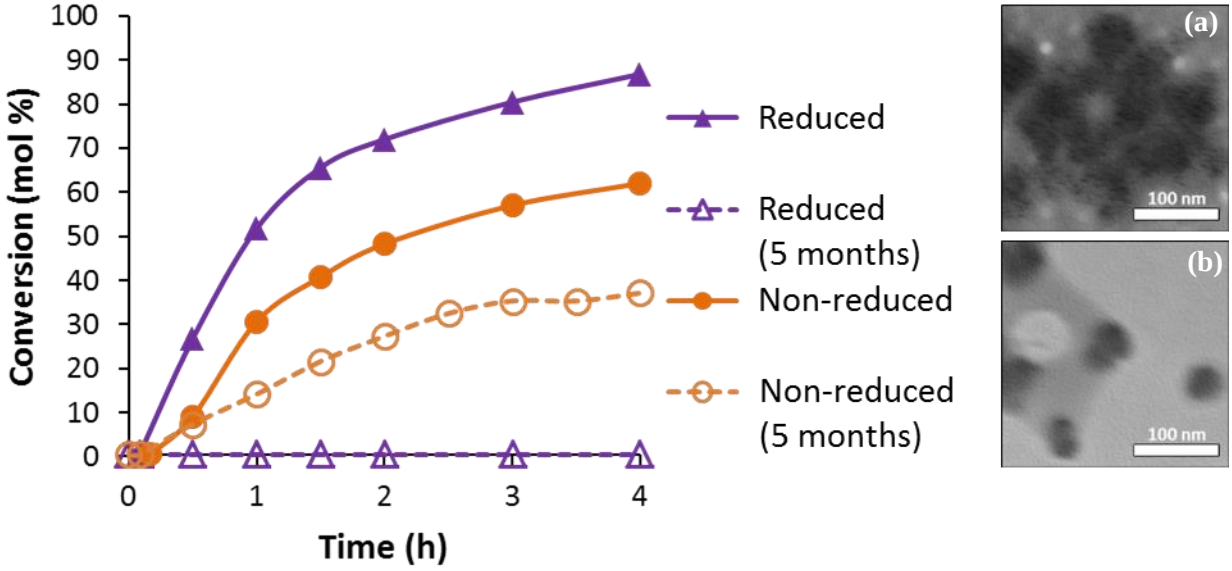

Figure 3.23 4-Methoxy-1,1'-biphenyl product formation in the Suzuki-Miyaura cross-coupling reaction between phenylboronic acid and 4-bromoanisole with 1 mol % Pd stabilized by *G*2PS-*g*-P2VP in ethanol/D_2O (85/15 v/v). The Pd catalyst was used prior to and after reduction, and after 5 months of aging. Electron micrographs after the reaction of (a) the reduced catalyst, and (b) the non-reduced catalyst.

These observations are in accordance with the leaching mechanism and the nature of the active species proposed in the Heck and SM reactions.[7,112–118] It was shown that during these coupling reactions a Pd(II) precursor such as $Pd(OAc)_2$ is first reduced to Pd(0) NPs. The nanosized pre-catalyst species can leach a small amount of Pd(0) during the oxidative addition of the aryl halide. The soluble and ligandless mono- or diatomic Pd species are extremely active and act as catalyst. The leached species are eventually quenched by re-deposition on the surface of the NPs or by the formation of Pd black. The prevalent quenching mechanism depends on the type of catalytic system and the metal concentration (following Le Chatelier's principle).[10,112]

3.4.4.3 Aging

The stability of the catalytic systems was also compared after 5 months of storage in solution and in contact with air under ambient conditions (Figure 3.23). Unfortunately, complete loss of catalytic activity was observed for Pd(0) in the *G*3 copolymer. A higher catalytic activity was displayed by the non-reduced Pd(II) complexes after 5 months, although decreased performance was also noted. In both cases there was no evidence for Pd black deposition. These results suggest that while the ACP-stabilized Pd NPs may aggregate or oxidize upon storage, the Pd species remain coordinated with the polymer host. Interestingly, oxidation of the Pd NPs in air was reported in DENs and DSNs.[112] Scott et al. also presented UV-vis spectrophotometry and XPS evidence for the oxidation of Pd(0) to salt-coordinated Pd(II) rather than a Pd oxide under these conditions.[17]

3.4.4.4 Recycling

Due to their large size, the polymer-stabilized catalysts were easily separated from the reaction products of the SM reaction by dialysis. The recovered *G*2PS-*g*-P2VP-Pd(0) catalyst was reused in 5 consecutives runs as shown in Figure 3.24. An exponential decrease in catalyst activity was observed, likely due to flocculation of the polymeric species during dialysis. The floc formed in ethanol was easily redispersed by stirring the solution, however. The TEM images shown in Figure 3.24 reveal the presence of polymeric aggregates with Pd domains (6.0 ± 1.9 nm) constituted of small NPs (1.4 ± 0.3 nm). Larger aggregates were formed after the second and fourth cycles, but the size of the embedded NPs remained unchanged. Flocculation is expected to impact negatively the colloidal dispersion of the catalyst and the diffusion rate of the substrate to the catalytic sites. Leaching of the catalytic

metal and/or Ostwald ripening are other routes to account of the progressive loss in activity observed. Additionally, possible oxidation of the Pd NPs upon exposure to air or inorganic salts (e.g., K_2CO_3, $B(OH)_2Br$) in the reaction medium may also account for the loss of activity observed. Certain salts (KCl in particular) were found to promote the oxidation of Pd DENs and the formation of salt-coordinated Pd.[17] It is noteworthy that no changes in size of the Pd DENs were observed after several cycles of oxidation and reduction.

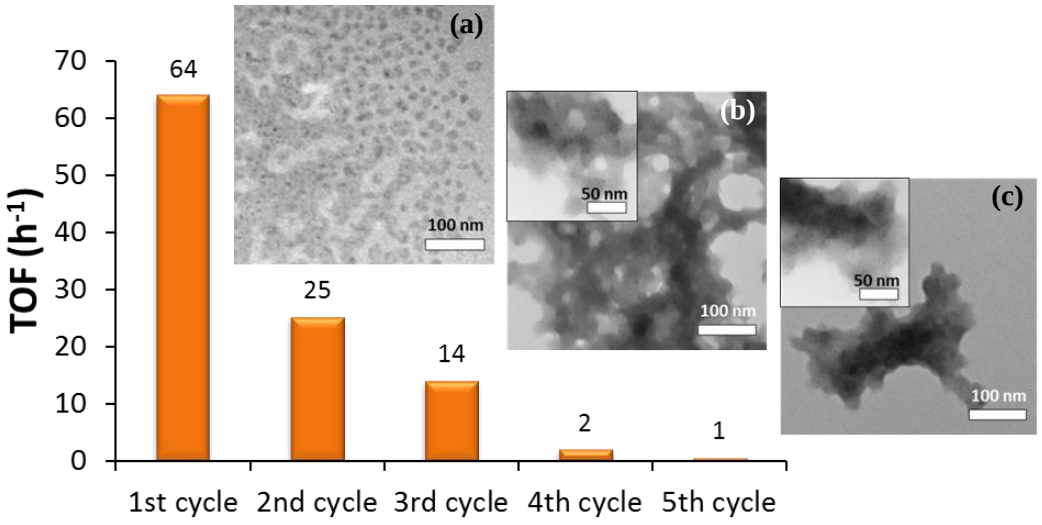

Figure 3.24 Recovery and recycling of *G*1PS-*g*-P2VP-Pd(0) in 5 different reaction cycles. The apparent rate constant is for 4-methoxy-1,1'-biphenyl formation in the SM cross-coupling reaction between phenylboronic acid and 4-bromoanisole, with 1 mol % Pd in ethanol/D_2O (85/15 v/v). Electron micrographs for the recovered catalyst after (a) the 1st cycle, (b) the 2nd cycle, and (c) the 4th cycle are also provided.

3.5 Conclusions

The utilization of well-defined arborescent copolymers, *Gn*PS-*g*-P2VP, (n = [-1,2], $n \in \mathbb{N}$) with sizes varying from 28 to 108 nm was demonstrated to synthesize Pd NPs. The copolymers had a number of 2VP units per micelle ranging from about 900 to 133,000 and displayed good solubility in ethanol, THF, DMF, and $CHCl_3$. Monomodal and narrow size distributions were observed in DLS measurements. The micellar structures could be deposited as monolayers on mica and characterization by AFM revealed flat, pancake-like topologies. Phase segregation between the polymeric blocks was found to depend upon the generation number, varying from fried-egg, uniform, to strongly phase-segregated morphologies.

Loading of the arborescent structures with Pd was performed in ethanol, which served as both solvent and reducing agent. By selecting the loading level, the reduction time and the generation number (*Gn*), control was achieved over the size of the nanoparticles formed. DLS measurements demonstrated the formation of stable colloidal solutions with broadening of the particle size distribution for the lower copolymer generations. Analysis by TEM revealed the formation of NPs with a diameter ranging from 0.7 to 3.4 nm within the micelles; the size of the NPs increased with both the loading level and the generation number. When assuming a cuboctahedron and fcc structure, the number of shells in the NPs ranged from 1 to 7. The polymer-metal hybrids displayed a raspberry-type morphology. UV-vis spectrophotometry confirmed complexation of the Pd(II) species by the 2VP units, and reduction was evidenced by both the disappearance of the MLCT band and a hyperchromic shift. The formation of the NPs was also monitored qualitatively by measuring the slope of

the absorbance spectra. Measurement of the Pd-loading by microplasma-OES indicated quantitative complexation of the 2VP unit with Pd(II). Loading of the *G*3 copolymer reached a maximum at a Pd/2VP ratio of 1.44 ± 0.33, which was explained by the presence of Pd(0) species.

Catalytic testing of the polymer-stabilized Pd species was performed in the SM cross-coupling reaction. The kinetics of the reaction were monitored by ^{1}H NMR spectroscopy and revealed a positive dendritic effect. The smaller *G*0 arborescent copolymer could not provide sufficient steric stabilization under the reaction conditions used and displayed the lowest catalytic activity. The larger arborescent copolymers (*G*1–*G*3) were more effective stabilizers and displayed good catalytic activities. However loss of activity was observed after 5 months of storage in contact with air, as well as after recycling of the catalyst, possibly due to oxidation. While further work is required to improve the stability and recyclability of the arborescent polymer-loaded Pd catalysts, it is clear that these hybrid materials present interesting properties for application in catalysis. The synthesis of bimetallic or multi-metallic NPs within such dendritic structures could also represent an interesting venue for the formation of catalysts with improved activity, stability, and recyclability

Chapter 4

Determination of the Loading and Stability of Pd in an Arborescent Copolymer in Ethanol by Microplasma-Optical Emission Spectrometry

4.1. Overview

We report, for the first time, the utilization of a microplasma-optical emission spectrometry system for the determination, without sample digestion, of the concentration of Pd loaded in a dendritic graft (arborescent) copolymer dissolved in ethanol. The preparation of polymer-stabilized colloidal Pd particles was achieved by adding palladium acetate to a solution of the copolymer, viz. arborescent polystyrene-*graft*-poly(2-vinylpyridine), in ethanol. No acid digestion was needed prior to the analysis, and only micro-amounts (μL) of sample were required. Calibration curves obtained for Pd in ethanol were linear in the concentration range of interest and the precision was better than 5%. The Pd detection limit was 28 pg (absolute) or 3 $ng \cdot mL^{-1}$ (when using 10 μL samples). The average Pd loading per mole of 2-vinylpyridine units was determined to be 99.5 ± 3.9 mol %. The kinetics of aggregation of the metallic species to Pd black were also determined. The Pd concentration in ethanol without polymer was found to abate to about one third of its initial value after 5 days. In presence of the copolymer, however, the concentration of Pd in solution remained constant for at least 10 days. The low electric power and gas consumption of the microplasma device, its low operating cost and detection limit, compatibility with organic solvents, and the small sample amount required make this system a greener and cheaper alternative to the inductively coupled plasma (ICP) spectrometers commonly used for Pd quantification.

4.2. Introduction

The unique and size-dependent properties of metallic nanoparticles (NPs) present great opportunities for a wide array of applications ranging from sensing to optoelectronics, medicine, and catalysis.[1,2] Since the first report by Faraday in 1857,[3] various methods have been developed for the preparation of colloidal metallic particles.[4] One of the most commonly used strategies involves the reduction of a salt precursor in the presence of a stabilizer in solution. Hirai et al. showed that alcohols could serve as reducing agents,[5] and that in the presence of a polymeric stabilizer Pd NPs could be prepared.[6] Using a similar strategy, poly(2-vinylpyridine) (P2VP) in the form of linear homopolymer,[7–10] block copolymers,[11–13] or nanospheres[14] was shown to complex with palladium species, even at high temperatures and pressures,[15] and to lead to the formation of Pd NPs after reduction of the metallic species. Gauthier et al. rather synthesized arborescent (dendritic graft) copolymers incorporating a branched polystyrene (PS) core and a corona of P2VP chains[16,17] to serve as templates for the complexation of Au(III) salts,[18] but also for the preparation and the stabilization of Pd NPs in ethanol (Chapter 3).[19] Polymer-stabilized Pd nanocatalysts were shown to be useful for a wide range of organic reactions such as carbonylation, hydrogenation, oxidation, reduction, and carbon-carbon cross-coupling reactions.[20–23]

An important way to assess the ability of a polymer to sequester a metal is by determining its loading capacity; that is, by determining the *amount of metal loaded per unit amount of stabilizer*. This is a key figure of merit for the evaluation of a catalyst system, which makes its precise and accurate determination essential. In cross-coupling reactions for instance, the Pd nanocatalyst concentrations used are typically in the low $\mu g \cdot mL^{-1}$ (parts per

million, or ppm) range, to even the $ng \cdot mL^{-1}$ (parts per billion, or ppb) range.[24–26] However, the determination of such low Pd concentrations in polymers dissolved in organic solvents has been reported to be challenging.[26–29]

Many analytical techniques have been applied to the determination of Pd concentrations in colloidal systems. This includes cyclic voltammetry,[30] UV-visible spectrophotometry,[31] neutron activation analysis (NAA),[32] X-ray fluorescence (XRF) – such as energy-dispersive (EDX)[33,34] or wavelength-dispersive (WDX)[35] X-ray spectroscopy, atomic absorption spectroscopy (AAS),[13,29,36] and inductively coupled plasma-optical emission spectrometry (ICP-OES).[33,34,37–39] Among these, ICP-OES is most widely used due to its desirable analytical performance characteristics, such as limits of detection (LODs) in the low-ppb to sub-ppb range for many elements. Despite their applicability, ICP systems are expensive to operate and have a relatively large carbon footprint. For example, a typical ICP instrument consumes about 20 $L \cdot min^{-1}$ of Ar gas and 1–2 kW of electric power.[40] In many cases the high cost-per-analysis prohibits the characterization of a large number of samples, as it would be essential for instance for the systematic "evaluation of catalysts and recycling systems before and after reaction and continuous monitoring of changes during reactions", as recommended by Molnár.[26] Furthermore, when using the most widely employed method to introduce samples into an ICP, viz. a pneumatic nebulizer, the total volume of sample required per analysis ranges from a few to several milliliters. The sample introduction efficiency of a nebulizer is low (1–5%); therefore over 95% of a sample must be collected and disposed of properly. Other issues also arise when using a nebulizer to introduce nanoparticles or polymers directly into an ICP. For instance clogging of the nebulizer by

nanoparticles, and sample-to-sample carry-over from polymer adhering to the walls of the spray chamber or on the tubing (memory effects) have been reported.[41] To overcome these issues polymer-stabilized nanocatalysts must be digested (or dissolved), typically with an acid. Although effective, acid digestion increases the risks of both analyte loss during sample processing and contamination from the digestion reagents.[42] Furthermore, if organic solvents are introduced into an ICP, the use of a mixed-gas Ar-O_2 plasma is required to eliminate plasma instability and to prevent carbon deposits from the solvents.[43] Such procedures further increase the complexity, cost-per-analysis, as well as the carbon footprint of the analytical procedure.

Weagant and Karanassios developed a low-cost and greener analytical method (vis-à-vis ICP) using microplasmas ($16 \times 2 \times 9$ mm^3, length × width × height) that have a low gas flow rate (0.23 $L \cdot min^{-1}$) and a low power consumption (<15 W).[44] The same group demonstrated its applicability to solid, liquid, and gaseous samples;[45] so far eleven elements have been characterized by that technique, primarily using dry residues derived from aqueous microsamples.[40] The LODs achieved ranged from 5 to 650 picograms (pg).

In this work, we demonstrate for the first time that this microplasma-based analytical method can be used for the direct determination (i.e., without digestion) of Pd loading in arborescent copolymers dissolved in organic solvents. We also apply this method to determine the kinetics of aggregation and the stability of palladium acetate, and of arborescent polymer-stabilized Pd nanoparticles in ethanol.

4.3. Experimental procedures

4.3.1. Materials

ICP-grade Pd standard solutions (Pd-Std) in 10% HCl, 1000 $\mu g \cdot mL^{-1}$ ± 0.5% (*Plasma*CAL, ICP-AES/MS standard, SCP Science, Baie d'Urfé, QC, Canada) were used. The solutions were freshly diluted using either ethanol (undenatured grade, anhydrous, Commercial Alcohols Inc., Brampton, ON, Canada) or Milli-Q water (18.2 MΩ·cm, EMD Millipore Systems, Billerica, MA, USA). The ethanol was distilled in a polytetrafluoroethylene (PTFE) apparatus, to eliminate the possibility of metal contamination from glassware. All the samples were stored in acid-washed low density polyethylene (LDPE, Nalgene®) bottles. All the polypropylene micropipette tips (Bevel Point, 1–20 µL, VWR, Mississauga, ON, Canada), LDPE bottles and vials used were acid-washed by soaking for at least 48 h in a 5% (w/v) nitric acid solution, and then rinsed with Milli-Q water. Drying was subsequently performed in a ventilated dust-free enclosure at room temperature for a minimum of 48 h. A Mettler-Toledo XS205 semi-micro balance with a 0.01 mg display was used for sample preparation. Pd-containing microsamples were pipetted with a Corning Lambda™ micropipette (1–20 µL, 1.0–5.0% accuracy, and better than 1.5% precision). The carrier gas, also used as the microplasma support gas, was a mixture of 97% Ar–3% H_2, v/v, (Praxair Canada Inc., Mississauga, ON, Canada). Palladium(II) acetate ($Pd(OAc)_2$, min. 98%, Strem Chemicals Inc., Newburyport, MA, USA) was the source of Pd.

4.3.2. Copolymer synthesis

A first-generation polystyrene-*graft*-poly(2-vinylpyridine) (*G*0PS-*g*-P2VP) arborescent copolymer was synthesized by Gauthier and Munam, by anionic polymerization and grafting techniques, according to a reported procedure.[17] The PS core of the copolymer was a comb-branched (or generation 0, *G*0) polymer prepared by grafting randomly about 17 PS side chains (each with $\bar{M}_n$ = 5500 g·mol^{-1}) onto a linear PS substrate ($\bar{M}_n$ = 5200 g·mol^{-1}). The comb-branched polymer was further grafted with 182 P2VP side chains ($\bar{M}_n$ = 5500 g·mol^{-1}), corresponding to a 2-vinylpyridine (2VP) units content of 91 mol % in the copolymer obtained. The molar-mass dispersity ($\bar{M}_w \cdot \bar{M}_n^{-1}$) of the sample was 1.08. The structure of the copolymer obtained, referred to as *G*1 (overall generation 1), is depicted in Scheme 4.1.

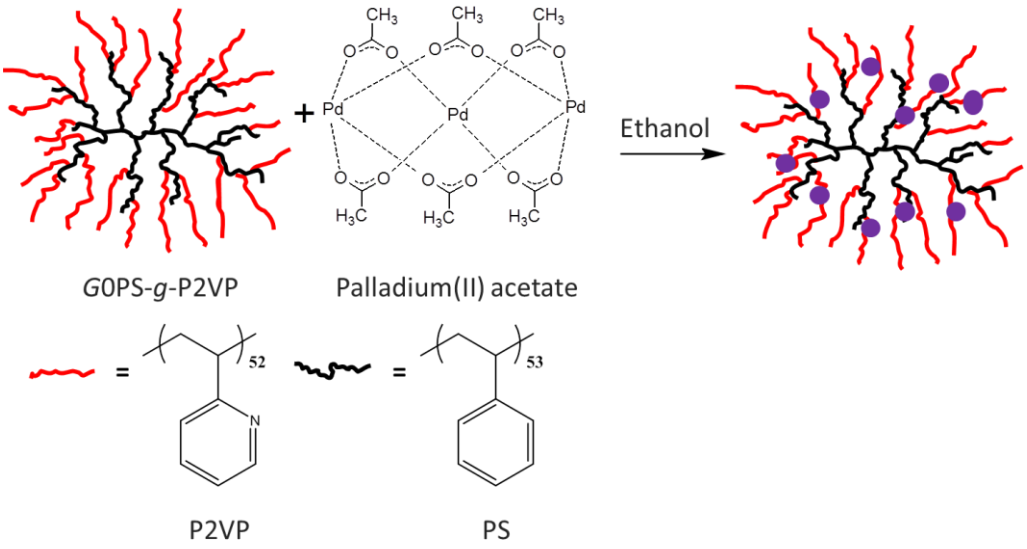

Scheme 4.1 Loading of the *G*1 arborescent copolymer (*G*0PS-*g*-P2VP) with Pd(OAc)$_2$ in ethanol.

4.3.3. Loading of Pd in the copolymer

Loading of the Pd catalyst was achieved by co-dissolution of $Pd(OAc)_2$ with the arborescent copolymer in ethanol solutions as follows: The polymer was dissolved overnight in ethanol (0.2 $mg \cdot mL^{-1}$) in a LDPE vial. Immediately after the dissolution of $Pd(OAc)_2$ in ethanol (0.25 $mg \cdot mL^{-1}$) and sonication for 2 minutes, the desired amount of catalyst solution (either 0.25 or 1.5 molar equiv of Pd per 2VP unit) was added to the polymer solution to obtain a yellow translucent solution (Scheme 4.1). The separation of free Pd from the polymer-bound Pd was achieved by transferring 15 mL of the polymer-catalyst solution to a dialysis membrane (1,000 molecular weight cut-off Spectra/Por® 7 regenerated cellulose), and stirring for 6 h in 200 mL of ethanol while changing the solvent thrice. The polymer-catalyst solution was then recovered from the dialysis membrane and diluted to obtain a 2VP unit concentration of 0.7 $\mu g \cdot g^{-1}$ (0.7 ppm).

4.3.4. Transmission electron microscopy imaging

Imaging by transmission electron microscopy (TEM) was performed in the bright-field mode on a Philips CM10 electron microscope operated at an accelerating voltage of 60 kV. The samples were prepared by depositing two drops of Pd-containing solution (0.07 $mg \cdot mL^{-1}$) onto a 300-mesh Formvar® carbon-coated copper TEM grid (Electron Microscopy Sciences, FCF300-Cu).

4.3.5. Instrumentation and operating conditions

A block diagram of the instrumentation used for the quantitative determination of Pd is shown in Figure 4.1a, while further details about the operating conditions used are reported in Table 4.1. Conceptually, the instrumentation consists of 5 parts: 1) a microsample introduction system; 2) a microplasma device; 3) a scanning monochromator (Heath, 0.35 m Czerny–Turner design equipped with a 1200 groove·mm^{-1} grating); 4) a photomultiplier tube (PMT) detector (Hamamatsu model R928 fitted inside a Heath EU-701-30 PMT module); and 5) an amplifier (SRS 570) with a data acquisition sub-system (National Instruments DAQCard 1200) including a computer running a locally developed LabVIEW program for data acquisition.

The electrothermal vaporization microsample introduction system (Figure 4.1a) consisted of a vaporization chamber and a cylindrical ceramic support equipped with a rhenium coiled filament at one end. Cables running through conduits in the ceramic support connected the filament to an external electric power supply. Deposition of the microsamples was performed by retracting the ceramic support from the vaporization chamber and pipetting a few microliters (between 3.0–10.0 µL) of solution onto the coil. The ceramic support, along with the sample-carrying coil, was then re-inserted into the vaporization chamber.

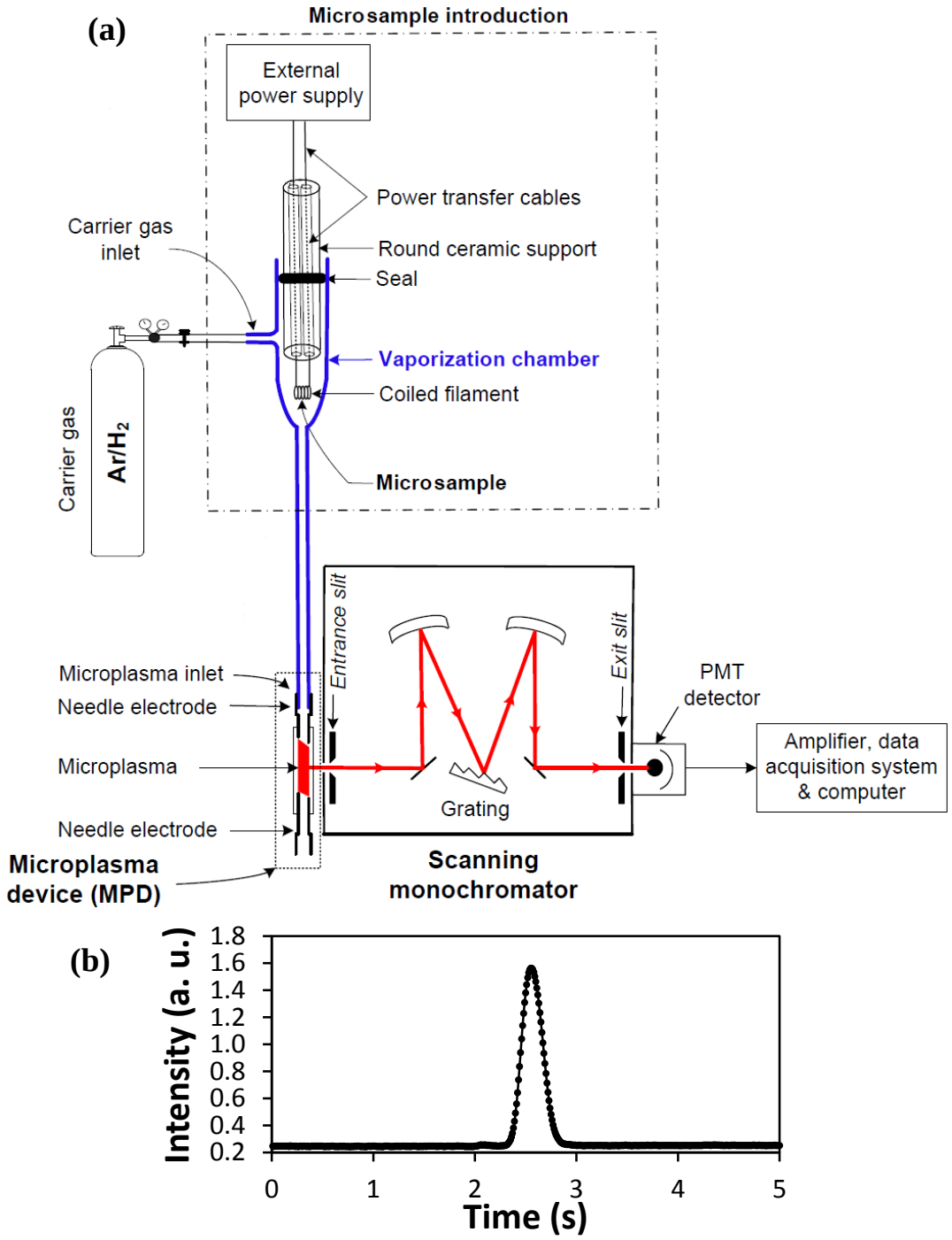

Figure 4.1 (a) Diagram of the microplasma-optical emission device used for the quantification of Pd (illustration not to scale). (b) Data points acquired within the time of one measurement.

Table 4.1 Operating conditions for the microplasma-optical emission spectrometry system.

Microplasma device	**Settings**
Microplasma channel length	16.3 mm
Microplasma channel width	2.0 mm
Microplasma channel depth	8.7 mm
Inter-electrode orientation	Anti-parallel
Inter-electrode distance	12 mm
Grounded needle electrode diameter	1.2 mm
High-voltage electrode diameter	1.6 mm
Nominal dc power applied to the MPD	4 W
High-voltage ac frequency	66 kHz
Microplasma warm-up time	60 s
Microsample introduction system	
Ar – H_2 flow rate	230 $mL \cdot min^{-1}$
Maximum drying power	2.21 W
Vaporization power	44.8 W
Photomultiplier tube	
Slit width	250 µm
Wavelength	340.458 nm
Sensitivity	500 $nA \cdot V^{-1}$

Solvent removal from the sample prior to the analysis was found essential to avoid microplasma instability: In the presence of ethanol, the plasma took on a purple color and displayed erratic background emission. It is well known that plasmas (regardless of their size), when unaided by mixing oxygen gas, do not tolerate organic solvent vapors. The

drying procedure used for such samples was the following: The electric power applied to the coil was first set to 0 W for 1 min (to allow for the bulk of the volatile solvent to vaporize at room temperature). The electric power was then increased to 0.12 W for 30 s. When the copolymer was present in the sample, an additional step was performed to char the dried polymer remaining on the coil. This was accomplished by applying progressively higher electric power levels; for example, 0.27 W for 15 s, then 0.44 W for 15 s, and subsequently 0.72 W for 30 s. After sample drying (and charring if required) the coil was allowed to cool for 60 s, with the Pd-containing residue remaining on the coil.

The microplasma was subsequently ignited and the visually stable, blue-colored microplasma was allowed to thermally equilibrate for 60 s. A higher electric power was then applied to the coil (e.g., 44.8 W corresponding to ca. 2500 °C) to vaporize the Pd-containing residue. This temperature was found sufficient to vaporize the residues from the finely dispersed Pd samples (vide infra), which are expected to display a lower vaporization temperature than their bulk counterparts.[46] The gas-phase metal atoms exited the vaporization chamber and were transported to the microplasma by the carrier gas (230 $mL \cdot min^{-1}$, $Ar–H_2$). Argon mixed with hydrogen (3% v/v) was used to prevent oxidation of the Re coil by the low-ppm levels of water and oxygen typically present in commercial compressed gas cylinders.[47] Interaction of the vaporized sample residue with the microplasma led to the atomic emission from Pd I at 340.458 nm which was measured by the PMT detector (Figure 4.1a). The output of the detector was amplified, digitized, and stored onto a computer system. An example of a representative signal so obtained is shown in Figure 4.1b.

Although the emitted signals lasted for only about 0.5 s, data were acquired for 5 s to monitor microplasma background emission during the pre-vaporization and post-vaporization time intervals (Figure 4.1b). Furthermore, when a polymer was present, the electric power was applied to the coil for an additional 5 s to remove any carbonaceous material potentially remaining on the coil. At the end of this sequence, the electric power was turned off and the coil was allowed to cool for 60 s before any subsequent run. A minimum of 3 consecutive runs were performed for each sample volume. It is worth noting that the above steps (drying, charring, and coil-cleaning procedure when applicable) were repeated for more than 1700 vaporization cycles (i.e., analytical runs) without evidence of carbon deposition, fouling of the microplasma electrodes, or coil alteration. The microplasma background emission was also stable for more than 10 h of continuous operation (Figure 4.2). It is estimated that the operating cost of the microplasma is roughly 100 times lower than for that of a current ICP-OES instrument.

4.4. Results and discussion

4.4.1. Pd standard solutions in water and ethanol

Both aqueous and ethanolic solutions, prepared from a Pd standard solution, were analyzed for the first time using the microplasma set-up shown in Figure 4.1a. A typical optical emission signal and stable microplasma background obtained during the pre- and post-vaporization time intervals are also displayed in Figure 4.1b. Calibration curves, obtained using the integrated area of the optical emission peaks, were linear and comparable

in the concentration range of interest (with typically R^2 = 0.99998 in ethanol, Figure 4.2 and Figure 4.3).

To improve the statistical confidence, three different injection volumes were used (viz. 3.0, 6.0 and 10.0 µL) for each standard solution or sample. In absolute units, the amount of Pd injected ranged between 3.0 and 10.0 ng. The precision, expressed in percent relative standard deviation (%RSD), was determined from at least triplicate runs for each of the injection volumes used (Figure 4.2). The %RSD obtained for the solution of Pd-Std in water was below 1.7% and for the Pd-Std solution in ethanol it ranged between 7.4 and 0.7% (Table 4.2). For the samples of Pd and polymer dissolved in ethanol, the %RSD was below 3.8%. In general, the %RSD was lower for the aqueous solutions, and for larger injection volumes. Solvent blanks (i.e., without any Pd added) did not show any emission signals.

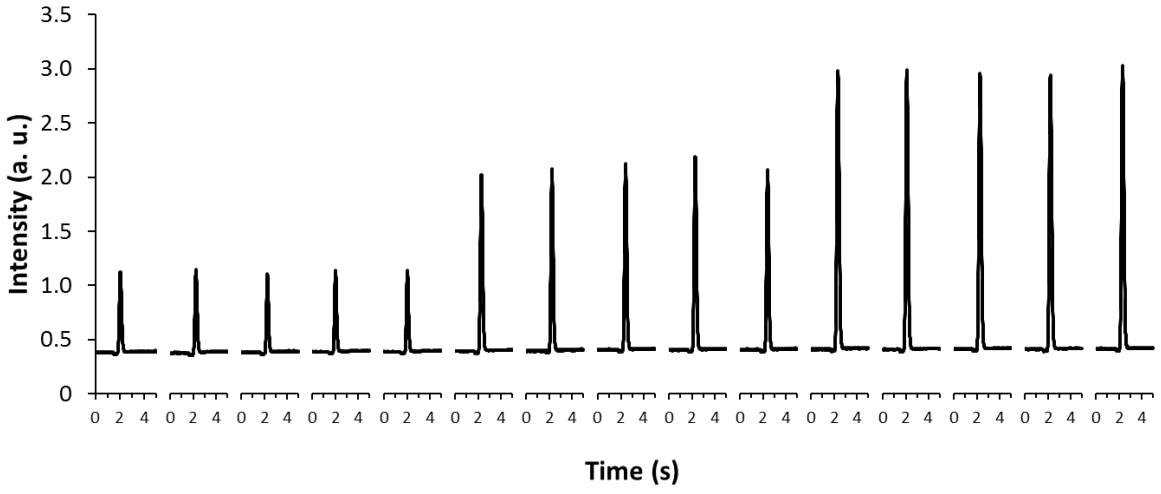

Figure 4.2 Emission signals acquired with the microplasma device over 5 successive runs for a Pd standard solution in water, using injection volumes of 3.0, 6.0 and 10.0 µL, respectively. The precision of the signals, and the stability of the background emission from the microplasma are noteworthy. Even though the latter was observed for more than 10 h, only a time-fraction is shown here.

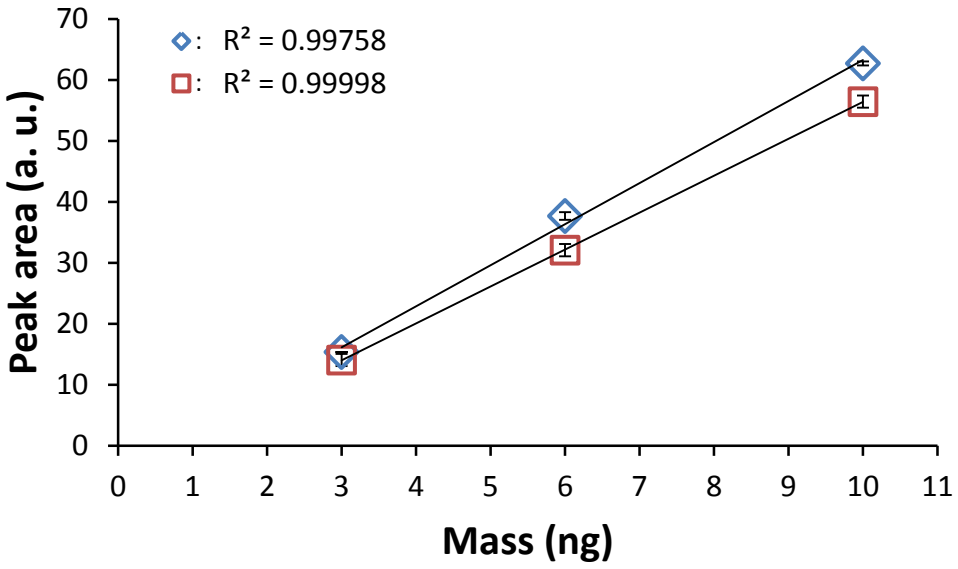

Figure 4.3 Calibration curves for Pd standard solutions in (a) water (blue diamonds) and (b) ethanol (red squares).

Table 4.2 Precision[a] and detection limit[b] for solutions of Pd-Std in water and ethanol, and *G*1-Pd(OAc)$_2$ in ethanol, determined for a Pd mass ranging from 3–10 ng.

Injection volume (µL)	Pd-Std in water		Pd-Std in EtOH		*G*1-Pd(OAc)$_2$ in EtOH	
	Precision (%RSD)	Detection limit (pg)	Precision (%RSD)	Detection limit (pg)	Precision (%RSD)	Detection limit (pg)
3.0	0.1	33	7.4	62	3.8	28
6.0	1.7	16	5.7	62	1.3	29
10.0	0.5	44	0.7	65	2.1	26
Average[c]		31 ± 14		63 ± 2		28 ± 2

[a] The precision was determined in terms of the peak area percent relative standard deviation (%RSD), and is the average of at least 3 measurements. [b] The detection limit was estimated using the 3σ criterion, and from a minimum of 3 measurements. [c] Average and standard deviation for all the injection volumes, determined from a minimum of 9 measurements.

4.4.2. Copolymer-stabilized Pd solutions in ethanol

The LOD (using the 3σ criterion) for Pd was estimated from the standard deviation of the background before the peak when using the same number of data points as for the peak.[48] The average LOD obtained using Pd standards diluted with ethanol and Pd-loaded polymers was 28 pg (expressed in absolute amount). When using 10 µL of Pd standard, this LOD corresponds to 3 $ng \cdot mL^{-1}$ (3 ppb, in relative concentration units). This limit of detection is about 15 times lower, for instance, than the concentration at which Pd impurities were found to be catalytically active (50 ppb).[49] This is also well below some of the "homeopathic" concentrations used (>500 ppb) in a variety of Heck and Suzuki cross-coupling reactions.[36,50–52]

4.4.3. Quantification of Pd loading in the arborescent copolymer

To determine the maximum amount of Pd that can be loaded inside the arborescent copolymer described earlier (*G*0PS-*g*-P2VP, Scheme 4.1), an excess of Pd atoms (1.5 molar equiv) with respect to the number of 2VP units was added. Dialysis of the polymer-Pd solution in ethanol was then used to remove any unbound metal. The residual Pd content in the polymer was measured and quantified based on a calibration curve constructed from non-dialyzed polymer-Pd solutions diluted in ethanol (R^2 = 0.9920). The calibration curve obtained and the amount of Pd measured are shown in Figure 4.4. The average Pd content per 2VP unit was found to be 99.5 ± 4.2 mol %, with %RSD below 3.3% (Table 4.3). In the remaining of the discussion, this Pd-loaded polymer sample will be referred to as *G*1-Pd[100 mol %].

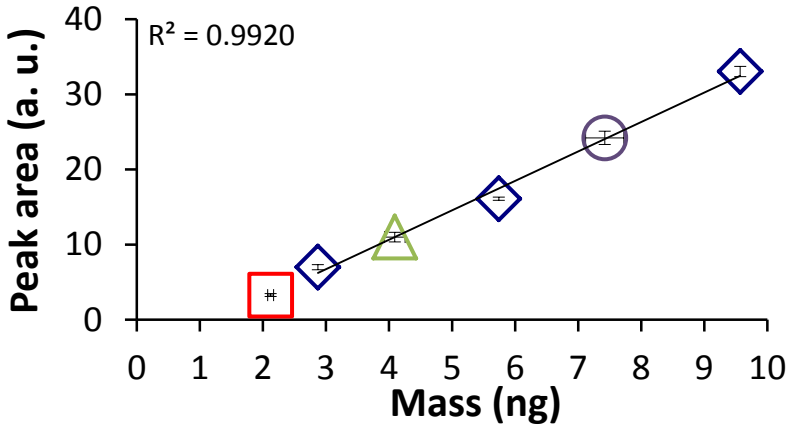

Figure 4.4 Calibration curve for Pd in a solution of *G*1-Pd(OAc)$_2$[1.5 equiv] in ethanol (blue diamonds), and analysis of the dialyzed sample *G*1-Pd(OAc)$_2$ using the following injection volumes: 3.0 µL (red square), 6.0 µL (green triangle) and 10.0 µL (purple circle).

Table 4.3 Pd quantification with 3.0, 6.0 and 10.0 µL injection volumes for solutions prepared with 1.5 molar equivalent of Pd per 2VP unit (*G*1-Pd[100 mol %]).

Injection volume (µL)	Calculated Pd mass (ng)[a]	Calculated Pd/2VP (mol %)	Pd attached (mol %)[b]	Precision (%RSD)[c]
3.0	2.12	98.4	66.1	2.3
6.0	4.09	96.3	64.6	3.3
10.0	7.42	103.9	69.7	3.0
Average[d]		99.5 ± 4.2	66.8 ± 2.8	4.2

[a] Mass measured with the microplasma-OES instrument, obtained from a minimum of 3 measurements. [b] Mole percent of Pd remaining after dialysis. [c] The precision is expressed in terms of the percent relative standard deviation, in relation to the mol % of Pd/2VP. [d] Average and standard deviation for all the injection volumes, determined from a minimum of 9 measurements. Based on pooled standard deviation and a t-test, it was found statistically valid (at the 95% confidence level) to retain the Pd mass (ng) determined using 3 µL volumes despite the slight extrapolation of the calibration curve to lower concentrations.

The Pd concentration was also determined in a polymer-stabilized Pd sample containing 0.25 equiv of Pd per 2VP unit. The amount of Pd was selected to insure complete loading of the micelles, and has been shown to lead to the formation of stable Pd(II)-polymer hybrid systems (Chapter 3). After dialysis, the overall Pd content measured using a minimum of 9 runs was 23.7 mol %, with a %RSD ≤ 5.4% (Figure 4.5, and Table 4.4). This corresponds to 93.3 mol % of the Pd added prior to dialysis. This sample will be referred to as *G*1-Pd[24 mol %] in the rest of the discussion.

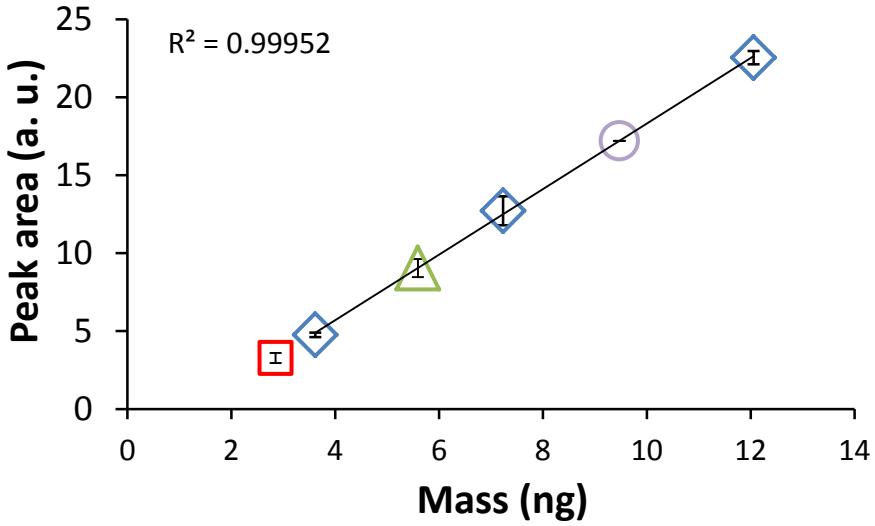

Figure 4.5 Calibration curve for Pd in a solution of *G*1-Pd(OAc)$_2$[0.25 equiv] in ethanol (blue diamonds), and analysis of dialyzed sample *G*1-Pd(OAc)$_2$ using injection volumes of 3.0 µL (red square), 6.0 µL (green triangle) and 10.0 µL (purple circle).

Table 4.4 Pd quantification with 3.0, 6.0 and 10.0 µL injection volumes for solutions prepared with 0.25 molar equivalent of Pd per 2VP units (*G*1-Pd[24 mol %]).

Injection volume (µL)	Calculated Pd mass (ng)[a]	Calculated Pd/2VP (mol %)	Pd attached (mol %)[b]	Precision (%RSD)[c]
3.0	2.85	23.8	93.9	5.4
6.0	5.59	23.4	92.1	4.9
10.0	9.47	23.7	93.6	2.7
Average[d]		23.7 ± 0.9	93.3 ± 3.7	3.9

[a] Mass measured with the microplasma-OES instrument, obtained from a minimum of 3 measurements. [b] Mole percent of Pd remaining after dialysis. [c] The precision is expressed in terms of the percent relative standard deviation, in relation to the mol % of Pd/2VP. [d] Average and standard deviation for all the injection volumes, determined from at least 9 measurements. The Pd mass (ng) determined from 3 µL was retained despite the slight extrapolation of the calibration curve (based on statistical tests detailed in the caption of Table 4.3).

Imaging by TEM of the polymer-Pd solutions confirmed the presence of Pd in the copolymer templates displaying an overall diameter of ca. 18 nm, as shown in Figure 4.6. Pd NPs 2–7 nm in diameter, presumably formed through an Ostwald ripening process, are also visible within *G*1-Pd[100 mol %].

It was thus concluded that the arborescent copolymer can successfully complex with the Pd(II) species present in solution. It also appears that all the 2VP units in the *G*1 arborescent copolymer are accessible to the metallic ions and can contribute to forming stable colloidal dispersions. These conclusions are in accordance with earlier work reporting the fast coordination of Pd(II) species,[53] and strong interactions[10,13,14] of Pd with the lone

electron pair of the nitrogen atom in the 2-vinylpyridine units in aqueous media, and even at high pressures and temperatures in organic solvents.[15] However the exact nature of the complex formed still requires further investigation. Bekturov et al. suggested a model for the complexation of $PdCl_2$ by P2VP which accounts for a 1:1 molar ratio of 2VP units and Pd.[7] However, more recently Fernandez et al. claimed that up to 1/3 of the Pd in commercial $Pd(OAc)_2$ could be in the form of Pd(0). These reduced species accounted for an excess of Pd measured in polymer brushes decorated with dipyridylamine ligands, when compared to the stoichiometric complexation expected with Pd(II) species.[54] The results obtained in the current study are consistent with the formation of a 1:1 complex between the 2VP units and Pd as suggested by Bekturov et al.

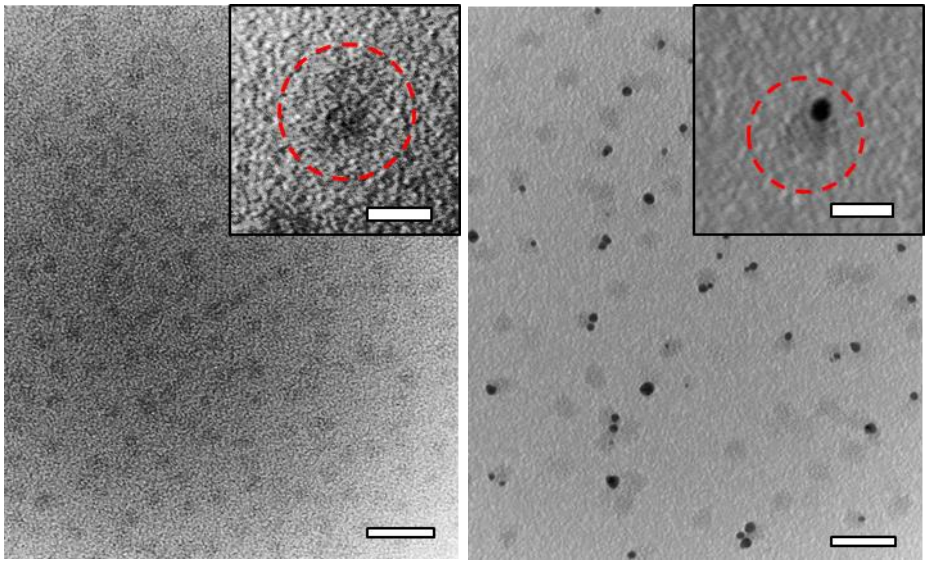

Figure 4.6 TEM images obtained from ethanol solutions of *G*1-Pd[24 mol %] (left), and *G*1-Pd[100 mol %] (right). The brightness and contrast were adjusted for better visualization (scale bars represent 50 nm). Inset: Magnification of a single micelle with a dotted circle added to help visualization; the scale bars represent 20 nm.

4.4.4. Stability and kinetic studies

4.4.4.1. Stability of Pd(II) in ethanol and water, and kinetics of aggregation

A solution of $Pd(OAc)_2$ in ethanol was prepared and its Pd concentration was determined daily over 6 consecutive days. The vial containing $Pd(OAc)_2$ in ethanol was stored in the dark, since light exposure has been reported to enhance the reduction rate of Pd(II).[55] The change in Pd concentration in the ethanolic solution was determined by calibrating the instrument with freshly prepared solutions of a Pd standard in water, these solutions being more easily prepared for rapid analysis (vide infra).

From the results shown in Figure 4.7, it can be concluded that even for a Pd concentration as low as 2.4×10^{-6} M (0.25 μg·mL^{-1}), there is a rapid decrease in the amount of Pd remaining dispersed in solution. After 5 days, for instance, only about one third of the initial Pd content was left in solution. Assuming a first-order rate process, one can write the aggregation rate as: $r = -\mathrm{d[Pd]}/\mathrm{d}t$. The apparent rate constant k_{app} is then obtained from $\ln([\mathrm{Pd}]/[\mathrm{Pd}]_0) = -k_{app}t$, where $[\mathrm{Pd}]_0$ and [Pd] represent the initial concentration of Pd in solution and the concentration at time *t*, respectively. The graphical method seems to confirm the validity of the first order assumption, and the apparent rate constant calculated for Pd aggregation from $Pd(OAc)_2$ in ethanol was $(k_{app})_{EtOH} = 9.89 \times 10^{-3}$ h^{-1} (Figure 4.8).

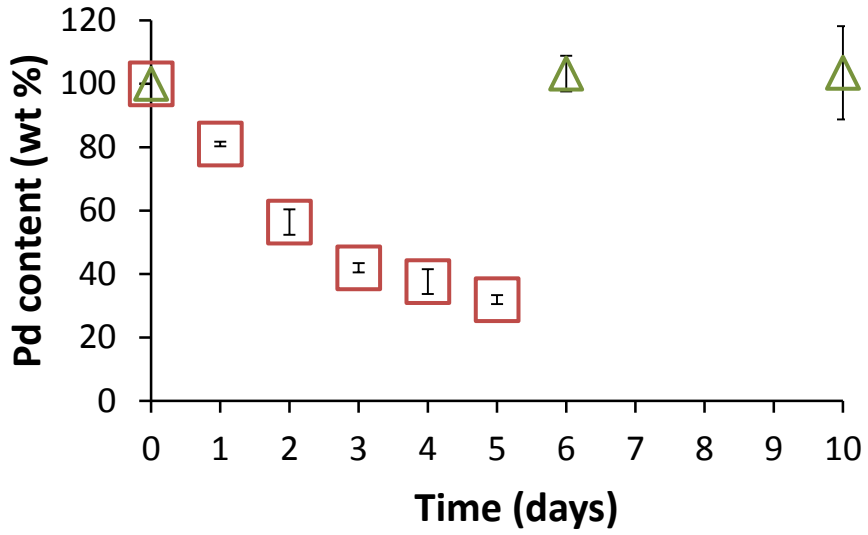

Figure 4.7 Evolution of the mass concentration of Pd in ethanol solutions of $Pd(OAc)_2$ (red squares), and *G*1-$Pd(OAc)_2$[0.25 equiv] (green triangles) as measured by microplasma-optical emission spectrometry.

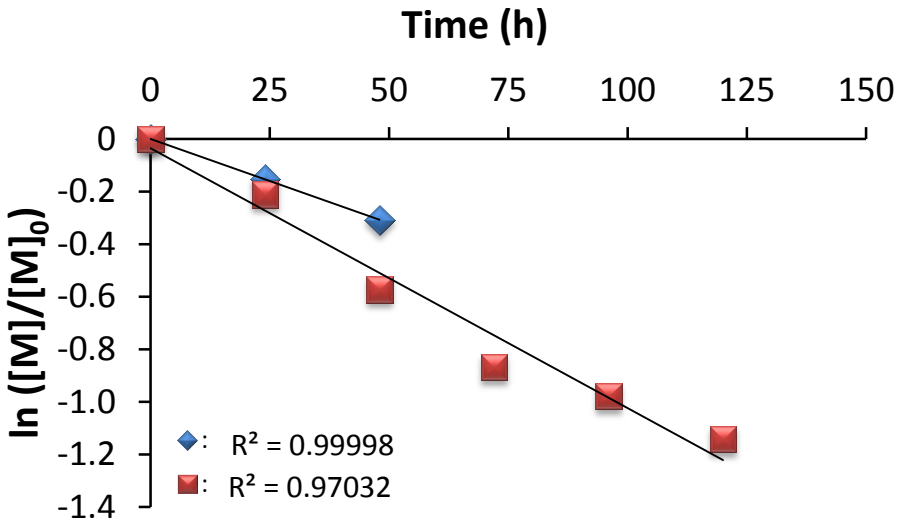

Figure 4.8 Graphical analysis of the first-order rate of aggregation of $Pd(OAc)_2$ in ethanol (red squares), and Pd in a standard solution in water (blue diamonds).

In more concentrated solutions and in the absence of a polymeric stabilizer, a deposit of Pd black was observed after only two hours, as shown in Figure 4.10b. The reduction of Pd(II) to Pd(0) in ethanol according to Scheme 4.2 is well-known; in fact this was taken advantage of in the preparation of various polymer-stabilized Pd nanoparticles.[6,10,14,34]

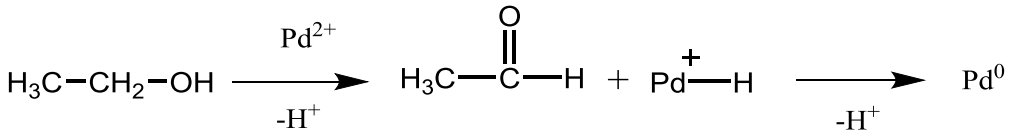

Scheme 4.2 Reduction of Pd(II) to Pd(0) in ethanol.

It should be noted that aqueous solutions prepared from a Pd standard solution (by dilution with Milli-Q water to 1 μg·mL^{-1} in Pd (9.40 μM) and pH 2.7) displayed a similar decrease in concentration, but a plateau was reached after 2 days at about 72 wt % of the initial Pd concentration (Figure 4.9). The first-order apparent rate constant of aggregation, determined before reaching the plateau, was $(k_{app})_{water} = 6.41 \times 10^{-3}$ h^{-1}. The diluted solutions remained yellow and translucent, as shown in Figure 4.10a; however, the formation of a chlorohydroxypalladium(II) precipitate has indeed been reported for Pd(II) at concentrations above 1 ppm, but this was thought to be less predominant at lower Pd concentrations.[56–58] Clearly, the solutions used for calibration purposes should be freshly prepared before use.

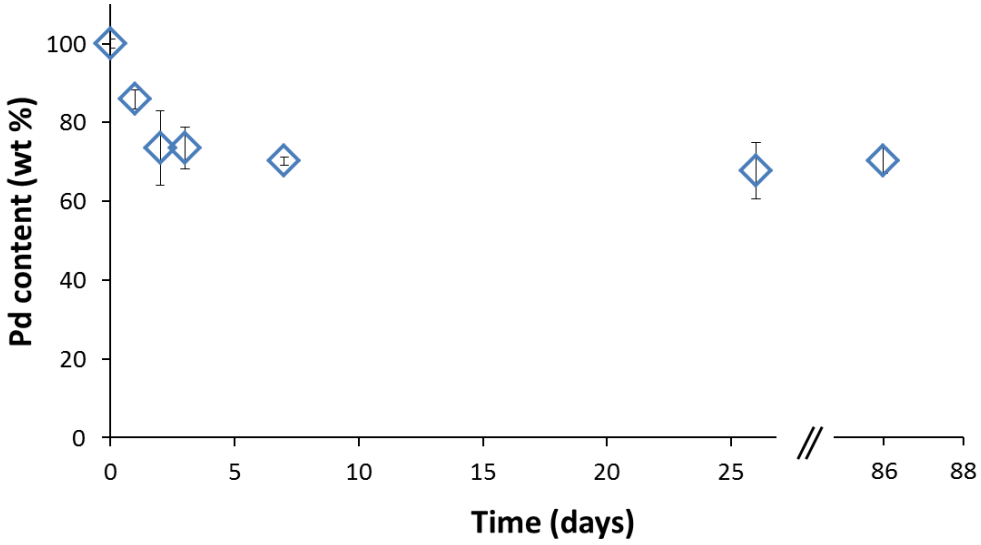

Figure 4.9 Evolution of the mass concentration of Pd in a standard solution in water as measured by microplasma-optical emission spectrometry.

4.4.4.2. Stability of $Pd(OAc)_2$ in the arborescent copolymer in ethanol

The analysis of *G*1-Pd[24 mol %] in ethanol revealed that the Pd concentration remained constant for at least 10 days (Figure 4.10). In the presence of the polymer, the solutions remained yellow (*G*1-Pd[24 mol %]) or brown (*G*1-Pd[100 mol %]) and translucent, with no indication of precipitate formation, as shown in Figure 4.10c and Figure 4.10d. This contrasts with the rapid drop in Pd concentration and the formation of Pd black observed in ethanolic solutions without polymer. Hoogsteen and Fokkink made a similar observation with linear P2VP-stabilized Pd, and showed that the polymer delayed the reduction of Pd(II) in water.[10] The arborescent P2VP template obviously also acts as a stabilizer to prevent the reduction and aggregation of the Pd(II) species in ethanol.

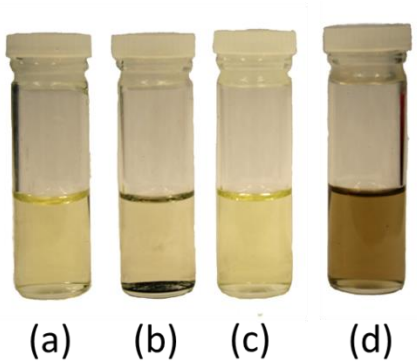

Figure 4.10 Appearance of (a) a Pd standard solution in water, and ethanolic solutions of (b) $Pd(OAc)_2$, (c) *G*1-Pd[24 mol %], and (d) *G*1-Pd[100 mol %].

4.5. Conclusions

We demonstrated the use of a microplasma-based method as an attractive alternative to the more expensive and widely employed ICP technique for Pd quantification. This method fulfills the requirements spelled out by Manning and Grow for a versatile atomic emission source,[59] and contributes to the greening of plasma spectrochemistry. The implementation of a charring step alleviated the need for oxygen-containing gas mixtures. The Re coiled filament was used for more than 1700 analytical runs without any noticeable degradation, and the microplasma emission background was stable for more than 10 h of continuous operation. The use of microsamples for the analysis also means that smaller amounts of reagents and catalysts are required. The %RSD achieved ranged from 7.4% to 0.1%, and the average Pd LOD (3σ) was estimated to be 28 pg (in absolute amount) or 3 $ng{\cdot}mL^{-1}$ (when using 10 μL volumes). Such a LOD was amply sufficient for the determination of Pd loading in microsamples of arborescent copolymers in ethanol. The maximum average Pd content per 2VP unit was determined to be 99.5 mol %.

The method developed also enabled kinetic studies of the stability of palladium acetate in ethanol. It was thus found that the apparent rate constant of aggregation in ethanol was 9.89×10^{-3} h^{-1}, with about 70% of the Pd precipitating out of solution after 5 days. A rapid drop in the Pd concentration before reaching a plateau was also observed in aqueous samples of a Pd standard solution. Clearly, Pd calibration standards must be freshly prepared prior to their use if meaningful Pd concentrations are to be obtained. In the presence of the arborescent copolymer, however, the Pd concentration in ethanol remained stable for at least 10 days.

Overall, the microplasma-based approach described above will help address the need for greener and cheaper quantitative analytical methods, and thus facilitate more widespread use of such methods in catalysis, as articulated by Molnár.[26] Work is in progress to evaluate other organic solvents (e.g., THF) and aqueous systems, with the aim of making the overall catalytic process greener and cheaper.

Chapter 5

Water-soluble Arborescent Copolymers by Complexation with Double-Hydrophilic Block Copolymers

5.1 Overview

The preparation of water-soluble micelles by complexation of an arborescent graft copolymer, viz. arborescent polystyrene-*graft*-poly(2-vinylpyridine) (*Gn*PS-*g*-P2VP, n = [-1,2]), and a double-hydrophilic block copolymer, viz. poly(acrylic acid)-*block*-poly(2-hydroxyethyl acrylate) (PAA-*b*-PHEA), is reported. The block copolymer was prepared by hydrolysis of poly(*tert*-butyl acrylate)-*block*-poly(2-trimethylsilyloxyethyl acrylate) [P*t*BA-*b*-P(HEA-TMS)], synthesized by atom transfer radical polymerization (ATRP). Polyion complex (PIC) micelles formed in ethanol at room temperature upon interaction between the acrylic acid and pyridine units of the polymers. The complexes aggregated into supramolecular micelles, exhibiting hydrodynamic diameters ranging from 132 to 354 nm and a size dispersity below 0.03 for $n \geq 0$. PIC micelles derived from a comb-branched copolymer (PS-*g*-P2VP) formed larger aggregates. The multi-molecular aggregates displayed reversible thermo-responsive properties in ethanol, dissociating upon heating to ca. 35 °C and reforming upon cooling. The aggregates were stable in water to at least 50 °C and displayed hydrodynamic diameters ranging from 110 to 306 nm, and a size dispersity $\leq$ 0.24. Characterization of the onion-type micelles was performed by dynamic light scattering (DLS), atomic force microscopy (AFM), and transmission electron microscopy (TEM). Loading of the PIC micelles with Pd yielded aqueous colloidal dispersions useful as catalysts for the Suzuki-Miyaura reaction in water.

5.2 Introduction

Micellar polymeric architectures are expected to contribute significantly to the development of applications such as vectors for polymeric therapeutics,[1,2] phase transfer catalysis,[3,4] metallic nanoparticle synthesis,[5] surface modification,[6] and other areas.[7] The combination of a hydrophobic core and a hydrophilic corona is often obtained by the self-assembly of amphiphilic block copolymers, a process that is entropically driven in water and enthalpically driven in organic solvents.[7] More recently the formation of polyion complex (PIC) micelles, obtained from charged block copolymers, has been reported.[8–10] The chain association, driven by electrostatic interactions or hydrogen bonding, was shown to conduce stable and narrowly distributed micelles in both aqueous and organic solvents.[11–13]

A wide range of block copolymers have been used for the preparation of PIC micelles.[10] For instance, block copolymers of poly(acrylic acid) (PAA) and poly(2-vinylpyridine) (P2VP) or poly(4-vinylpyridine) (P4VP) were shown to assemble through hydrogen bonding and electrostatic interactions. Zhang et al. also prepared micelles with a narrow size distribution by the complexation in ethanol of P4VP and poly(ethylene glycol)-*block*-poly(acrylic acid) (PEG-*b*-PAA),[14] P4VP and polystyrene-*block*-poly(acrylic acid) (PS-*b*-PAA),[15] and PEG-*b*-P4VP and PS-*b*-PAA.[16] Lefèvre et al. likewise obtained micelles in *N*,*N*-dimethylformamide from PAA and PS-*b*-P4VP.[17] Fourier transform infrared (FTIR) and X-ray photoelectron spectroscopy (XPS) measurements on films of the PAA/P2VP complexes deposited from ethanol/water (1/1 v/v) mixtures confirmed the formation of hydrogen bonding and ionic interactions.[18] In water, thermo-responsive micelles were

prepared by the complexation of poly(*N*-isopropylacrylamide-*co*-4-vinylpyridine) onto core-shell microspheres of poly(styrene-*co*-methacrylic acid) by Wang et al.[19]

Branched polymers such as star copolymers,[20] comb-branched copolymers,[21] and dendritic polymers[22–26] have also been employed in the preparation of PIC micelles that proved promising for drug delivery. For instance, complexes derived from poly(amidoamine) (PAMAM) dendrimers and poly(ethylene glycol)-*block*-poly(*n*-propyl methacrylate-*co*-methacrylic acid) could be loaded with nucleic acids,[26] and the complexation of poly(ethylene glycol)-*block*-poly(L-lysine) with phthalocyanine-based aryl ether dendrimers served in the preparation of photosensitive PIC micelles for photodynamic therapy.[23] PIC micelles were also used to stabilize Pd nanoparticles as catalysts for hydrogenation[27] and aqueous Suzuki and Heck reactions.[28]

Another interesting approach for the preparation of supramolecular micelles consists in the utilization of double-hydrophilic block copolymers (DHBC) to induce stimuli-responsive properties.[29,30] These polymers have received rapidly growing interest[29] since the first report detailing their synthesis in 1972.[31] This is largely motivated by their ability to interact with both ionic and non-ionic drugs, and their anticipated biomedical applications.[32]

Poly(2-hydroxyethyl acrylate) (PHEA) is both biocompatible and hydrophilic,[33–35] similarly to the more widely used poly(2-hydroxyethyl methacrylate) (PHEMA);[36] however, the former has found limited applications in the formation of PIC micelles.[37] Many techniques have been reported for the polymerization of HEA including free radical polymerization,[37–40] atom transfer radical polymerization (ATRP),[41–45] reversible addition-fragmentation transfer (RAFT),[46] and nitroxide-mediated polymerization (NMP).[47–49] The

polymerization of 2-trimethylsilyloxyethyl acrylate (HEA-TMS), followed by the hydrolysis of the trimethylsilyl group, is sometimes preferred to limit the occurrence of side reactions. This approach has been reported for both free radical polymerization[50] and ATRP.[42,51–53] The preparation of DHBC with a PHEA block has been reported by copolymerization with PAA using controlled radical polymerization. PHEA-*b*-PAA was used for the preparation of water-soluble hybrid PIC micelles by complexation with various metal polycations.[52,54,55]

Gauthier et al. reported the synthesis of amphiphilic arborescent copolymers incorporating an arborescent PS core grafted with P2VP side chains.[56–58] The arborescent (dendrigraft) polymer core, synthesized by successive grafting cycles of polymeric chains (Scheme 5.1), have a cascade-branched architecture akin to that of dendrimers. However, the utilization of polymeric chains rather than small molecules in the synthetic protocol allowed a rapid increase in molar mass while maintaining a low molar-mass dispersity ($Đ_M \leq 1.1$).[59] Dissolution of the macromolecules in aqueous HCl solutions yielded cationic polyelectrolytes behaving like unimolecular micelles[56,57] that could solubilize polycyclic aromatic hydrocarbons.[60] Complexation with Au(III)[61] and Pd(II)[62] was also demonstrated in organic solvents. Interestingly a second generation arborescent copolymer, obtained by grafting a first generation PS core with P2VP chains (*G*1PS-*g*-P2VP), displayed reversible thermo-responsive properties in toluene. Aggregation of the unimolecular micelles to supramolecular assemblies was induced by lowering the temperature below a critical self-assembly temperature.[63]

In this Chapter, we report the formation of PIC micelles by complexation of arborescent polystyrene-*graft*-poly(2-vinylpyridine) (*Gn*PS-*g*-P2VP, n = [-1,2]) copolymers

with a double-hydrophilic PAA-*b*-PHEA copolymer. The block copolymer was obtained by sequential ATRP of *tert*-butyl acrylate (*t*BA) and 2-trimethylsilyloxyethyl acrylate (HEA-TMS), followed by acid hydrolysis. The solubility characteristics of the PIC micelles were examined in ethanol and water by dynamic light scattering (DLS), and films were imaged by transmission electron microscopy (TEM) and atomic force microscopy (AFM). The formation of supramolecular aggregates with reversible thermo-responsive properties was observed in ethanol. The micelles were used to solubilize Pd in water, to yield useful catalysts for the Suzuki-Miyaura cross-coupling reaction in that medium.

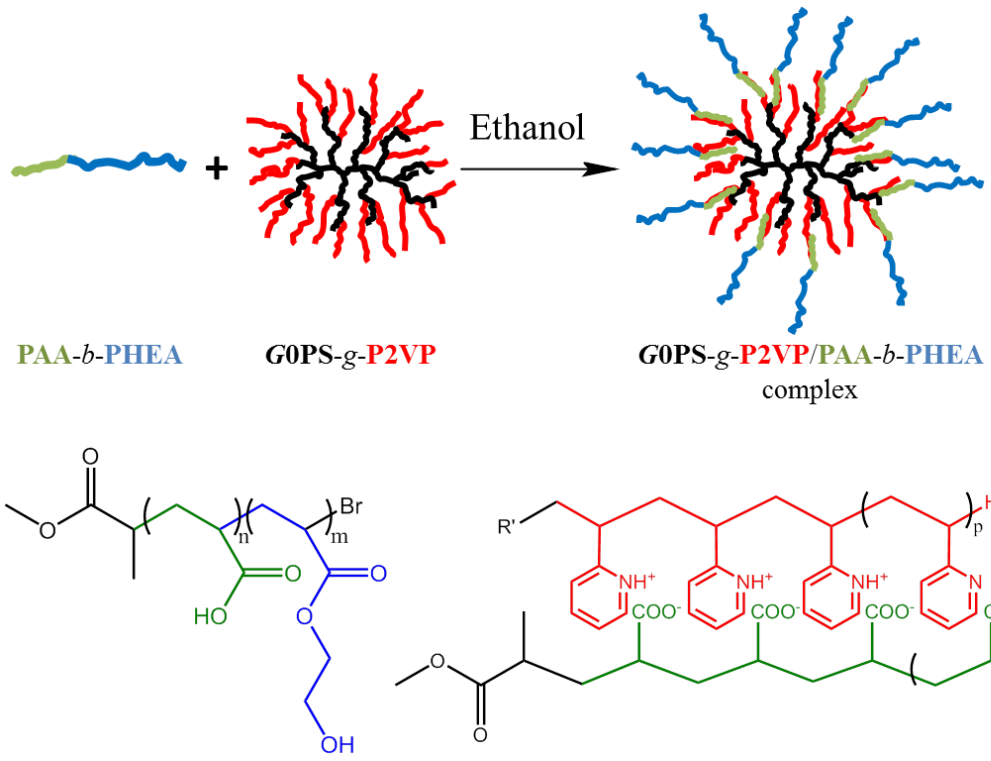

Scheme 5.1 Schematic representation of the formation of a polyion complex between PAA-*b*-PHEA and *G*0PS-*g*-P2VP in ethanol.

5.3 Experimental procedures

5.3.1 Materials

Copper(I) bromide (CuBr, Sigma-Aldrich, 99.999%) was purified by stirring successively in glacial acetic acid (Caledon, >99.7%), absolute ethanol (Commercial Alcohols Inc.), and diethyl ether (Sigma-Aldrich, anhydrous, ACS reagent, ≥99.0%). The white powder was then dried under vacuum for 5 h and stored under N_2. Triethylamine (Et_3N, EMD, ≥99.5%), *tert*-butyl acrylate (*t*BA, Sigma-Aldrich, 98%) and *N*,*N*′,*N*″,*N*‴-pentamethyldiethylenetriamine (PMDETA, Sigma-Aldrich, 99%) were distilled under reduced pressure and stored under N_2. Methyl-2-bromopropionate (Sigma-Aldrich, 98%), acetone (Caledon, >99.7%), trimethylsilyl chloride (TMS-Cl, Sigma-Aldrich, ≥98.0%), dichloromethane (Caledon, >99.8%), ethyl acetate (Caledon, >99.8%), tetrahydrofuran (THF, Caledon, >99%), ethanol (Fisher, reagent, 88-91%, 4-5% methanol, 4.5-5.5% 2-propanol), and trifluoroacetic acid (TFA, Caledon, reagent, >99.9%) were used as received from the suppliers. Milli-Q water (18.2 MΩ·cm) was obtained from a Milli-Q RG (EMD Millipore Systems) deionized water purification system with a QPAK 2 purification pack.

The monomer 2-hydroxyethyl acrylate (HEA, Sigma-Aldrich, 96%) was first purified by extraction as follows to remove diacrylates and acrylic acid impurities.[42] HEA (300 mL, 2.6 mol) was first dissolved in deionized water (100 mL, 25% v/v) and washed 10 times with *n*-hexanes (Sigma-Aldrich, ACS reagent, ≥98.5%). The aqueous phase was then saturated with sodium chloride (ca. 80 g) before extraction of the HEA with diethyl ether (Sigma-Aldrich, ACS reagent, ≥99.0%, 4 × 500 mL). The ethereal solution was dried by adding anhydrous $MgSO_4$ (Fisher, Powder certified), and concentrated by rotary evaporation. The

monomer was stored at -15 °C after the addition of hydroquinone (BDH Chemicals, ≥99.0%, 300 mg, 3 mmol, 0.1% w/w) used as an inhibitor. The monomer was further purified by distillation under reduced pressure before use.

The arborescent graft copolymers used in this study were synthesized earlier by anionic polymerization and grafting.[58] The polymers consisted of different generations of arborescent polystyrene substrates grafted with poly(2-vinylpyridine) chains. Purification from low molar mass contaminants was performed with at least 3 successive cycles of precipitation/fractionation from 5 $g \cdot L^{-1}$ solutions in THF/methanol (4/1 v/v) with *n*-hexane. The characteristics of the copolymers are provided in Table 5.1, and their structure is depicted in Scheme 5.1.

Table 5.1 Characterization data for the arborescent copolymers templates. Adapted with permission from Reference 58. Copyright 2012 The Royal Society of Chemistry.

Sample	P2VP side chains		Graft copolymer				
	$\bar{M}_n$ (10^3 g/mol)[a]	$\bar{M}_w/\bar{M}_n$	$\bar{M}_n$ (10^3 g/mol)[a]	$\bar{M}_w/\bar{M}_n$	f_n[b]	2VP (mol %)[c]	2VP groups[d]
PS-*g*-P2VP	5.1	1.15	74	1.08	13	96	900
*G*0PS-*g*-P2VP	5.5	1.15	1,100	1.08	182	95	9,600
*G*1PS-*g*-P2VP	6.2	1.10	8,400	1.09	1177	91	66,500
*G*2PS-*g*-P2VP	4.1	1.14	20,400[e]	n/a[e]	3693	91	144,000

[a] Absolute values from SEC-MALLS and light scattering measurements. [b] Branching functionality: Number of branches grafted in the last cycle per molecule. [c] From ^{1}H NMR analysis. [d] From $\bar{M}_n$ and f_n. [e] Interaction of the *G*3 copolymer with the SEC column prevented elution. Estimated values obtained from the absolute $\bar{M}_n$ of the substrate and the composition measured by ^{1}H NMR spectroscopy.

5.3.2 Synthesis of poly(*tert*-butyl acrylate) macroinitiator

The synthesis of a low molar mass P*t*BA-Br was performed via ATRP, by adapting a procedure reported by Davis and Matyjaszewski[64] as illustrated in Scheme 5.2 and in Appendix A5.1. Briefly, CuBr (0.225 g, 1.6 mmol, 0.4 equiv), methyl-2-bromopropionate (0.4 mL, 3.6 mmol, 1 equiv), acetone (2.7 mL), *t*BA (10.3 mL, 70 mmol, 20 equiv), and PMDETA (0.32 mL, 1.5 mmol, 0.4 equiv) were added in an oven-dried round-bottomed flask (rbf). The reagents were degased with 3 freezing-evacuation-thawing cycles as follows: The rbf was placed in liquid nitrogen for 15 min, then evacuated for 10 min, and the solution was thawed in a water bath. After filling the rbf with N_2, the solution was stirred at room temperature for 10 min. The cycle was repeated two additional times. The dark green mixture was then placed in an oil bath at 60 °C for 3 h before cooling to room temperature. Dichloromethane (30 mL) was then added to the rbf and the Cu catalyst was extracted with deionized water (6 × 250 mL) until a clear organic phase remained. After removal of the organic solvent by rotary evaporation, the polymer was dissolved in acetone (15 mL) and further purified by dialysis (1,000 MWCO Spectra/Por® 7 regenerated cellulose) against 600 mL of acetone. The solvent was changed three times over 1 day, and the polymer was recovered by removal of the solvent under vacuum. $\bar{M}_n$ (SEC) = 1660, $\bar{M}_n \cdot \bar{M}_w^{-1}$ = 1.06. ^{1}H NMR ($CDCl_3$, 300 MHz): $\bar{M}_n$ = 1660, $\bar{X}_n$ = 13, δ (ppm): 1.06-1.17 (b, 3H), 1.18-1.25 (b, 1H), 1.28-1.67 (b, 125H), 1.71-2.02 (b, 6H), 2.03-2.62 (b, 14H), 3.63 (s, 3H), 4.00-4.19 (m, 1H); ^{13}C NMR ($CDCl_3$, 300 MHz) δ (ppm): 27.71 (CH_2), 28.03 (C-(CH_3)$_3$), 30.33 (CH_2-CH-Br), 34.24 (CH-CH_3), 80.53 (C-(CH_3)$_3$), 168.27 (CO).

5.3.3 Silylation of 2-hydroxyethyl acrylate

The protection of HEA was performed according to a procedure by Mühlebach et al.,[42] illustrated in Scheme 5.3. Briefly, the monomer HEA (46 mL, 0.40 mol, 1.0 equiv), purified as described in Section 5.3.1 was added to dichloromethane (500 mL) and triethylamine (85 mL, 0.61 mol, 1.5 eq) in a 1-L rbf, and the solution was cooled to 0 °C in an ice bath. The drop-wise addition of trimethylsilyl chloride (70 mL, 0.55 mol, 1.4 equiv) was performed under N_2, and the formation of a white precipitate ($Et_3N{\cdot}HCl$) was observed. The solution was then allowed to warm to room temperature and the precipitate was removed by suction filtration (Whatman® filter paper, grade 4). The solvent was removed by rotary evaporation and the liquid residue was filtered once more. The product, 2-trimethylsilyloxyethyl acrylate (HEA-TMS), was then dissolved in ethyl acetate (300 mL) and washed with water (300 mL) three times. Anhydrous $MgSO_4$ (ca. 5 g) was added to the solution and the solvent was removed under vacuum. ^{1}H NMR ($CDCl_3$, 300 MHz) δ (ppm): 0.07 (s, 9H), 3.76 (t, *J* = 4.8 Hz, 2H), 4.17 (t, *J* = 4.8 Hz, 2H), 5.77 (d, *J* = 9.0 Hz, 1H), 6.04 (d, *J* = 10.1 Hz, 1H), 6.11 (d, *J* = 10.1 Hz, 1H), 6.36 (d, *J* = 15.9 Hz, 1H). ^{13}C NMR ($CDCl_3$, 300 MHz) δ (ppm): -0.62 (Si-$(CH_3)_3$), 60.55 (*C*H_2-O-$SiMe_3$), 65.60 (*C*H_2-O-CO), 128.24 (CH), 130.72 (*C*H_2-CH), 166.01 (CO).

5.3.4 Synthesis of poly(*tert*-butyl acrylate)-*block*-poly(2-trimethylsilyloxyethyl acrylate) [P*t*BA-*b*-P(HEA-TMS)]

The polymerization of HEA-TMS was performed by ATRP using P*t*BA-Br ($\bar{M}_n$ = 1600) as a macroinitiator. In a 25-mL Schlenk tube were added CuBr (10.8 mg, 75 μmol, 1.1 equiv), P*t*BA-Br (109.2 mg, 66 μmol, 1.0 equiv), and freshly distilled HEA-TMS (4.5 mL,

24.2 mmol, 325 equiv). The addition of PMDETA (34 mg, 19.6 mmol, 2.6 equiv) resulted in a light blue solution, which was degased by three successive freezing-evacuation-thawing cycles as described in Section 5.3.2. The tube was then filled with N_2 and heated to 90 °C for 3.5 h. The dark green viscous solution was then cooled to room temperature, diluted with dichloromethane (50 mL), and the copper catalyst was removed by extraction with deionized water (3 × 100 mL). After removal of the solvent by rotary evaporation and redissolution of the solid in acetone (10 mL), the polymer was further purified by dialysis against acetone (500 mL). The solvent was changed thrice over 2 days and a clear solution was obtained. $\bar{M}_{n,abs}$ (SEC) = 28000, and $\bar{M}_n \cdot \bar{M}_w^{-1}$ = 1.18. ^{1}H NMR ($CDCl_3$, 300 MHz): $\bar{X}_{n,PHEA\text{-}TMS}$ = 141, δ (ppm): 0.14 (s, 1371H), 1.38-1.50 (b, 125H), 1.50-1.59 (b, 49H), 1.59-1.84 (b, 197H) 1.84-2.14 (s, 78H), 2.14-2.22 (b, 13H), 2.22-2.55 (b, 152H), 3.77 (b, 329H), 4.11 (b, 341H); ^{13}C NMR ($CDCl_3$, 300 MHz), δ (ppm): -0.55 (Si-Me_3), 1.21 (*C*H_3-CH_2), 27.92 (*C*H_2-CH), 41.11 (CH), 60.08 (*C*H_2-O-$SiMe_3$), 65.14 (*C*H_2-O-CO), 174.04 (CO).

5.3.5 Hydrolysis of P*t*BA-*b*-P(HEA-TMS)

A solution of P*t*BA-*b*-P(HEA-TMS) (527 mg, 26% w/w) in THF (1.5 g) was transferred to a 20-mL screw-cap vial with a magnetic stirring bar and ethanol (7.3 g, 85% v/v). After placing the vial in an ice-water bath and with vigorous stirring, trifluoroacetic acid (9.6 g, 30 equiv) was added drop-wise. A white precipitate formed during the addition of the first 3 g (2 mL) of TFA, but the solution cleared up and turned slightly cloudy afterwards. After about 1.5 h the solution turned white again, but was left stirring for 24 h. The solvent was then evaporated under vacuum. A solvent change was performed by adding Milli-Q

water (5 g) and evaporating the solution under vacuum. Another 5 g aliquot of Milli-Q water was then added (9.5% w/w), and the viscous solution was transferred to a dialysis bag (Spectra/Por® CE, MWCO 500) for dialysis against a mixture of methanol/H_2O (50/50 v/v, 500 mL) for 48 h with 6 solvent changes. The polymer was then dialyzed against 500 mL of methanol for another 24 h, changing the solvent thrice. The clear solution was recovered and stored at 10 °C. Complete removal of the acid was confirmed by ^{19}F NMR analysis, by the absence of peak at δ = -75.0 ppm (relatively to the reference signal of $CFCl_3$). $\bar{M}_{n,app}$ [SEC, DMF LiCl (1 g·L^{-1})] = 96800, and $\bar{M}_n \cdot \bar{M}_w^{-1}$ = 1.29. ^1H NMR (DMSO-d_6, 300 MHz) δ (ppm): 1.21-1.67 (b, 243H), 1.67-1.93 (b, 75H), 2.07-2.39 (b, 164), 3.08-3.16 (b, 14H), 3.16-3.40 (b, 64H), 3.40-3.68 (b, 337H), 3.80-4.13 (b, 329 H), 4.56-4.85 (b, 147H); ^{13}C NMR (DMSO-d_6, 300 MHz), δ (ppm): 34.74 (CH), 59.19 (CH_2-O), 66.02 (CH_2-OH), 174.44 (CO).

5.3.6 Complexation of the arborescent copolymer with PAA-*b*-PHEA

Coupling of PAA-*b*-PHEA with the arborescent copolymers (*G*nPS-*g*-P2VP) was achieved by adding 1.5 g of the DHBC ethanolic solution (1.3% w/w, 20 mg of polymer) to 2.6 g of a solution of the arborescent copolymer in ethanol (0.76% w/w, 20 mg, 1 mass equiv). After stirring for 1 h, 7.5 mL of Milli-Q water were added to obtain a 25/75 v/v water/ethanol mixture (0.3% w/w in *G*[*n*+1]). After stirring vigorously for another 2.5 h, the solution was transferred to a dialysis bag (Spectra/Por®7, MWCO 25,000), and dialyzed against water/ethanol 25/75 v/v (500 mL), changing the solvent every 3 h, 3 times; and against Milli-Q water (500 mL) for 48 h, changing the solvent 6 times.

5.3.7 Pd loading and Suzuki-Miyaura cross-coupling reaction

The arborescent copolymer *Gn*PS-*g*-P2VP and PAA-*b*-PHEA were first dissolved overnight in ethanol in separate vials (1 mg·mL^{-1}, and 10 mg·mL^{-1}, respectively). $Pd(OAc)_2$ (ca. 10.6 mg, 0.5 mol equiv) was then added to the first solution, which was heated to 40 °C in an oil bath and stirred for 1 h. The arborescent copolymer/Pd solution was then added drop-wise to 1 mL of the PAA-*b*-PHEA solution to obtain a ratio $m_{Gn\text{PS-}g\text{-P2VP}}/m_{\text{PAA-}b\text{-PHEA}}$ = 1. After stirring overnight, the solvent was removed by rotary evaporation to obtain a brown powder which was soluble in Milli-Q water.

The Suzuki-Miyaura (SM) cross-coupling reactions were conducted by dissolving 4-bromoanisole (187 mg, 1 mmol), phenylboronic acid (183 mg, 1.5 mmol), and K_2CO_3 (277 mg, 2 mmol) in 4 mL of D_2O. The polymer-stabilized Pd catalyst prepared above (3 mg, m_{Pd} = 1 mg, n_{Pd}/n_{2VP} = 0.5) was then added to the solution to obtain a Pd content of 0.5 mol % (concentration ca. 1.2 mmol·L^{-1}). The solution was stirred at room temperature and 0.3 mL aliquots of the solution were removed at predetermined time intervals. After dilution in ethanol (1.0 mL) and D_2O (0.5 mL), the sonicated samples were analyzed by ^{1}H NMR spectroscopy to monitor the progress of the reaction.

5.3.8 Characterization

5.3.8.1 Size-exclusion chromatography (SEC)

The absolute molar mass of the P*t*BA macromonomer, and the apparent molar mass of P*t*BA-*b*-P(HEA-TMS) were determined by size-exclusion chromatography (SEC) analysis

on a Viscotek GPCmax instrument (VE2001) equipped with a TDA 305 triple detector array consisting of refractive index (RI), light scattering at low (7°) and right angles (LALS and RALS, respectively; λ = 670 nm), and viscometer detectors, as well as a UV photodiode array detector (Viscotek 2600). The instrument was calibrated with a polystyrene standard with a peak molar mass $\bar{M}_p$ = 99,500 and $\bar{M}_n \cdot \bar{M}_w^{-1}$ = 1.03 (Viscotek); reported values of the refractive index increment (d*n*/d*c*) = 0.185 mL·g^{-1}, and of the intrinsic viscosity = 0.477 dL·g^{-1}. Three PolyAnalytik SupeRes™ Series (PAS-103-L, PAS-104-L, PAS-105-L), 8 mm (I. D.) × 300 mm (L) linear mixed-bed columns having a linear polystyrene molar mass range of 10^3 to 10^6 were used in the analysis. The mobile phase was THF at a flow rate of 1.0 mL·min^{-1} and a temperature of 35 ºC. The specific refractive index increment (d*n*/d*c*) for P*t*BA in THF was taken as 0.0593 mL·g^{-1}.[65] Analysis of the chromatograms was performed with the OmniSEC 4.6.1 software package.

The PAA-*b*-PHEA copolymers were analyzed by SEC on an analytical system consisting of a Waters 510 HPLC pump, a 50-µL injection loop, and a Waters 2410 differential refractometer (DRI) detector in series with a 3-angle (45°, 90°, 135°) Wyatt MiniDAWN laser light scattering detector (λ = 690 nm) used for absolute molar mass characterization. Separation was achieved on a 500 mm × 10 mm Jordi Gel DVB mixed-bed linear column with a linear PS molar mass range of 10^2–10^7. The mobile phase was DMSO with LiCl (1 g·L^{-1}) at room temperature, at a flow rate of 1.0 mL·min^{-1}. The analysis was performed using the software package Astra®, version 4.70 (Wyatt Technology Corp.).

5.3.8.2 Nuclear magnetic resonance (NMR) spectroscopy

The silylation of HEA, the composition of the polymers, and the Suzuki-Miyaura reaction were monitored by ^{1}H and ^{13}C NMR spectroscopy analysis on Bruker Avance-300 (300 MHz) or Avance-500 (500 MHz) nuclear magnetic spectrometers equipped with a z-gradient QNP 5 mm sample serving as the reference frequency. Each spectrum comprised 16 scans, and the concentration of the samples for the analysis ranged from 10–30 $mg \cdot mL^{-1}$.

5.3.8.3 Transmission electron microscopy (TEM)

Imaging of the arborescent copolymers and PIC micelles was achieved by transmission electron microscopy (TEM) on a Philips CM10 electron microscope operated at 60-80 kV accelerating voltage in the bright-field mode. The samples were prepared by depositing two drops of solution (ca. 0.1 $mg \cdot mL^{-1}$) onto 300-mesh Formvar® carbon-coated copper TEM grids (Electron Microscopy Sciences, FCF300-Cu) placed onto a filter paper used as a wicking medium. After deposition of the solution, the grid was transferred onto a new piece of filter paper in a Petri dish and dried overnight at room temperature. Staining of the samples in a closed container was done by exposure to iodine vapors for 15 h, or RuO_4 vapors for 30 min. The images were recorded with an Advance Microscopy Techniques 11 megapixel digital camera and the Image Capture Software Engine version 5.42.558. The feature size and size distribution were measured with the open source processing program ImageJ (version 1.46r).[66] Fifty measurements were made for the determination of the average micelle size and size distribution. Contrast adjustment was also performed on some of the micrographs to improve visualization and help with the feature size measurements.

5.3.8.4 Dynamic light scattering (DLS)

The light scattering measurements were performed on a Zetasizer Nano ZS90 (Malvern Instruments) equipped with a 4 mW He-Ne laser operating at 633 nm. The temperature was varied from 25.0 to 50.0 ± 0.1 °C and the scattering angle was 90°. Each sample was measured in triplicate. The samples were prepared at least 24 h before the measurements unless otherwise stated, and were filtered at least four times either through a PTFE membrane with a nominal pore size of 0.45 µm (ethanolic solutions) or a mixed cellulose ester membrane with a nominal pore size of 0.8 µm (aqueous solutions). A quartz cuvette (ethanolic solutions) or disposable PS cuvettes (aqueous solutions) with a 1-mL capacity were used for the measurements. The concentration of the samples ranged from 5 $mg \cdot mL^{-1}$ (linear polymers) to 0.1 $mg \cdot mL^{-1}$ (*G*3 arborescent copolymer solutions). The refractive index of ethanol at 25 °C was taken as 1.361,[67] and was calculated up to 50 °C using the temperature dependence factor dn/dt = -4.29 10^{-4} $°C^{-1}$.[68] The viscosity of ethanol was calculated from the quasi-polynomial equation $\ln(\eta) = -6.21 + 1614T^{-1} + 0.00618T - 1.132\times10^{-5}\ T^2$, with η in cP and T in K.[69] The refractive indices of the water-ethanol mixtures were calculated with the Wiener equation.[70] The viscosity of the mixtures was obtained by calculating the viscosity deviation with the Redlich-Kister equation and the fitting parameters determined by Gonzáles et al.[71]

The intensity-weighted autocorrelation function $g^{(2)}(t)$ (ACF) was measured by the correlator of the instrument, and analyzed by the methods of cumulants[72,73] by the proprietary software Zetasizer Software 6.32 (Malvern Instruments). The size dispersity, calculated by the software using cumulants analysis, is given by $\mu_2/\ \Gamma^2$, where μ_2 represents the second

moment from cumulants analysis and Γ is the decay rate. The size distributions, also obtained from the Zetasizer software, were calculated by the non-negatively constrained least-squares method (NNLS).[74]

5.3.8.5 Atomic force microscopy (AFM)

Muscovite mica discs (9.9 mm diameter, NanoAndMore GmbH) were adhered onto stainless steel discs with a double-sided adhesive tape (NanoAndMore GmbH), and a fresh surface was exposed by cleaving with a strip of tape (Scotch® MultiTask tape). Polymer solutions were prepared either in ethanol, Milli-Q water or a mixture thereof at concentrations ranging from 0.2 to 0.05 $mg \cdot mL^{-1}$. The solutions were deposited on the mica substrates with a Pasteur pipet and spin-coated at about 3000 rpm for 60 s under ambient conditions. After solvent evaporation, AFM imaging was carried out on a Nanoscope IIIa instrument (Digital Instruments, model MMAFM-2, scan stage J) in the tapping mode to acquire simultaneously height and phase data. The instrument was housed in a NanoCube acoustic isolation cabinet and mounted on a Halcyonics Micro 40 vibration isolation table. The cantilever probes used were VistaProbes, T300 silicon tip (spring constant 40 $N \cdot m^{-1}$, resonant frequency 300 kHz), with the following characteristics: length 125 μm, width 40 μm, tip height 14 μm, and tip radius < 10 nm. NanoScope Analysis v1.40 software was used for the image analysis. The scan rate was typically set between 0.7 to 1.0 Hz, at a scan angle of 0°, acquiring 512 samples/line. The drive amplitude was varied between 30–50 mV, and the amplitude set-point was between 0.50–0.85 V to adjust the force applied on the surface. The feedback loop sensitivity was controlled by adjusting the integral gain to 0.5, and the proportional gain to 6.0 typically.

5.4 Results and discussion

5.4.1 Block copolymer synthesis

The synthesis of PAA-*b*-PHEA was performed via ATRP in a multistep process. This polymerization technique allows the preparation of well-defined homopolymers and copolymers with narrow size distributions, and has been widely used in the preparation of various polyacrylates.[64,75] A low molar mass P*t*BA sample was first prepared by ATRP, using methyl 2-bromopropropionate and CuBr/PMDETA at 60 °C as shown in Scheme 5.2. Acetone was also added to obtain a homogeneous solution.[64]

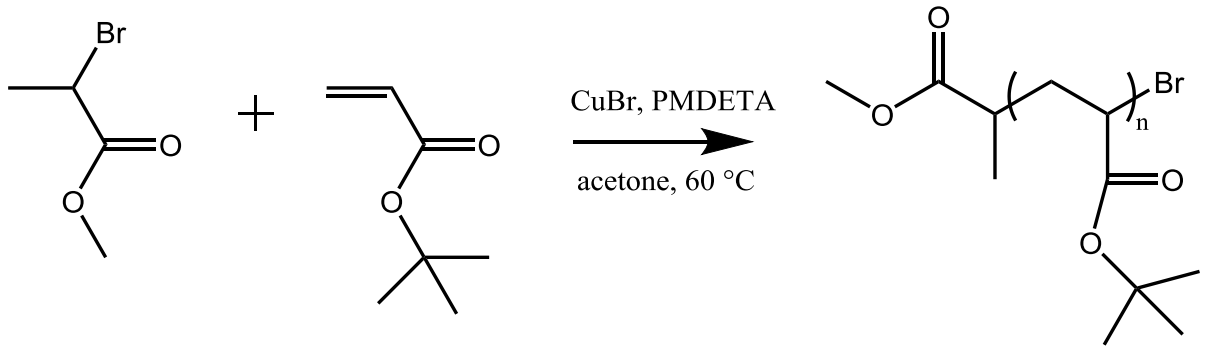

Scheme 5.2 Synthesis of P*t*BA via ATRP.

Based on SEC-triple detection array analysis the polymer obtained had $\bar{M}_{n,}$ = 1660 g·mol^{-1} (corresponding to 13 repeat units) and $\bar{M}_n \cdot \bar{M}_w^{-1}$ = 1.06 (Figure 5.1). ^{1}H NMR spectroscopy analysis of P*t*BA (Figure 5.2) confirmed the $\bar{M}_n$ obtained by SEC.[76] The methine proton geminal to the terminal bromine atom has a distinct chemical shift at 4.00-4.19 ppm (*a*) as compared to the methine protons in the repeat units at δ 2.03-2.62 ppm (*c*), the isotactic and syndiotactic[77] methylene protons at δ 1.83 and 1.53 ppm (*d*) and (*e*), and the

tert-butyl protons at δ 1.43 ppm (*f*). The ratio of the sum of the peak areas (c) to (f) to the peak area (*a*) yielded $\bar{M}_n$ = 1660 g·mol^{-1} ($\bar{X}_n$ = 13), which is identical to $\bar{M}_n$ obtained by SEC analysis. Additionally, the peak area ratio for the methoxy proton at δ 3.63 ppm (*b*) to (*a*) is exactly 1/3, indicating the termination of every polymer chain with an ω–bromine group.

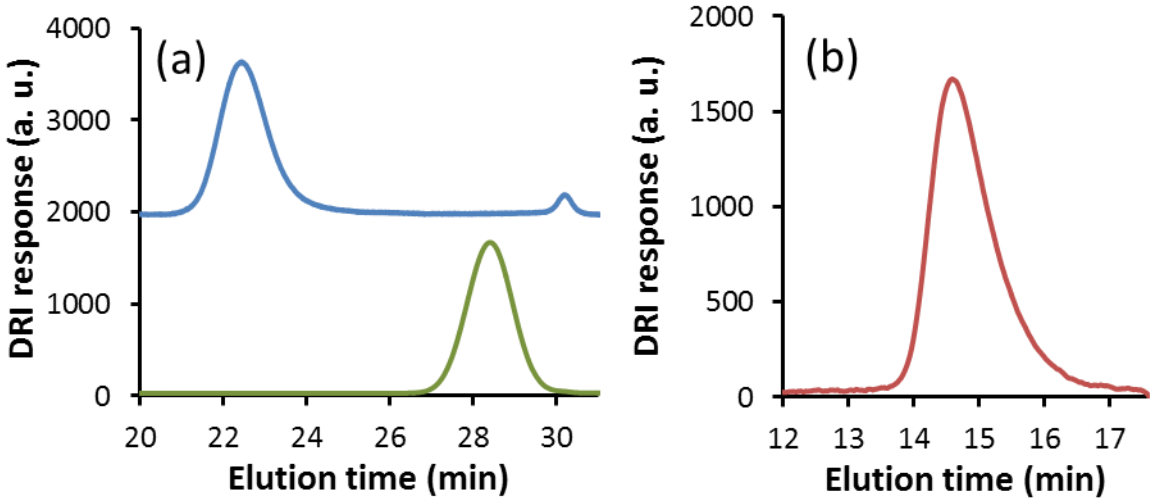

Figure 5.1 Size-exclusion chromatograms for (a) P*t*BA (bottom), and P*t*BA-*b*-PHEA-TMS (top) in THF, and (b) PAA-*b*-PHEA in DMSO-LiCl (1 g·mL^{-1}).

The secondary bromine end-group allowed further reaction of the oligomer, as a macroinitiator, for the preparation by ATRP of a block copolymer. HEA was first protected with a trimethylsilyl group as shown in Scheme 5.3, to limit the occurrence of side reactions and promote higher conversions (vide infra).[42,43]

The synthesis of P*t*BA-*b*-(PHEA-TMS), illustrated in Scheme 5.4, was performed with the same catalyst system employed in the preparation of P*t*BA; however, acetone was not required in that case, as the CuBr/PMDETA complex was soluble in the reaction

medium. The polymer obtained, based on a PS standard calibration, had $\bar{M}_{n,}$ = 28,000 g·mol^{-1} (corresponding to 141 HEA-TMS repeat units) and $\bar{M}_n \cdot \bar{M}_w^{-1}$ = 1.18. The SEC chromatograms shown in Figure 5.1 confirm the narrow size distribution of the polymers obtained and the increase in molar mass after the second polymerization reaction.

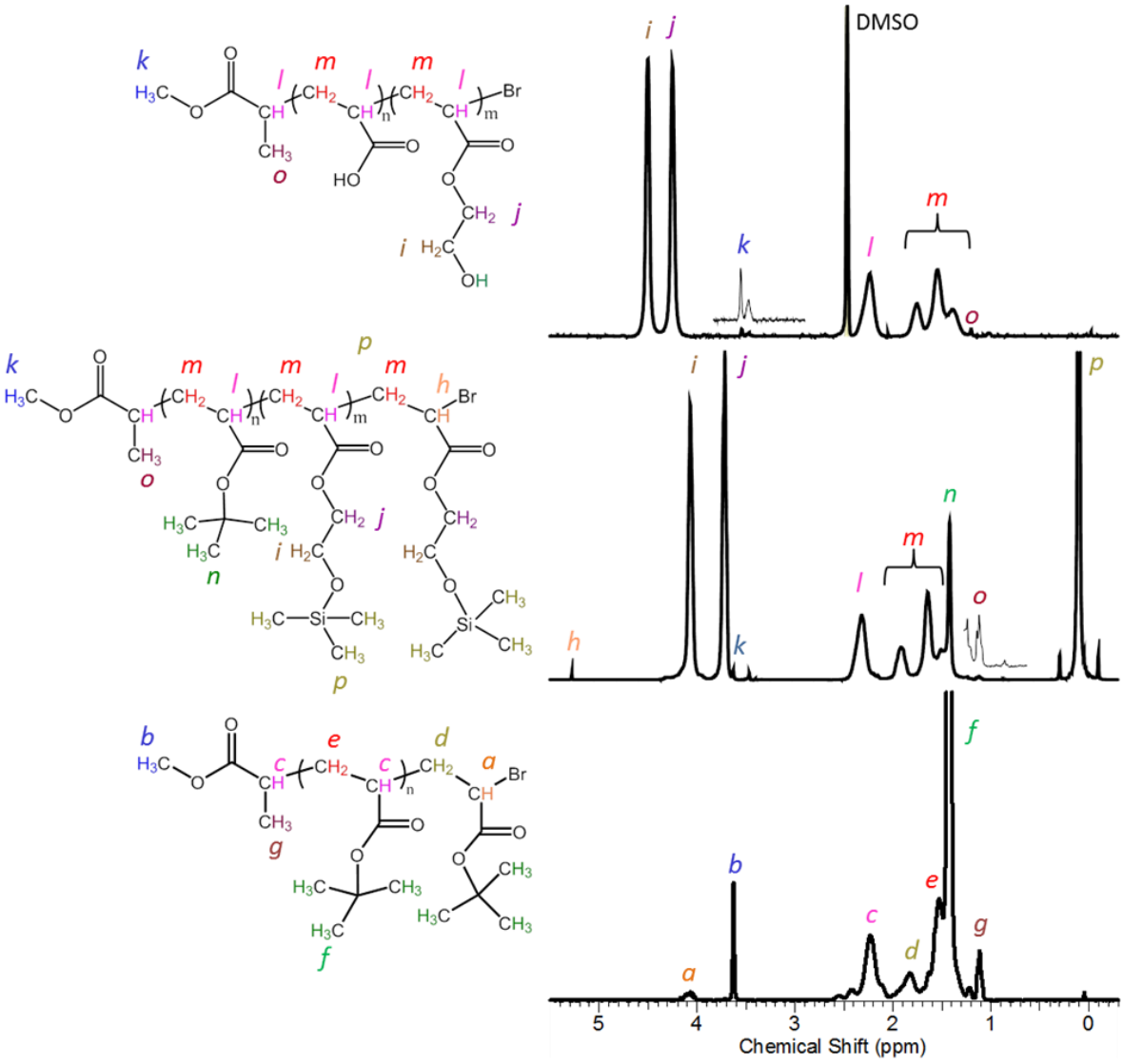

Figure 5.2 ^{1}H NMR (300 MHz) spectra for P*t*BA, P*t*BA-*b*-P(HEA-TMS) in $CDCl_3$, and PAA-*b*-PHEA in DMSO-d_6 (from bottom to top).

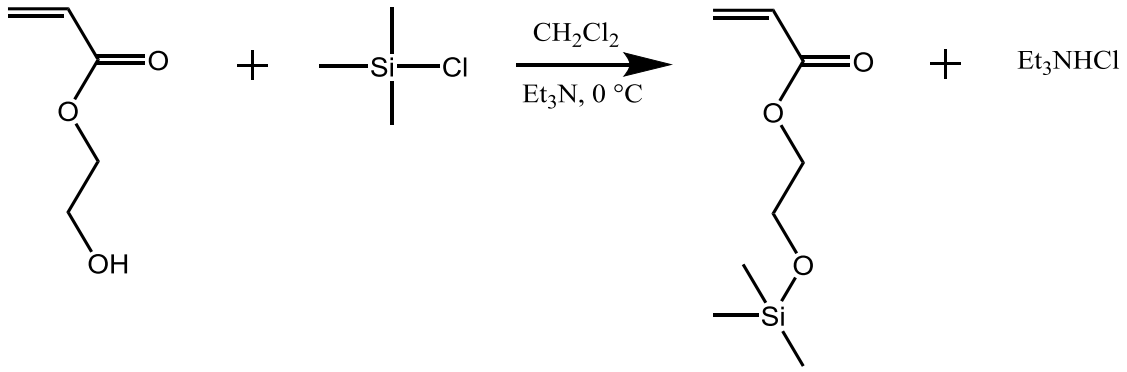

Scheme 5.3 Silylation of HEA.

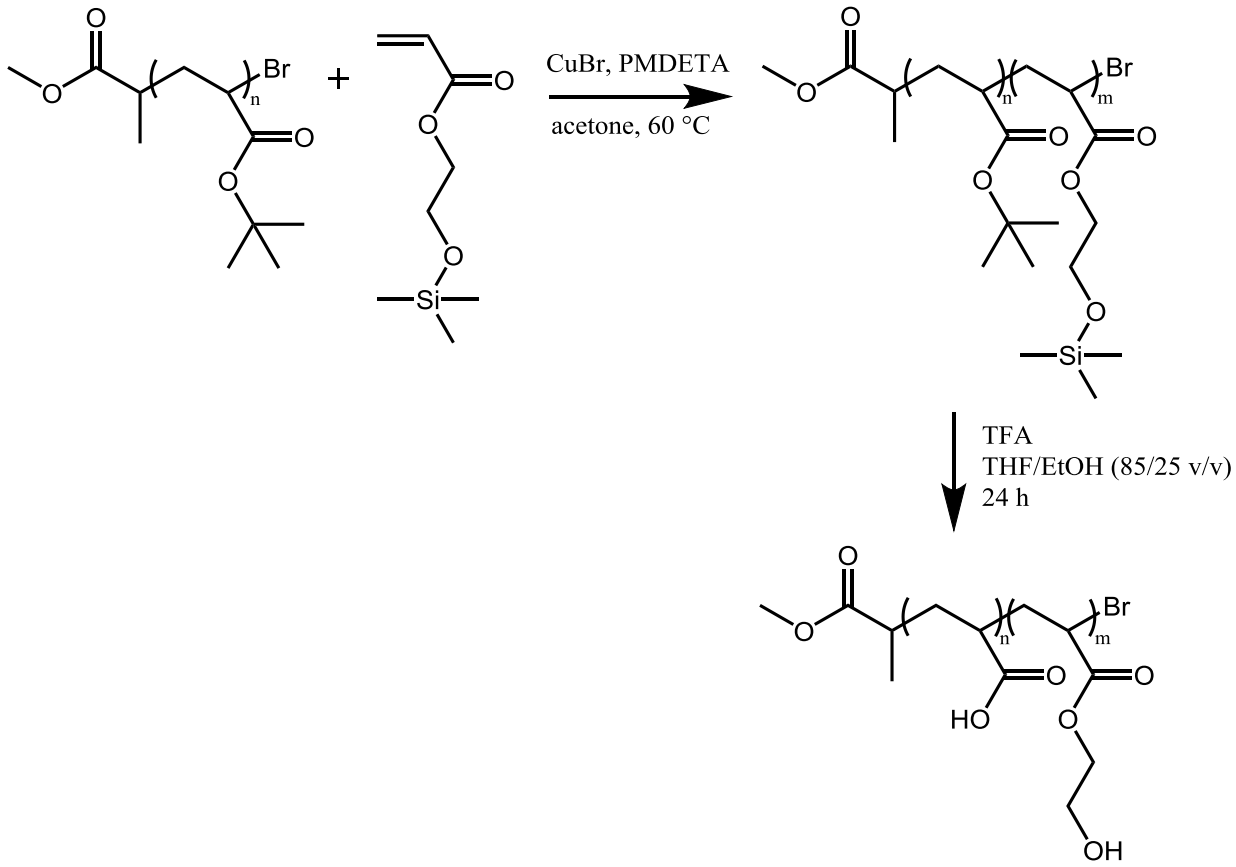

Scheme 5.4 Synthesis of P*t*BA-*b*-PHEATMS via ATRP and deprotection with TFA to yield PAA-*b*-PHEA.

Characterization of the copolymer by ^{1}H NMR,[37,41] shown in Figure 5.2, clearly reveals the presence of the methylene protons for the HEA-TMS block at δ 3.71 (*i*) and 4.07 ppm (*j*), as well as the trimethylsilyl protons at δ 0.10 ppm (*p*). The peaks corresponding to the methyl groups at δ 1.11 ppm (*o*), and the methine group geminal to the bromine atom at δ 5.28 ppm (*h*) are also observed and can be used for the determination of the absolute number-average degree of polymerization. From the ratio of the peak areas for (*p*) to (*o*), the calculated $\bar{M}_n$ was 28,140 g·mol^{-1}, which is similar to the value obtained by SEC analysis.

The direct synthesis of P*t*BA-*b*-PHEA was also attempted by ATRP, by reacting the P*t*BA macroinitiator with the HEA monomer under the same conditions employed for the HEA-TMS monomer (Section 5.3.4). Although the molar mass of the copolymer ($\bar{M}_{n,app}$ = 29,700 g·mol^{-1}) was comparable to the silylated copolymer, a broader size distribution ($\bar{M}_n \cdot \bar{M}_w^{-1}$ = 1.34) and gel formation also resulted. Similar observations and limited monomer conversions (<50%) have been reported previously in the ATRP of HEA.[42,43] Reactions with the protected monomer were therefore preferred.

The hydrolysis of both the *t*BA and TMS pendant groups was accomplished by reacting the copolymer with an excess of TFA in a THF/ethanol (15/85 v/v) mixture for 24 h. The acid was removed by evaporation and azeotropic distillation under reduced pressure, and the polymer further purified by dialysis. The latter step was found to be essential for the complete removal of TFA, as confirmed by the absence of a resonance at δ -75.0 ppm in ^{19}F NMR analysis. As shown in Figure 5.2, quantitative removal of the *tert*-butyl group was evidenced by ^{1}H NMR analysis in DMSO-d_6, and the absence of a peak at δ 1.43 ppm (*f*). The labile TMS group was likewise readily hydrolyzed by TFA, as indicted by the

disappearance of the resonance at δ 0.10 ppm (*p*) in Figure 5.2. After the deprotection reaction the size distribution remained relatively narrow ($\bar{M}_n \cdot \bar{M}_w^{-1}$ = 1.29), as seen on the SEC chromatogram obtained in DMSO (Figure 5.1). The apparent molar mass ($\bar{M}_{n,app}$ = 96,800 g·mol^{-1}) was however larger than for the protected polymer by a factor of about 3.5. Matyjaszewski et al. reported a similar increase, by a factor of 2-3, in the apparent molar mass of P(HEA-TMS) after deprotection when measured by SEC analysis in DMF, as well as broader size distributions.[41,42] The formation of secondary structures (aggregates) in DMF was hypothesized by this group to account for the broader mass dispersities.[42] It is expected that a comparable difference exists in DMSO between the hydrodynamic volume of PAA-PHEA and PS chains with an equivalent molar mass, which renders the PS standards calibration inappropriate for the analysis. From end-group analysis by ^{1}H NMR, the calculated $\bar{M}_{n,NMR}$ = 18,500 g·mol^{-1} – corresponding to 152 HEA repeat units, and obtained from the ratio of the peak area (*j*) to (*k*) – compares well with the value obtained for the protected polymer.

5.4.2 Polyion complex micelles

5.4.2.1 PAA-*b*-PHEA in ethanol

As a hydrophilic copolymer, PAA-*b*-PHEA is soluble in aqueous media without micelle formation.[78] The DHBC synthesized was also soluble in ethanol at 25 °C at a concentration of 5.9 mg·mL^{-1}, with a single size population having a hydrodynamic diameter of 6.4 ± 1.5 nm measured by DLS on a volume basis (Figure 5.3b), while 2 populations were detected on an intensity basis (Figure 5.3a).

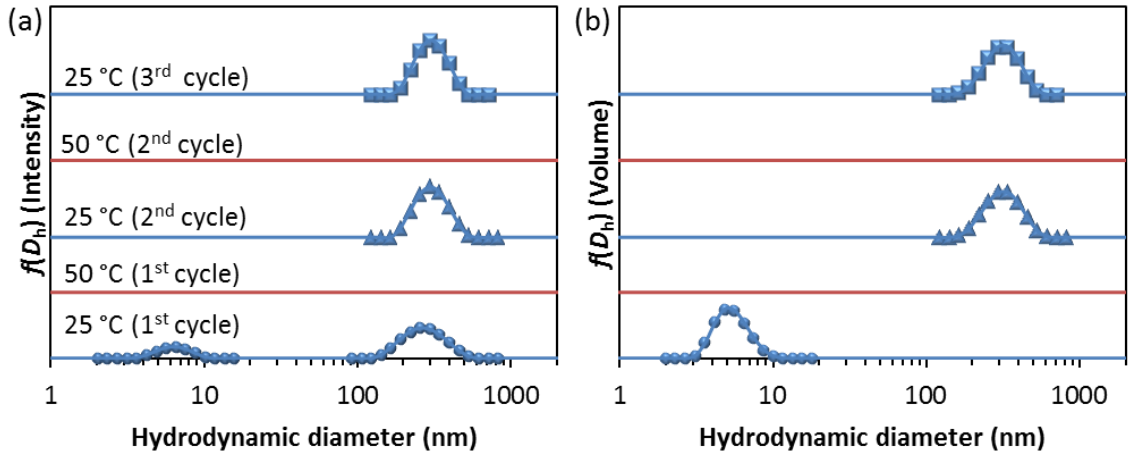

Figure 5.3 Temperature dependence of the (a) intensity- and (b) volume-weighted hydrodynamic diameter distributions for PAA_{13}-*b*-$PHEA_{140}$ in ethanol (5.9 mg·mL^{-1}).

The molecular dimensions for the smaller population are comparable to the hydrodynamic diameter calculated for a chain with restricted bond rotations, $D_{h,calc}$ = 6.2 nm, as delineated in Appendix A5.2. The aggregates with D_h = 280 ± 84 nm observed in the intensity-weighed distributions (Figure 5.3a) are absent in the volume distributions shown in Figure 5.3b, and the photon counting rate was low during the acquisition (21 kilocounts per second – kc·s^{-1}). It can therefore be inferred that a very small amount of aggregates exist in the sample at 25 °C. The contribution from large particles in intensity-weighted distributions is dominant, as it is proportional to D_h^{6}.[79] The aggregates dissociated when the temperature was increased to 50 °C, and a homogeneous solution resulted as evidenced by the absence of scattered light (Figure 5.3). By cooling to 25 °C micelle formation was promoted, and aggregates with D_h = 273 nm and a size dispersity $Đ_p$ (μ_2/Γ^2) = 0.15 were obtained by

cumulants analysis of the DLS signal. The photon count rate also increased to 252 kc·s^{-1}. The micelles dissociated readily when the solution was warmed again to 50 °C, and reformed at 25 °C with a comparable size (D_h = 282 nm) and a somewhat narrower size distribution ($Đ_p$ = 0.09).

Although both polymer blocks are soluble in ethanol,[35,80] it can be argued that the poly(acrylic acid) block had less favorable interactions with the solvent molecules than PHEA. Calculations of the interaction parameters between PAA and ethanol, χ_{PAA} = 0.42, and PHEA and ethanol, χ_{PHEA} = 0.33, were performed using the Hansen solubility parameters of the solvent and the polymers blocks as detailed in Appendix A5.3. Both values satisfy the Flory-Huggins condition, ($\chi \leq 0.5$)[81] for polymer-solvent miscibility. The lower value of χ_{PHEA} suggests better solvency for PHEA than for PAA in ethanol, however. As a matter of fact, limited solubility of high molar mass PAA in the acid form has been reported in ethanol.[82] Additionally, the segregation of block copolymers in common good solvents has been observed for various poly(meth)acrylate copolymers by AFM and viscometry measurements. In these systems, transitions between segregated conformations and pseudo-Gaussian (non-segregated) conformations was induced by a change in temperature over a narrow range.[83–85] For the PAA_{13}-*b*-$PHEA_{140}$ copolymer, comparable molecular segregation induced by conformational transitions below a critical temperature in the 25-50 °C range may also account for the low aggregation level observed.

Hydrogen bonding between the carboxylic acid groups of the PAA segments and the hydroxyl groups of the PHEA segments is also expected to contribute to aggregate formation. Hydrogen bonding between hydroxyl groups and carbonyl groups, as well as between the

hydroxyls groups of PS-*b*-PHEA[86] and PHEMA[87] was indeed evidenced by FTIR measurements on films deposited from chloroform and methanol solutions, respectively.

The influence of the solvent on intermolecular association in solution is also important.[88,89] Aliphatic alcohols such as ethanol may favor polymer aggregation due to their lower hydrogen bonding ability than the polymer.[89–91] The dielectric constant ε of solvents is useful to evaluate the strength of polymer-solvent interactions. For protic solvents, a lower ε reflects decreased hydrogen-bonding ability between the solvent molecules and increased interactions between the polymer and the solvent.[89] Since increasing the temperature from 25 to 50 °C decreases the dielectric constant of ethanol from ε = 24.43 to 20.78,[92] greater interactions between the polymer chains and ethanol are expected at higher temperatures,[89] thereby favoring aggregate dissociation as observed experimentally (vide supra).

5.4.2.2 Polyion complex micelles in ethanol

5.4.2.2.1 Room temperature

Characterization of the arborescent copolymers in ethanol by DLS yielded D_h values ranging from 14.2 to 112 nm, as shown in Table 5.2 and Figure 5.4. The size of the arborescent macromolecules determined on the Zetasizer Nano was comparable to the results obtained on a Brookhaven BI-2030AT 201 instrument, reported in Chapter 3. The size distribution was narrow for all the arborescent copolymers investigated (*Gn*PS-*g*-P2VP, with n = [0,2]), with $Đ_p < 0.1$. The comb-branched copolymer had a slightly broader size distribution, with $Đ_p = 0.23$, suggesting a low level of aggregation in the alcoholic solvent.

This is attributed to the relatively open structure of the comb (*G*0 overall) copolymer as compared to the arborescent copolymers (*G*1 ≥ 1 overall).[57]

After the addition of 10 mass equivalents of PAA_{13}-*b*-$PHEA_{140}$ to the arborescent copolymers in ethanol the solutions turned opalescent, indicating the rapid formation of larger polymer complexes in solution. This composition corresponds to a molar ratio of acrylic acid to 2-vinyl pyridine units, n_{AA}/n_{2VP}, ranging from 1.2 to 1.4 for the *Gn*PS-*g*-P2VP series with *n* = -1 to 2 respectively, i.e. mixing ratios f_+ = 0.45 to 0.42, respectively; f_+ being the fraction of positively ionizable monomers n_{2VP} in the mixture:[10]

$$f_+ = \frac{n_{2VP}}{n_{2VP} + n_{AA}} \tag{5.14}$$

Table 5.2 Hydrodynamic diameter and size dispersity of PAA-*b*-PHEA, *Gn*PS-*g*-P2VP, and *Gn*PS-*g*-P2VP/PAA-*b*-PHEA complexes in ethanol measured by DLS.[a]

Generation number (*n*)	PAA-*b*-PHEA[b]		*Gn*PS-*g*-P2VP		*Gn*PS-*g*-P2VP/ PAA-*b*-PHEA (25 °C, initial)[c]		*Gn*PS-*g*-P2VP/ PAA-*b*-PHEA (25 °C, final)[d]	
	D_h (nm)	$Đ_p$	D_h (nm)	$Đ_p$	D_h (nm)	$Đ_p$	D_h (nm)	$Đ_p$
-1	6.4	0.13	14.2	0.23	488	0.17	817	0.08
0	6.4	0.13	32.3	0.09	258	0.01	180	0.10
1	6.4	0.13	57.3	0.04	354	0.03	348	0.13
2	6.4	0.13	111.7	0.06	132	0.03	169	0.03

[a] Z-average diameter and size dispersity ($Đ_p$) from cumulants analysis. [b] From NNLS analysis. [c] For freshly prepared complexes at 25 °C. [d] After heating to 50 °C and cooling to 25 °C.

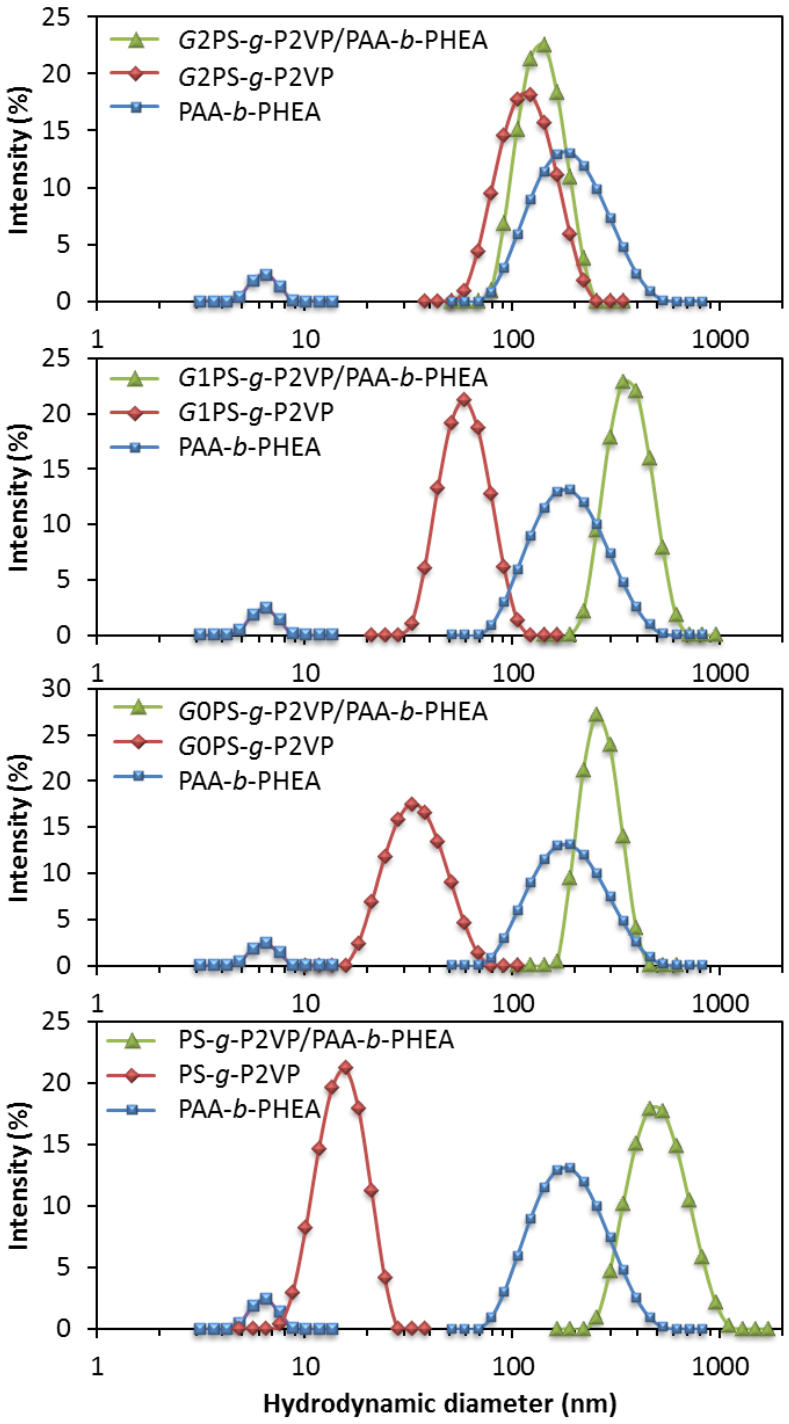

Figure 5.4 Size distributions for PAA-*b*-PHEA (2.5 mg·mL^{-1}), PS-*g*-P2VP (3 mg·mL^{-1}), *Gn*PS-*g*-P2VP, *n* = [0,2] (0.1 mg·mL^{-1}), and *Gn*PS-*g*-P2VP/PAA-*b*-PHEA, *n* = [-1,2] (0.1 mg·mL^{-1}/1.0 mg·mL^{-1}) PIC micelles in ethanol at 25 °C.

It is expected that interaction between the P2VP and the PAA segments should occur rapidly in solution through hydrogen bonding and electrostatic interactions. Although hydrogen bonding between the 2VP units and PHEA is possible, the strong interactions between the polyacid and the polybase should dominate complex formation. This mechanism is akin to the rapid interactions reported by Matějíček et al. between P2VP and polystyrene-*block*-poly(methacrylic acid) in a 1,4-dioxane/water mixture,[93] or between PS-*b*-PAA and PEG-*b*-P4VP in ethanol by Zhang et al.[94] This mechanism was also suggested for complex formation between PEG-*b*-PAA and PS-*b*-P4VP in ethanol.[16] Zhou et al. presented evidence for the formation of hydrogen bonds and ionic interactions between P2VP and PAA by FTIR and XPS analysis, for powders precipitated from water/ethanol solutions.[18] In the present study, the PAA chains were assumed to penetrate the P2VP corona of the arborescent copolymers in ethanol to form compact interpolymer complexes as illustrated in Scheme 5.1. Characterization results for the solutions by DLS, provided in Table 5.2 and Figure 5.4, indicate the presence of large aggregates with hydrodynamic diameters ranging from 132 to 488 nm. The size of the aggregates for *Gn*PS-*g*-P2VP (n = -1 to 2) increased by factors of 34, 8, 6, and 1.2, respectively, in comparison to the size of the arborescent copolymers alone. The size distribution remained narrow for all the aggregates, with $Đ_p \leq 0.03$, although a broader size distribution was again observed for the comb-branched copolymer ($Đ_p = 0.17$). An estimate of the overall D_h of the micelles formed by complexation of one layer of PAA-*b*-PHEA can be made on the basis of a low surface coverage approximation (mushroom regime). In this regime, the chains in the corona adopt a distribution approximating their preferred random-coil conformation, measured to be 6.4 ± 1.5 nm by DLS for PAA-*b*-PHEA

in ethanol (vide supra). The aggregation numbers (number of polyion complex micelles per aggregate; calculated by assuming spherical morphologies) are reported in Table 5.3, and strongly suggest the presence of supramolecular aggregates. The aggregation number decreases from 5890, 187, 129 to 1 for the *G*0 to *G*3 complexes, respectively. Similar calculations on the basis of a high-density surface coverage (brush regime) can be made by estimating the chains dimension as the fully-extended length (38.5 nm). The aggregation numbers in this case are about 3 to 38 times lower (Table 5.3). It is noteworthy that the aggregation number decreases with the generation number. For complexes formed by the *G*3 copolymer, D_h approaches the values calculated for the mushroom regime. Complexes with the *G*0 copolymer formed significantly larger aggregates in ethanol, suggesting poor steric stabilization. This trend correlates with the rigidity of the arborescent structures, and reveal the influence of the generation number on the stability of the interpolymer complexes and their aggregation: Increased rigidity of the PIC micelles favored greater colloidal stability and limited the formation of multi-molecular aggregates.

The narrow size distributions for complexes of arborescent copolymers *G*1 to *G*3 ($Đ_p \leq 0.03$) hint at the formation of supramolecular aggregates according to a closed association model. According to this model, a dynamic equilibrium exists in solution between aggregated and non-aggregated species, the former being characterized by a uniform size distribution.[95] As shown in Figure 5.5, the relative independence of D_h for the aggregates of *G*1/PAA-*b*-PHEA complexes on the concentration below 0.13 $mg \cdot mL^{-1}$ is further indication of a closed association mechanism. Deviations from the model are however noted at higher concentrations, with broadening of the size distribution.

Table 5.3 Calculated hydrodynamic diameters and aggregation numbers for *Gn*PS-*g*-P2VP/PAA-*b*-PHEA complexes in ethanol, assuming low-density (mushroom regime) and high-density (brush regime) surface coverages.

Generation number (*n*)	D_h measured[a] (nm)	D_h calculated (nm)[b]		Aggregation number[c]	
		Mushroom regime	Brush regime	Mushroom regime	Brush regime
-1	488	27	91	5890	153
0	258	45	109	187	13
1	354	70	134	129	18
2	132	125	189	1	0.3

[a] From DLS analysis (Table 5.2). [b] $D_h = D_h(Gn) + 2 \times D_h$(PAA-*b*-PHEA). [c] $[(4\pi/3) \times (0.5 \times D_{h,calculated})^3]/[(4\pi/3) \times (0.5 \times D_{h,measured})^3]$.

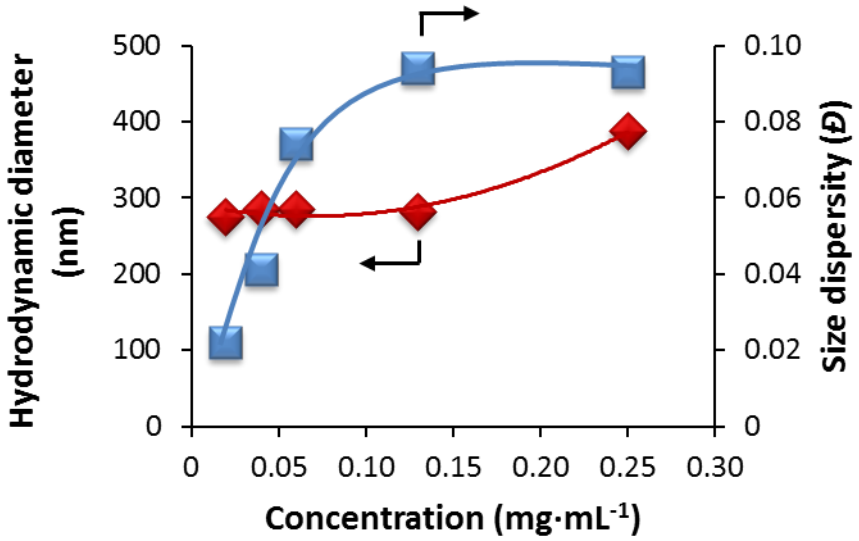

Figure 5.5 Hydrodynamic diameter and size dispersity for the *G*0PS-*g*-P2VP/PAA-*b*-PHEA complexes as a function of the concentration of *G*0PS-*g*-P2VP. In all cases $m_{G0PS\text{-}g\text{-}P2VP}/m_{PAA\text{-}b\text{-}PHEA}$ = 1/10.

5.4.2.2.2 Critical temperature

The temperature dependence of the supramolecular aggregate diameter in ethanol was monitored by DLS. Figure 5.6 depicts the variations in size and scattered intensity upon heating from 25 to 50 °C, and then cooling back to 25 °C, for the different samples.

For all the complexes investigated, a large drop in D_h and scattered intensity was observed upon reaching a critical temperature T_c. The size distributions of the aggregates in the vicinity of T_c are also depicted in Figure 5.6 (left). Most multi-molecular aggregates dissociated at $T_{c,\ heating}$ = 35 °C, while $T_{c,\ heating}$ = 40 °C was obtained for the *G2* arborescent copolymer (Figure 5.6f). Interpolymer complex and multi-molecular aggregate formation relies on two opposite contributions to the Gibbs free energy of mixing, viz. (i) a favorable enthalpy of mixing driven by acid/base interactions and hydrogen bonding, and (ii) an unfavorable entropy of mixing stemming from constrained chain conformation.[87] An increase in solvent quality for the PAA and PHEA segments as the temperature was raised may account for the dissociation observed above T_c, by lowering the contribution of the negative enthalpic term. The aggregates formed by *G*2 and *G*3 complexes recovered their size as the temperature was decreased below $T_{c,\ cooling}$ = 35 °C. The multi-molecular species formed by *G*0 and *G*1 were larger and smaller, respectively, as the temperature returned to 25 °C. Apart from *G*1PS-*g*-P2VP, which displayed a T_c differing by 5 °C upon heating and cooling, both the hydrodynamic diameter and scattered intensity of the aggregates were generally reproducible in cooling the solutions. This behavior is suggestive of good thermodynamic stability of the complexes and illustrates the rapid and reversible response of the aggregates

to temperature changes. The hysteresis observed for the second generation polymer may be explained in terms of the structure rigidity of the arborescent copolymer as discussed below.

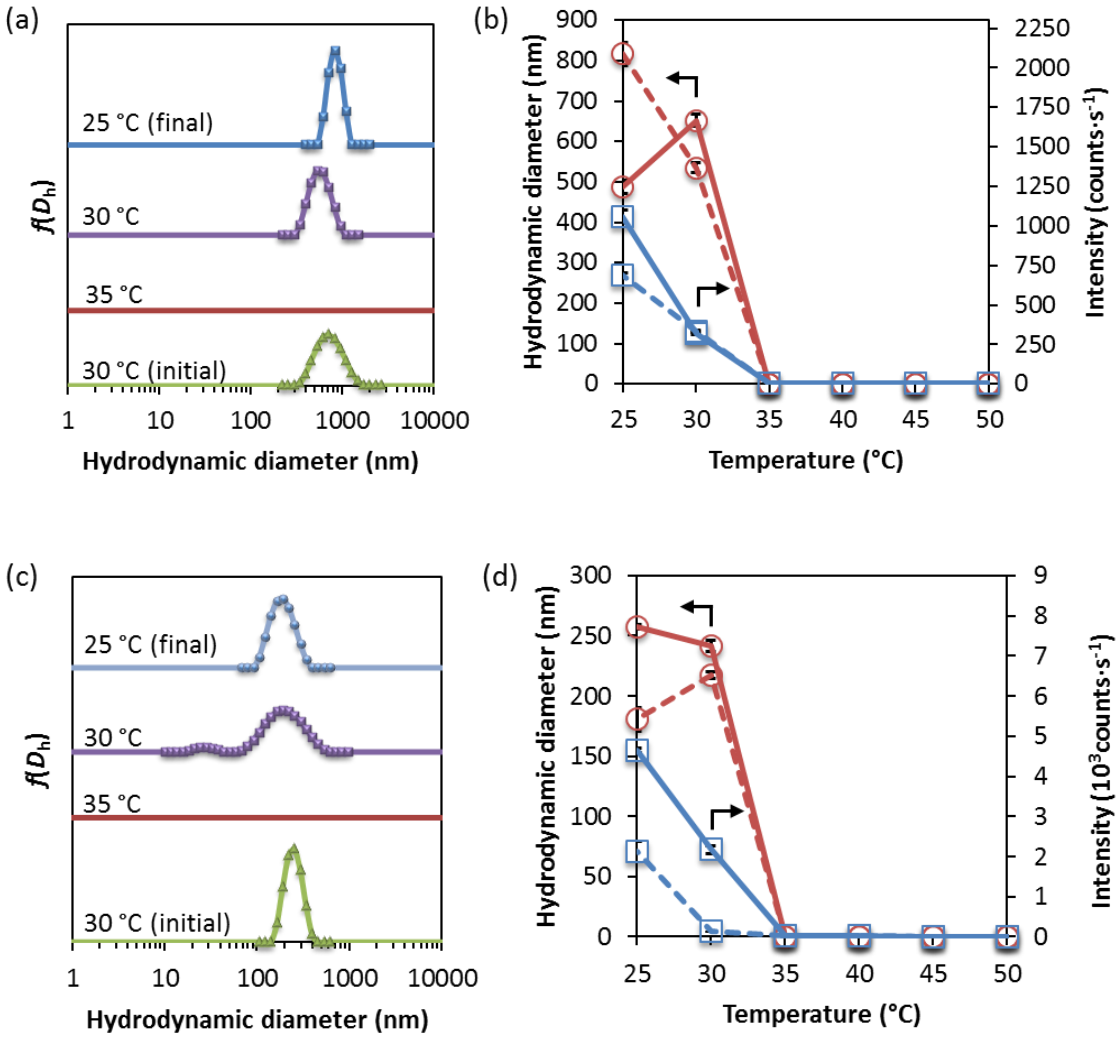

Figure 5.6 Size distributions for PAA-*b*-PHEA in ethanol in the presence of (a) PS-*g*-P2VP and (c) *G*0PS-*g*-P2VP near the critical temperature. The corresponding plots of the hydrodynamic radii (circles) and scattered intensity (in counts per seconds, squares) when heating from 25 °C to 50 °C (solid line), and then cooling back to 25 °C (dotted line), are shown on the right (b and d, respectively). In all cases $m_{G0PS\text{-}g\text{-}P2VP}/m_{PAA\text{-}b\text{-}PHEA}$ = 1/10, and *G*0PS-*g*-P2VP concentration *c* = 0.1 mg·mL^{-1}. (*continued*)

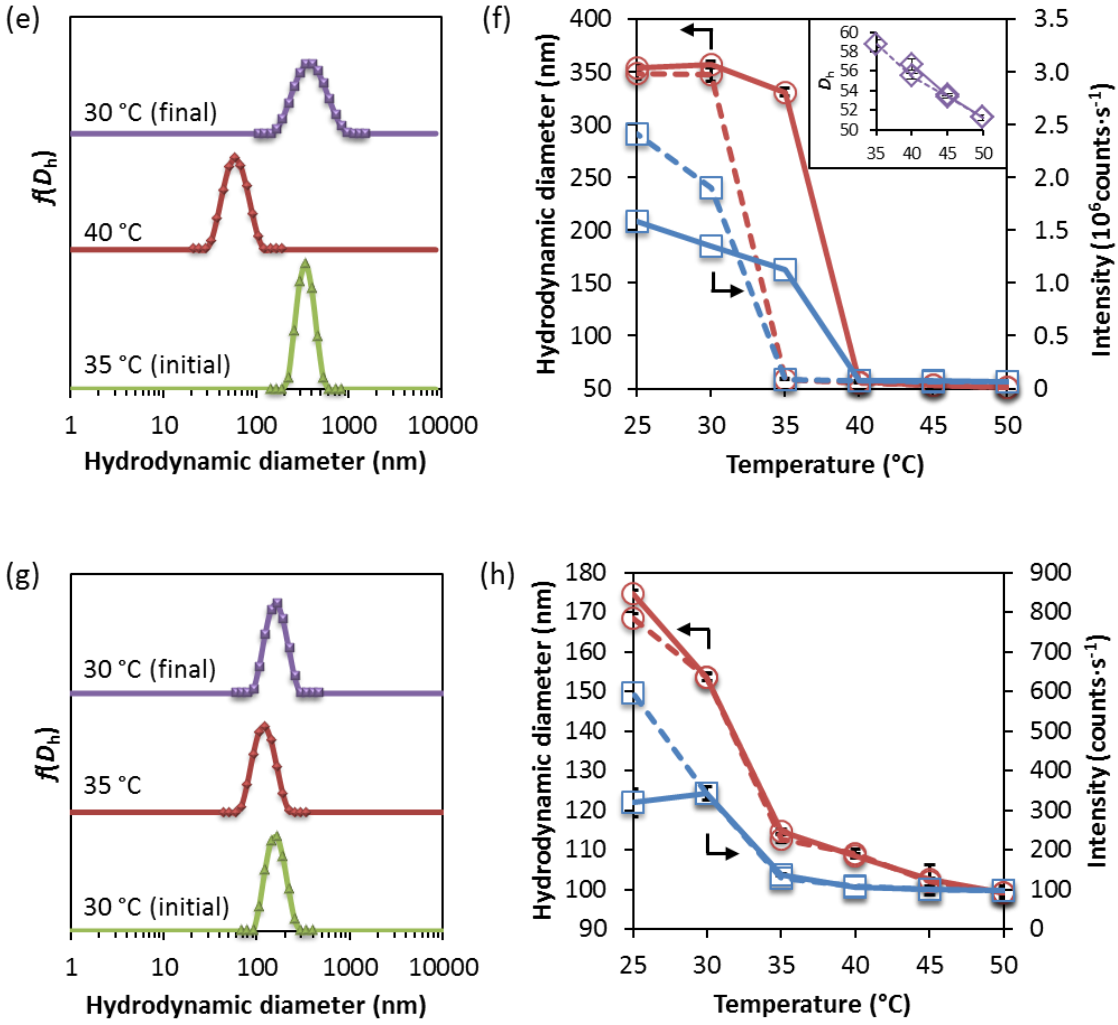

Figure 5.6 (*continued*) Size distributions for PAA-*b*-PHEA in ethanol in the presence of (e) *G*1PS-*g*-P2VP, and (g) *G*2PS-*g*-P2VP near the critical temperature. The corresponding plots of the hydrodynamic radii (circles) and scattered intensity (in counts per seconds, squares) when heating from 25 °C to 50 °C (solid line), and then cooling back to 25 °C (dotted line), are shown on the right (f and h, respectively). In all cases $m_{G0PS\text{-}g\text{-}P2VP}/m_{PAA\text{-}b\text{-}PHEA}$ = 1/10, and *G*0PS-*g*-P2VP concentration c = 0.1 mg·mL^{-1}.

5.4.2.2.3 PS-*g*-P2VP/PAA-*b*-PHEA complexes

As illustrated in Figure 5.6a and Figure 5.6b, the light scattering intensity from a mixture of PS-*g*-P2VP and PAA-*b*-PHEA became negligible when the temperature reached T_c = 35 °C. When taking into account the influence of the temperature dependence of d*n*/d*c* and the refractive index of the solvent on the scattered intensity, the intensity would be expected to decrease by about 9%;[68,96] while a drop by over 98% was observed experimentally, clearly indicating dissociation of the multi-molecular aggregates in solution. Because of the relatively low molar mass of the individual polymeric components, no significant scattering was detected at arborescent copolymer and DHBC concentrations in ethanol of 0.09 mg·mL^{-1} and 0.9 mg·mL^{-1}, respectively (Figure 5.6a, and Figure 5.6c).

It is noteworthy that the scattered intensity for the PS-*g*-P2VP/PAA-*b*-PHEA solution only decreased by about 2/3 from 25 to 30 °C, hinting at the presence of residual aggregates of lower mass at the higher temperature, while D_h increased by about 1/3 (from 488 to 653 nm). One can expect that the relatively open structure of the (comb-branched) *G*0 copolymer led to the formation of poorly stabilized multi-molecular aggregates at 25 °C. Upon increasing the temperature and the solvent quality for PAA-*b*-PHEA, the dissociation of a fraction of the chains occurred and less compact aggregates resulted. Rearrangements may also have occurred between the PAA-*b*-PHEA chains and the outer 2VP shell, leading to aggregates with a lower aggregation number (i.e., overall mass). A similar mechanism involving partial dissociation and rearrangement was invoked by Topouza et al. to account for the behavior of PS-*b*-P2VP/PMAA complexes in 1,4-dioxane as a function of temperature.[97] While the initial scattered intensity was recovered upon cooling the solution

from 35 to 30 °C, multi-molecular aggregates with lower D_h and narrower size distributions resulted (D_h = 653 nm, $Đ_p$ = 0.16 initially versus D_h = 535 nm, $Đ_p$ = 0.08 upon cooling). Further cooling to 25 °C yielded larger aggregates with a narrower size distribution (D_h = 817 nm, $Đ_p$ = 0.08) and a slightly lower scattering intensity (1058 kc·s^{-1} initially versus 787 kc·s^{-1}). This can be explained by rapid cooling favoring the formation of larger but less compact aggregates, as thermodynamic equilibrium was not achieved under these conditions.

5.4.2.2.4 *G*0PS-*g*-P2VP/PAA-*b*-PHEA complexes

As shown in Figure 5.6c and Figure 5.6d, the *G*0PS-*g*-P2VP/PAA-*b*-PHEA system also displayed a critical temperature T_c = 35 °C above which complete dissociation of the aggregates occurred. A bimodal particle size distribution was noted as T was lowered to 30 °C. A population with a relatively large D_h (190 nm) corresponds to supramolecular micelles, while the second population with D_h = 28.2 nm is for individual interpolymer complexes. The size of the PIC micelles was comparable to that of the substrate at this temperature (D_h(*G*1) = 32.3 nm). A 53% drop in scattered intensity for *G*0PS-*g*-P2VP/PAA-*b*-PHEA was also noted from 25 to 30 °C, but the decrease in size of the aggregates was modest (6%). This suggests that the small complexes favored the formation of compact aggregates with a relatively low aggregation number in ethanol. While dissociation of the aggregates still occurred above T_c, only limited size variations were observed for these more rigid structures as the temperature was decreased below T_c. This is consistent with the compact structure of the PIC micelles limiting multi-molecular aggregate reformation. The monomodal particle size distribution obtained as the temperature was further decreased to 25

°C could be explained by redistribution of the hydrophilic chains, taking place through a fast insertion/ expulsion mechanism and a slower merging/splitting mechanism as proposed by Holappa et al.[98] The decreased scattering intensity at 25 °C also indicates a mass decrease for the aggregates in solution.

5.4.2.2.5 *G*1PS-*g*-P2VP/PAA-*b*-PHEA complexes

The aggregates of *G*1PS-*g*-P2VP and PAA-*b*-PHEA had a critical temperature $T_{c,\ heating}$ = 40 °C, above which D_h and the scattered intensity decreased by 83% and 93%, respectively (Figure 5.6e, and Figure 5.6f). This T_c is higher than for the other arborescent copolymers and suggests the formation of particularly stable aggregates with a compact structure, hindering their dissociation. Above $T_{c,\ heating}$, dissociated PIC micelles with a size ranging from 51.3 nm at 50 °C to 58.8 nm at 35 °C were detected by DLS (see inset of Figure 5.6f). The size measured from 40 to 50 °C was lower than for the substrate (D_h(*G*2) = 57.3 nm), which was independent of the temperature in that range. These results are in agreement with the more compact structure observed for the PIC micelles obtained with the *G*1 copolymer, decreasing in size as the temperature was increased. Interestingly a D_h = 58.8 nm, larger than for the substrate, was measured at $T_{c,\ cooling}$ = 35 °C in the cooling cycle, which is likely associated with the onset of multi-molecular aggregation. Hysteresis was noted upon cooling the solution, with supramolecular aggregates reforming at $T_{c,\ cooling} < T_{c,\ heating}$. As noted earlier, the denser structure of the larger PIC micelles may have hindered the reformation of supramolecular aggregates. Indeed, slow molecular rearrangements have been invoked to account for the hysteresis in temperature-responsive diblock PIC micelles.[99]

Below $T_{c,\ cooling}$, the size of the aggregates remained constant with a narrow size distribution (Table 5.2), although the scattered intensity continued to increase by 27% as presumably more PAA-*b*-PHEA chains diffused within the sterically hindered core of the polymer aggregates without affecting their overall size.

5.4.2.2.6 *G*2PS-*g*-P2VP/PAA-*b*-PHEA complexes

The critical aggregation temperature of the *G*2PS-*g*-P2VP/PAA-*b*-PHEA complexes was found to be T_c = 35 °C, lower than for the *G*2 ACP, suggesting the formation of less stable aggregates (Figure 5.6h). It can be inferred that the more compact *G*2PS core of the *G*3 copolymer hindered the diffusion of the PAA chains, such that complexation occurred mainly on the outside of the P2VP corona, leading to loosely bound block copolymer chains. Interestingly, upon heating from 25 to 30 °C a decrease in D_h from 175 to 154 nm was noted, while the size distribution remained narrow ($Đ_p$ = 0.04) and the scattered intensity was unchanged. This may hint at rearrangement of the multi-molecular aggregates as the temperature was increased, while a constant aggregation number (i.e., constant mass) was maintained. Above T_c the aggregates dissociated and the free *G*2PS-*g*-P2VP copolymer, with a size ranging from 115 nm at 35 °C to 99 nm at 50 °C and $Đ_p$ = 0.07, was observed by DLS (Figure 5.6g and h). As noted earlier, the size of the PIC micelles was lower than that of the substrate (D_h = 111.7 nm) at $T > T_c$ and decreased with increasing temperature. A slightly larger size was again observed at the onset of multi-molecular aggregation, i.e. $T = T_c$. By lowering the temperature below T_c, the aggregates reformed with identical sizes and narrow size distributions (Table 5.2). Interestingly, the scattered intensity continued to increase from

30 to 25 °C, possibly due to redistribution of the polymer chains and an increase in aggregation number after the temperature cycle.

5.4.2.3 Polyion complex micelles in water

5.4.2.3.1 Solution properties

In aqueous media, PAA_{13}-*b*-$PHEA_{140}$ is soluble without aggregate formation while the arborescent *Gn*PS-*g*-P2VP copolymers are insoluble. Water is indeed a good solvent under neutral conditions for both the PHEA and PAA segments,[80] the latter being a weak polyelectrolyte with a p*K*a of ca. 6.5.[100] Hydrogen bonding can occur between the carboxylic acid groups of PAA and the hydroxyl groups of PHEA, and a study by Mun et al. revealed a low complexation ability for PHEA with PAA in water.[101] Water is a non-solvent for the PS segments, while P2VP is a weak polyelectrolyte that is hydrophobic at pH > 4.8.[102] The addition of 10 mass equiv of DHBC to the arborescent copolymers (n_{AA}/n_{2VP} = 1.2–1.4, f_+ = 0.45–0.42) was first accomplished in ethanol as a common solvent, followed by progressive transfer to water by dialysis in water/ethanol mixtures, and then to pure water. Solubilization of the arborescent micelles in water was evidenced by the absence of precipitate, and the formation of clear and homogenous solutions.

As shown in Table 5.4 and Figure 5.7, characterization by DLS of the aqueous solutions revealed micelles with relatively broad size distributions ($Đ_p$ = 0.14–0.24) at 25 °C, with $D_h \approx 111$ nm for PS-*g*-P2VP to *G*1PS-*g*-P2VP. It is noteworthy that the D_h of the multi-molecular aggregates in water was much smaller than in ethanol and independent of the arborescent copolymer size. However the supramolecular micelles formed by *G*2PS-*g*-P2VP

in water were about 2.3 times larger than in ethanol, and 2.8 times larger than for the lower generation copolymer complexes in water. The high molar mass *G*2PS-*g*-P2VP apparently induced the formation of large aggregates. It should be noted that a solution of PAA_{13}-*b*-$PHEA_{140}$ (1 mg·mL^{-1}) in water did not yield any significant scattered intensity in DLS analysis.

Table 5.4 Hydrodynamic diameter and size dispersity for *Gn*PS-*g*-P2VP/PAA-*b*-PHEA aggregates in water and for *Gn*PS-*g*-P2VP in ethanol, measured by DLS.[a]

Arborescent PS core generation *Gn*	*Gn*PS-*g*-P2VP/PAA-*b*-PHEA (water)						*Gn*PS-*g*-P2VP (ethanol)	
	25 °C initial[b]		50 °C		25 °C final[d]		25 °C	
	D_h (nm)	$Đ_p$	D_h (nm)	$Đ_p$	D_h (nm)	$Đ_p$	D_h (nm)	$Đ_p$
*G*0	110	0.24	103	0.20	106	0.18	14.2	0.23
*G*1	114	0.18	81	0.13	129	0.04	32.3	0.09
*G*2	110	0.14	76	0.18	110	0.20	57.3	0.04
*G*3	306	0.17	105/464[d]	0.17/0.28[d]	281	0.20	111.7	0.06

[a] Z-average diameter (D_h) and size dispersity ($Đ_p$) from cumulants analysis. The concentrations of *Gn*PS-*g*-P2VP and PAA-*b*-PHEA were 0.1 and 1.0 mg·mL^{-1}, respectively. [b] Measurements at 25 °C for freshly prepared complexes. [c] Measurements at 25 °C after cycling the solution to 50 °C. [d] Hydrodynamic diameter and size dispersity ($Đ_p$) from NNLS analysis; bimodal distribution.

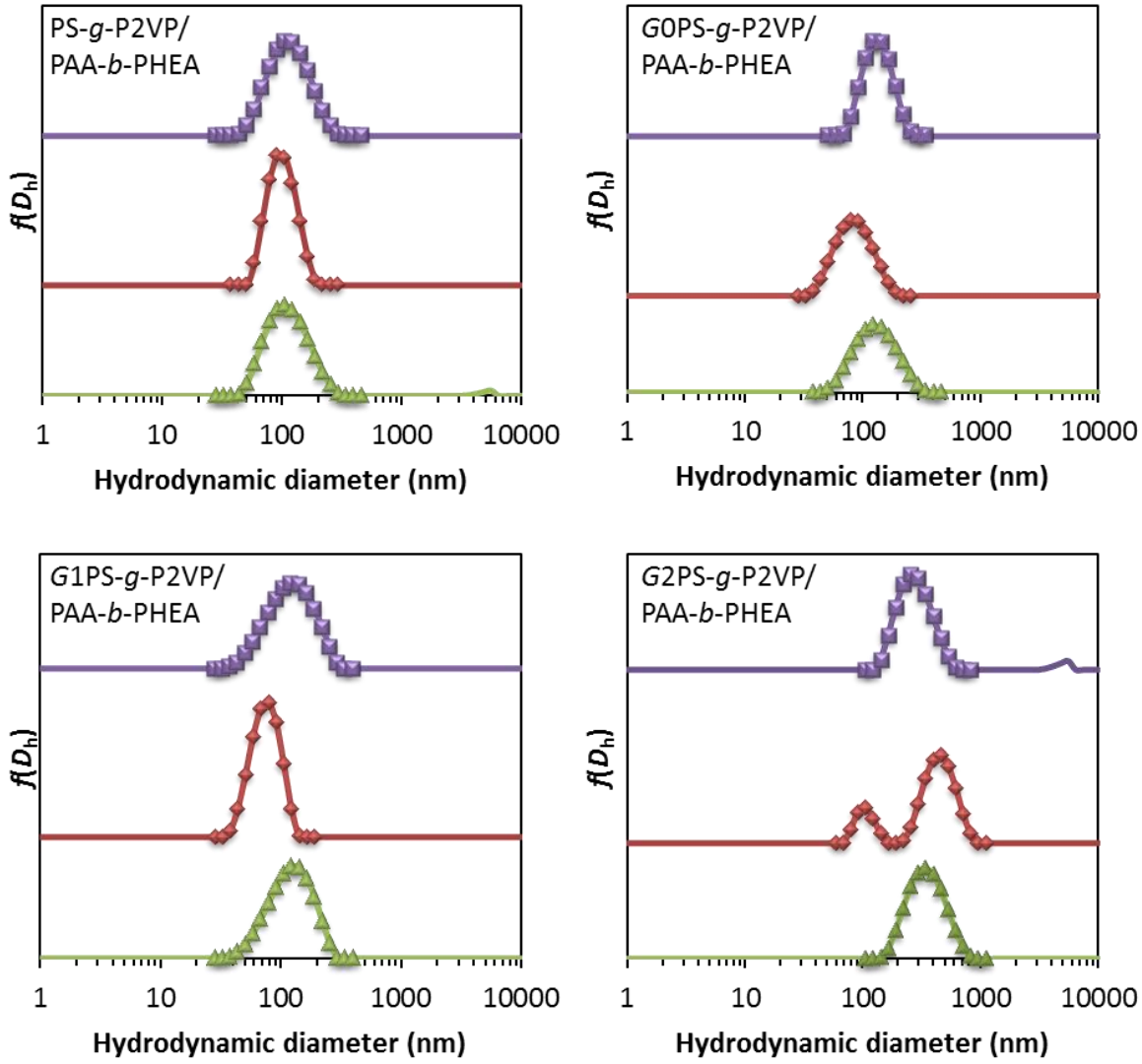

Figure 5.7 Size distributions for aqueous solutions of *Gn*PS-*g*-P2VP (*n* = [-1,2]) complexed with PAA-*b*-PHEA, obtained when heating from 25 °C (triangle) to 50 °C (diamonds), and then cooling back to 25 °C (squares). In all cases $m_{GnPS\text{-}g\text{-}P2VP}/m_{PAA\text{-}b\text{-}PHEA}$ = 1/10, and *Gn*PS-*g*-P2VP concentration *c* = 0.1 mg·mL^{-1}.

The size of the aggregates also varied with temperature in water, but no critical temperature was noted in the range of 25 to 60 °C. The monotonic decrease in D_h and size dispersity observed for the PS-*g*-P2VP/PAA-*b*-PHEA complexes are illustrated in Figure 5.8.

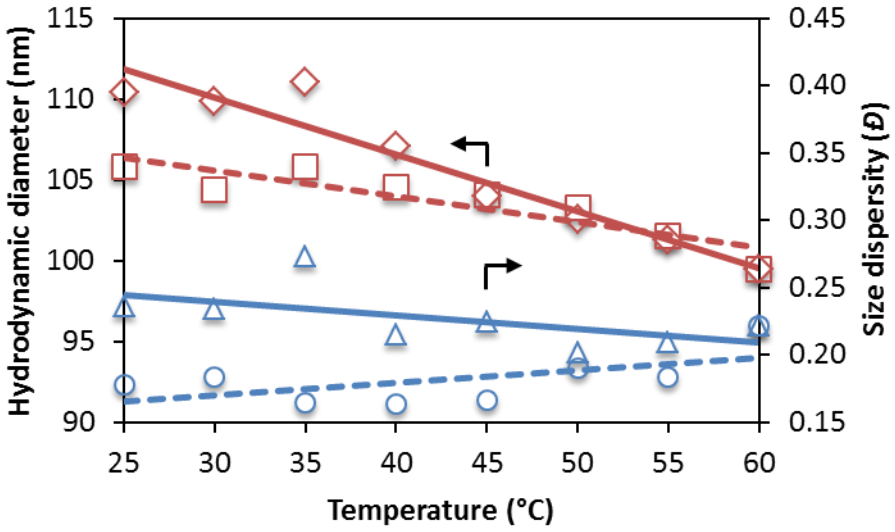

Figure 5.8 Hydrodynamic diameter and size dispersity ($Đ_p$) of PS-*g*-P2VP/PAA-*b*-PHEA in water as a function of the temperature, when heating from 25 to 60 °C (solid line) and cooling back to 25 °C (dashed line).

The size and size distributions of the supramolecular micelles formed by *Gn*PS-*g*-P2VP, with n = -1 to 1, and PAA-*b*-PHEA at 50 °C are also provided in Table 5.4 and in Figure 5.7. It can be seen that the size of the aggregates in water decreased by factors of 0.94, 0.71, and 0.69, for n = -1, 0, and 1, respectively after temperature cycling, corresponding to the order of increasing compactness of the arborescent copolymers as noted in ethanol. The intensity-weighted size distribution obtained for the *G*2PS-*g*-P2VP micellar structures had a bimodal distribution at 50 °C, with small (D_h = 105 nm) and larger aggregates (D_h = 464 nm)

identified by DLS. These results may be explained by enhanced collapse of the *Gn*PS-*g*-P2VP substrates in water as the temperature was increased. The larger aggregates formed by *G*2PS-*g*-P2VP were less stable, dissociating into smaller structures comparable in size to the PS-*g*-P2VP/PAA-*b*-PHEA complexes, and larger aggregates. The initial molecular dimensions were recovered (within experimental errors) for all the supramolecular aggregates as the temperature was brought back to 25 °C (Table 5.4 and Figure 5.8).

5.4.2.3.2 Solid state properties

The associative behavior of the polymers was further investigated by AFM imaging after deposition from the aqueous solutions onto freshly cleaved mica substrates. Even though the nature of the mica surface is very different from the solution state, AFM imaging has proved to be useful for the characterization of the size, size distribution, and secondary aggregation of interpolymer micelles.[103] As shown in Figure 5.9, supramolecular micelles were deposited from the aqueous solutions; but individual micelles were also visible for the samples containing the *G*0–*G*2 arborescent copolymers and PAA-*b*-PHEA. Unimolecular species for the *G*1 arborescent copolymer are visualized embedded within a matrix of the DHBC, while fewer block copolymer species are present in the area probed for the *G*0- and *G*2-containing samples. Section analysis of the images, also shown in Figure 5.9, revealed non-spherical structures stemming from particle deformation due to adsorption on the hydrophilic mica surface, and the broadening effect of the AFM tip. The characteristic *fried egg* morphologies observed are consistent with the presence of a hydrophilic corona interacting more strongly with the mica surface.

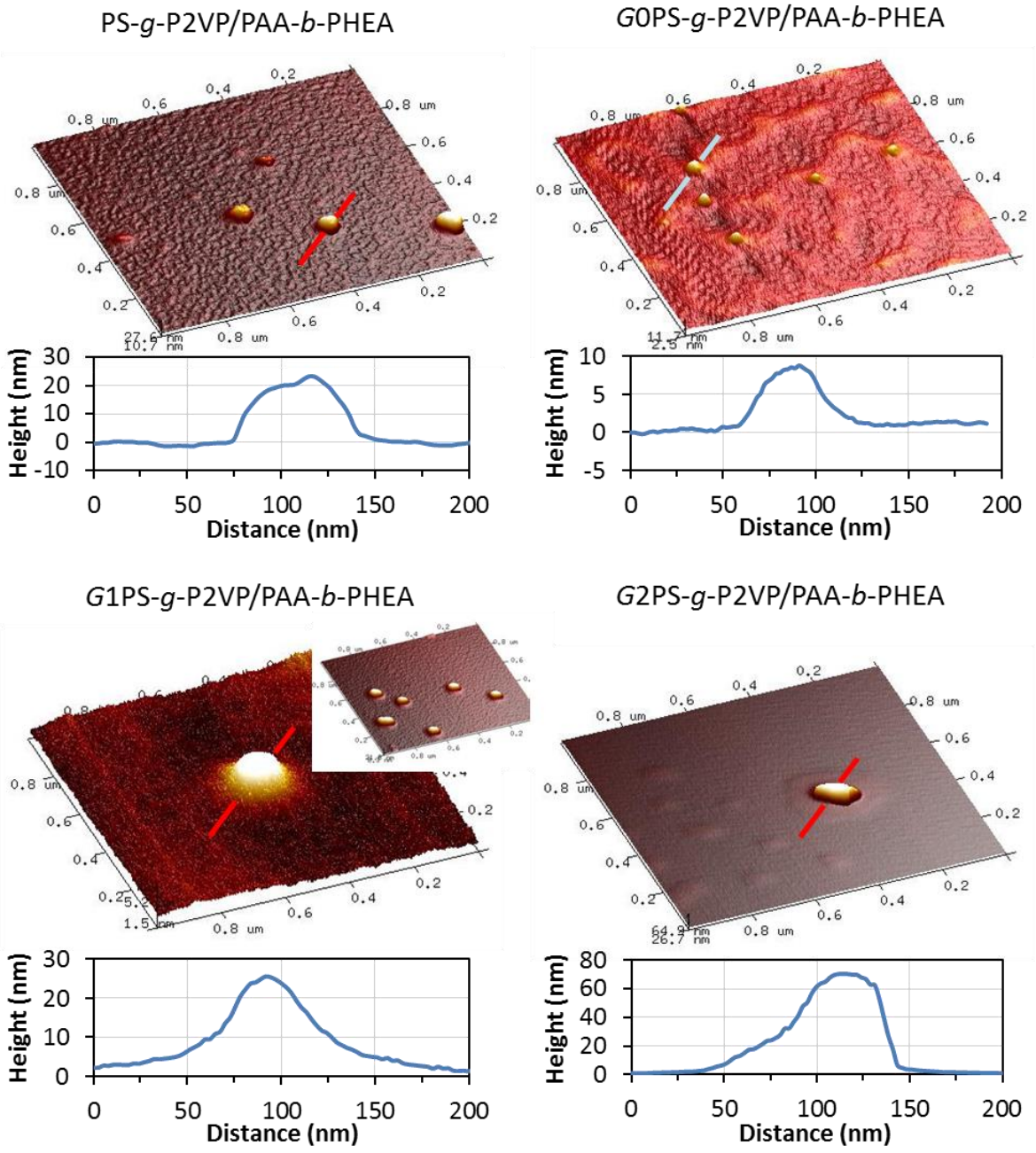

Figure 5.9 AFM imaging in the height mode of samples prepared from aqueous solutions of *Gn*PS-*g*-P2VP, *n* = [-1,2] complexed with PAA-*b*-PHEA (top), and coresponding phase profile (bottom). The magnification is 1 × 1 μm^2, $m_{Gn\text{PS-}g\text{-P2VP}}/m_{\text{PAA-}b\text{-PHEA}}$ = 1/10, and *Gn*PS-*g*-P2VP concentration *c* = 0.1 mg·mL^{-1} in all cases.

Irregular circular structures 2 nm in height and 102 nm in diameter were also observed on the mica surface for the *G*2PS-*g*-P2VP/PAA-*b*-PHEA sample (Figure 5.9). These presumably correspond to aggregates of PAA-*b*-PHEA chains forming flat structures through hydrophilic interactions with the mica surface. These micelles were also detected on some micrographs acquired for the other interpolymer systems (not displayed).

As seen in Figure 5.10, AFM imaging in the phase mode was informative about the composition of the aggregates. The phase shift observed at the periphery of the aggregates obtained from the *G*0 and *G*1 samples supports the presence of a hydrophilic corona. The micelles assembled from the larger arborescent copolymers exhibited structures with larger domain segregation, presumably stemming from the more rigid structure of the arborescent copolymers. Adsorbed PAA-*b*-PHEA chains are also visible on the mica surface for all the samples, and particularly noticeable for the *G*0PS-*g*-P2VP sample as noted earlier.

TEM imaging of the interpolymer complexes after RuO_4 staining, shown in Figure 5.11, revealed spherical particles for all the samples, although aggregated particles were visible for complexes of PS-*g*-P2VP and *G*2PS-*g*-P2VP. The feature size for the *G*0 system, measured from the micrographs and summarized in Table 5.5 (second column), revealed 2 populations with diameters of 25.4 ± 2.2 and 46.1 ± 8.1 nm. The aggregates formed by the *G*0 to *G*3 arborescent copolymers and PAA-*b*-PHEA chains had diameters ranging from 25.6 ± 3.5 to 51.7 ± 6.2 nm, slightly larger than *Gn*PS-*g*-P2VP loaded with 0.5 equiv of Pd and measured by TEM (Table 5.5, first column; and Chapter 3).

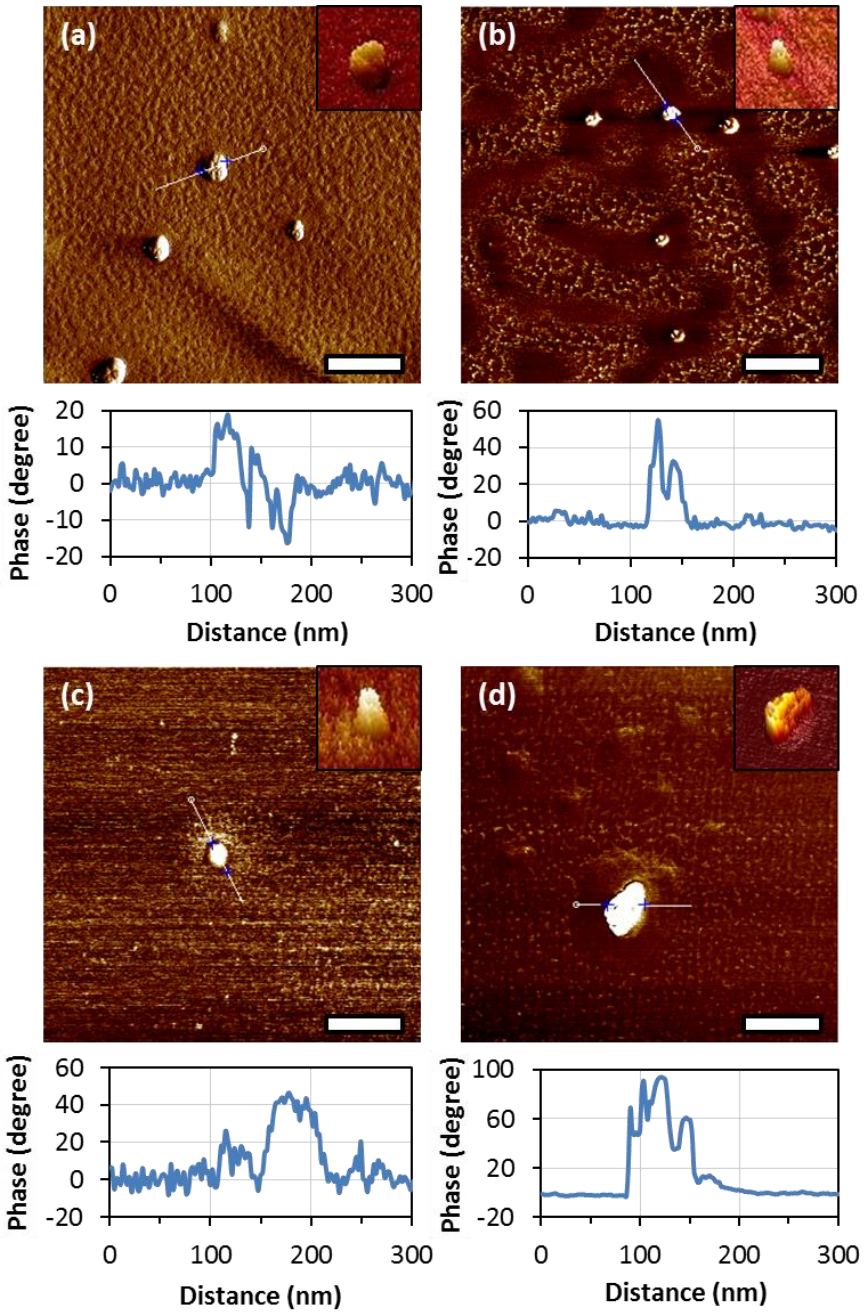

Figure 5.10 AFM imaging in the phase mode for complexes of PAA-*b*-PHEA and (a) PS-*g*-P2VP, (b) *G*0PS-*g*-P2VP, (c) *G*1PS-*g*-P2VP, and (d) *G*2PS-*g*-P2VP prepared in aqueous solutions. The magnification is 1 × 1 μm^2 and the length of the scale bar is 20 nm. Inset: Phase-mode 3D AFM images of the particles. In all cases $m_{GnPS\text{-}g\text{-}P2VP}/m_{PAA\text{-}b\text{-}PHEA}$ = 1/10, and *Gn*PS-*g*-P2VP concentration *c* = 0.1 mg·mL^{-1}.

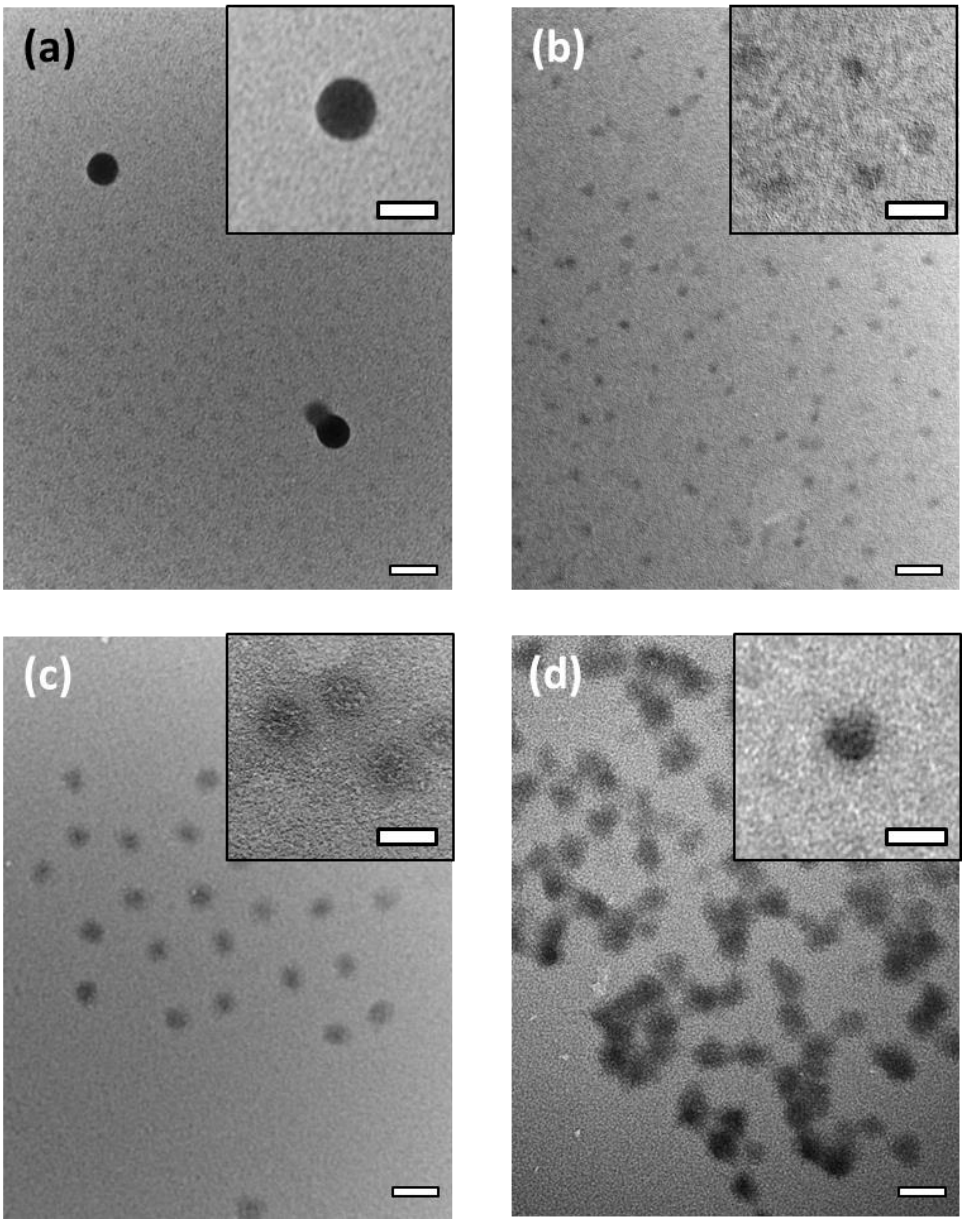

Figure 5.11 TEM images for samples cast from aqueous solutions of PAA-*b*-PHEA complexes with (a) PS-*g*-P2VP, (b) *G*0PS-*g*-P2VP, (c) *G*1PS-*g*-P2VP, and (d) *G*2PS-*g*-P2VP. Samples stained with RuO_4 (scale bar = 100 nm). Inset: Magnification of the micelles (scale bar = 50 nm). In all cases $m_{GnPS\text{-}g\text{-}P2VP}/m_{PAA\text{-}b\text{-}PHEA}$ = 1/10, and *Gn*PS-*g*-P2VP concentration c = 0.1 mg·mL^{-1}.

Table 5.5 Particle diameter (nm) measured from transmission electron micrographs and DLS for complexes of *Gn*PS-*g*-P2VP, Pd, and PAA-*b*-PHEA.[a]

Polymer	Without PAA-*b*-PHEA	With PAA-*b*-PHEA[b]		
	Pd (0.5 equiv)[c]	RuO_4 staining	Pd (0.5 equiv)	Pd (0.5 equiv) DLS[d]
PS-*g*-P2VP	3.2 ± 0.8	25.4 ± 2.2 46.1 ± 8.1	17.7 ± 4.2	236 ± 143
*G*0PS-*g*-P2VP	21.2 ± 2.4	25.6 ± 3.5	28.3 ± 2.9	47 ± 12 245 ± 101
*G*1PS-*g*-P2VP	36.1 ± 3.2	41.0 ± 4.4	45.0 ± 6.8	183 ± 79
*G*2PS-*g*-P2VP	50.8 ± 5.9	51.7 ± 6.2	59.2 ± 8.0	301 ± 144

[a] Diameter measured from TEM images or as indicated. [b] Preparation in aqueous solutions with $m_{Gn\text{PS-}g\text{-P2VP}}/m_{\text{PAA-}b\text{-PHEA}}$ = 1/10, and *Gn*PS-*g*-P2VP concentration c = 0.1 mg·mL^{-1}. [c] Loading with 0.5 molar equiv of Pd(II), deposited from ethanolic solutions. [d] Measured by DLS with NNLS analysis; size distributions provided in Appendix A5.4.

5.4.2.3.3 Palladium loading

The rapid complexation of Pd(II) by *Gn*PS-*g*-P2VP in ethanol was reported in Chapter 3 and led to the formation of stable colloidal solutions with catalytic properties. To achieve solubility in water, complexation of the arborescent copolymers with 0.5 molar equiv of Pd(II) was first performed in ethanol with $Pd(OAc)_2$ as reported previously. PAA-*b*-PHEA dissolved in ethanol was then added to the orange-colored homogeneous solution, to induce the formation of the *Gn*PS-*g*-P2VP/Pd/PAA-*b*-PHEA complexes. Upon addition of the hydrophilic copolymer, a light white floc precipitated out of the ethanolic solution. The

ethanol was evaporated and the complex was redissolved in Milli-Q water. The solution thus obtained was homogeneous, with an orange tinge.

Analysis by DLS, shown in Figure 5.12 and Table 5.5 (fourth column), revealed the presence of colloidal particles with a size distribution broader than for the metal-free micelles, as is typically observed for polyion complexes.[10] The hydrodynamic diameter was about twice as large as that measured in water for the complexes without Pd (Table 5.4). A notable exception was the complex formed by *G*2PS-*g*-P2VP, which displayed a comparable diameter with and without Pd loading. A bimodal distribution was also observed for the metal-loaded complexes of *G*0PS-*g*-P2VP, with smaller aggregates having D_h = 47 ± 12 nm.

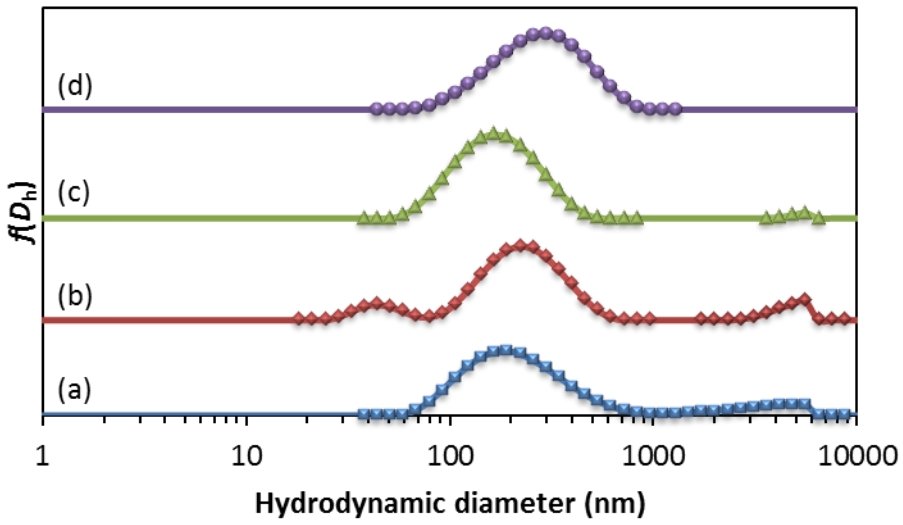

Figure 5.12 Size distribution for aqueous solutions of (a) PS-*g*-P2VP, (b) *G*0PS-*g*-P2VP, (c) *G*1PS-*g*-P2VP, and (d) *G*2PS-*g*-P2VP complexed with Pd(II) and PAA-*b*-PHEA in water. In all cases $m_{GnPS\text{-}g\text{-}P2VP}/m_{PAA\text{-}b\text{-}PHEA}$ = 1/10, [Pd]/[2VP] = 0.5, and *Gn*PS-*g*-P2VP concentration c = 0.02 mg·mL^{-1}.

TEM imaging of the Pd-loaded interpolymer complexes confirmed the presence of Pd in the micelles (Figure 5.13). The size of the Pd-loaded complexes, provided in Table 5.5 (third column), was generally larger than for the *Gn*PS-*g*-P2VP/PAA-*b*-PHEA complexes stained with RuO_4, in analogy to the DLS results. The Pd-loaded aggregates deposited from aqueous solutions were also somewhat larger than the arborescent copolymers loaded with 0.5 molar equiv of Pd(II) without PAA-*b*-PHEA, deposited from ethanolic solutions (Chapter 3 and Table 5.5). The size discrepancy ranged from 17 to 33% and decreased as the generation number (rigidity) of the arborescent copolymer increased. The complexes derived from the comb-branched copolymer were an exception, as noted previously: They formed multi-molecular aggregates about 5.5 times larger than their PAA-*b*-PHEA-free counterpart. It is assumed that the less compact structure of the *G*0 polymer facilitated the aggregation of the Pd-loaded micelles, as for the metal-free polymer.

The Pd-loaded micelles obtained by complexation of *Gn*PS-*g*-P2VP/Pd(II) with PAA-*b*-PHEA clearly yielded stable dispersions in water. While broader size distributions were observed by DLS, TEM imaging of deposited films only suggested a moderate level of aggregation.

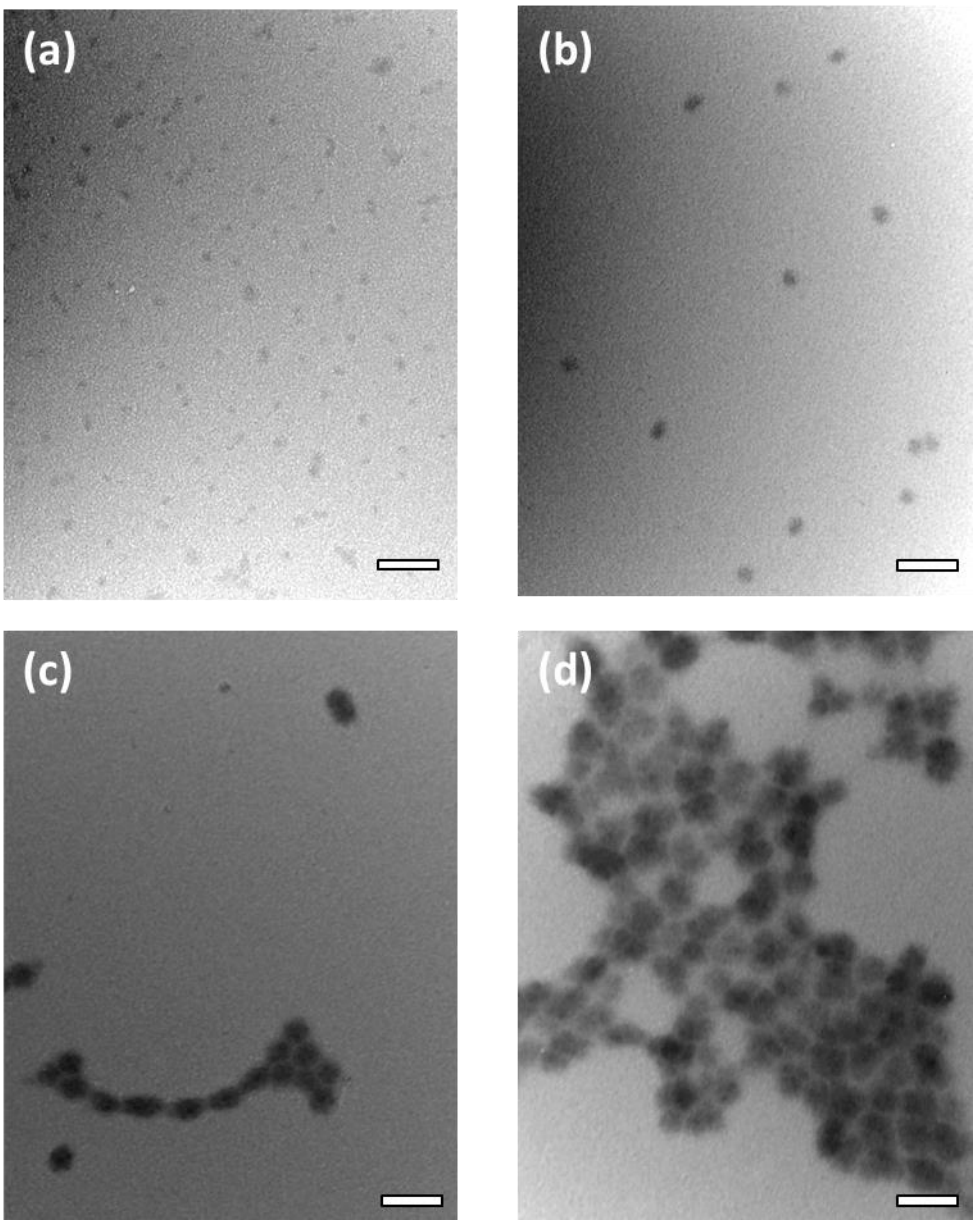

Figure 5.13 TEM images for Pd-loaded samples prepared from aqueous solutions of PAA-*b*-PHEA complexes with (a) PS-*g*-P2VP/Pd, (b) *G*0PS-*g*-P2VP/Pd, (c) *G*1PS-*g*-P2VP/Pd, and (d) *G*2PS-*g*-P2VP/Pd. The scale bars represent 100 nm. In all cases $m_{Gn\text{PS-}g\text{-P2VP}}/m_{\text{PAA-}b\text{-PHEA}}$ = 1/10, [Pd]/[2VP] = 0.5, and *Gn*PS-*g*-P2VP concentration *c* = 0.1 mg·mL^{-1}.

5.4.2.4 *Gn*PS-*g*-P2VP complexed with 1 mass equivalent of PAA-*b*-PHEA

5.4.2.4.1 Solution properties

Interpolymer complexes were also prepared by the addition of 1 mass equivalent of PAA-*b*-PHEA to *G*2PS-*g*-P2VP in ethanol, i.e. $f_+ = 0.88$. The size ($D_h = 106.5 \pm 0.5$ nm) and size dispersity ($Đ_p = 0.10 \pm 0.1$ nm) obtained by DLS analysis in ethanol (Figure 5.14) were comparable to the multi-molecular aggregates formed with 10 mass equiv of hydrophilic copolymer (Table 5.2). Both values remained constant in water/ethanol mixtures when the water content was below 50% (v/v). A slight decrease in D_h was noted at 50% (v/v) ($D_h = 96.2 \pm 0.9$ nm), as the P2VP segment presumably collapsed within the interpolymer complex in the non-solvent. The aggregates nonetheless remained soluble and had a low size dispersity ($Đ_p = 0.06 \pm 0.02$), suggesting good stabilization by the hydrophilic layer. In pure water the size of the aggregates increased further to $D_h = 204.1 \pm 1.0$ nm, and the size dispersity to $Đ_p = 0.10 \pm 0.01$. This corresponds to about 2/3 of the size of the multi-molecular aggregates formed with 10 mass equiv of hydrophilic chains. Aggregation of the interpolymer complexes is therefore likely responsible for the larger sizes observed. The lower D_h measured with 1 mass equiv of PAA-*b*-PHEA suggests however a lower level of aggregation as the hydrophilic copolymer content is decreased.

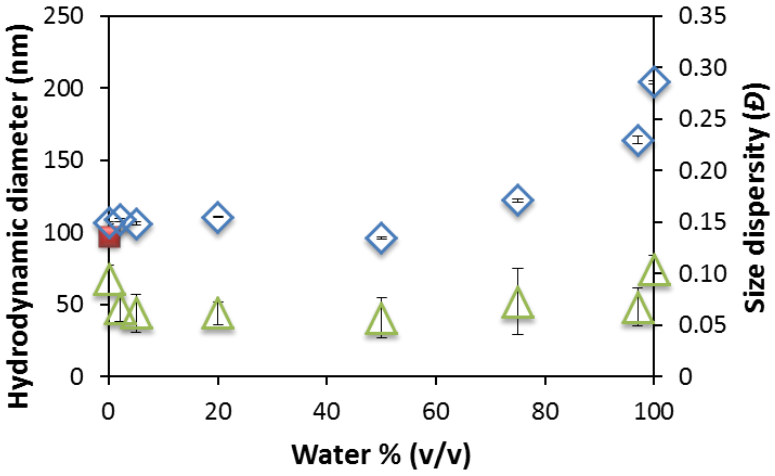

Figure 5.14 Evolution of the size (diamonds) and size dispersity ($Đ_p$, triangles) of *G*2PS-*g*-P2VP/PAA-*b*-PHEA complexes in water/ethanol mixtures measured by DLS. The size of *G*2PS-*g*-P2VP is shown for comparison (square). In all cases $m_{G0PS\text{-}g\text{-}P2VP}/m_{PAA\text{-}b\text{-}PHEA}$ = 1/1, and *G*0PS-*g*-P2VP concentration *c* = 0.1 mg·mL^{-1}.

5.4.2.4.2 Catalytic activity

The catalytic activity of the arborescent copolymers *G*0PS-*g*-P2VP and *G*2PS-*g*-P2VP loaded with Pd (Pd/2VP = 0.5) and complexed with a 1:1 mass equivalent PAA-*b*-PHEA was evaluated in the Suzuki-Miyaura (SM) cross-coupling reaction between phenylboronic acid (PBA) and 4-bromoanisole (BA) in D_2O, as shown in Scheme 5.5.

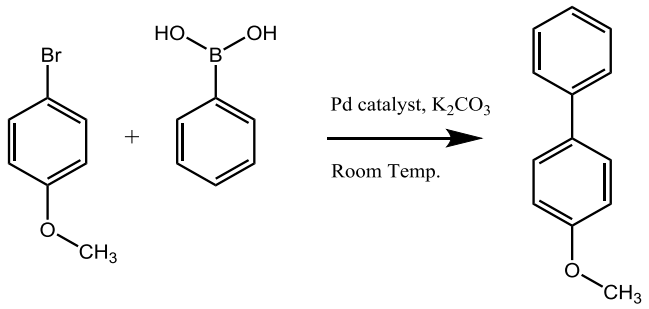

Scheme 5.5 Suzuki-Miyaura cross-coupling reaction between 4-bromoanisole and phenylboronic acid with 0.5 mol % of Pd catalyst in D_2O.

In recent years *on-water chemistry* has gained popularity, as water is an environmentally benign solvent, cheap, non-hazardous, and abundant. The SM reaction has been performed in water with hydrophobic reactants before, by taking place in a biphasic medium.[106,107] For instance, Pd complexes supported on an amphiphilic PS resin were used for the SM reaction but displayed limited activity in neat water.[108] Meise and Haag reported the preparation of hyperbranched polyglycerol functionalized with Pd complexes that displayed large TONs (59,000) in neat water and could be reused five times without loss of activity.[109] Sawoo et al. demonstrated the preparation of PEG-stabilized Pd NPs in water that were efficient catalysts in the SM reaction in this medium.[110] PAA-stabilized Pd NPs were also prepared by Coulter et al. and were found to catalyze SM coupling reactions even at low Pd loadings (0.01 mol) in water.[111]

In the present study, the reaction was performed in neat D_2O to investigate the applicability of the catalytic systems under green conditions. In this solvent the reaction was heterogeneous, as both BA and the reaction product, 4-methoxy-1,1'-biphenyl (MBP), displayed limited solubility in water. By sampling aliquots of the aqueous solution during the reaction and dilution with ethanol, the conversion was monitored by ^{1}H NMR spectroscopy as illustrated with a representative set of spectra in Figure 5.15.

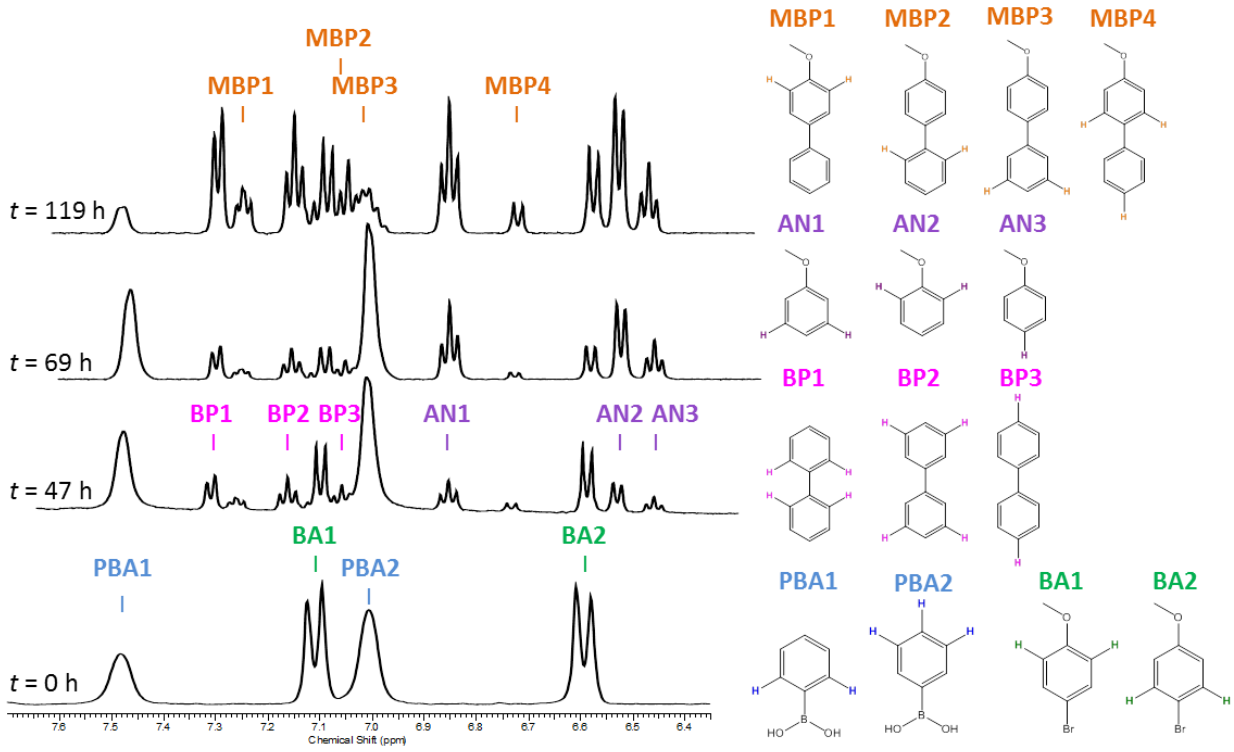

Figure 5.15 Time-dependent ^{1}H NMR spectra for the Suzuki-Miyaura cross-coupling reaction between phenylboronic acid and 4-bromoanisole in D_2O catalyzed with *G*1PS-*g*-P2VP/Pd[0.5 eq]/PAA-*b*-PHEA ([Pd] = 0.5 mol %). The peak assignments are indicated for each signal.

In spite of its limited solubility in water, the catalyst precursor $Pd(OAc)_2$ used without polymeric stabilizer displayed some catalytic activity, with a conversion of 12 mol % reached after 6 h, as shown in Figure 5.16a. The low solubility of the reagents and Pd species was clearly detrimental to the catalytic activity however; for comparison, a conversion of 50 mol % was reached within 1 h under similar conditions in ethanol (Chapter 3). At longer reaction times the conversion of the substrate reached a plateau, as deactivation of the catalyst occurred. A similar asymptotic profile was observed in ethanol after 1 h.

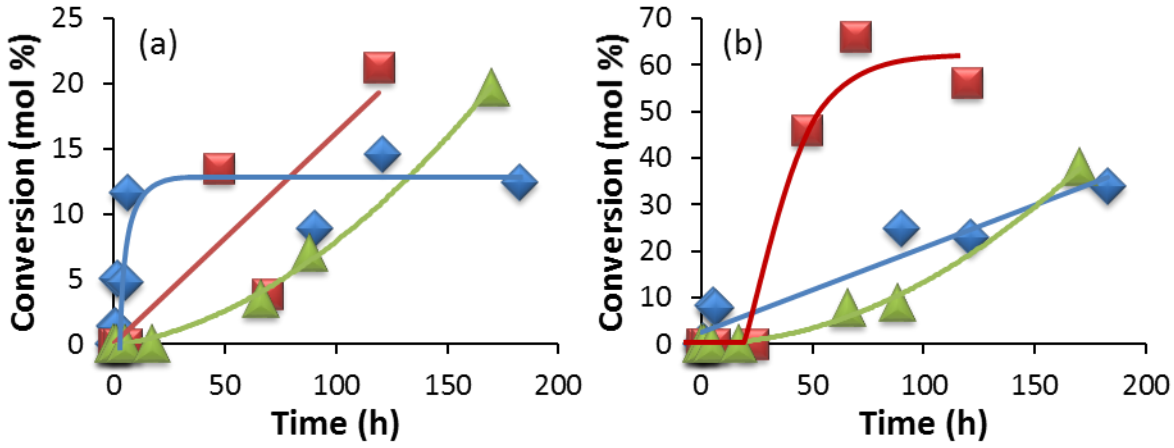

Figure 5.16 Formation of (a) 4-methoxy-1,1'-biphenyl and (b) anisole side product in the Suzuki-Miyaura cross-coupling reaction between phenylboronic acid and 4-bromoanisole in D_2O, with 0.5 mol % Pd, and in presence of *G*0PS-*g*-P2VP/PAA-*b*-PHEA (squares), *G*2PS-*g*-P2VP/PAA-*b*-PHEA (triangles), and no stabilizer (diamonds). In all cases $m_{Gn\text{PS-}g\text{-P2VP}}/m_{\text{PAA-}b\text{-PHEA}}$ = 1/1, [Pd]/[2VP] = 0.5.

Using *G*0PS-*g*-P2VP/PAA-*b*-PHEA as stabilizer, a conversion of about 12 mol % was achieved after 47 h, although large variability in the results resulted from sampling of the heterogeneous solution. The catalyst nevertheless remained active and the conversion reached 21 mol % after 5 days (Figure 5.16a). When using *G*2PS-*g*-P2VP/PAA-*b*-PHEA, the conversion reached 20 mol % after 1 week. The slower kinetics of MBP formation suggested restricted access of the substrate molecules to the compact core of the arborescent copolymer in water. The absence of deactivation hints at greater stabilization of the Pd catalyst within the polyion complex micelles, however. It should be noted that the interpolymer complexes used without Pd did not display any significant catalytic activity even after 8 days.

The formation of anisole as a side product was favored for the *G*1/Pd/PAA-*b*-PHEA system after 47 h, with 46 mol % of BA being dehalogenated (Figure 5.16b). Slower rates of side product formation were noted for the *G*3 micelles, and without stabilizer. In presence of the polymers, an induction period appears to be present before the dehalogenation reaction, These preliminary results hint at the usefulness of the arborescent PIC micelles as catalyst stabilizers in water, although further investigation is needed to optimize their catalytic performance in water or mixed (ethanol/water) media.

5.5 Conclusions

The preparation of polyion complex micelles was demonstrated using arborescent copolymers, *Gn*PS-*g*-P2VP, of overall generations ranging from *G*0 to *G*3, and a double-hydrophilic block copolymer, PAA-*b*-PHEA. The later was obtained by deprotection of P*t*BA-*b*-P(HEA-TMS), synthesized by ATRP. Hydrogen bonding and electrostatic interactions between the arborescent polybase and the polyacid led to rapid complexation of the polymers and the formation of supramolecular aggregates in ethanol. The PIC micelles had hydrodynamic radii D_h ranging from 354 to 488 nm and a size dispersity $Đ_p \leq 0.03$ in ethanol. The multi-molecular aggregates derived from the comb-branched (*G*0) copolymer had a broader size distribution ($Đ_p = 0.17$). In ethanol the supramolecular micelles displayed thermo-responsive properties, dissociating above a critical temperature of ca. 35 °C and reforming upon cooling.

The *Gn*PS-*g*-P2VP/PAA-*b*-PHEA complexes with $n \leq 1$ formed water-soluble aggregates with $D_h \approx 110$ nm and $Đ_p \approx 0.2$. More extensive aggregation was observed for the

larger *G*3 copolymer micelles. In aqueous solution the supramolecular micelles were stable to at least 50 °C, with D_h below 103 nm. Imaging of the water-soluble aggregates by AFM and TEM revealed compact structures. The size of the micellar complexes derived from *G*0 and *G*1 copolymers were comparable to the arborescent substrate, while aggregation was noted for the other substrates. Phase imaging by AFM confirmed the presence of the DHBC in the corona of the micelles. Loading of the PIC micelles with Pd(II) was demonstrated by TEM, and DLS measurements indicated water-soluble species with a rather broad size distribution. Interpolymer complexes were also formed by complexation with 1 mass equiv of PAA-*b*-PHEA, and these were also stable in water/ethanol mixtures. Loading with Pd of the PIC micelles yielded water-soluble Pd catalysts for the Suzuki-Miyaura reaction. In addition to phase separation, steric hindrance appeared to limit the activity of the catalyst. After further optimization, the PIC micelles prepared may be useful as catalysts and for the preparation of metallic nanoparticles in aqueous medium.

Chapter 6

Nickel Nanocatalysts by Thermal Decomposition of $Ni(CO)_4$ and Their Polymeric Stabilization

6.1 Overview

This study aims at comparing the catalytic activity of novel nickel nanopowders, synthesized by thermal decomposition of $Ni(CO)_4$, with other commercial catalysts including Raney® and QSI-Nano® nickel. The specific surface area of the nanopowders investigated ranged from 6.4 to 97.2 $m^2 \cdot g^{-1}$. The activity of the catalysts in the reduction of adiponitrile and mesityl oxide with hydrogen was higher for the nanopowders than for the commercial catalysts in some cases, and treatment of the particles with diethylenetriamine led to further improvement in catalytic activity. Aggregation of the nanopowders could be prevented with polymeric stabilizers. The structure and composition of these polymers was tailored to maximize the dispersibility and the catalytic activity of the particles. The polymeric dispersing agents examined included block copolymers of polystyrene (PS) with poly(ethylene oxide) (PEO) or poly(2-vinylpyridine) (P2VP), viz. PEO-*b*-PS-*b*-PEO and P2VP-*b*-PS-*b*-P2VP, and telechelic polymers of PEO. The materials obtained were useful as high-performance catalysts for hydrogenation reactions, demonstrating the benefits of polymer stabilization for nanoparticle catalysts.

6.2 Introduction

The fast development of nanotechnology has provided new dynamism to many research fields, as the properties observed for nanomaterials are often unique. For example, the synthesis of nanoparticles (NPs) has become increasingly controlled: Small particles with narrow size distributions can be obtained.[1] Metallic nanoparticles can display exceptional catalytic activity due to their large surface area and the influence of confinement (nanosize) effects.[2–9] Magnetic nanomaterials, in particular, have attracted attention to minimize catalyst leaching and facilitate metal recovery by magnetic filtration.[10] These materials have also shown promise in areas including energy production,[11] data storage,[12] sensing,[13] ferrofluids,[14] photonics,[12] biology, and medicine.[11,12,14,15]

Among the ferromagnetic catalysts, nickel is of notable relevance due to its good chemical stability, resistance to poisoning, and ease of recyclability.[16] Nickel nanocatalysts have been applied to hydrogenation,[17,18] dehydrogenation,[19] oxydation,[20] condensation,[21] alkylation,[22] carbonylation,[23] cycloaddition,[24] and different cross-coupling reactions (Stille,[25] Kumada,[26] Negishi,[27] Heck,[28] Suzuki[29]). Applications in proton exchange membranes (PEM),[30] solid oxide fuel cell (SOFC) assemblies,[31] and in the synthesis of carbon nanotubes[32] are also foreseen.

The size, shape, and composition of the NPs have been shown to depend markedly on the preparation method, which in turn affects the catalytic[18] and magnetic[14,33] properties of these materials. While they have been relatively less investigated than other ferromagnetic metals,[14] different methodologies have been devised for the preparation of Ni NPs ranging from top-down to bottom-up approaches.[14] Physical methods include sputtering,[34] pulsed

laser ablation,[35] spray pyrolysis,[36] reactive ball-milling,[37] microwave irradiation,[38] spark discharge,[39] chemical vapor deposition,[40] and vacuum evaporation.[41] Chemical reduction methods encompass electron transfer reduction by electrochemical methods[42,43] or multifarious reducing agents (hydrazine,[44] polyalcohols - polyol process,[45–47] super-hydrides,[48–51] hydrogen,[52]) and by the reduction of intermediate metal complexes.[53–55] The sonochemical[56,57] and thermal decomposition of metal complex precusors[58–60] have also found widespread use.

Chemical reduction methods have been favored because of their simplicity, low cost, and the control they offer over the size of the NPs.[16] Unfortunately, oxidation of the particles during *wet syntheses* represents an important limitation of these protocols.[11,14,16,61]

A novel method allowing the preparation of nickel NPs at a very competitive cost as compared to the wet chemistry methods was developed recently at Vale-Inco.[62] This technique is based on the thermolysis of nickel carbonyl ($Ni(CO)_4$) using streams of hot and cold gases in a flow reactor. The advantage of this approach is that nickel carbonyl is an inexpensive intermediate used in the nickel refining process. While still experimental, this method has potential for the production of nanoparticles with tunable size and characteristics on a large scale.[62]

To benefit fully from the high catalytic activity of NPs, their aggregation – favored by their high surface energy and curvature[5] – must be prevented, while maintaining unhindered access to their surface. Different methods are available to minimize the aggregation of nanoparticles including the use of specific solvents,[63,64] surfactants,[49,65,66] ligands,[48] and polymers.[55,67] The first three methods give rather unstable products under demanding

catalytic conditions[68] unless strong interactions (usually also detrimental for catalytic applications) with the stabilizer are present. However polymers can exhibit multiple weak interactions with the NPs surface, providing simultaneously strong stabilization and access of the substrate molecules to the catalytic sites.[69] The polymer chains may furthermore protect magnetic particles from aerial oxidation, although a limited number of polymers have been investigated for this purpose.[61]

The influence of polymers on catalytic activity, selectivity, and bonding interactions has been examined in various metallic colloidal systems;[8,69] however, relatively few investigations involved colloidal Ni NPs.[68,70] Umegaki et al. reported improved durability for an amorphous Ni catalyst stabilized by poly(*N*-vinyl-2-pyrrolidone) (PVPy), while the catalytic activity for the hydrolysis of ammonia borane was unaffected by the presence of the macromolecules.[70] Ould Ely et al. investigated the influence of the molar mass of the polymer on the stability of Ni NPs. They demonstrated efficient encapsulation by relatively low molar mass PVPy and highlighted the influence of the solvent on the conformation and wrapping of the polymer chains around the NPs. They also presented evidence for the protective role of the polymer against particle oxidation by air.[55] Rashid et al. prepared poly(vinyl methyl ether)-stabilized Ni NPs that were efficient catalysts for both inorganic and organic reactions in water. The catalyst could be recycled at least 8 times.[61] Liaw *et al.* observed a 1.5- to 3-fold increase in catalytic activity for NiB nanoparticles in the hydrogenation of carbonyl and olefinic groups when using PVPy as stabilizer. They suggested that the polymer coordinated weakly with NiB at multiple sites through the lone electron pairs of the pyrrolidone groups, leading to strong overall interactions with the

polymer.[68] Other polymeric stabilizers used with Ni NPs include pluronic triblock copolymers,[71] hydroxypropyl methylcellulose,[16] polystyrene-*block*-poly(2-vinylpyridine),[72] poly(methacrylic acid),[67] and polyacrylamide.[67]

On the basis of the above observations, we proposed to evaluate the catalytic performance of a series of Ni NPs synthesized by a gas-phase process developed at Vale-Inco. The catalytic activity of the particles, in both their bare and polymer-stabilized forms, was compared to that of other commercial catalysts, with emphasis on the specific surface area and the composition of the particles (passivated vs. non-passivated). More generally, we aimed to demonstrate the usefulness of polymer stabilization to improve the colloidal stability and the performance of nickel nanocatalysts, as well as to investigate the effect of the macromolecules on areal oxidation.

6.3 Experimental procedures

6.3.1 Materials

6.3.1.1 Reagents, catalysts and polymers

The reagents diethylenetriamine (DETA, Sigma-Aldrich, ReagentPlus®, 99%), 1,6-hexanedinitrile (ADN, adiponitrile, Sigma-Aldrich, 99%), mesityl oxide (MO, Fluka, technical grade, ≥90%), methyl isobutyl ketone (MIBK, Baker analyzed®, ACS reagent, ≥98.5%), 4-methyl-2-pentanol (MIBC, methyl isobutyl carbinol, Sigma-Aldrich, 98%), phenylmagnesium chloride (PhMgCl, Sigma-Aldrich, 2.0 M in THF), thionyl chloride (Fluka, ≥99%), acetone (Caledon, HPLC grade, ≥99.7%), dichloromethane (Chromasolv®,

HPLC grade, ≥99.8%), diethyl ether (Sigma-Aldrich, anhydrous, ACS reagent, ≥99.0%), methanol (Caledon, ACS reagent), 1-propanol (IPA, Fisher Certified), anhydrous 2-propanol (Alfa Aesar, ≥99.5%), K_2CO_3 (Sigma-Aldrich, ACS reagent, ≥99.0%), and activated alumina (Sigma-Aldrich, neutral, Brockmann I) were used without further purification. Triethylamine (Sigma-Aldrich, ≥99%) was purified by stirring with calcium hydride overnight and distillation under reduced pressure. Ethylene oxide (EO, Air Liquide) was purified using calcium hydride and PhMgCl under vacuum, as described in Appendix A6.1.2. Toluene (Caledon, HPLC grade, ≥99.8) was purified by refluxing with oligostyryllithium under dry N_2 atmosphere. Raney® nickel (WR Grace and Co. Raney® 2400 and 2800, slurry in water), QSI-Nano® nickel (QuantumSphere Inc.), Aldrich nickel nanopowder (Sigma-Aldrich, <100 nm particle size, ≥99% trace metals basis), the Inco nickel nanopowders, polyethyleneimine solution (PEI, Sigma-Aldrich, $\bar{M}_n$ = 60,000 g·mol^{-1}, 50 wt % in water), and poly(*N*-vinyl-2-pyyrolidone (PVPy, Sigma-Aldrich, $\bar{M}_w$ = 10,000 and 1,300,000 g·mol^{-1}) were used as received. Poly(ethylene glycol) monomethyl ether (MPEG, Polysciences, $\bar{M}_n$ = 1900 g·mol^{-1}) was purified by azeotropic distillation with dried toluene.

6.3.1.2 Inco nickel nanopowders synthesis

The nickel nanoparticles provided by Vale-Inco Technical Services Limited (VITSL, Mississauga, Ontario, Canada) were synthesized by the thermal decomposition of nickel tetracarbonyl. A schematic representation of the apparatus employed is given in Figure 6.1. Briefly, a $Ni(CO)_4$ stream was injected in a vertical chemical vapor deposition (CVD) reactor through a hot gas stream (ca. 400 °C). Decomposition of the carbonyl precursor in the reactor

resulted in the nucleation of fine particles. Rapid quenching of the particles in liquid nitrogen (powder consolidator) prevented sintering and further particle growth, thereby offering control over the size and specific surface area (SSA) of the particles formed. Further control over particle growth was achieved by adjusting the length of the reactor. Under these conditions the concentration of the incoming gas determined the concentration of nuclei, ultimately colliding and increasing in size; and therefore a lower $Ni(CO)_4$ concentration yielded a lower SSA. This reactor yielded ca. 10 g of particles per hour, with a short starting time, and around 30 min flushing with nitrogen at the end of the run to remove residual $Ni(CO)_4$ and allow safe opening of the reactor. The bottom of the reactor housing the filter (discharge container) was then disconnected, capped rapidly to prevent particle oxidation by the air (Figure 6.1), and transported to a glove box to transfer the particles under inert atmosphere. **Caution**: Nickel tetracarbonyl is volatile, extremely toxic, and may be fatal if absorbed through the skin or inhaled. Nickel nanoparticles are toxic, suspected carcinogens,[73] and flammable. Both should be handled with proper laboratory technique, and under a well-ventilated fume hood or with proper protective equipment.

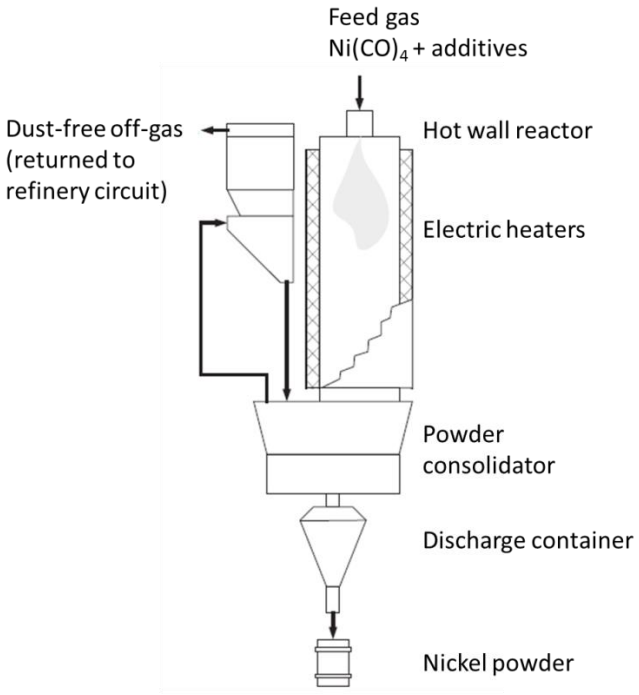

Figure 6.1 Gas pyrolyzer used in the production of Ni nanopowders from $Ni(CO)_4$. Reprinted with permission from Reference 62. Copyright 2008 American Scientific Publishers.

6.3.2 Hydrogenation reactions

6.3.2.1 High pressure hydrogenation

The hydrogenation of adiponitrile (ADN) and mesityl oxide (MO) was performed using hydrogen gas under pressure. **Caution**: Hydrogen has a high flammability (explosive limit of 4% per volume in air at standard temperature and pressure),[74] so suitable safety precautions are required. The experiments were carried out in stainless steel, high pressure Parr reactors. Hydrogen was introduced in the reactors through ¼" stainless steel tubing with

a pressure rating of 41.4 MPa (6000 psig), and residual gas was vented to an explosion-proof fume hood after the reactions, in a laboratory designed for high-pressure hydrogenation.

The hydrogenation of ADN was performed at a pressure of 6.9 MPa (1000 psig) in a 1-L Parr autoclave (model 4011) in a rocker-type shaking base (Figure 6.2a). The hydrogenation of MO was performed at 1.4 MPa (200 psig), in a 600 mL Parr autoclave equipped with a sampling tube (Figure 6.2b). The temperature was controlled by a proportional–integral–derivative (PID) controller (Fuji Electric PXZ-9), and the stirring rate was adjusted with a tachometer at ± 5 revolutions per minute (rpm).

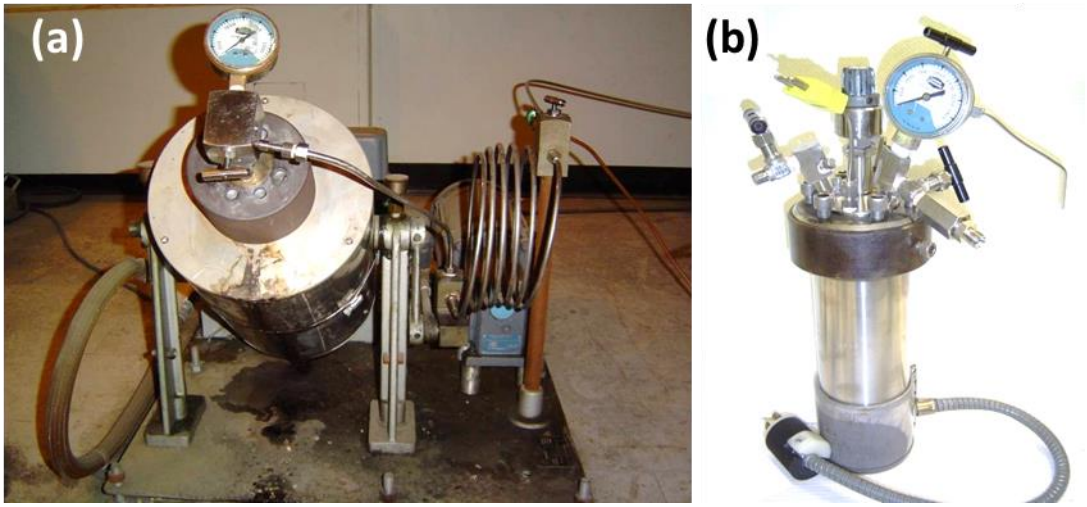

Figure 6.2 (a) Parr reactor in rocker-type shaking base for the hydrogenation of adiponitrile, and (b) Parr reactor for the hydrogenation of mesityl oxide.

6.3.2.2 Hydrogenation of adiponitrile

6.3.2.2.1 Passivated catalysts

The experimental conditions employed for the catalytic hydrogenation of ADN were adapted from the procedure of Freidlin et al.[75] The nickel nanoparticles (30–250 mg) were weighed into a beaker; methanol (100 mL) and ADN (5 g, 46 mmol) were added, and the solution was sonicated (Bransonic® Branson 2210R-MTH bath) for 10 min. When using Raney® nickel (RaNi), the catalyst as slurry in water (ca. 310 mg) was transferred to a centrifuge tube and subjected to 3 cycles of washing with methanol, centrifugation, and decantation in order to remove the water. The particles (ca. 270 mg) were then transferred to a beaker with the solvent and the substrate, and sonicated for 10 min.

The reaction mixture was transferred to the reactor which was flushed with nitrogen, sealed, and returned to the base of the apparatus pre-heated to 50 °C. The temperature returned to 50 °C again after ca. 5 h. The reactor was flushed 3 times with hydrogen at 0.7 MPa (100 psig), and pressurized to 6.9 MPa. Shaking was maintained for 24 h. The pressure was then released from the reactor which was allowed to cool for 3 h, and the solution was removed. The catalyst was decanted with a magnet for 3 h, and the clear supernatant was filtered through filter paper (Whatman®, grade 4). When employing NPs, the solution was rather filtered through a polytetrafluoroethylene (PTFE) filter (Omnipore™ Millipore) with a nominal pore size of 0.1 μm. The solvent was removed on a rotary evaporator, the sample dried under vacuum (<13 Pa, 0.1 mm Hg) for 3 h, and the residue was analyzed by ^{1}H NMR spectroscopy. The reactor was washed with methanol, soapy water, rinsed with methanol, and dried with air to prevent catalyst carryover.

6.3.2.2.2 Non-passivated catalysts

The non-passivated nickel particles from VITSL and QuantumSphere Inc. (QSI) were stored under inert atmosphere and manipulated under N_2 in a glove bag, and transferred to a nitrogen-purged vial for weighing. The ADN substrate (5 g, 46 mmol) was added to methanol (100 mL) in a flask sealed with a septum and the solution was deoxygenated by bubbling N_2 for 10 min. The solution was sonicated for 10 min inside the glove bag and a syringe was used to transfer the solution mixture to the reactor. The hydrogenation reaction and the workup procedure were carried out as described in Section 6.3.2.2.1.

6.3.2.3 Hydrogen reduction of the nickel nanopowders

Reduction of the oxidized particles was performed under hydrogen by loading the particles (ca. 250 mg) in the 1-L Parr reactor which was evacuated, charged twice with hydrogen at 3.5 MPa (500 psig) before releasing the pressure, filled with hydrogen at 6.9 MPa, and heated to 250 °C for 2 h. After releasing the pressure and cooling the reactor, the methanolic adiponitrile solution (0.46 $mol \cdot L^{-1}$) was transferred to the reactor under N_2 atmosphere.

6.3.2.4 Decoking of the nickel nanopowders

Decoking of the nanoparticles was carried out by loading the particles (ca. 250 mg) in a glass column in the presence of silica (50 wt %) and treatment with 10% (v/v) H_2/N_2 at 500 °C for 5 h at a flow rate of 110 $mL \cdot min^{-1}$.

6.3.2.5 DETA treatment

The Ni particles (140 mg) were loaded in a test tube (13 × 115 mm^2) sealed with a septum. Deionized water (10 mL), degassed by bubbling N_2 through it for at least 20 min was added, followed by diethylenetriamine (DETA, 1 mL, 9 mmol) drop-wise, after degassing in a similar fashion. An exothermic reaction occurred and after a few seconds a purple tinge was observed in the vicinity of the particles at the bottom, and hydrogen gas was evolved. The particles were redispersed by sonication of the test tube, centrifuged (Clay Adams, 3400 rpm), and the supernatant was removed with a syringe under N_2 atmosphere. This process was repeated 3 times; the particles were then washed 3 times by adding degassed 2-propanol (IPA, ca. 10 mL), sonication, centrifugation, and decantation. Drying of the particles was achieved under vacuum (13 Pa) for 1 h before storage under N_2. **Caution**: These nickel particles are pyrophoric and should be stored under inert atmosphere or in slurry form.

6.3.2.6 Hydrogenation of mesityl oxide

The desired amount of catalyst (30–100 mg) was weighed on a balance in a glove box maintained under N_2 atmosphere. Anhydrous 2-propanol (100 mL) and MO (5 g, 51 mmol) were degassed in an Erlenmeyer flask and added to the catalyst in the glove box. The flask capped with a septum was removed from the glove box and sonicated for 30 min. The dispersion was then transferred to the nitrogen-purged reactor with a cannula. The reactor was flushed 3 times with hydrogen at 0.69 MPa (100 psig), and pressurized at 1.38 MPa (200 psig) for the reaction. The reduction was performed at 50 °C and 1.38 MPa H_2, at a stirring rate of 330 rpm, for 3–6 h. The progress of the reactions was monitored by sampling ca.

1 mL of solution every 30 minutes (after discarding 8 mL of solution each time, to take into account the dead volume in the sampling tube). The sampled solution was decanted over a magnet and the supernatant was transferred to an Eppendorf centrifuge tube. After centrifugation for 1 h, the supernatant was recovered and a known amount (ca. 0.02 g, 0.025 mL, 0.3 mmol) of 1-propanol was added as an internal standard. The time-dependent conversion of the reaction was determined by gas chromatography (GC) analysis.

6.3.3 Polymer synthesis

6.3.3.1 Synthesis of PEO-*b*-PS-*b*-PEO and P2VP-*b*-PS-*b*-P2VP

Triblock copolymers of poly(ethylene oxide)-*block*-polystyrene-*block*-poly(ethylene oxide) (PEO-*b*-PS-*b*-PEO) and poly(2-vinylpyridine)-*block*-polystyrene-*block*-poly(2-vinylpyridine) (P2VP-*b*-PS-*b*-P2VP) were synthesized by anionic polymerization, using potassium naphthalide as initiator. The detailed procedures are included in Appendix A6.1.

6.3.3.2 Synthesis of MPEG-DETA

A commercial poly(ethylene glycol) (PEG) monomethyl ether sample ($\bar{M}_n$ = 1900 g·mol^{-1}) was chlorinated by a procedure described by Zalipsky et al.[76] The reaction started with the azeotropic purification of 0.01 mol (20 g) of MPEG with 100 mL of dry toluene, to remove residual water. The polymer was then redissolved in 100 mL of toluene and transferred to a round-bottomed flask with a refluxing condenser. Distilled triethylamine (0.01 mol) was added, followed by thionyl chloride (0.03 mol) drop-wise over 45 min. The

reaction was allowed to proceed for 4 h at reflux before cooling to room temperature. The triethylammonium hydrochloride salt formed was filtered from the solution and the solvent was evaporated. The residue was redissolved in dichloromethane (60 mL) and dried over anhydrous K_2CO_3 (2.5 g). After filtration on a Büchner funnel, the filtrate was treated with activated alumina (25 g) to remove residual salts and water. The polymer was finally precipitated in cold diethyl ether and was obtained in 60% yield (12 g). The reaction scheme and ^{13}C NMR spectra for this reaction are provided in Appendix A6.2. ^{1}H NMR (300 MHz, $CDCl_3$): 3.35 (CH_3−O), 3.62 (CH_2-O), 4.19 (Cl−CH_2) ppm. ^{13}C NMR (300 MHz, $CDCl_3$): 42.7 (CH_2−Cl), 59.0 (CH_3−O), 70.5 (CH_2−O), 71.3 (Cl−CH_2−*C*H_2), 71.9 (CH_3−O−*C*H_2) ppm.

The chloride groups were then reacted with diethylenetriamine (DETA). The procedure used was based on a method previously reported by Gauthier and Frank.[77] The polymer (0.49 mmol equiv of chloro groups, 0.936 g) was dissolved in 2.5 mL of THF. This solution was added drop-wise within one hour to 7.4 mmol of DETA (15-fold excess to avoid the formation of dimers) and placed in an oil bath at 50 °C. After heating for 1 h, 2.5 mL of methanol was added and the reaction was allowed to proceed for 36 h. The solvent was removed; the polymer redissolved in 50 mL of THF, and shaken in a separatory funnel with 50 mL of 5% aqueous NaOH solution, to deprotonate the amine salt formed. The polymer in the THF (top) layer was recovered, evaporated, redissolved in chloroform (20 mL), and precipitated in hexane. The final product was obtained in 98% yield (0.917 g). The reaction scheme, and ^{13}C NMR spectra are shown in Appendix A6.2. ^{1}H NMR (300 MHz, $CDCl_3$): 1.74 (NH_2−), 2.66 (O−CH_2−*C*H_2−N), 2.72 (NH_2−CH_2−*C*H_2−N), 2.78 (C*H*$_2$−NH_2), 3.36

(CH_3−O), 3.62 (CH_2−O) ppm. ^{13}C NMR (300 MHz, $CDCl_3$): 41.3 (CH_2−NH_2), 49.1 (N−*C*H_2−CH_2−NH_2), 51.2 (O−CH_2−*C*H_2−N), 59.0 (CH_3−O), 70.6 (CH_2−O), 71.9 (CH_3−O−*C*H_2) ppm.

6.3.4 Adsorption isotherms

The amount of polymer bound to the nickel nanoparticles was determined by the following protocol. In a glove box, the particles (ca. 50 mg) were added to a predetermined amount of polymer in a 20 mL vial. After the addition of toluene (ca. 10 mL), the vial was sonicated for 30 min. The solvent was evaporated under vacuum (<13 Pa, 0.1 mm Hg) and the samples were kept under nitrogen. A fraction of the sample (ca. 3.5 mg) was then added to IPA (10 mL), and MO (500 mg, 0.05 mol) if applicable, and immersed in an oil bath pre-heated at 50 °C. After 3 h of vigorous stirring, the solution was cooled to room temperature and centrifuged at 15000 rpm (27000 G) for 30 min. The supernatant was recovered and the solvent was evaporated by placing the vial in a warm water bath and under nitrogen flow. Tetrahydrofuran (1 g, 1.1 mL) was added to the vial, and the solution was sonicated and filtered with a 0.22 µm PTFE filter (Omnipore^{TM} Millipore). Quantification of the polymer in solution was performed by size-exclusion chromatography (SEC) analysis, by integration of the peak obtained from a calibrated differential refractive index (DRI) detector.

6.3.5 Characterization

6.3.5.1 Size-exclusion chromatography (SEC)

Characterization of the molar mass and dispersity of the polymers was achieved by SEC analysis. The system used consisted of a Waters 510 HPLC pump, a 50-µL injection loop, a Waters 2410 differential refractometer (DRI) detector, and a Wyatt MiniDAWN laser light scattering detector operating at 690 nm. Separation was achieved with a 500 × 10 mm^2 Jordi Gel DVB mixed-bed column with a linear PS molar mass range of 10^2–10^7. The mobile phase used was THF at a flow rate of 1 $mL \cdot min^{-1}$, at room temperature.

6.3.5.2 Nuclear magnetic resonance (NMR) spectroscopy

The composition of the polymers and the conversion of the reactions were determined by ^1H and ^{13}C NMR spectroscopy, on a Bruker Avance-300 (300 MHz) nuclear magnetic spectrometer equipped with a z-gradient QNP 5 mm sample probe. $CDCl_3$ or DMSO-d_6 were used as solvents, and the chemical shift of the lock solvent was used as the reference frequency. Each spectrum comprised 16 scans, and the concentration of the samples for the analysis ranged from 10–30 $mg \cdot mL^{-1}$.

6.3.5.3 Gas chromatography (GC)

Monitoring of the reduction reactions was accomplished by gas chromatography (GC) analysis on an Agilent 6890N chromatograph equipped with a flame ionization detector (FID), a J&W Scientific DB-WAX capillary column (30 m × 0.53 mm ID × 1 µm film

thickness), and a 7683 Series autosampler injector. 1-Propanol served as internal standard, and calibration of the detector was performed with standard solutions.

6.3.5.4 Transmission electron microscopy (TEM)

Imaging of the nanopowders and polymer-stabilized samples was achieved by transmission electron microscopy (TEM) on a Philips CM10 electron microscope operated at 60 kV accelerating voltage in the bright-field mode. The samples were prepared by depositing two drops of solution (ca. 0.5 $mg \cdot mL^{-1}$) onto 300-mesh Formvar® carbon-coated copper TEM grids (Electron Microscopy Sciences, FCF300-Cu) placed onto filter paper used as wicking medium. After deposition of the solution, the grids were transferred onto a new piece of filter paper in a Petri dish and dried overnight at room temperature. Image recording was achieved with an Advance Microscopy Techniques 11 megapixel digital camera and the Image Capture Software Engine version 5.42.558. The feature size and size distribution were measured with the open source processing program ImageJ (version 1.46r).[78] A minimum of fifty measurements were made for the determination of the particle size and size distribution. Contrast adjustment was also performed on some of the micrographs, to improve visualization and help with the feature measurements.

6.3.5.5 Analysis at Vale-Inco

Particle characterization performed by VITSL included the determination of the specific surface area by the BET (Brunauer, Emmett and Teller) procedure, scanning electron microscopy (SEM), elemental analysis, and laser diffraction analysis.

6.4 Results and discussion

6.4.1 Nickel nanopowders

6.4.1.1 Synthesis, surface area and composition

The nickel nanopowders were synthesized at VITSL by a top-down approach based on the thermal decomposition of $Ni(CO)_4$. The Mond (or carbonyl) process,[79] developed in 1890, has been widely employed in the purification and the production of Ni powders. Large-scale production based on this process has been in place at Vale-Inco for many decades.[62] More recently, this technology has been exploited in the production of nanosized Ni powders by thermal decomposition of the carbonyl precursor in a modified CVD reactor (Figure 6.1).[62]

The first part of the project aimed at testing the catalytic activity of the bare particles, to fine tune the experimental conditions used in their synthesis and to achieve control over their surface area and composition. A series of 16 nanopowders was produced; the measured SSA and elemental composition of the samples are summarized in Table 6.1. The BET procedure – commonly applied to this type of system[80] – was used to determine the surface area of the particles at VITSL, and yielded values ranging from 6.4 $m^2 \cdot g^{-1}$ (Inco 73011) to 97.2 $m^2 \cdot g^{-1}$ (Inco 982174). Two series of particles were prepared; the first series (9 samples) was stored under inert atmosphere after their synthesis, while the second series (7 samples) was passivated by controlled exposure to oxygen. Without passivation, the nanoparticles were prone to rapid areal oxidation and reacted exothermically in contact with air. However controlled and progressive passivation of the particles was cardinal, as sintering and a concomitant decrease in SSA otherwise occurred for the finer particles (e.g., Inco 982714,

SSA = 97.2 $m^2 \cdot g^{-1}$; see Section 6.3.1.2). Particles with SSA greater than 85.5 $m^2 \cdot g^{-1}$ were obtained for both series (Table 6.1). The surface area obtained in some cases was larger than for other commercial nickel catalysts such as RaNi 2800 (28.6 $m^2 \cdot g^{-1}$) and Aldrich Ni nanopowder (8.4 $m^2 \cdot g^{-1}$). It was also comparable to the SSA of Ni NPs produced by QuantumSphere Inc. (QSI) (84.0 $m^2 \cdot g^{-1}$), obtained by a more expensive and energy-demanding CVD-based process.[81]

As shown in Figure 6.3, the surface area of six non-passivated Ni nanopowder samples was monitored over a period of 8 months. The SSA, ranging from 40.9 to 60.5 $m^2 \cdot g^{-1}$, remained constant over that period of time. Similar measurements on the Ni nanopowder with the largest SSA (97.2 $m^2 \cdot g^{-1}$) revealed a small decrease in value, stabilizing around 86.0 $m^2 \cdot g^{-1}$ after 106 days. Although the Ni nanoparticles with intermediate SSA displayed greater stability towards rearrangement, surface area stabilization nevertheless occurred for the sample with the largest SSA.

Table 6.1 Nickel catalysts specific surface area and composition.

Catalysts	Specific surface area[a] ($m^2 \cdot g^{-1}$)	O content[b] (wt %)	C content[b] (wt %)
Commercial particles			
QSI-Nano®	84.0	2.1	0.53
Raney® nickel 2400	140[c]	n/a[d]	n/a
Raney® nickel 2800	28.6	n/a	n/a
Aldrich Ni nanopowder	8.4	n/a	n/a
Vale-Inco passivated particles			
113132	85.5	n/a	n/a
34113	57.0	n/a	n/a
80852 (NiO)	31.2	21.0	0.17
54074	30.3	5.5	0.59
85109	24.7	4.4	0.29
108775	13.9	n/a	n/a
73011	6.4	0.3	0.79
Vale-Inco non-passivated particles			
982714	97.2	n/a	1.5
112376	73.6	n/a	n/a
98814	60.5	11.4	n/a
95911	50.8	10.0	0.82
97502	46.3	9.4	n/a
98478	46.2	9.4	n/a
98952	40.9	5.0	n/a
92831	26.5	n/a	n/a
43386	18.8	n/a	n/a

[a] Measured by the BET method at VITSL. [b] Elemental analysis at VITSL for selected samples only. [c] From Duch and Allgeier.[82,83] According to the supplier, SSA = 125–140 $m^2 \cdot g^{-1}$ after drying the particles under N_2 at 130 °C for 1 hour; the composition also included 2.0–3.0 wt % iron and 2.0–3.0 wt % chromium as promoters. [d] Measurement not attempted.

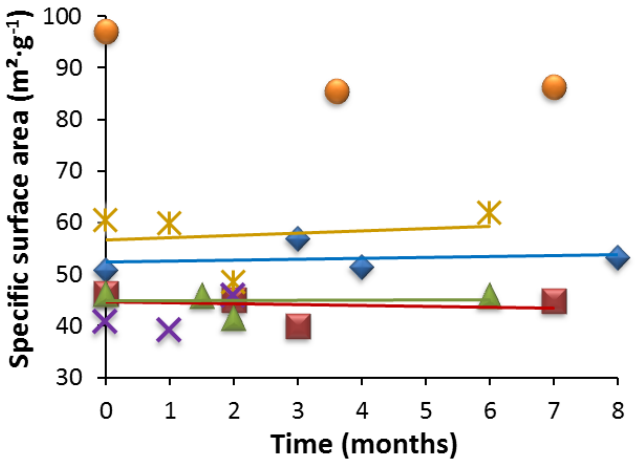

Figure 6.3 Evolution of the specific surface area (BET) with time for selected Ni nanopowders 98814 (stars), 95911 (diamonds), 98478 (triangles), 97502 (squares), 98592 (crosses), and 982174 (circles).

The synthetic method allowed the preparation of nickel nanopowders with controllable characteristics; however, the presence of CO in the process led to residual carbonaceous and oxygenated species, as determined by elemental analysis (Table 6.1). The minimum oxygen content measured was 0.3% by mass (wt %) for the passivated Inco 73011 sample, which was stable in air but also displayed the lowest SSA (6.4 $m^2 \cdot g^{-1}$). In both passivated and non-passivated Ni particles the oxygen content increased with the SSA, as shown in Figure 6.4. Thus the oxygen content of the passivated particles reached 5.5 wt % for a SSA of 30.3 $m^2 \cdot g^{-1}$ (Inco 54074), and up to 11.4 wt % for non-passivated particles (Inco 98814, with a SSA of 60.5 $m^2 \cdot g^{-1}$). The oxygen atoms may play a role as stabilizers during the Ni NPs synthesis, as smaller particle grain sizes were obtained (i.e., larger SSAs) when a higher concentration of residual oxygen was present.[84]

NiO particles (Inco 80852) were also synthesized by the thermal decomposition process, with an oxygen content of 21.0 wt % (theoretical composition: 21.4 wt %). While their oxygen content was much higher than for the other Inco Ni nanopowders, the SSA (31.2 $m^2 \cdot g^{-1}$) of the NiO particles was comparable to that of passivated Ni powders with 5.5 wt % oxygen (Inco 54074, Figure 6.4).

For the passivated particles, the residual C content of the Ni nanopowders ranged from 0.29-0.79 wt %. This is slightly higher than for the non-passivated samples (0.82-1.5 wt %). The fraction of residual C generally increased with the SSA of the particles (Table 6.1).

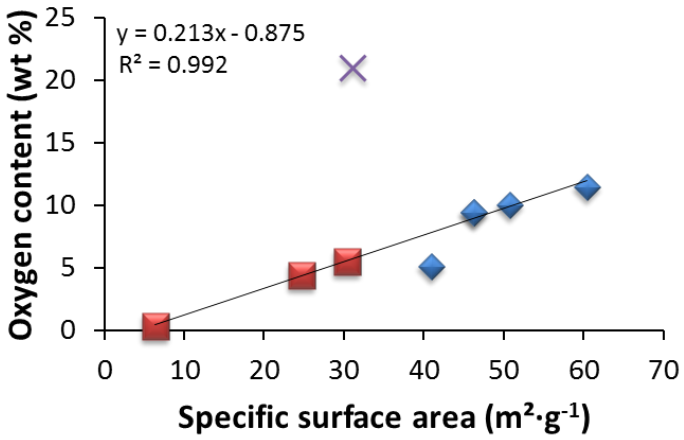

Figure 6.4 Evolution of the oxygen content with the SSA for passivated (squares) and non-passivated (diamonds) Inco Ni nanopowders, and comparison with NiO nanopowder (cross).

6.4.1.2 SEM and TEM imaging

It can be seen from SEM imaging of samples Inco 95911 and 982174 (Figure 6.5 and Figure 6.6, respectively) that the nanoparticles are not spherical, but rather form strand-like aggregates. The size distribution of the particles, measured by laser diffraction analysis, indicated a rather broad size distribution centered around 60 nm (Figure 6.5). For sample Inco 982174, the SEM and TEM images shown in Figure 6.6 revealed a much thinner strand-like shape. The grain size of the smallest features was about 9.4 ± 2.0 nm in diameter.

Exposure of the large SSA particles to air led to sintering upon exothermic oxidation. As shown in the SEM image of Figure 6.7, significant grain growth occurred and the SSA dropped from 97.2 to 38.8 $m^2 \cdot g^{-1}$. The large size increase attests to the high reactivity of the particles, which must be stored under inert atmosphere to prevent sintering.

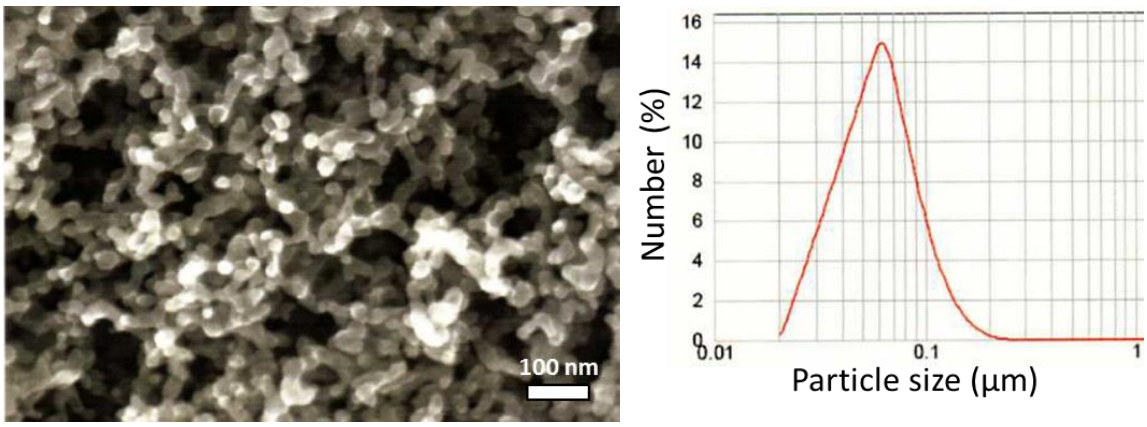

Figure 6.5 SEM image (left) and particle size distribution (right) measured by laser diffraction of the Inco 95911 sample produced by $Ni(CO)_4$ decomposition (50 $m^2 \cdot g^{-1}$).

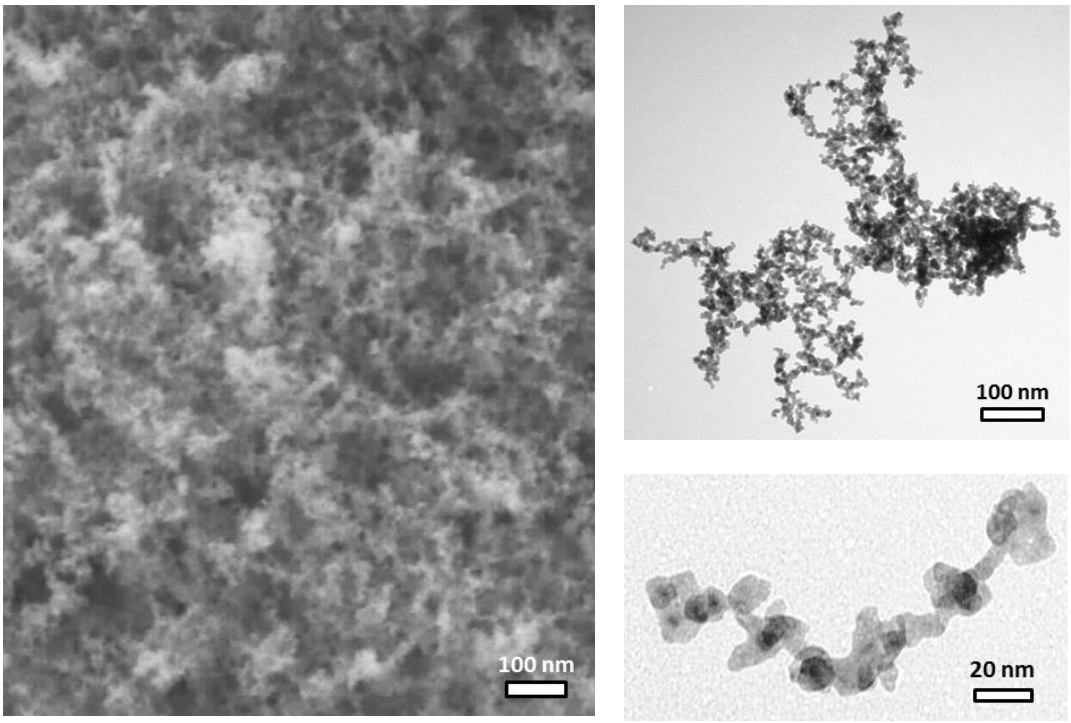

Figure 6.6 SEM (VITSL), and TEM images for Inco 982174 sample (97.2 $m^2 \cdot g^{-1}$).

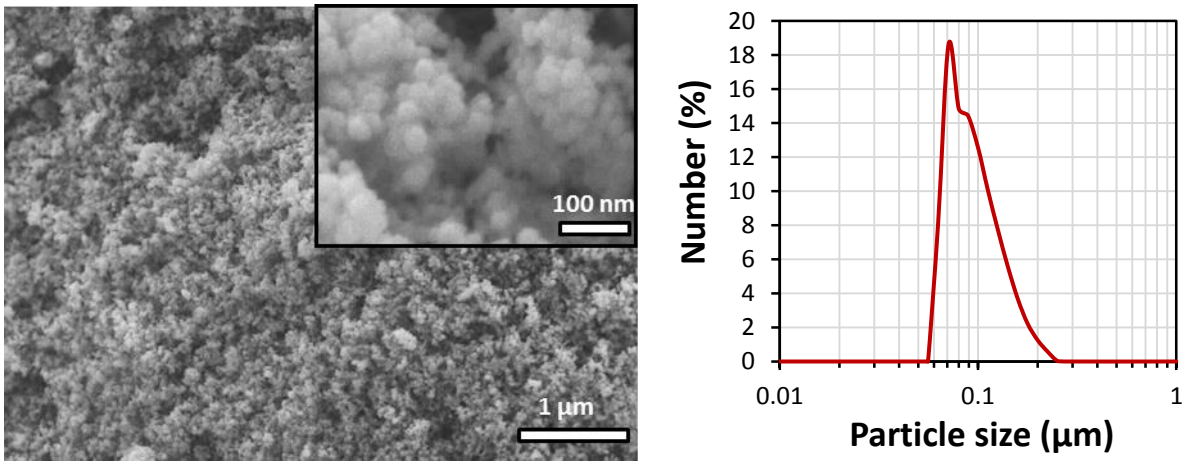

Figure 6.7 SEM image (left), and particle size distribution (right) measured by laser diffraction of Inco 982174 sample after exposure to air (38.8 $m^2 \cdot g^{-1}$).

Imaging by SEM of sample Inco 982174 after 214 days of storage under N_2 revealed further increase in grain size, as shown in Figure 6.8, to become comparable to the sintered sample (Figure 6.7). The decrease in SSA remained modest, however, at 86.4 $m^2 \cdot g^{-1}$. Possible sintering during the SEM measurements could also account for the discrepancies between the SSA and the grain size, since passivation of the particle was performed prior to imaging.

Figure 6.8 SEM image for Inco 982174 sample after 214 days (86.4 $m^2 \cdot g^{-1}$). Sintering may have occurred during sample preparation before the measurements (see text).

6.4.2 Hydrogenation of adiponitrile

6.4.2.1 Reaction mechanism

To evaluate the catalytic performance of the nickel nanoparticles, their activity and selectivity were tested for comparison with commercial nickel catalysts. The reduction of an α,ω-dinitrile (adiponitrile, ADN) to a diamine (1,6-hexamethylenediamine, HMD) was selected, as this reaction plays an important role in the industrial production of amines used as solvents, textile additives, detergents, and monomers for plastics synthesis, among

others.[85–88] In particular, HMD – the most widely used diamine[86] – is pivotal in the polymer industry for the production[89,90] and recycling[82] of polyamides.

The selective catalytic hydrogenation of adiponitrile has been the topic of several studies,[75,82,85,86,89–99] and its industrial production commonly employs Raney® nickel as a catalyst.[90,97] The reaction mechanism was suggested to proceed stepwise, through the formation of intermediate aldimines. The reactive intermediates are then readily converted to primary amines to yield HMD (Scheme 6.1).[90,100–103] It was further suggested that the adsorption mode of the nitrile on the catalyst surface occurs via an equilibrium between end-on (σ, or η^1) and side-on bonding (π, or η^2).[90] However the formation of secondary amines is a common side reaction which stems from coupling of the aldimine intermediate with a primary amine to form an aminal. The loss of ammonia from the aminal yields a secondary imine (Schiff base), which upon hydrogenation forms the secondary amine (Scheme 6.2).[83,86,104] Similarly, tertiary amines can be formed by the reaction of a secondary amine with the imine.[85,105] In the case of α,ω-dinitriles, aminal formation can also proceed via both intramolecular and intermolecular mechanisms, and yield cyclic or oligomeric products, respectively.[83,106] Other byproducts reported include 1,2-diaminocyclohexane and 2-aminomethylcyclopentylamine.[87,107,108]

More recently, Huang and Sachtler rather suggested a concerted mechanism to account for amine formation.[83,103,109] The reaction was proposed to proceed through H atom transfer from a donor to the C atom of the nitrile bonded to the metal surface. Further reduction of the adsorption complex, $RCH_2–N=M$, leads to the formation of a primary amine.

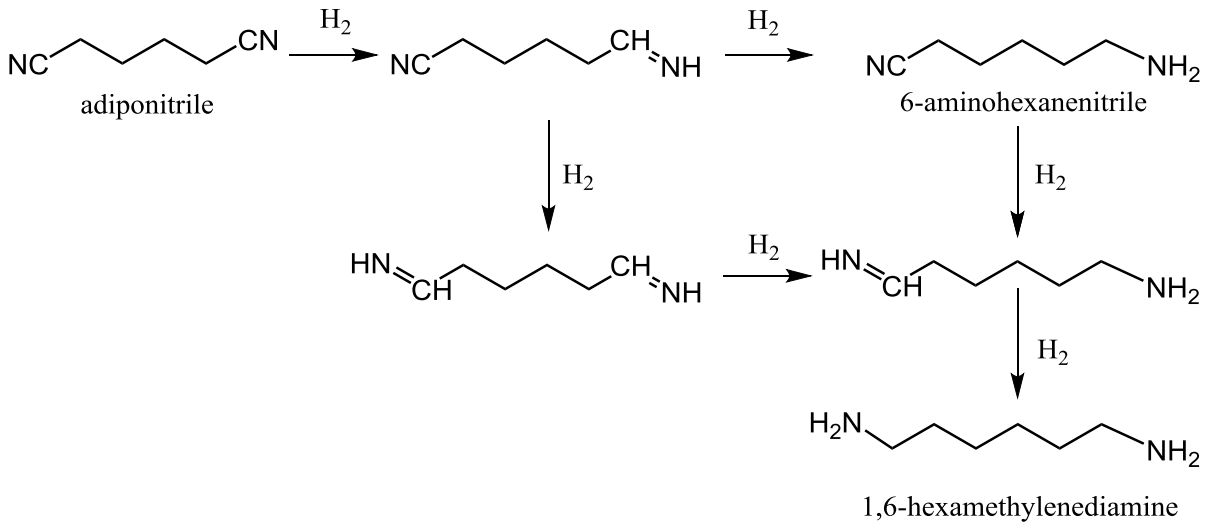

Scheme 6.1 Hydrogenation of adiponitrile to 1,6-hexamethylenediamine via the formation of 6-aminohexanenitrile. Adapted with permission from Reference 97. Copyright 2003 Elsevier.

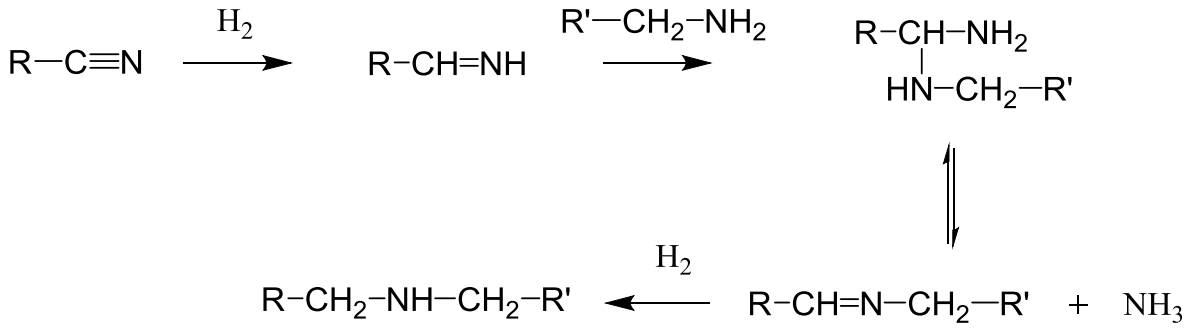

Scheme 6.2 Secondary amine byproduct formation through amine-aldimine condensation in the hydrogenation of nitriles. Adapted by permission from Reference 83. Copyright 2001 Marcel Dekker.

6.4.2.2 Average reaction rates

The catalytic activity and selectivity of the bare (non-stabilized) Ni nanopowders was determined in terms of the conversion of ADN to HMD as estimated by ^{1}H NMR analysis after 24 h (Table 6.2 and Appendix A6.3), for comparison to commercial Ni catalysts (QSI-Nano® nickel NPs, Aldrich nickel nanopowder, and 2 different samples of Raney nickel: WR Grace Raney® nickel 2400 and 2800). The mass of catalyst used was ca. 30 mg in most cases, although for catalysts displaying a low activity the mass was increased up to 250 mg. Under the experimental conditions employed (50 °C, 6.9 MPa) the catalysts did not hydrogenate ADN to HMD selectively; secondary and tertiary amine byproducts were also formed (Table 6.2). The Inco 92831 particles displayed a selectivity for HMD formation almost twice as large as the QSI NPs (66 ± 40 mol % vs. 37 ± 3, respectively), albeit with a large standard deviation (over 4 runs) stemming presumably from the broad size distribution of the particles. Greater selectivity was also obtained with the Inco 92831 particles than the RaNi catalysts 2800 and 2400 (27 ± 10 and 17 ± 14 mol % HMD formation, respectively).

The rate of the reaction was normalized per unit catalyst mass to obtain the specific activity of the catalyst (Equation 6.1); alternatively, the areal activity was also calculated by dividing the conversion rate by the mass (g) and the specific surface area ($m^2 \cdot g^{-1}$) of the catalyst (Equation 6.2).

$$\text{Specific activity} = r_{1,\text{m}} = \frac{\text{ADN moles converted}}{\text{time} \times \text{mass of catalyst}} \tag{6.1}$$

$$\text{Areal activity} = r_{1,sa} = \frac{\text{ADN moles converted}}{\text{time} \times \text{mass of catalyst} \times \text{specific surface area of catalyst}} \tag{6.2}$$

Table 6.2 Catalyst performance in the reduction of adiponitrile to 1,6-hexamethylene-diamine in methanol (t = 24 h, T = 50 °C, P_{H_2} = 6.9 MPa, $[ADN]_0$ = 0.5 mol·L^{-1}, m_{cat} = 0.03–0.25 g).[a]

Catalyst	Conversion[b] (mol %)	HMD selectivity[c] (%)
QSI-Nano®	100 ± 0	37 ± 3
Inco 92831	92 ± 6	66 ± 40
Inco 112376	73 ± 2	18 ± 4
Inco 113132	56 ± 15	16 ± 6
Inco 95911	52 ± 14	13 ± 5
Inco 108775	51 ± 14	14 ± 7
Raney® Nickel 2800	48 ± 18	27 ± 10
Inco 85109	46 ± 20	20 ± 4
Raney® Nickel 2400	35 ± 16	17 ± 14
Inco 92831 (heptane)	33 ± 1	14 ± 5
Aldrich NPs	14 ± 15	40 ± 1
Inco 73011	7 ± 7	11 ± 4

[a] Averages and standard deviations obtained from at least 2 measurements.

[b] Conversion (mol %) $= \frac{\text{initial ADN moles} - \text{final ADN moles}}{\text{initial ADN moles}} \times 100.$

[c] Selectivity (%) $= \frac{\text{HMD moles formed}}{\text{initial ADN moles} - \text{final ADN moles}} \times 100.$

The data of Figure 6.9 show that the QSI NPs had the highest specific catalytic activity ($r_{1,m}$ = 13.0 ± 0.2 µmol·s^{-1}·g^{-1}) among the particles tested, although both Inco 113132 and 112376 yielded comparable but less reproducible results. Among the Inco NPs tested, the highest activity was observed for nanopowders with a relatively large SSA and both non-passivated (Inco 112376, 73.0 m^2·g^{-1}) and passivated (Inco 113132, 85.5 m^2·g^{-1}). It is noteworthy that these catalysts demonstrated a specific activity more than 9-fold higher than the Raney® Ni 2800 catalyst, and more than 21-fold higher than the Aldrich NPs.

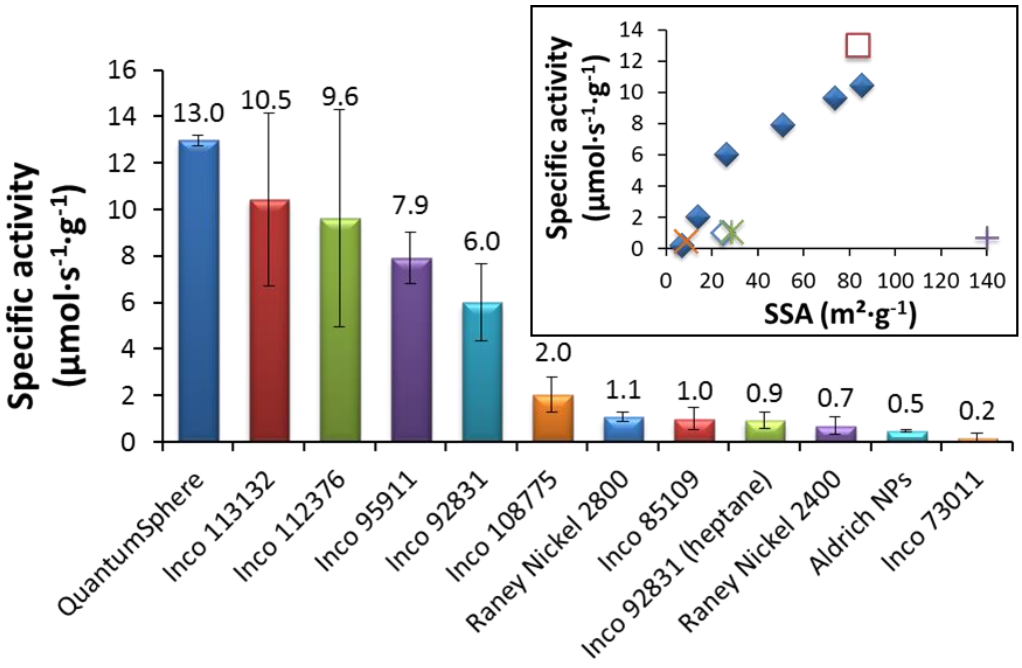

Figure 6.9 Specific activity of Inco nanopowders and commercial Ni catalysts in the reduction of adiponitrile to 1,6-hexamethylenediamine in methanol (*t* = 24 h, *T* = 50 °C, P_{H2} = 6.9 MPa, $[ADN]_0$ = 0.5 mol·L^{-1}, m_{cat} = 0.03-0.25 g). Inset: Comparison of the specific activity of Inco nanopowders (solid diamonds; Inco 85109 hollow diamonds), with Raney® nickel 2400 (+), Raney® nickel 2800 (∗), Aldrich nanopowder (×), and QSI-Nano® nickel NPs (hollow square).

The Inco 92831 particles, when stored under nitrogen, displayed good activity; however, the same sample stored in heptane was marred by significant deactivation. It is likely that hydrocarbon contamination of the surface resulted in fouling by coke formation or poisoning of the catalyst.[110] Aside from the Inco 85109 particles, the specific activity increased logarithmically with the SSA of the Inco nanopowders (inset of Figure 6.9). The other nanosized commercial catalysts also followed this trend, although RaNi 2400 was an exception (inset of Figure 6.9).

A comparison of the areal activity of the catalysts, shown in Figure 6.10, gave a rather different distribution, and the Inco 92831 nanopowder was found to be the most active catalyst by this criterion ($r_{1,\mathrm{sa}}$ = 0.23 ± 0.06 μmol·s^{-1}·m^2). Among the remaining particles, two distinct catalyst groups can be identified. With the exception of the Inco 85109, 73011, and 92831 nanopowders stored in heptane, all the Inco catalysts and the QSI nanoparticles had a comparable areal activity ($\bar{r}_{1,\mathrm{sa}}$ = 0.14 μmol·s^{-1}·m^2). The other commercial catalysts and Inco nanopowders were about 4 times less active ($\bar{r}_{1,\mathrm{sa}}$ = 0.03 μmol·s^{-1}·m^2). As noted above, the passivated Inco 85109 nanopowder also exhibited a specific activity versus SSA different from the trend displayed by the other catalysts (inset of Figure 6.9). Possible fouling or poisoning of the catalyst may account for this low activity. A minimum SSA also appears to be required for the onset of a catalytic activity, as the passivated particles Inco 73011 with a low SSA were poor catalysts in the reduction of ADN. The deleterious effect of heptane as a solvent was already discussed in regard to the low activity displayed by the Inco 92831 particles (vide supra). It is noteworthy that the Ni nanopowders still performed significantly

better than the Raney catalysts or the Aldrich NPs both in terms of specific and areal activities.

From a practical viewpoint, the rate per unit catalyst mass (i.e., the specific activity) is considered most significant since it reflects the amount of catalyst required to attain a certain conversion under the conditions used. However, comparison of the areal activities of the Inco Ni nanopowders suggests that the rate of the reduction reaction is independent of the SSA, i.e. structure-insensitive. While the particle size dependence of the reduction of ADN over Ni remains unclear,[97] hydrogenation reactions are often considered to be structure-insensitive.[111]

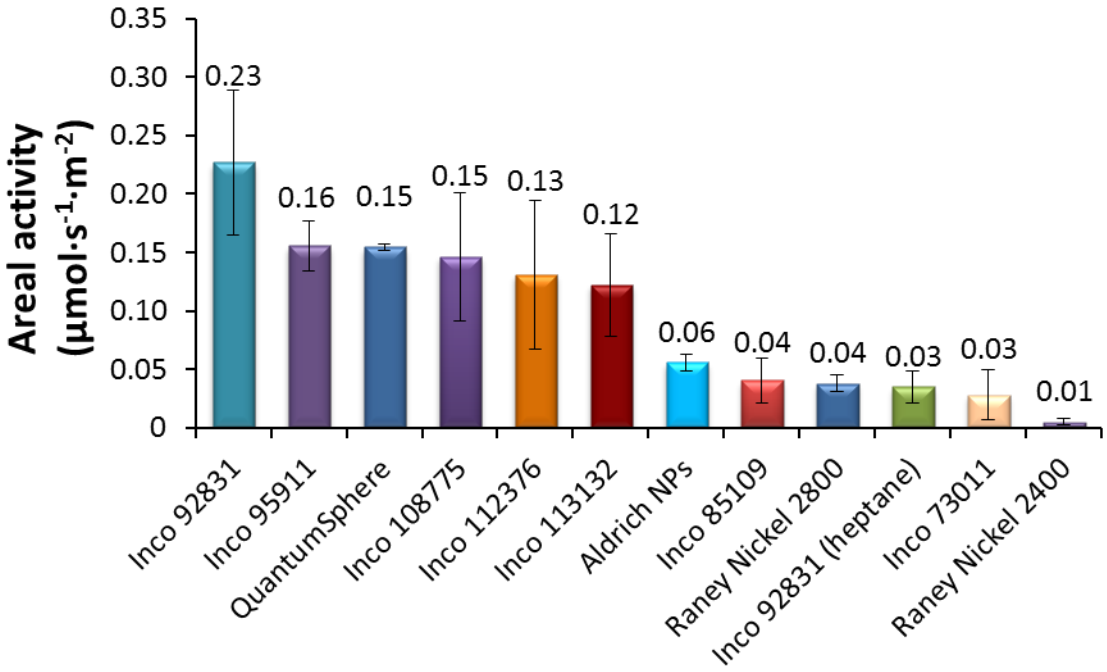

Figure 6.10 Areal activity of Inco nanopowders and commercial Ni catalysts in the reduction of adiponitrile to 1,6-hexamethylenediamine in methanol (*t* = 24 h, *T* = 50 °C, P_{H_2} = 6.9 MPa, $[ADN]_0$ = 0.5 mol·L^{-1}, m_{cat} = 0.03-0.25 g).

6.4.3 Hydrogenation of mesityl oxide

6.4.3.1 Mesityl oxide substrate

To further investigate the performance of the Ni catalysts prepared at VITSL, as well as to study the influence of polymeric stabilizers on their catalytic activity, mesityl oxide was chosen as a substrate. This compound presents several advantages making it attractive for use in a benchmark hydrogenation reaction. First of all, MO contains two reactive functional groups (an alkene and a ketone), allowing an investigation of selectivity for reduction of the more reactive alkene group (see Scheme 6.3). This occurs under relatively mild conditions and presents fewer side reactions than ADN. Furthermore, MO and its reduction products do not contain any functional groups potentially interfering with the binding of amine-functionalized polymeric dispersants on the surface of the particles. Finally, MO and its reduction products can be conveniently analyzed by gas chromatography.[112]

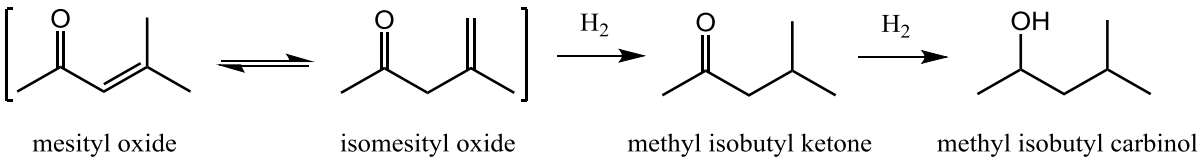

Scheme 6.3 Hydrogenation of mesityl oxide. Adapted with permission from Reference 112. Copyright 2005 Elsevier.

Mesityl oxide serves in the production of methyl isobutyl ketone (MIBK), an important solvent used in paints and resin coatings. MIBK also finds applications in pharmaceuticals and metallurgical processes, as well as in the production of surfactants and other specialty chemicals.[112,113] The production of MO from acetone is a three-stage process

starting from the aldol condensation of acetone to form the intermediate compound diacetone alcohol, followed by dehydration over an acid catalyst leading to the formation of MO. The final step (Scheme 6.3) requires the catalytic hydrogenation of MO to yield MIBK.[112]

6.4.3.2 Initial reaction rates

The hydrogenation of MO was performed in a batch reactor in 2-propanol; and in contrast to the reactions using ADN, the reactor was equipped with a sampling tube allowing monitoring of the kinetics of the reaction (Figure 6.2b). The concentration of MO was monitored over a 3–6 h period. Figure 6.11 displays typical concentration versus time profiles obtained using nickel nanocatalysts QSI-Nano®, and the Inco 982174 and 112376 nanopowders.

The initial reaction rate for the different catalysts was determined by fitting the concentration profile to a second-order polynomial given by Equation 6.3.

$$C(t) = c_1 + c_2 t + c_3 t^2 \tag{6.3}$$

An expression for the rate of the reaction as a function of time was then obtained from the derivative of Eq. 6.3, where the constant c_2 represents the initial rate of the reaction and c_3 the initial concentration of MO.[112] The rates were normalized either per unit mass of catalyst, or per unit surface area to obtain the specific ($r_{2,m} = c_2 \cdot m_{cat}^{-1}$) and areal ($r_{2,sa} = c_2 \cdot SSA_{cat}^{-1}$) initial rates, respectively.

The specific initial rate of reaction for experiments performed at a partial pressure of 1.38 MPa H_2 and 50 °C is shown in Figure 6.12. The mass of catalyst used was typically ca.

30 mg, but for catalysts displaying a low activity ($r_{2,m}$ < 1 mol·L^{-1}·g^{-1}·h^{-1}) the amount of metal was increased up to 3-fold. The activity of the commercial nickel catalysts QSI-Nano® and RaNi 2400 was compared to representative samples of non-passivated (Inco 112376) and passivated (Inco 85109) Inco nanopowders. As in the reduction of ADN, the performance of the QSI particles was found to be highest with an initial specific rate constant of 10.1 mol·L^{-1}·h^{-1}. The Inco 112376 nanopowders displayed a significantly lower catalytic activity, 0.7 mol·L^{-1}·h^{-1}, but were still 3 times as active as the RaNi 2400 catalyst. The passivated Inco 85109 particles stored in contact with air for several months were inactive in the hydrogenation of MO.

The substrate used contained 3.8 ± 0.4 mol % of isomesityl oxide (IMO), as determined by GC analysis. IMO was converted readily (within 30 min) to MIBK over all the catalysts except RaNi, which displayed poor activity for the hydrogenation of both MO and IMO. All the catalysts were selective for the formation of MIBK however, and under the experimental conditions employed no formation of methyl isobutyl carbinol (MIBC) was noted.

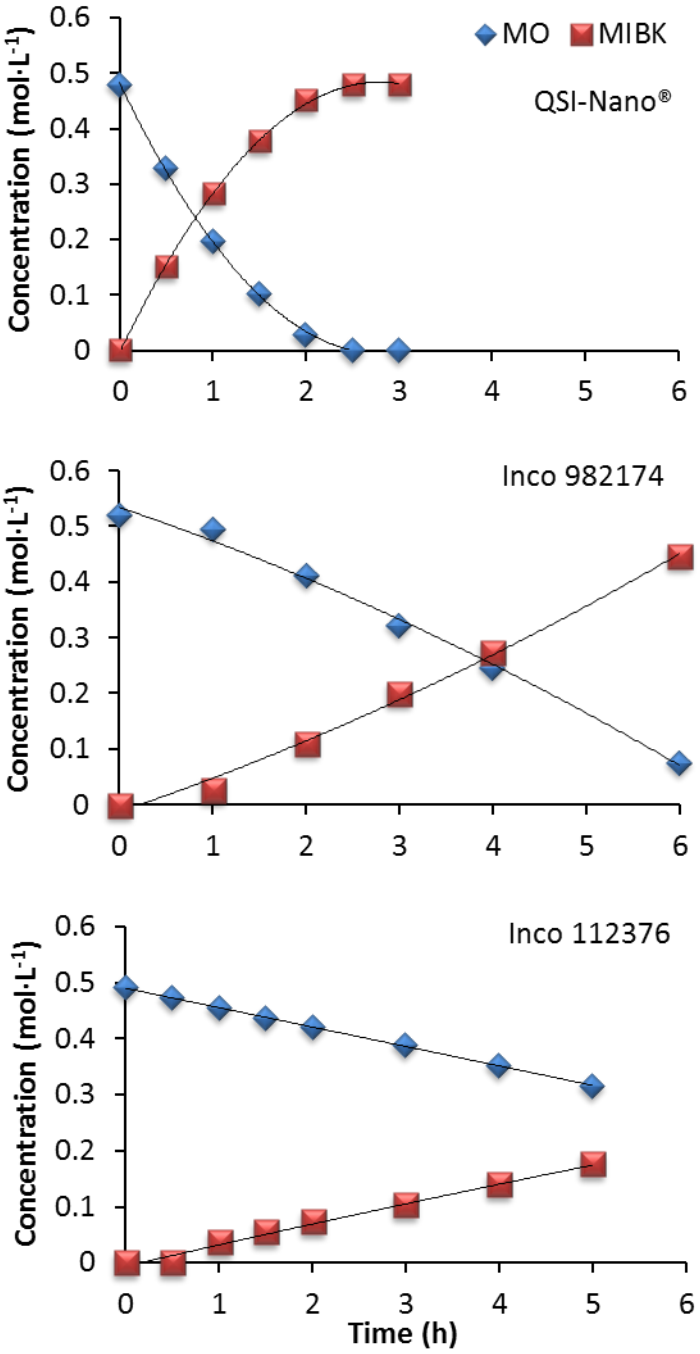

Figure 6.11 Representative concentration-time profiles for the hydrogenation of mesityl oxide (diamonds) to methyl isobutyl ketone (squares) over QSI-Nano® with the Inco 982174, and Inco 112376 catalysts (T = 50 °C, P_{H_2} = 1.38 MPa, $[MO]_0$ = 0.5 mol·L^{-1}, ω = 330 rpm, m_{cat} = 30 mg).

6.4.3.3 Reduction of the nickel catalyst

To decrease the oxygen content of the nickel particles and thus increase their catalytic activity, reduction under hydrogen atmosphere was first attempted. Passivated sample Inco 73011, characterized by a low degree of oxidation (0.26 wt % oxygen content) and a low SSA (6.4 $m^2 \cdot g^{-1}$), displayed an average areal activity in the reduction of adiponitrile comparable to RaNi 2400 ($r_{1,m}$ = 0.03 $\mu mol \cdot L^{-1} \cdot g^{-1} \cdot h^{-1}$, and 0.01 $\mu mol \cdot L^{-1} \cdot g^{-1} \cdot h^{-1}$, respectively). After purging of the reactor, the particles were reduced at P_{H_2} = 6.89 MPa and 250 °C for 2 h. The catalytic activity of the non-passivated particles for the formation of HMD decreased 5-fold after 24 h however. Decoking of the nanoparticles was also attempted by thermal treatment under flow of 10% (v/v) H_2/N_2 at 500 °C for 5 h, at a flow rate of 110 $mL \cdot min^{-1}$, in presence of SiO_2. This treatment led to complete deactivation of the catalyst. While the origin of the deactivation in both experiments has not been determined, it could stem from sintering of the particles and/or contamination of the catalyst surface by the silica.

Another approach explored to decrease the oxygen content of the particles was chemical treatment of their surface. It was found that treatment of the particles with diethylenetriamine (DETA) led to a significant increase in the catalytic activity of the particles. For instance the Inco 85109 sample, stored in contact with air for several months, was totally deactivated. Upon addition of DETA, an exothermic reaction was observed and after a few seconds a purple tinge was observed in the vicinity of the particles. Hydrogen gas was evolved, as typically observed in the reduction of Ni(II).[114] This effect was particularly prominent for the Raney nickel and Inco 112376 samples. As shown in Figure 6.12a, upon exposure to DETA the catalytic activity of the Inco 85109 particles increased dramatically

(from zero activity to $r_{2,m}$ = 6.4 mol·L^{-1}·g^{-1}·h^{-1}), while the activity of RaNi 2400 increased 13-fold. If a constant surface area is assumed the activity of the former catalysts, when normalized per unit surface area, became over twice as large as that of the QSI particles without treatment (Figure 6.12b). The treated catalysts were also selective for the reduction of the internal alkene, and no MIBC was formed.

A promoting effect of amine additives was noted by Kajitani et al., for instance in the hydrogenation of 2-naphtol over a Ni catalyst, but its exact origin was not determined.[115] Amines are also well-known complexing agents for Ni(II),[116,117] used industrially in processing nickel oxides ores.[118] It is noteworthy that amine exposure had no effect on the performance of Inco 112376, and led to total deactivation of the QSI catalyst. In these cases the amine treatment seems to have resulted in poisoning of the catalyst surface, in contrast to the exothermic reaction observed for the other particles (Figure 6.12).

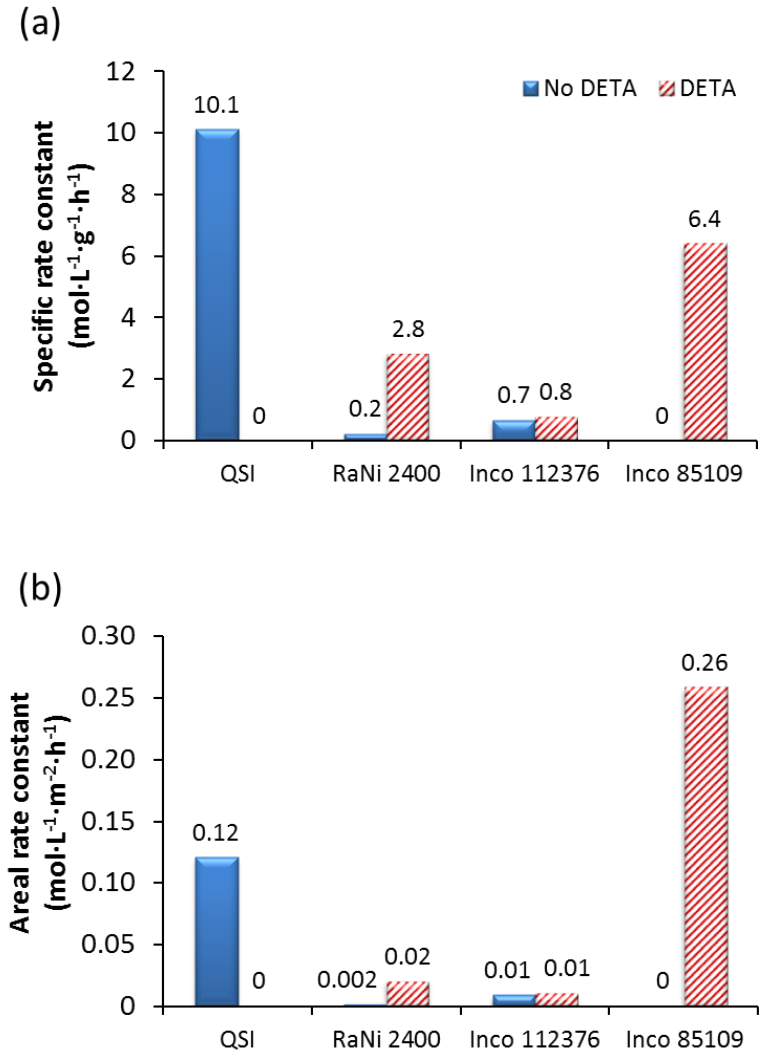

Figure 6.12 Effect of DETA treatment on the (a) specific catalytic activity and (b) areal activity of Ni nanocatalysts (T = 50 °C, P_{H_2} = 1.38 MPa, $[MO]_0$ = 0.5 mol·L^{-1}, ω = 330 rpm, m_{cat} = 30–100 mg).

6.4.3.4 Nanopowder Inco 982174

To further improve the catalytic activity of the Ni nanopowders, a fresh sample (Inco 982174) was synthesized at VITSL by the method previously described. A short residence time in the reactor and rapid quenching in liquid nitrogen were used to promote fast nucleation over particle growth. The Ni nanoparticles thus obtained had a SSA of 97.2 $m^2 \cdot g^{-1}$, greater than the QSI NPs (84.0 $m^2 \cdot g^{-1}$) prepared by a CVD process.

A series of experiments using the Inco 982174 particles (Figure 6.13) yielded rather low initial reaction rates and poor reproducibility ($r_{2,m}$ = 1.0 ± 1.1 $mol \cdot L^{-1} \cdot g^{-1} \cdot h^{-1}$ over 10 runs). In comparison, the QSI nanoparticles displayed 10 times the activity of the Inco sample in the reduction of MO in 2-propanol, with a narrow standard deviation ($r_{2,m}$ = 10.1 ± 0.5 $mol \cdot L^{-1} \cdot g^{-1} \cdot h^{-1}$, over 3 runs). Differences in colloidal properties and rate of aggregation of the particles in the solvent may explain the differences in catalytic performance of the catalysts, and were further investigated.

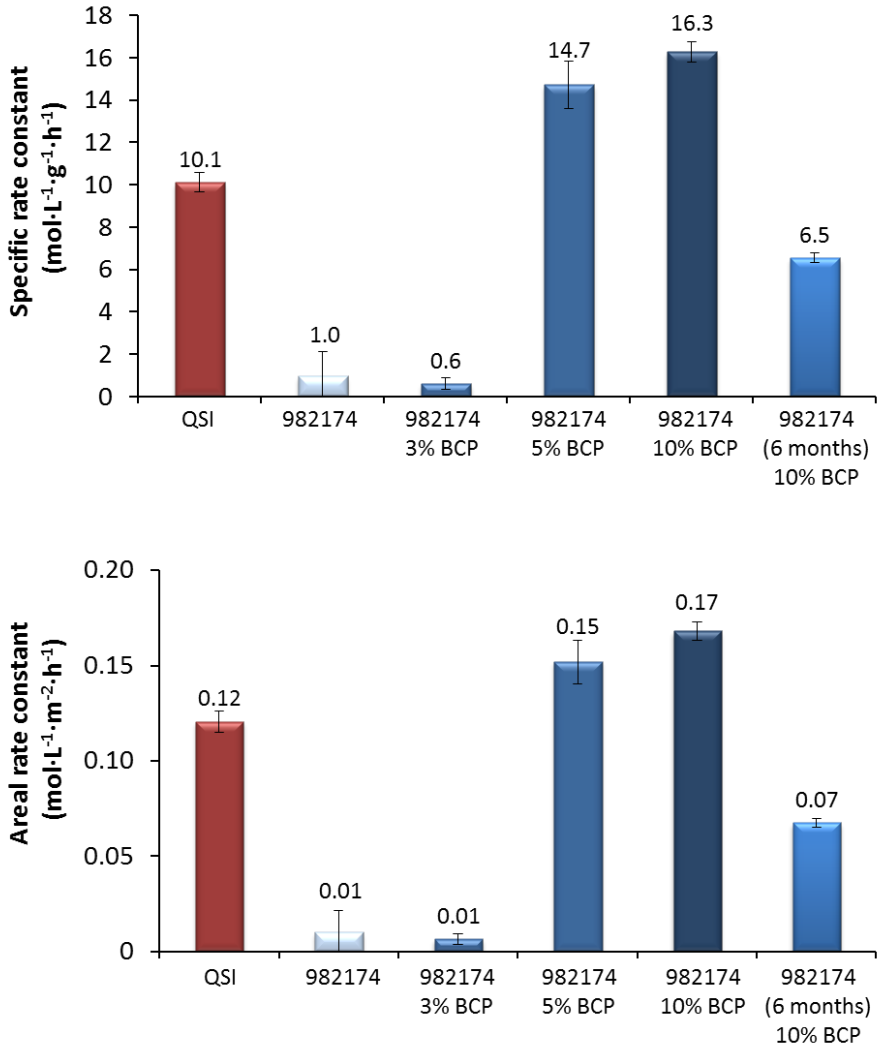

Figure 6.13 Specific (top) and areal (bottom) initial rate constants for the reduction of mesityl oxide using QSI Ni nanoparticles; freshly prepared Inco 982174 nickel bare particles and stabilized by 3, 5 and 10 wt % P2VP$_{8k}$-*b*-PS$_{6k}$-*b*-P2VP$_{8k}$; and Inco 982174 nanopowder stored 6 months and stabilized by 10 wt % P2VP$_{8k}$-*b*-PS$_{6k}$-*b*-P2VP$_{8k}$ (T = 50 °C, P_{H2} = 1.38 MPa, [MO]$_0$ = 0.5 mol·L^{-1}, ω = 330 rpm, m_{cat} = 30 mg).

6.4.4 Colloidal stabilization

6.4.4.1 Colloidal stabilization in catalysis

Colloidal particles are subjected to attractive forces that can lead to their aggregation, particularly for large particles. Short-range van der Waals attractive forces can be opposed either by electrostatic or steric repulsive forces to improve the colloidal stability of particles in a dispersion medium.[119] The latter approach is preferred when dealing with demanding catalytic conditions, and is typically achieved through adsorption on the particles of a polymer layer soluble in the dispersion medium, as depicted in Figure 6.14a.

The stabilization mechanism depends on the type of polymer involved. Homopolymers can provide a protective layer by surrounding the particles through the formation of multiple interactions,[55,69] although aggregation is still possible via a bridging mechanism (vide infra). For block copolymers containing both hydrophobic and hydrophilic segments, stabilization can be achieved in polar as well as non-polar solvents. In the former solvents, the polar polymer block interacts favorably with the solvent while the non-polar groups adsorb on the particles through hydrophobic interactions; the opposite situation occurs in non-polar solvents.[71,72] In addition to adsorbing on the catalyst particles, block copolymers are prone to micelle formation in solution above the critical micelle concentration (CMC) of the system, while remaining at equilibrium with unassociated polymer chains in solution. A similar situation may also exist for telechelic polymers (with a functional group at one or both chain ends), but in this case anchoring of the polymer on the surface of the particles occurs at a single site while the rest of the chain contributes to the stabilization of the particles.

A negative effect of polymeric additives is that they may lead to flocculation of the particles rather than their stabilization. For instance, a phenomenon known as bridging flocculation occurs when the same polymer chain adsorbs on two or more particles, linking them together and thus inducing their flocculation (Figure 6.14b). This can take place when a large surface area is available for the polymer segments, or when the polymer chains can interpenetrate each other at short distances. Expectedly, bridging is most commonly observed for high molar mass polymers.[120] Depletion flocculation is another mechanism induced by non-adsorbing chains: Elastic repulsions are engendered by the loss of configurational entropy of the polymer coils upon approach to a particle surface, and results in flocculation as illustrated in Figure 6.14c.[121]

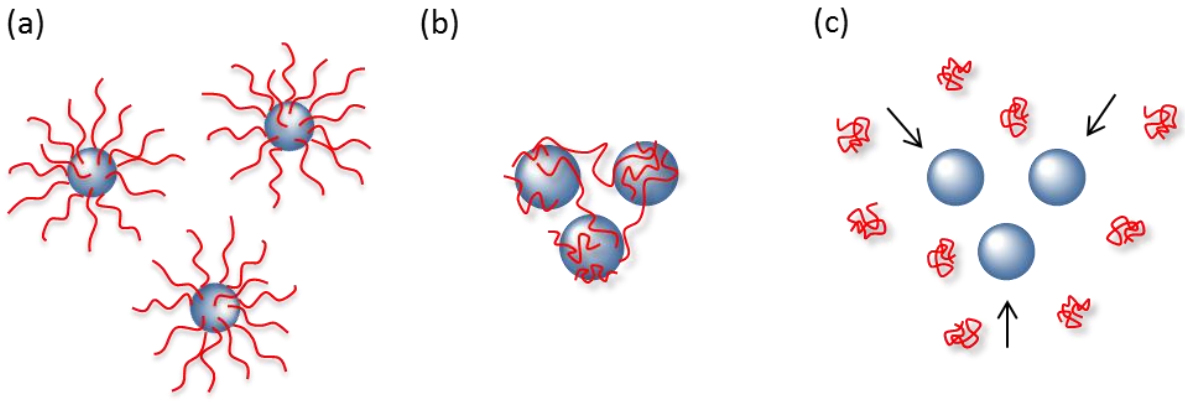

Figure 6.14 Schematic representation of (a) steric stabilization, (b) bridging flocculation, and (c) depletion flocculation.

The first step in a heterogeneous catalysis process requires the reactants and catalyst to come in contact; it is thus strongly dependent on steric hindrance. Clearly, polymer chains forming a stabilizing layer can cause such steric hindrance. If the interactions between the

polymer and the catalyst are strong, there may be few vacant catalytic sites remaining at the surface. It may then prevent the substrate molecules from adsorbing on the surface, thereby greatly hindering the occurrence of catalytic reactions. Conversely, if stabilizing polymer chains have very weak interactions with the surface of the catalyst, the substrate can more easily compete for coordinating sites on the catalyst surface.[69] It should be noted that even if the polymer-catalyst interactions are relatively weak, a large number of interacting sites along the polymer chain (for instance at every repeating unit) may still lead to strong combined interactions.[68,69]

Optimal stabilization can be achieved by tailoring the characteristics of the stabilizing moieties. By using polymers with relatively few anchoring groups one can minimize catalytic sites hindrance, while a sufficiently long solvophilic chain is required for steric stabilization of the particles. For this purpose, we compared the use of telechelic polymers such as poly(ethylene glycol) (PEG) end-functionalized with chelating agents (DETA), triblock copolymers with a midblock anchoring site and end blocks providing steric stabilization, and homopolymers.

6.4.4.2 Effect of solvent

The influence of the solvent on the dispersibility of the particles is important. For example, a dispersion of 30 mg of Inco 982174 in 2-propanol remained stable for 4 days, while in toluene the particles settled after 1 minute. As shown in Figure 6.15, the Inco 85109 nanoparticles dispersed in solvents displayed greater colloidal stability as the polarity of the solvent increased, although water was a significant exception to this rule as the particles aggregated within 3 h.

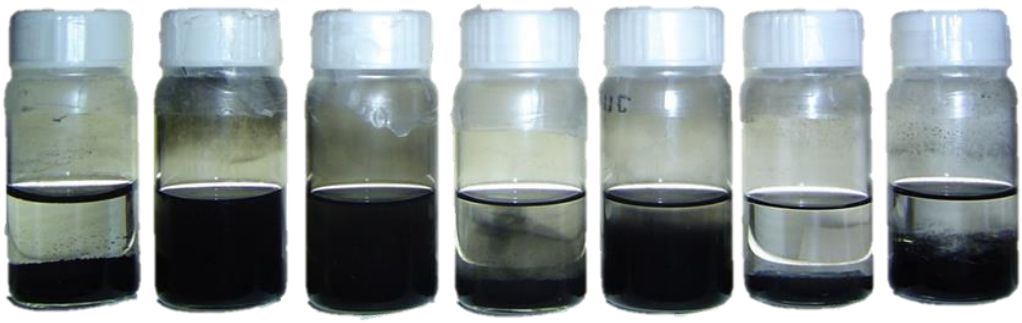

Solvent	**Water**	**Methanol**	**2-Propanol**	**Acetone**	**THF**	**Dichloro-methane**	**Toluene**
Dielectric constant[a]	88.1	33.0	20.2	21.0	7.5	8.9	2.4
Aggregation time[b]	3 h	4 days	4 days	1 day	1 day	6 h	1 min

[a] Data from CRC handbook of Chemistry and Physics, 94th ed.[122] [b] Time for the particles to settle, and the solution to become clear.

Figure 6.15 Colloidal stability of Inco 85109 in various solvents (m_{cat} = 30 mg, $V_{solvent}$ = 10 mL).

6.4.4.3 Polymer stabilization

A more in-depth investigation of the rate of aggregation was performed in water by UV-visible spectrophotometry, as shown in Figure 6.16. The bare Inco 85109 particles settled quickly in water, within a few hours. To promote dispersion, linear homopolymers including PVPy, polyethyleneimine (PEI), poly(ethylene glycol) methyl ether (MPEG), as well as telechelic polymers based on MPEG were added to the particles. The emphasis was set on PEG dispersants because of their relatively good solubility in a wide range of low- to

high-polarity solvents. Amine groups are also of particular interest because of their known ability to bind many transition metals including nickel. Homopolymers are good stabilizers as they have a large number of functional groups interacting with the surface of the nanoparticles, but this may also hinder the catalytic sites. Telechelic polymers are interesting to provide steric stabilization while minimizing hindrance of the surface, due to their small number of interacting groups.

The particles (ca. 30 mg), and solvent (10 mL) were added to a 20 mL vial and sonicated for 30 min. After the addition of 75 wt % ($m_{stabilizer}/m_{total}$) of polymer and sonication the rate of aggregation was reduced in all cases, although only the homopolymers with a high molar mass provided steric stabilization over extended time periods (weeks). Stabilization by PVPy with a molar mass of 6.0×10^4 g·mol^{-1} was poor, but it was greatly improved when the molar mass reached 1.3×10^6 g·mol^{-1}. Low molar mass telechelic polymers ($\bar{M}_n = 1.9 \times 10^3$ g·mol^{-1}) offered limited steric stabilization, although the rate of aggregation was slightly decreased when the MPEG was end-functionalized with DETA, as well as when the mass of polymer added was increased from 75 to 85 wt % (Figure 6.16).

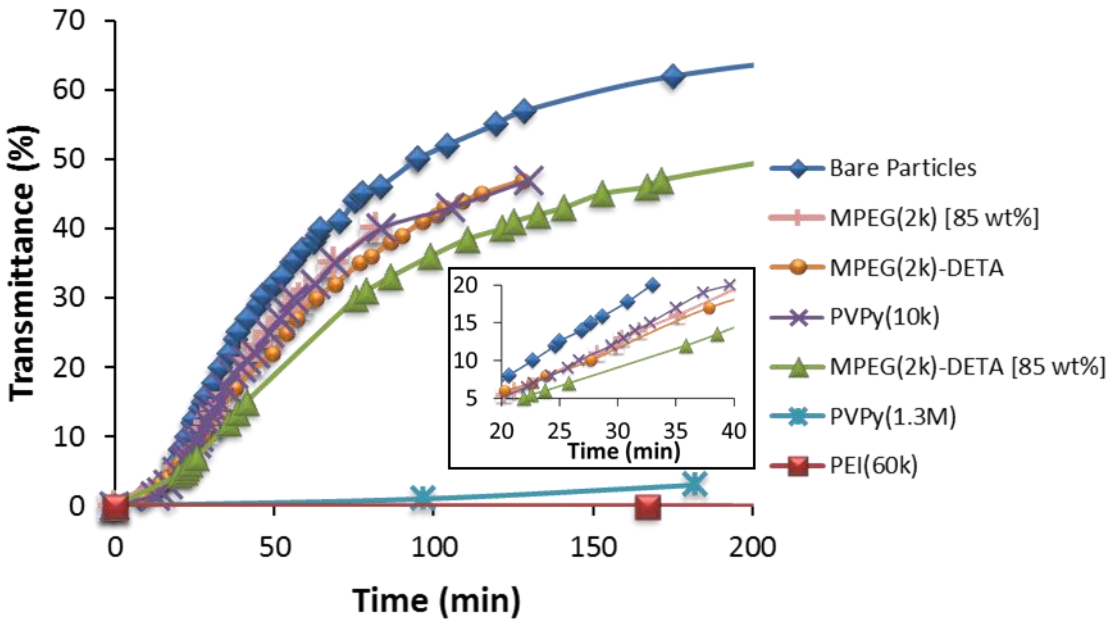

Figure 6.16 Colloidal stability of Inco 85109 nickel nanopowders in water measured by UV-visible spectrophotometry at λ = 500 nm. Comparison of bare and polymer-stabilized particles ($m_{particles}$ = 20 mg, V_{water} = 10 mL, $m_{stabilizer}$ = 60 mg [75 wt %] or 120 mg [85 wt %]). Inset: Percent transmittance over the 20-40 min time period.

Addition of the bare particles to methanol or 2-propanol yielded more stable dispersions, which settled within 4 days (Figure 6.16) rather than a few hours (as in water). The addition of telechelic polymers proved detrimental in these cases however, and led to flocculation of the particles. Depletion flocculation may be induced by free polymer chains in solution. The stabilizing ability of the telechelic MPEG dispersants was most noticeable in low polarity solvents (e.g., toluene), the settling time of the particles becoming about 2-3 times longer than for the bare particles.

The utilization of triblock copolymers to promote stronger anchorage of the polymer chains to the metal surface, favoring steric stabilization, was explored using $PEO_{6.6k}$-*b*-PS_{700}-

b-$PEO_{6.6k}$ (the subscript indicates the $\bar{M}_n$, of the PS and PEO segments) and P2VP-*b*-PS_{800}-*b*-P2VP block copolymers (with $\bar{M}_{n,P2VP}$ = 700, 1200, and 3000 g·mol^{-1}) prepared by anionic polymerization as described in Appendix A6.1. As in the case of telechelic polymers, the addition of the triblock copolymers induced the flocculation of Inco 85109 particles in methanol within 4 h (Figure 6.17). Increasing the length of the midblock segment from 800 to 6.0 × 10^3 g·mol^{-1} ($P2VP_{8k}$-*b*-PS_{6k}-*b*-$P2VP_{8k}$) was also found inadequate: Flocculation and settling of the particles was observed in less than 30 min, with the opalescent appearance of the supernatant indicating the formation of micelles.

An alternate procedure for the addition of the polymer to the particles was devised to minimize the formation of micelles and promote the adsorption of the copolymer to the surface of the catalyst. The copolymer ($P2VP_{8k}$-*b*-PS_{6k}-*b*-$P2VP_{8k}$) was first dissolved in toluene, a solvent for both the P2VP and PS segments, and added to the particles with sonication. The solvent was then evaporated before adding 2-propanol drop-wise with sonication, to redisperse the particles. Under these conditions, $P2VP_{8k}$-*b*-PS_{6k}-*b*-$P2VP_{8k}$ provided good particle stabilization over 1 day, with larger particles settling while the solution remained brown (Figure 6.17), hinting at the stabilization of very fine particles over an extended time period (25 days). In comparison, the addition of P2VP-*b*-PS_{800}-*b*-P2VP with different P2VP block lengths to the particle dispersions by the same method led to flocculation after 2 h in methanol, suggesting weak anchoring through the short PS mid-block of that copolymer.

These results indicate clearly that the structure and the composition of the copolymers must be tailored so that sufficient anchoring of the polymer chains on the surface of the

particles and good colloidal stability can be achieved. Such a goal can be attained using block copolymers with sufficiently large anchoring blocks.

Figure 6.17 Colloidal stability in methanol of Inco 85109 Ni nanopowder stabilized by (left) $PEO_{6.6k}$-*b*-PS_{700}-*b*-$PEO_{6.6k}$ after 4 h, and (right) $P2VP_{8k}$-*b*-PS_{6k}-*b*-$P2VP_{8k}$ after 25 days.

6.4.4.4 Adsorption isotherms

The determination of the amount of polymer bound to the Inco 982174 particles was performed using a concentration-sensitive diffraction refractive index detector (DRI) on a SEC instrument. The polymer-stabilized particles were first separated from the solvent by centrifugation, and any free polymer chains in the supernatant were recovered and transferred to THF. Quantification of the polymer was achieved by calibration of the DRI detector with a sample of the same triblock copolymer.

As shown in Figure 6.18, the analysis of solutions prepared with 10 and 15 wt % ($m_{stabilizer}/m_{total}$) of stabilizer did not reveal the presence of free chains. The measurements were carried out after dispersing the particles for 3 h in IPA at 25 or 50 °C, or in IPA with 0.5 M of mesityl oxide at 50 °C, the latter conditions being akin to the conditions used for the

hydrogenation reactions. When increasing the initial amount of polymer to 20 wt %, the maximum amount of chains remaining attached was 18 ± 1 wt %, which indicates a limiting value for the surface coverage.

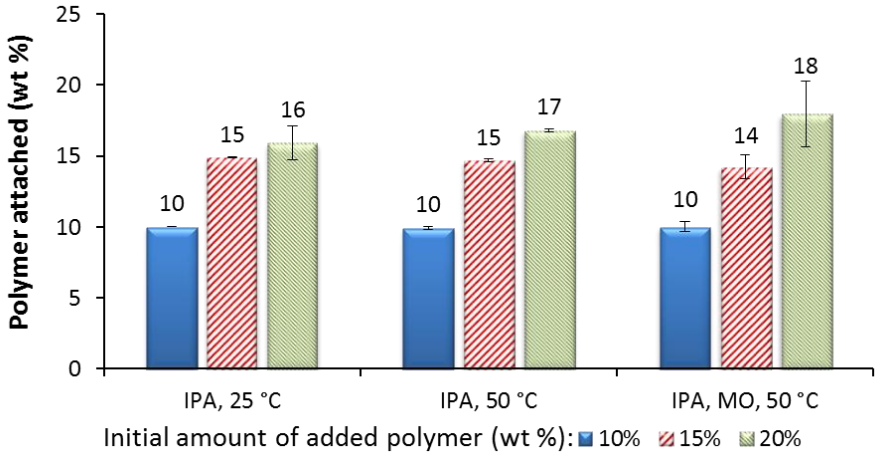

Figure 6.18 Fraction of polymer bound to Inco 982174 Ni nanopowder when using 10, 15, and 20 wt % ($m_{stabilizer}/m_{total}$) of P2VP$_{8k}$-*b*-PS$_{6k}$-*b*-P2VP$_{8k}$ in 2-propanol (IPA) at 25 or 50 °C, and in mixtures of IPA and mesityl oxide (MO), at 50 °C. The amount of non-bound polymer was determined by SEC-DRI analysis (m_{cat} = 4.8 mg, $m_{polymer}$ = 0.5–1.2 mg, V_{IPA} = 10 mL, [MO] = 0.5 mol·L^{-1}, t = 3 h).

6.4.4.5 Catalytic activity of polymer-stabilized particles and TEM imaging

Previous results (Section 6.4.3.4) demonstrated that the catalytic activity of the bare Inco 982174 nanoparticles in the reduction reaction of MO was low and irreproducible ($r_{2,m}$ = 1.0 ± 1.1 mol·L^{-1}·g^{-1}·h^{-1}, Figure 6.13), which was attributed to aggregation of the nanoparticles. As shown in Figure 6.13, by employing P2VP$_{8k}$-*b*-PS$_{6k}$-*b*-P2VP$_{8k}$ as stabilizer, the specific activity of the Inco 982174 nanoparticles increased more than 15-fold with both

5 wt % polymer ($r_{2,m}$ = 14.7 ± 1.1 mol·L^{-1}·g^{-1}·h^{-1}, over 2 runs) and 10 wt % polymer ($r_{2,m}$ = 16.3 ± 0.5 mol·L^{-1}·g^{-1}·h^{-1}, over 2 runs). The particles stabilized by 5 wt % polymer displayed a slightly lower activity than with 10 wt % polymer, but their activity was nonetheless respectively 46% and 61% higher than for the QSI sample ($r_{2,m}$ = 10.1 ± 0.5 mol·L^{-1}·g^{-1}·h^{-1}, over 3 runs). In contrast, the activity of the Inco nanoparticles with only 3 wt % polymer ($r_{2,m}$ = 0.6 ± 0.3 mol·L^{-1}·g^{-1}·h^{-1}, over 4 samples) remained comparable to the naked particles. In terms of areal rate, the Inco nanopowders with 10 wt % polymer were ca. 40% more active than QSI-Nano® nickel (the SSA of the Inco product is higher than for the QSI product, i.e. 97.2 m^2·g^{-1} versus 84.0 m^2·g^{-1} respectively).

These results clearly highlight the benefits of polymeric stabilizers to enhance the dispersion stability and activity of catalysts. Furthermore, the visual appearance of the Inco 982174 sample with 5 wt % and 10 wt % polymer was a fine powder comparable to the QSI sample whereas the sample stabilized by 3 wt % polymer had a much coarser appearance, comparable to the naked Inco particles. As expected, a minimum amount of polymer is required to provide sufficient steric stabilization and prevent aggregation of the particles.

To investigate the influence of the polymer on catalyst aging, the block copolymer was added either immediately after the synthesis of the particles or after 6 months of storage. While the activity of the former catalyst remained unchanged after 6 months, the nanopowder in the latter case displayed a specific catalytic activity 60% lower; albeit still ca. 7 times higher than the bare particles. These results buttress the role of the polymer as a protective coating limiting the oxidation of the particles and extending their storage lifetime.[61]

As shown in Figure 6.19, TEM imaging of the polymer-stabilized solutions revealed the presence of spherical micelles about 45 ± 7 nm in diameter, loaded with Ni metal. This is indication of the presence of very fine, catalytically active particles in solution. Larger nickel particles, ca. 110 nm in diameter and coated with a polymer matrix, were also observed.

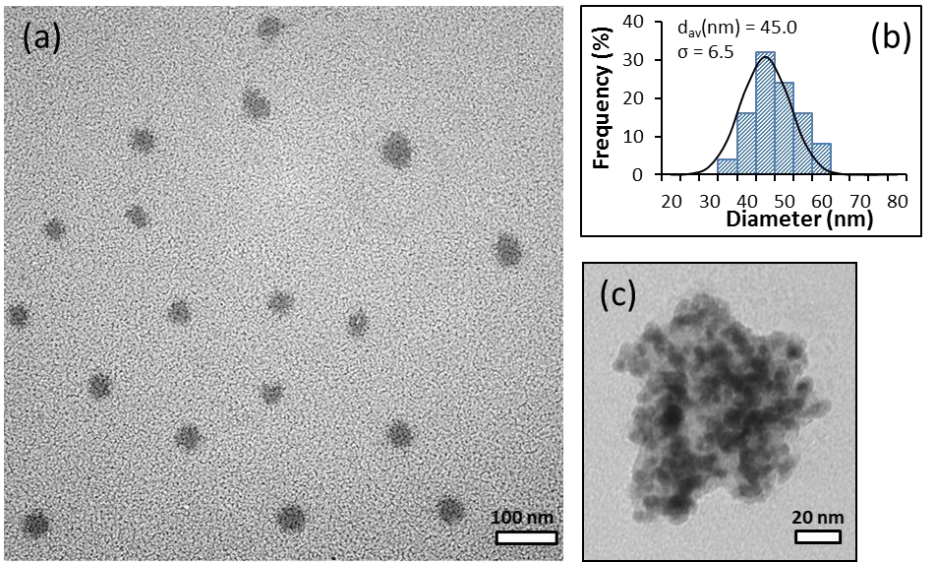

Figure 6.19 (a) TEM image for Inco 982174 Ni nanopowder stabilized by P2VP$_{8k}$-*b*-PS$_{6k}$-*b*-P2VP$_{8k}$, and (b) the particle size distribution. (c) Larger polymer-stabilized particles are also visible.

6.5 Conclusions

The discovery of interesting tunable properties for magnetic nanoparticles has fostered great interest in different fields of research including catalysis. A novel method based on the thermal decomposition of $Ni(CO)_4$ was developed at VITSL for the synthesis of nickel nanopowders. The method relied on $Ni(CO)_4$ used in the nickel refining process, and allowed the production of nanosized powders with SSA ranging from 6.4 to 97.2 $m^2 \cdot g^{-1}$. The utilization of the carbonyl gas led to residual oxygen and carbon atoms in the particles

ranging from 0.6 to 11.4 wt % for O, and 0.29 to 0.82 wt % for C. A NiO nanopowder sample was also prepared by this method. The oxygen content increased with the SSA of the particles. The nanopowders reacted exothermically with the oxygen in air and had to be stored under inert atmosphere (non-passivated form), or passivated by controlled oxidation. The SSA of the particles remained stable for at least 6 months when the SSA reached 60.5 $m^2 \cdot g^{-1}$. The nanopowders with a SSA of 97.2 $m^2 \cdot g^{-1}$ exhibited a decrease in SSA to 86.0 $m^2 \cdot g^{-1}$ after 4 months. Their exposure to air led to sintering however, and the SSA decreased to 38.8 $m^2 \cdot g^{-1}$. Imaging by SEM and TEM revealed strand-like structures about 60 nm in size and with a broad size dispersity. The particles with the largest SSA displayed thinner thread-like structures, with features about 9.4 ± 2.0 nm in diameter.

Experimental protocols were developed to evaluate the catalytic performance of the nickel nanopowders, using the reduction of either adiponitrile or mesityl oxide with hydrogen as benchmarks reactions. High conversions were observed for the non-passivated Inco particles in the reduction of adiponitrile, and their specific activity ($r_{1,m}$ = 10.0 ± 3.8 $\mu mol \cdot s^{-1} \cdot g^{-1}$) was significantly higher than for Raney® nickel 2800 and 2400 ($r_{1,m}$ = 0.9 ± 0.3 $\mu mol \cdot s^{-1} \cdot g^{-1}$), and comparable to the QSI-Nano® NPs ($r_{1,m}$ = 13.0 ± 0.2 $\mu mol \cdot s^{-1} \cdot g^{-1}$) prepared by CVD. The increased catalytic activity was linked to an increase in SSA for the materials. Passivated Inco particles with a low SSA (<24.7 $m^2 \cdot g^{-1}$) were much less active, as was the Aldrich nanopowder. Storage of the particles in heptane proved detrimental to their catalytic performance. In terms of areal activity, non-passivated Inco particles 92831 were particularly active ($r_{1,sa}$ = 0.23 ± 0.06 $\mu mol \cdot s^{-1} \cdot m^2$), while other Inco and QSI nanocatalysts displayed

comparable activity ($\bar{r}_{1,sa}$ = 0.14 ± 0.04 μmol·s^{-1}·m^2), consistently with a structure-insensitive reduction reaction. Raney® nickel 2800, 2400 and the Aldrich nanopowder had much lower areal activities ($\bar{r}_{1,sa}$ < 0.06 μmol·s^{-1}·m^2). The catalysts were not selective for the formation of 1,6-hexamethylenediamine, with secondary and tertiary amines being formed, but the QSI and Inco 92831 particles showed the highest selectivity (66 ± 40 and 37 ± 3 mol %, respectively).

The kinetics of the hydrogenation of MO were monitored by GC. The specific initial rate of the reaction was highest for the QSI product ($r_{2,m}$ = 10.1 ± 0.5 mol·L^{-1} g^{-1}·h^{-1}). Raney® nickel 2400 and Inco 112376 had lower activities, while the passivated Inco 85109 particles were inactive. Reduction of the particles under hydrogen at 250 or 500 °C was ineffective, possibly due to sintering of the particles. Treatment of the powders with DETA, in contrast, led to a 13-fold increase in catalytic activity for RaNi 2400, and a drastic improvement in the specific activity of Inco 85109 ($r_{2,m}$ from 0 to 6.38 mol·L^{-1} g^{-1}·h^{-1}). Interestingly, similar treatment of the QSI nanoparticles poisoned the catalyst. In terms of areal activity, the Inco 85109 sample was twice as active as non-treated QSI NPs.

A high SSA sample (Inco 982174, 97.2 m^2·g^{-1}) freshly prepared at VITSL displayed poor catalytic performance. The colloidal stability of the particles increased with the polarity of the dispersion medium, water being a notable exception. The stability of the dispersions in water was improved with polymeric stabilizers, high molar mass PEI, and PVPy being more effective than the lower molar mass telechelic MPEG and MPEG−DETA. Significant improvement was observed for PVPy with a molar mass of 1.3 ×10^6 g·mol^{-1} as compared

with 1.0×10^4 g·mol^{-1}. In alcohols, the telechelic polymers induced the flocculation of the dispersions. To limit the surface coverage of the particles for catalytic applications the triblock copolymers PEO-*b*-PS-*b*-PEO and P2VP-*b*-PS-*b*-P2VP were synthesized and investigated. Polymers with a short PS segment (800 and 1000 g·mol^{-1} respectively) were found ineffective and induced flocculation. Depletion flocculation due to micelle formation by $P2VP_{8k}$-*b*-PS_{6k}-*b*-$P2VP_{8k}$ was also noted. The addition of the polymer to the particles in a non-selective solvent, and their redispersion in 2-propanol led to the formation of more stable dispersions. A minimum size was required for the stabilizing moiety, as a polymer with a short PS segment was ineffective.

Application of the nickel catalysts stabilized by 5 or 10 wt % of polymer in the hydrogenation of MO led to an increase by more than 15-fold in specific catalytic activity as compared to the bare particles. The polymer was also effective at preventing areal oxidation under storage. Polymer adsorption measurements by SEC-DRI revealed that a maximum of 18 wt % of polymer could be bound to the particles. TEM imaging demonstrated the formation of micelles 45 ± 7 nm in diameter, loaded with nickel, and the presence of larger polymer-encapsulated particles ca. 110 nm in diameter.

In conclusion, the concept of polymer stabilization to increase catalyst activity appears to be highly pervasive, as it is potentially applicable to a wide range of heterogeneous (particulate) catalysts of commercial importance. This could ultimately allow significant improvements in catalytic activity in a wide range of industrial processes, provided that the composition and the structure of the polymer additives can be tailored to the specific process conditions (e.g., solvent, temperature) being used.

Chapter 7

Concluding Remarks and Recommendations for Future Work

7.1 Summary and original contributions to knowledge

The focus of the research presented in this Thesis pertains to the synthesis, characterization, and application of polymeric stabilizers for the preparation of metallic nanocatalysts. In particular, novel polymeric architectures and characterization techniques were designed to further expand fundamental understanding in this field of research. Briefly summarized below are the four main research areas investigated, which include: i) palladium nanocatalysts, ii) metal loading characterization by a novel microplasma-based technique,[1,2] iii) polyion complex micelle-metal hybrid structures, and iv) nickel nanocatalysts.

The unique size-dependent and non-monotonic properties exhibited by nanosized materials have attracted great interest from the research community, notably in catalysis. Although heterogeneous catalysis has long been concerned with the preparation and application of metallic nanostructures, the controlled supramolecular assembly of nanomaterials, coupled with the use of novel characterization methods, set apart nanocatalysis as a new field of research.[3,4] To maintain their small size (i.e., large specific surface area) and high catalytic activity, nanoparticles necessitate the use of stabilizers; polymers have emerged as extremely successful candidates for that purpose. The role of the polymer is not limited to providing colloidal stability but is central to the synthesis, solubilization, catalytic performance, recovery and recycling of the metallic species.[5,6]

A variety of polymeric structures investigated for the preparation of Pd nanoparticles were reviewed in Chapter 2. Dendritic architectures (primarily dendrimers) appeared to be promising candidates for catalytic applications.[7] Dendrigrafts (arborescent) copolymers also belong to the dendritic polymer family, and are characterized by a semi-controlled cascade-

branched architecture reminiscent of dendrimers. Their synthesis relies on grafting polymeric chains rather than small molecules however, and yields dendritic architectures with a high molar mass in few synthetic steps.[8] In Chapter 3, we investigated the solution and solid-state properties of previously synthesized *Gn*PS-*g*-P2VP arborescent copolymers by dynamic light scattering (DLS) and atomic force microscopy (AFM). The unimolecular micelles exhibited good colloidal stability in organic solvents, and narrow size distributions. The molecules deposited onto mica substrates displayed a *fried egg* morphology and a closed-pack organization for the *G*1 and *G*2 copolymers. Phase segregation between the PS and P2VP segments was evidenced from the micrographs, particularly for the upper generation copolymers ($Gn \geq 2$). The preparation of stable colloidal Pd nanoparticles using these dendrigraft copolymers templates was reported for the first time. By employing an alcohol reduction protocol, Pd nanoparticles (ranging from 0.7 to 3.4 nm diameter) with a narrow size dispersity were encapsulated within the unimolecular micelles. The size of the nanoparticles was found to depend on the loading level, the reduction time, as well as the arborescent copolymer generation. The catalytic activity of the colloidal Pd nanoparticles was evaluated in terms of conversion in the Suzuki-Miyaura (SM) cross-coupling reaction under *green* conditions, in mixtures of ethanol and deuterated water, and was followed in situ by proton nuclear magnetic resonance. A good catalytic activity and a positive dendritic effect were evidenced, although air sensitivity and flocculation affected the activity and recycling of the catalyst.

The determination of the metal concentration in polymer-stabilized systems largely relies on inductively coupled plasma measurements. This characterization technique is

marred by several important limitations however.[2] In Chapter 4, we demonstrated for the first time the application of a novel microplasma-based technique for the direct determination of the concentration of Pd in arborescent polymer-stabilized systems in organic solvents.[1,2] Quantification of the metal content by microplasma-optical emission spectrometry revealed stoichiometric complexation of the Pd salt by the pyridine pendant groups. Kinetics studies of aggregation were also performed and highlighted the beneficial role of the polymer to provide colloidal stabilization. The low cost of the method, ease of use, and small sample requirements greatly facilitate the performance of a large number of measurements.

The utilization of nanocatalysts in green chemistry applications is an important avenue of research; however, the solubilization of catalysts and reagents in neat water remains a challenge. We reported in Chapter 5 the first synthesis of polyion complex micelles from arborescent copolymers and double-hydrophilic block copolymers. The latter, viz. poly(acrylic acid)-*block*-poly(2-hydroxyethyl acrylate), was obtained by acid-catalyzed hydrolysis of poly(*tert*-butyl acrylate)-*block*-poly(2-trimethylsilyloxyethyl acrylate), which was synthesized by atom transfer radical polymerization. The self-assembled supramolecular structures obtained by complexation of these polymers exhibited hydrodynamic diameters ranging from 132 to 354 nm and narrow size distributions. The supramolecular assemblies exhibited thermo-responsive properties in ethanol, dissociating above a critical temperature of ca. 35 °C and reforming upon cooling. The polyion complex aggregates were also stable in water, with hydrodynamic diameters ranging from 110 to 306 nm. These structures were also used for the solubilization of Pd nanocatalysts in aqueous Suzuki-Miyaura reactions.

Lastly, in Chapter 6 a study was undertaken on the properties of nickel nanoparticles prepared by a novel thermal decomposition method developed at Vale-Inco. The nanopowders exhibited a specific surface area ranging from 6.4 to 97.2 $m^2 \cdot g^{-1}$, and catalytic activity in the hydrogenation of adiponitrile and mesityl oxide higher than for commercial catalysts in some cases. Treatment of the nanoparticles with diethylenetriamine led to further improvement in catalytic activity. Aggregation of the nanopowders was prevented with polymeric stabilizers, whose structure and composition were tailored to maximize the dispersibility and the catalytic activity. The structures investigated included triblock copolymers of polystyrene with poly(ethylene oxide) or poly(2-vinylpyridine), and telechelic polymers of poly(ethylene glycol). Application of the polymer-stabilized nickel catalysts in hydrogenation reactions led up to 15-fold increases in specific catalytic activity as compared to the bare particles. Polymer adsorption measurements by size-exclusion chromatography with a differential refractive index detector revealed that up to 18 wt % of polymer could be bound to the particles. Transmission electron microscopy imaging demonstrated the formation of micelles, 45 ± 7 nm in diameter, containing nickel. The polymer was also effective at preventing areal oxidation under storage.

7.2 Proposed future work

7.2.1 Polymer-metal hybrid nanostructures

We demonstrated the preparation of Pd colloids stabilized by arborescent copolymers of different generations with applications in the Suzuki-Miyaura reaction. It is well-known that the intrinsic composition of nanoparticles has an important influence on the performance

of a catalyst. For instance, bimetallic and multimetallic structures with synergetic properties between the metallic species have been shown to display enhanced catalytic performance as compared to their monometallic counterparts. Bimetallic Au-Pd,[9] and even trimetallic Au-Ag-Pd[10] nanoparticles were more active than Pd nanoparticles in hydrogenation and SM reactions, respectively. The investigation of the influence of the composition of the nanoparticles would be an interesting development for arborescent polymer-stabilized nanocatalysts, to promote their catalytic activity. These templates have already been shown to complex readily with $HAuCl_4$ in organic solvents, and to yield Au nanoparticles upon reduction in solution.[11] Bimetallic or multi-metallic nanoparticles could be obtained by successive loading of the micelles with different metal salts, using the method introduced by Turkevich and Kim.[12] Alternately, co-dissolution of different metal salts in solution has been shown to form bimetallic structures with improved catalytic activity.[13] Reduction of the metallic salts content to increase the turnover number of the catalyst is another venue worth investigating. Several reports have demonstrated high catalytic activity for dendrimer-stabilized Pd nanoparticles under *homeopathic* (parts per million levels) conditions.[14]

Interestingly, arborescent copolymers loaded with Au(III) were shown to exhibit unique phase segregation, including sphere-in-sphere and cylinder-in-sphere morphologies.[15] Such phase segregation may be useful to control the shape and size of the nanoparticles formed within the polymeric template. Since the activity of metallic nanoparticles has been shown to depend markedly on their morphology,[16] novel polymeric templates such as the arborescent copolymers could prove promising to provide *locus control*[17] over self-assembly processes.

Arborescent copolymers may also constitute valuable templates for the controlled assembly of hierarchical metallic nanostructures. For instance, the hexagonal packing of monolayers of the spherical molecules – as imaged by AFM – could serve to prepare nanoscopic patterns with long-range ordering.[18] Such structures may find important applications in areas including data storage, optoelectronics, and nanolithography.[19]

Another promising utilization of arborescent polymer-metal hybrid systems lies in the preparation of self-assembled supramolecular nanostructures. The groups of Manners and Winnik have reported the synthesis of cylindrical block copolymer micelles by the crystallization-driven self-assembly of poly(ferrocenyldimethylsilane) (PFS)-based block copolymers.[20,21] Control over the growth of the micelles allowed the formation of cylindrical co-micelles with a triblock architecture.[22] Supramolecular architectures could be obtained by grafting living PFS-based block copolymers to arborescent polymers (Scheme 7.1). Various routes can be considered for the preparation of such structures, including the attachment of the block copolymer to the dendritic polymer via a "click" reaction (azide-alkyne,[23] Diels-Alder,[24] etc.) or electrostatic interactions (e.g., polyion complexes). Additionally, hybrid systems could be obtained by complexation of the block copolymer micelles and/or the supramolecular assemblies with metallic salts. Reduction of the metallic species would result in the formation of a metallic network. For instance, palladium acetate complexes readily with the 2-vinylpyridine units of the block copolymers, and can be reduced to Pd(0) by warming in alcoholic solutions.[1] Possible applications of such structures range from catalysis, optoelectronics, materials science, medicine, to data storage and energy harvesting.[25]

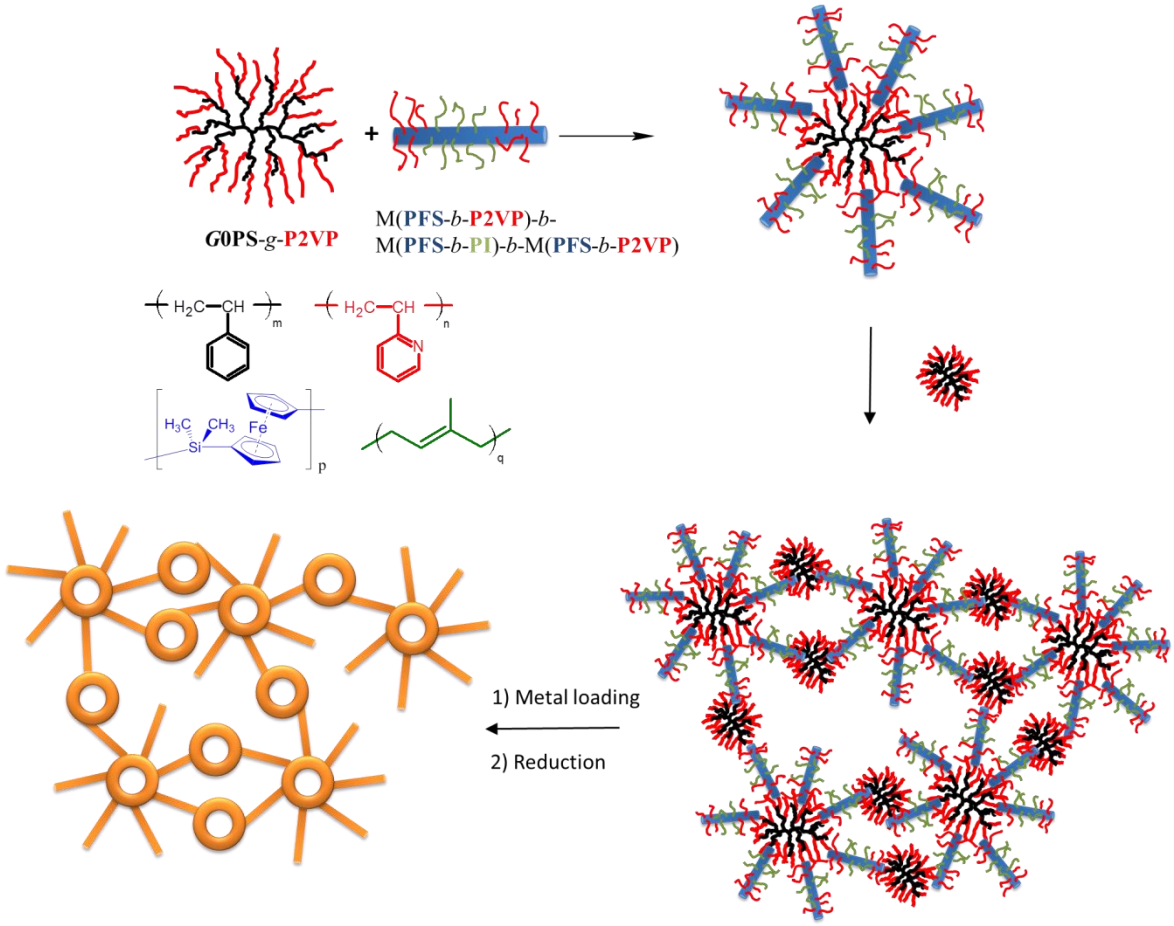

Scheme 7.1 Proposed supramolecular assembly from arborescent copolymers and crystallizable core-forming block copolymers for the preparation of metallic nanonetworks.

7.2.2 Microplasma-based multiplexed bioassay

We have shown that microplasma-optical emission spectrometry (MOES) is an enticing alternative to inductively coupled plasma-OES (ICP-OES).[1] We demonstrated that the concentration of Pd complexed with an arborescent copolymer could be determined with a detection limit in the low parts-per-billion. This novel characterization technique can also

perform rapid multi-element concentration determinations in solution, and presents an enticing avenue of research for the development of multiplexed bioassays (simultaneous detection of multiple analytes). Current efforts in biochemical analysis are directed towards the detection of multiple biomarkers in individual cells,[26] and ICP-mass spectrometry has been proposed for multiplexed detection.[27] The numerous advantages offered by the microplasma device over ICP may position this characterization technique as a powerful alternative. As shown in Figure 7.1, metal-chelating polymers can be conjugated with antibodies to determine biomarker expression in cells. Lanthanide metals have been widely applied as elemental tags for mass cytometry. Using a similar approach, the microplasma-based technique could be applicable to the selective characterization of lanthanide nanoparticles in metal-chelating polymers. Such a technique would simplify the diagnosis for diseased cells, and increase the effectiveness of therapeutic procedures.

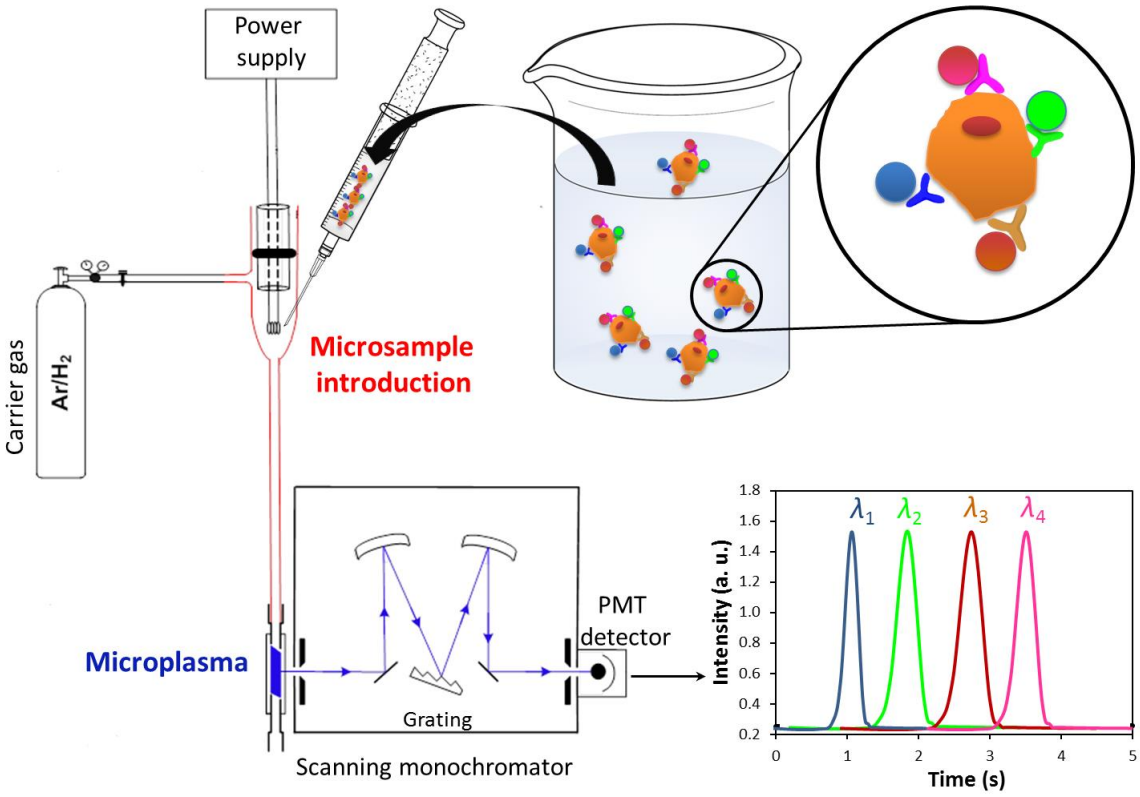

Figure 7.1 Proposed determination of the concentration of lanthanides by microplasma-optical emission spectrometry for multiplexed bioassay.

Appendices

Chapter 3 Supporting Information

A3.1 Pd nanoparticle size and size distributions

Table A3.1 Diameter of the Pd NPs formed in *Gn*PS-*g*-P2VP after reduction at 60 °C in ethanol for 3 h, measured from the electron micrographs.

Generation/	Diameter NPs (nm)		
Loading	0.25	0.5	1.0
*G*0	6.0 ± 0.5	14.5 ± 1.9	3.0 ± 1.1
*G*1	0.7 ± 0.04	1.3 ± 0.3	1.7 ± 0.7
*G*2	2.0 ± 0.3	1.9 ± 0.4	2.9 ± 0.3
*G*3	1.4 ± 0.3	1.4 ± 0.3	3.4 ± 1.0

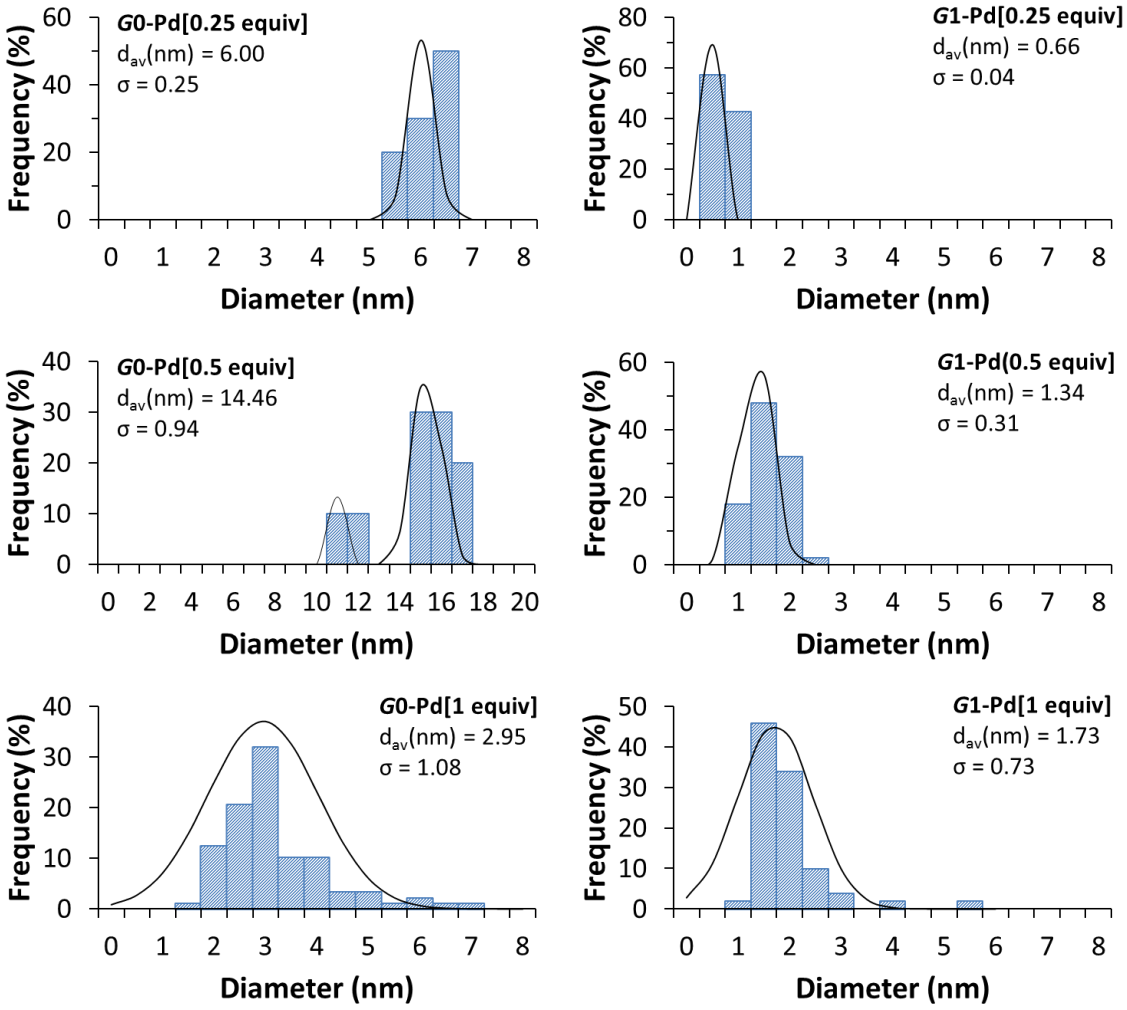

Figure A3.1 Size distribution for Pd NPs formed in *Gn*PS-*g*-P2VP (*n* = 0, 1) micelles after reduction in ethanol at 60 °C for 3 h.

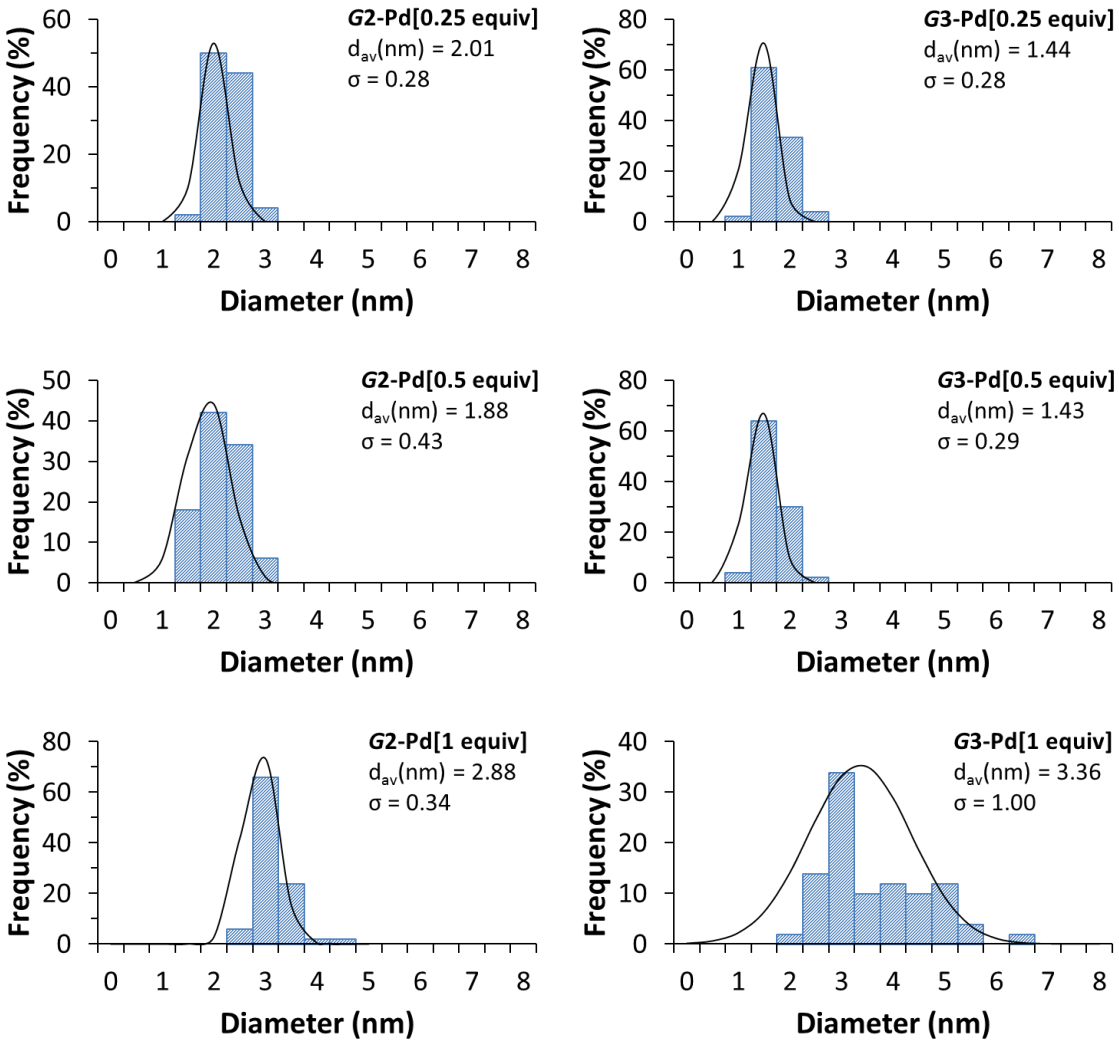

Figure A3.2 Size distribution for Pd NPs formed in *Gn*PS-*g*-P2VP (*n* = 2, 3) micelles after reduction in ethanol at 60 °C for 3 h.

A3.2 NMR analysis of the Suzuki-Miyaura reaction

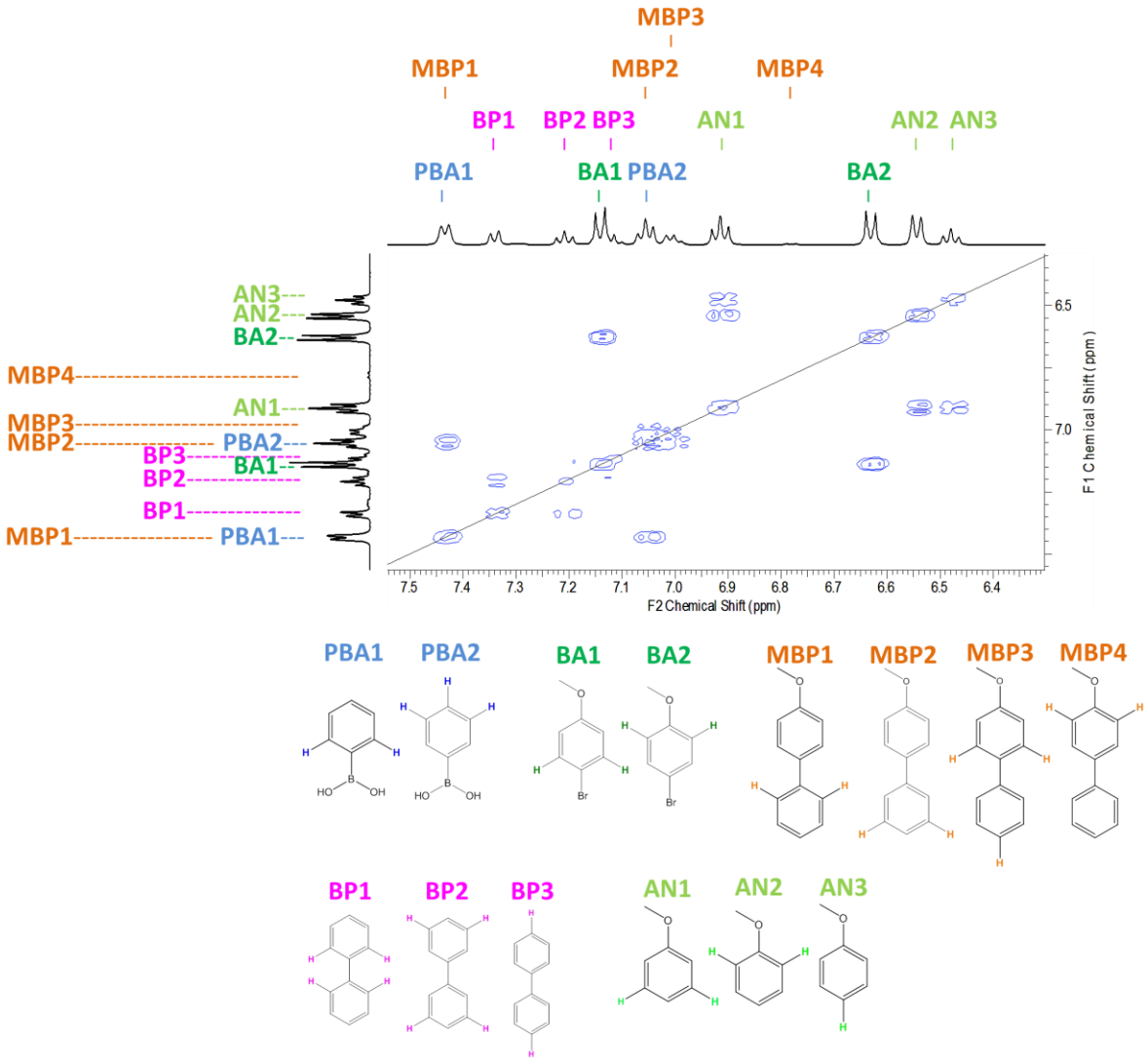

Figure A3.3 2D [^{1}H ^{1}H] COSY spectrum for the SM reaction in ethanol/D_2O (85/15 v/v). (Bruker Avance 500 MHz).

Chapter 5 Supporting Information

A5.1 Polymerization of *t*BA

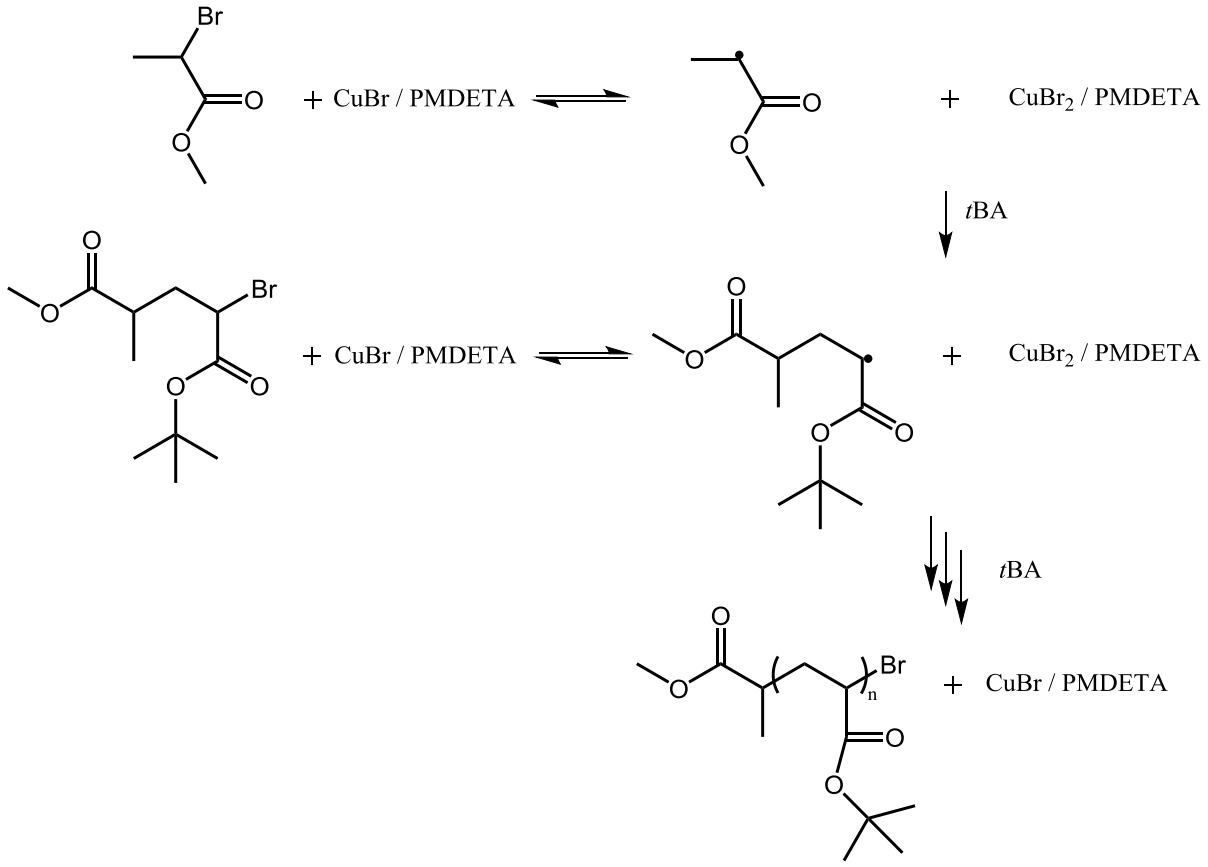

Scheme A5.1 Mechanism for the polymerization of *t*BA by ATRP. Adapted with permission from References 1 and 2. Copyright 2005 and 2001, respectively, American Chemical Society.

A5.2 Calculation of the chain dimensions of PAA_{13}-*b*-$PHEA_{140}$

The radius of gyration of a linear polymer can be calculated by considering a chain with rotational restrictions. Assuming unperturbed chain dimensions, the root-mean-square end-to-end distance $\langle r^2 \rangle_0^{1/2}$ is given by Equation A5.1.[3]

$$\langle r^2 \rangle_0^{1/2} = nl^{1/2} \left(\frac{1 - cos\theta}{1 + cos\theta} \right)^{1/2} \sigma \tag{A5.1}$$

Where, l, n, and θ represent, respectively, the bond length, the number of bonds in the chain, and the bond angle. The steric factor σ is a measure of the effect of hindrance to free rotation about the bonds, i.e. the chain flexibility. For a vinyl polymer l = 0.154 nm and cos θ = -1/3, and for PAA_{13}-*b*-$PHEA_{140}$, n = 2 × (13 + 140) = 306. The steric factor typically ranges from 1.5 to 2.5; it was found to be 2.09 for poly(2-hydroxyethyl methacrylate) in methanol.[4] This value of σ was selected as representative of the flexibility of DHBC in ethanol, and the calculated $\langle r^2 \rangle_0^{1/2}$ was 11.3 nm.

The radius of gyration R_g obtained from Equation A5.2 was calculated as 4.6 nm.[5]

$$R_g = \frac{\langle r^2 \rangle_0^{1/2}}{\sqrt{6}} \tag{A5.2}$$

For linear, monodispersed chains, the hydrodynamic radius R_h given by Equation A5.3[6] was found to be 3.1 nm for PAA_{13}-*b*-$PHEA_{140}$.

$$R_h = R_g \frac{3\sqrt{\pi}}{8} \tag{A5.3}$$

The hydrodynamic diameter D_h was therefore 6.2 nm.

A5.3 Calculation of the solubility and interaction parameters

The spontaneous dissolution of an amorphous polymer in a solvent is described thermodynamically by the Gibbs free energy change upon mixing ΔG_m, expressed in Equation A5.4 as a function of the enthalpy change ΔH_m, the entropy change ΔS_m, and the temperature T.

$$\Delta G_m = \Delta H_m - T\Delta S_m \quad \text{(A5.4)}$$

The dissolution of a polymer generally occurs with a limited gain in entropy, and the Gibbs free energy of mixing is mainly governed by the enthalpic term.[7] Hildebrand and Scott,[8] and Scatchard[9] proposed an expression for ΔH_m, shown in Equation A5.5, that depends on the volume fraction of the solvent φ_s and the polymer φ_p, the volume of the mixture V, and the difference in the solubility parameters of the solvent δ_s and the polymer δ_p.

$$\Delta H_m = \varphi_s \varphi_p V(\delta_s - \delta_p)^2 \quad \text{(A5.5)}$$

For polymer-solvent miscibility, the term (δ_s-δ_p) must be small to favor the small entropic term over the enthalpic term, i.e. yield a negative net free energy change (Equation A5.4).

Although they are useful for non-polar solutions, the Hildebrand solubility parameters do not always account for the behavior of polar systems.[7,10] Hansen proposed to take into consideration molecular interactions in polar systems, by introducing separate solubility parameters for different types of interactions, namely dispersive δ_D, dipole-dipole δ_P, and hydrogen bonding δ_H interactions.[11]

The relation between the Hildebrand and Hansen solubility parameters is given in Equation A5.6.

$$\delta^2 = \delta_{\mathrm{D}}^2 + \delta_{\mathrm{P}}^2 + \delta_{\mathrm{H}}^2 \tag{A5.6}$$

The Hansen solubility parameters can also be related to the well-known Flory-Huggins interaction parameter χ_{12} describing polymer-solvent interactions, as given in Equation A5.7, where V_s is the molar volume of the solvent and R is the ideal gas constant.[12]

$$\chi_{12} = \frac{V_s}{RT}\left[(\delta_{\mathrm{D2}} - \delta_{\mathrm{D1}})^2 + \frac{1}{4}(\delta_{\mathrm{P2}} - \delta_{\mathrm{P1}})^2 + \frac{1}{4}(\delta_{\mathrm{H2}} - \delta_{\mathrm{H1}})^2\right] \tag{A5.7}$$

The Hildebrand solubility parameters for PAA and PHEA in ethanol, calculated from reported Hansen solubility parameters,[13] and the calculated interaction parameters are provided in Table A5.1.

Table A5.1 Hansen solubility parameters and calculated Hildebrand solubility parameters for ethanol, poly(acrylic acid) and poly(2-hydroxyethyl acrylate), and calculated interaction parameters.

Compound	Hansen solubility parameters[a] ($MPa^{1/2}$)			δ^b ($MPa^{1/2}$)	Molar volume[a] ($cm^3 \cdot mol^{-1}$)	$\chi_{12}{}^c$
	δ_D	δ_P	δ_H			
Ethanol	15.8	8.8	19.4	26.5	58.5	
PAA	18.4[d]	6.1[d]	13.3[d]	23.5	68.5	0.42
PHEA	16.0	13.2	13.4	24.7	114.9	0.33

[a] From Hansen.[13] [b] Calculated from Eq. A5.6. [c] Calculated from Eq. A5.7. [d] From Barton.[14]

A5.4 Size distributions for the polyion complex micelles

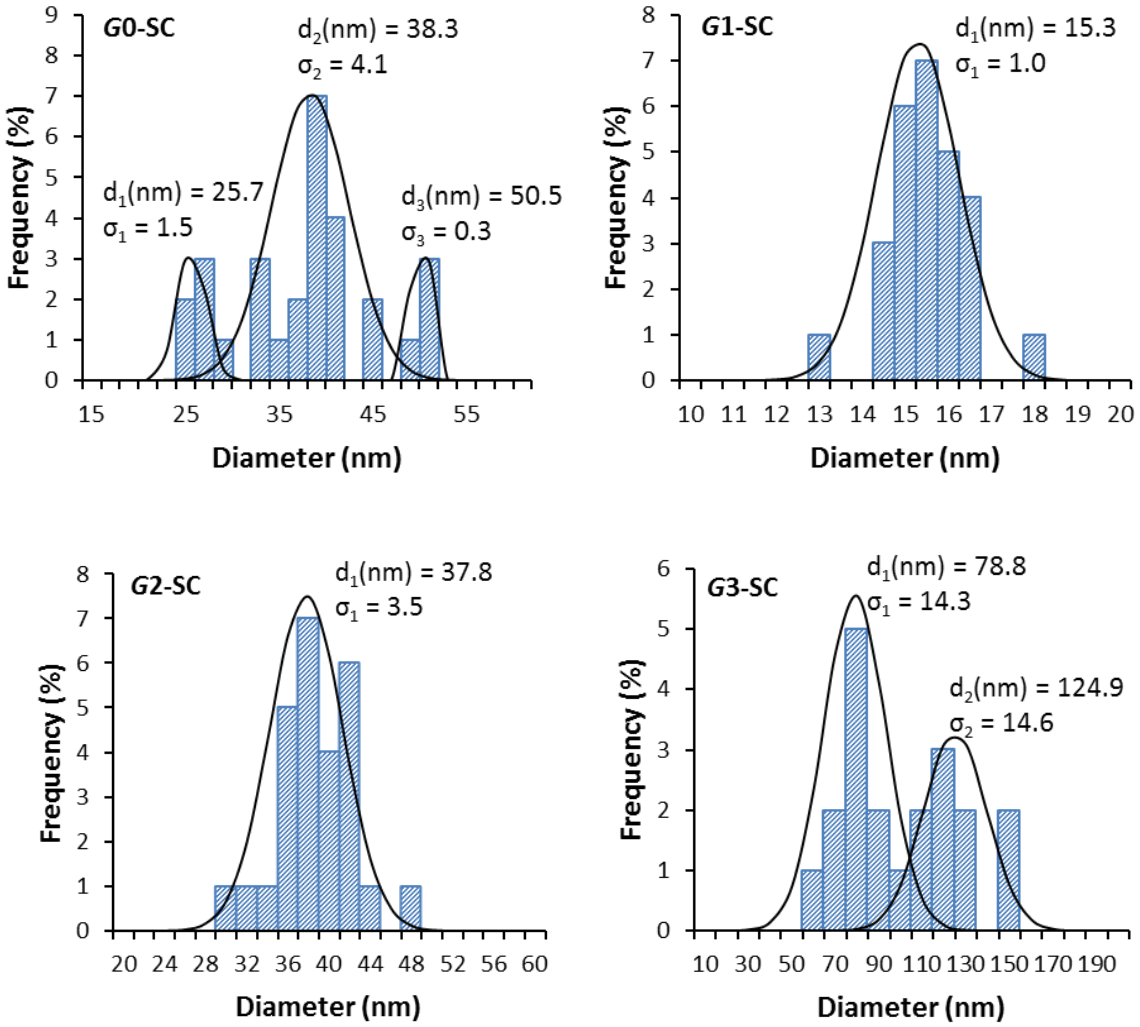

Figure A5.1 Size distributions for PIC deposited from aqueous solutions of *Gn*PS-*g*-P2VP, (*n* = -1 to 1) and PAA-*b*-PHEA (SC), as measured by AFM.

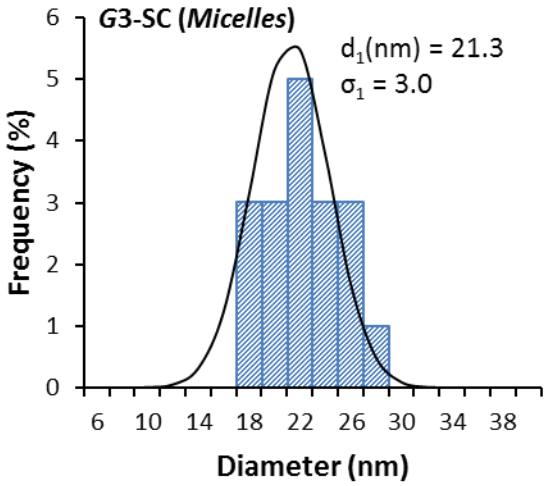

Figure A5.2 Size distribution for PAA-*b*-PHEA micelles deposited from an aqueous solution of *G*2PS-*g*-P2VP (*G*3) and PAA-*b*-PHEA (SC), as measured by AFM.

Chapter 6 Supporting Information

A6.1 Synthesis of PEO-*b*-PS-*b*-PEO and P2VP-*b*-PS-*b*-P2VP

A6.1.1 Reaction apparatuses and solvent purification

Due to the sensitivity of anionic polymerization to (protic) impurities, all the glassware utilized in the polymerization reactions was flamed under high vacuum (<1.4 mPa, 10^{-5} mm Hg). The final purification of the monomers was carried out under high vacuum and the polymerization was performed under dry N_2 atmosphere. The ampoules (thick-wall ampoules for ethylene oxide) were fitted with polytetrafluoroethylene (PTFE) stopcocks and ground glass joints to be mounted onto the manifolds and the polymerization reactor attached to the vacuum line. Tetrahydrofuran (THF; Caledon, reagent grade) was distilled from sodium-benzophenone ketyl under N_2, and toluene (Caledon, ACS reagent) was distilled from oligostyryllithium. Both solvents were transferred directly from the stills to the manifolds through PTFE tubing.

A6.1.2 Ethylene oxide purification

Caution: Ethylene oxide is a highly toxic and flammable gas (bp 10 °C) that should be handled with care in a well-ventilated fume hood, and cooled whenever possible to avoid pressure build-up. The EO was transferred to a manifold mounted on the high-vacuum line, comprising a 250-mL round-bottomed flask (rbf) and a thick-walled (double thickness) ampoule with a PTFE stopcock containing about 5 g of CaH_2 and a magnetic stirring bar (Figure A6.1). After evacuation of the manifold and the ampoule, the system was flame-dried

before purging with N_2. A solution of phenylmagnesium chloride (PhMgCl, Sigma-Aldrich, 2.0 M in THF, 12.5 mL, 25 mmol) was transferred with a syringe to the rbf against N_2 flow, and the system was evacuated to remove the THF. The EO (ca. 110 g) was then condensed from the cylinder into the rbf immersed in liquid nitrogen (L-N_2). The monomer was then degased, and dried over PhMgCl with three successive freeze-evacuation-thawing cycles as follows: The rbf was placed in an ice bath at 0 °C, and the liquid EO stirred over the Grignard reagent for 15 min. The rbf was then replaced in liquid nitrogen, and evacuated after freezing of the monomer. The cycle was repeated twice more. The rbf was finally brought to 0 °C, and EO slowly recondensed to the ampoule placed in L-N_2, by opening the PTFE stopcock. The weight of transferred EO was 36.8 g (0.84 mol).

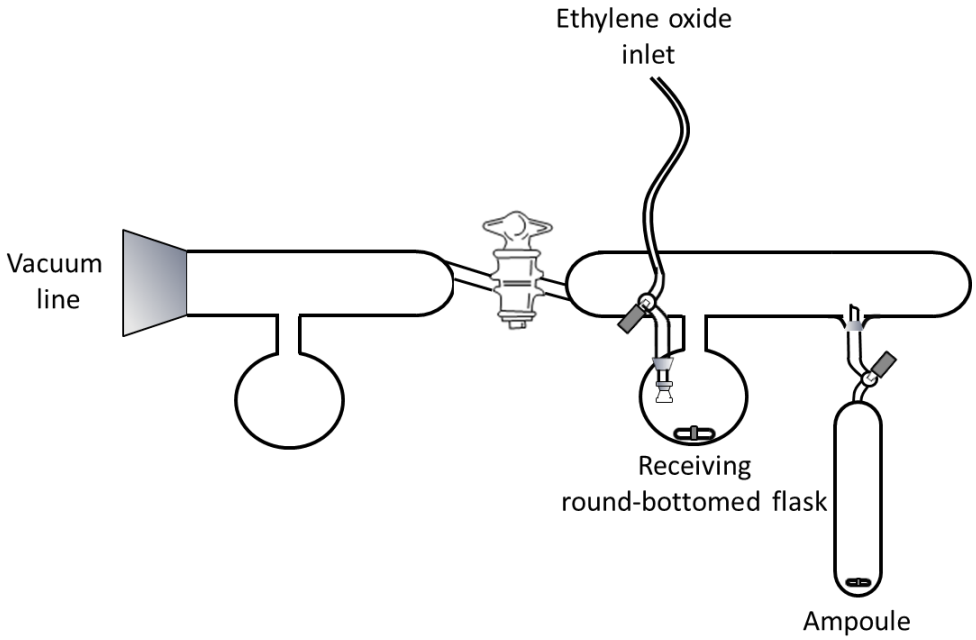

Figure A6.1 Manifold for the purification of ethylene oxide.

A6.1.3 Initiator synthesis

Potassium naphthalide was prepared by stirring naphthalene (20 g, 0.16 mol) with freshly cut potassium (ca. 4 g) in dry THF (200 mL) overnight under N_2. The dark-green solution was filtered with a Schlenk funnel under N_2 and stored in a Schlenk flask. The concentration of the solution (0.41 $mol \cdot L^{-1}$) was determined by titration of a 2,6-bis(1,1-dimethylethyl)-4-methylphenol solution in dry THF under N_2.

A6.1.4 Styrene purification

Styrene (Sigma-Aldrich, ReagentPlus®, with 4-*tert*-butylcatechol stabilizer, ≥99%) was stirred with calcium hydride overnight and distilled under vacuum. Further purification of ca. 2 mL of the monomer was achieved by stirring with PhMgCl (0.2 mL, 0.4 mmol) and 3 freezing-evacuation-thawing cycles as described above. The monomer (2.1 g, 20 mmol) was recondensed under vacuum to an ampoule and stored under N_2.

A6.1.5 Synthesis of PEO-*b*-PS-*b*-PEO

The polymerization reaction was carried out in a 250-mL round-bottomed glass reactor with a magnetic stirring bar, attached to a manifold mounted on the vacuum line. The ampoule containing the EO monomer was also attached to the manifold. Dry THF (100 mL) was added to the reactor under N_2 and titrated by drop-wise addition of the initiator solution until a persistent green color was observed. The flask was then cooled to -78 °C and the initiator solution (5 mL, 2 mmol, for a target $\bar{X}_n$ = 415) was added with a syringe. Styrene (1 mL, 9 mmol) was then added to the reactor, which was immersed in L-N_2 to freeze its content, and evacuated. The EO (36.8 g, 0.84 mol) was then recondensed to the reactor by

opening the ampoule. Once the monomer was completely transferred, the solution was warmed to 0 °C using an ice bath. The reaction vessel was then heated to 50 °C in an oil bath. After 24 h, the reaction was terminated with 0.5 mL of aqueous HCl (HCl/water 1/10 v/v). The solvent was evaporated, and the polymer redissolved in THF. After reprecipitation in cold diethyl ether, the polymer was recovered by suction filtration, and dried under vacuum, overnight. Yield: 37.7 g (44.4%). The reaction schemes, and ^{1}H NMR spectrum are shown in Scheme A6.1 to Scheme A6.3, and in Figure A6.2, respectively. $\bar{M}_{n,app}$ = 14000 g·mol^{-1}, $\bar{M}_w \cdot \bar{M}_n^{-1}$ = 1.13. From SEC and ^{1}H NMR analysis: $\bar{M}_{n,PS}$ = 730 g·mol^{-1}; $\bar{M}_{n,PEO}$ = 2 × 6600 g·mol^{-1}.

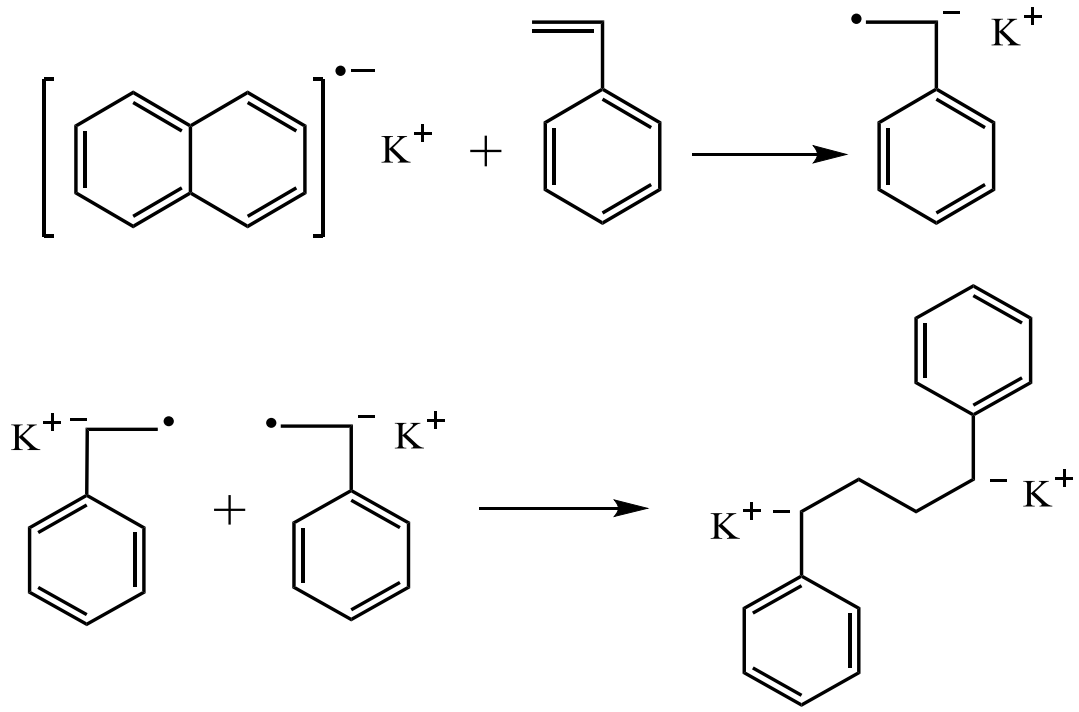

Scheme A6.1 Initiation of styrene polymerization with the formation of a styrenyl dianion.

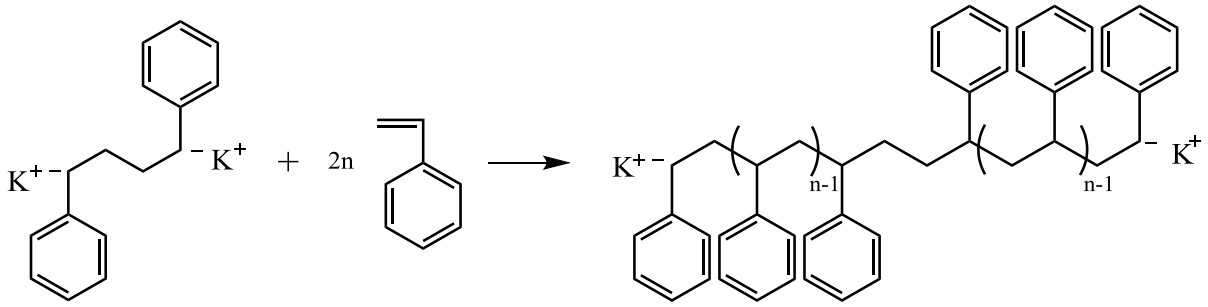

Scheme A6.2 Anionic propagation from the difunctional initiator with the addition of styrene monomer.

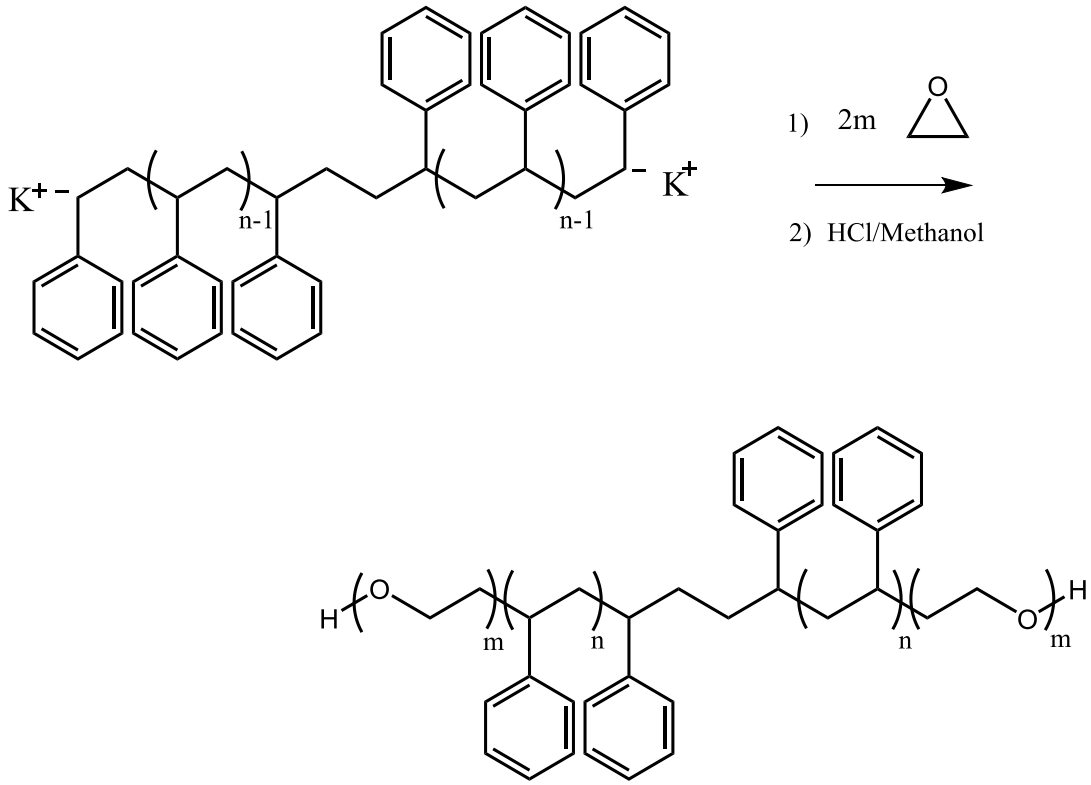

Scheme A6.3 Anionic propagation after the addition of the second monomer (ethylene oxide), and termination of the polymer chains by a proton donor species.

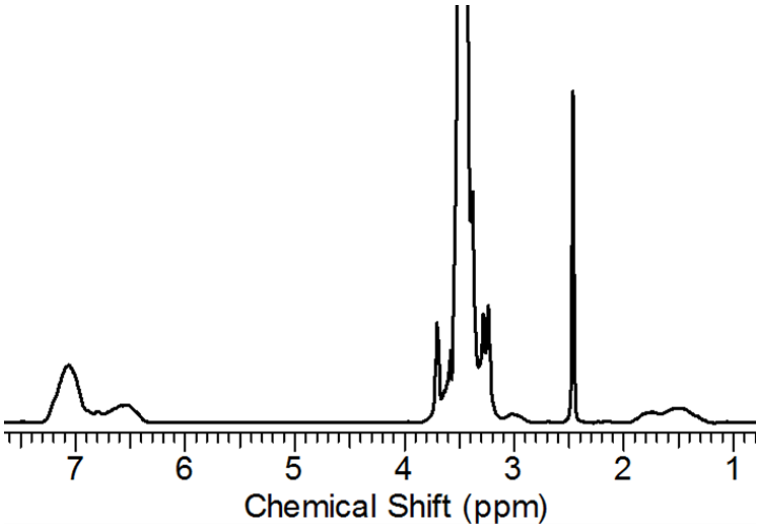

Figure A6.2 ^{1}H NMR spectrum in DMSO-d_6 for $PEO_{6.6k}$-*b*-PS_{700}-*b*-$PEO_{6.6k}$.

A6.1.6 Synthesis of P2VP-*b*-PS-*b*-P2VP

The synthesis of poly(2-vinylpyridine)-*block*-polystyrene-*block*-poly(2-vinylpyridine) (P2VP-*b*-PS-*b*-P2VP) was carried out by anionic polymerization. The procedure employed was similar to the one described for the synthesis PEO-*b*-PS-*b*-PEO, the main difference being the use of 2-vinylpyridine (2VP) and 1,1-diphenylethylene (DPE) rather than EO.

A6.1.6.1 Reagents purification

Styrene was purified by the procedure described in Section A6.1.4. The 2VP monomer was dried over CaH_2 under N_2 overnight, distilled under reduced pressure, and stored under nitrogen in a solvent storage flask. A second distillation of 2VP (10 mL, 93 mmol) over CaH_2 (3.7 g) was performed just before the polymerization reaction. The capping agent DPE (Sigma-Aldrich, 97%) was titrated in a rbf against nitrogen flow by adding a

solution of *n*-butyllithium (Sigma-Aldrich, 2.5 M in hexanes) until a persistent deep red coloration, indicative of 1,1-diphenylhexyllithium formation, was observed. The monomer was then distilled under reduced pressure in a dry Schlenk flask. Further drying of an ampoule containing DPE (0.4 mL, 2.3 mmol) was obtained by azeotropic purification with dry THF.

A6.1.6.2 Polymerization of P2VP-*b*-PS_{800}-*b*-P2VP

Three P2VP-*b*-PS-*b*-P2VP copolymers were obtained from a PS mid-block with a molar mass of ca. 800 $g \cdot mol^{-1}$. Ampoules containing purified styrene, 2VP, DPE and the THF line were mounted onto a 2-L round-bottomed glass reactor connected to the high-vacuum line, equipped with a mechanical stirrer. After evacuation and flame-drying the reactor was purged with nitrogen, and dry THF (400 mL) was added to the vessel. Few drops of a solution of potassium naphthalide in THF (0.406 $mol \cdot L^{-1}$) were introduced with a syringe until a persistent pale green coloration was observed. The addition of 3.68 mL (1.5 mmol) of the initiator solution ensued. Styrene (1.85 mL, 16 mmol, 11 equiv) was added drop-wise, after which the solution took a red coloration. After 3 min, 15 mL of the solution was removed with a syringe. DPE (0.4 mL, 2.3 mmol, 1.5 equiv) dissolved in 15 mL of THF was then added to the reaction medium; after 3 min, the addition of 9.5 mL (8.8 mmol, 59 equiv) of 2VP monomer ensued. Fifty milliliters of the solution were sampled at this stage, before the addition of another 7.48 mL of 2VP (6.9 mmol, 46 equiv). After sampling another 50 mL of solution, a final addition of 2VP (12.76 mL, 118 mmol, 79 equiv) took place. The polymers were recovered by precipitation in *n*-hexanes from a 10 $mg \cdot mL^{-1}$ solutions in THF,

after termination with methanol/HCl (10/1 v/v), and concentration by rotary evaporation. The recovery yields ranged from 33–45%. The reaction scheme, and a representative ^{1}H NMR spectrum are shown in Scheme A6.4 and Figure A6.3, respectively. $\bar{M}_{n,\,PS}$ = 755 g·mol^{-1}, $\bar{M}_w \cdot \bar{M}_n^{-1}$ = 1.15; $\bar{M}_{n,\,P2VP_{700}\text{-}b\text{-}PS_{800}\text{-}b\text{-}P2VP_{700}}$ = 2100 g·mol^{-1}, $\bar{M}_w \cdot \bar{M}_n^{-1}$ = 1.34; $\bar{M}_{n,\,P2VP_{1.2k}\text{-}PS_{800}\text{-}P2VP_{1.2k}}$ = 3100 g·mol^{-1}, $\bar{M}_w \cdot \bar{M}_n^{-1}$ = 1.35; $\bar{M}_{n,\,P2VP_{3k}\text{-}b\text{-}PS_{800}\text{-}b\text{-}P2VP_{3k}}$ = 6400 g·mol^{-1}, $\bar{M}_w \cdot \bar{M}_n^{-1}$ = 1.22.

A6.1.6.3 Polymerization of P2VP-*b*-PS$_{6k}$-*b*-P2VP

Another series of P2VP-*b*-PS-*b*-P2VP samples was prepared from a PS block with a molar mass of 6600 g·mol^{-1} according to a procedure similar to the one described in the previous section. In that case the amount of potassium naphthalide solution in THF added was 0.98 mL (0.406 mol·L^{-1}, 0.4 mmol), followed by styrene (2.20 mL, 19 mmol, 48 equiv), DPE (0.3 mL, 1.7 mmol, 4 equiv) in 15 mL THF, and 3 successive additions of 2VP: i) 1.64 mL, 15 mmol, 38 equiv; ii) 1.45 mL, 13 mmol, 43 equiv; and iii) 2.50 mL, 23 mmol, 58 equiv). The reaction scheme, and a representative ^{1}H NMR spectrum are shown in Scheme A6.4 and in Figure A6.3, respectively. $\bar{M}_{n,\,PS}$ = 6600 g·mol^{-1}, $\bar{M}_w \cdot \bar{M}_n^{-1}$ = 1.30; $\bar{M}_{n,P2VP_{2.7k}\text{-}b\text{-}PS_{6k}\text{-}b\text{-}P2VP_{2.7}}$ = 11900 g·mol^{-1}, $\bar{M}_w \cdot \bar{M}_n^{-1}$ = 1.28; $\bar{M}_{n,\,P2VP_{5k}\text{-}b\text{-}PS_{6k}\text{-}b\text{-}P2VP_{5k}}$ = 17100 g·mol^{-1}, $\bar{M}_w \cdot \bar{M}_n^{-1}$ = 1.40; $\bar{M}_{n,\,P2VP_{8k}\text{-}b\text{-}PS_{6k}\text{-}b\text{-}P2VP_{8k}}$ = 23300 g·mol^{-1}, $\bar{M}_w \cdot \bar{M}_n^{-1}$ = 1.50.

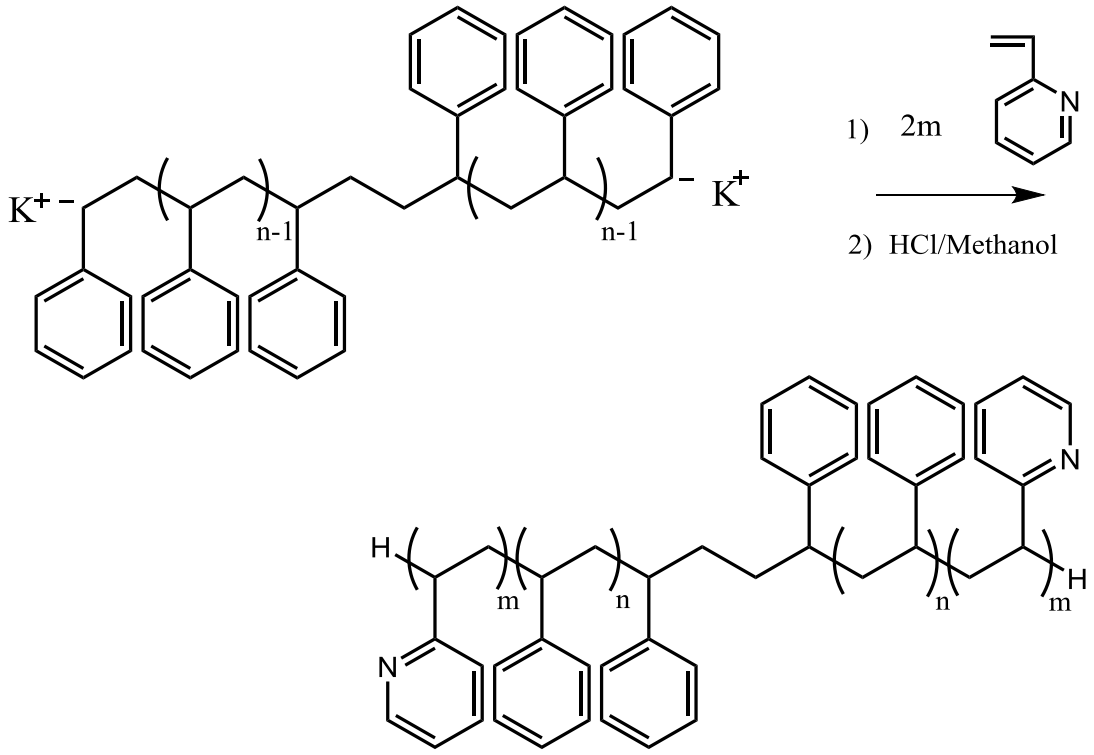

Scheme A6.4 Anionic propagation after the addition of the second monomer (2-vinylpyridine), and termination of the polymer chains by a proton donor species. The initiation mechanism is the same as for PEO-*b*-PS-*b*-PEO (Section A6.1.5).

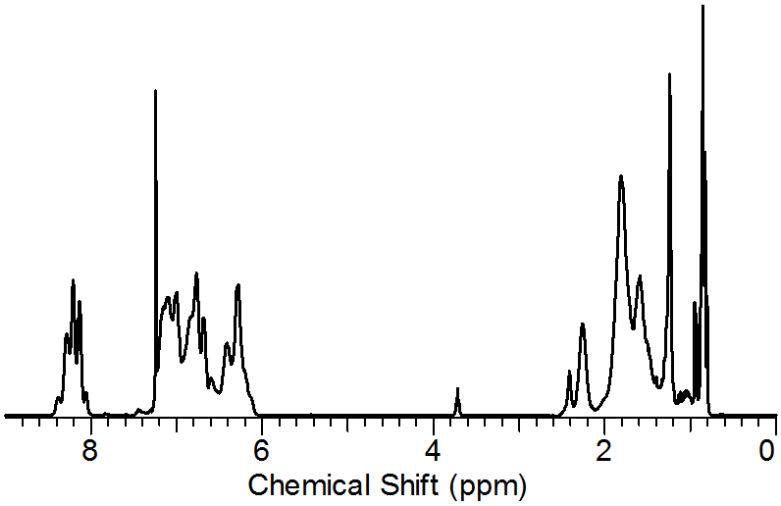

Figure A6.3 ^{1}H NMR spectrum in $CDCl_3$ for $P2VP_{3k}$-*b*-PS_{800}-*b*-$P2VP_{3k}$.

A6.2 Synthesis of MPEG-DETA

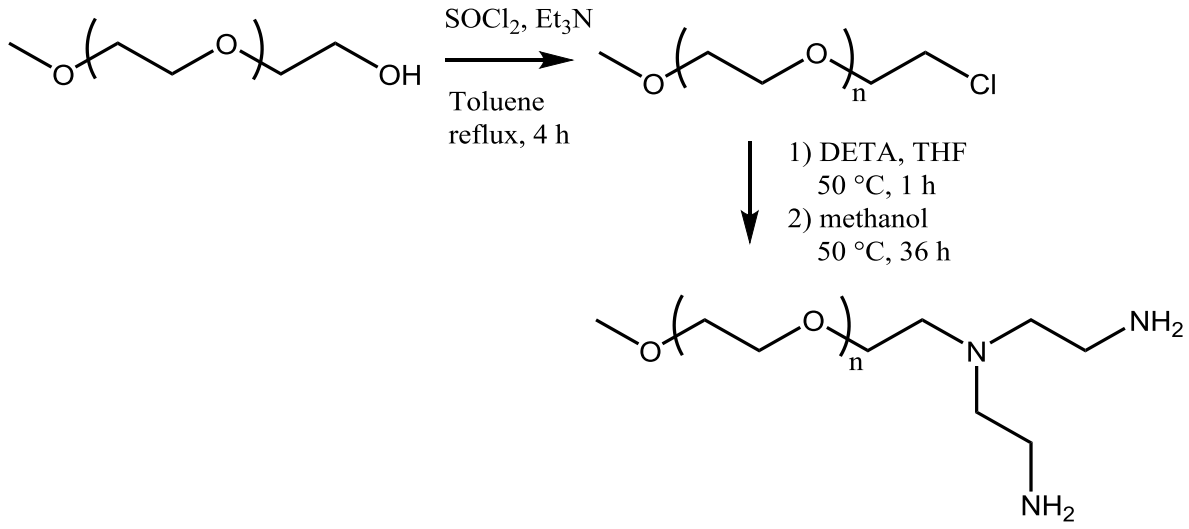

Scheme A6.5 MPEG functionalization with DETA.

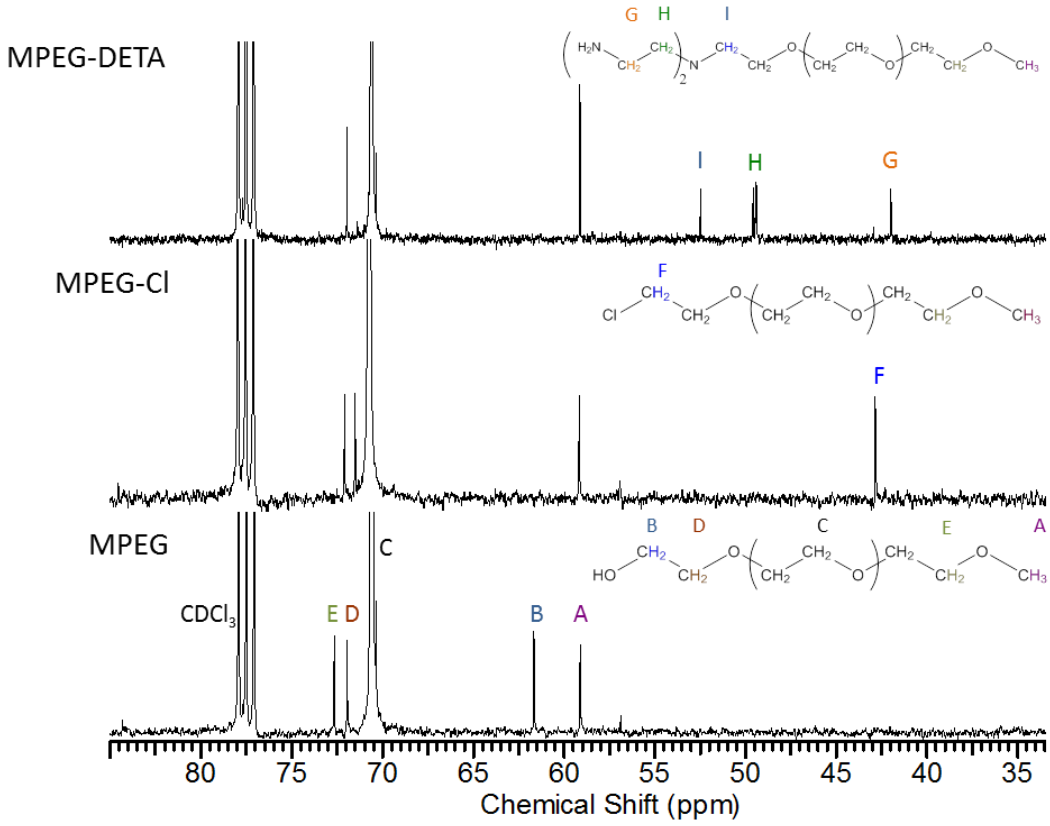

Figure A6.4 ^{13}C NMR (300 MHz) spectra for MPEG, MPEG−Cl, and MPEG−DETA in $CDCl_3$.

A6.3 ^{1}H NMR characterization of the reduction of adiponitrile

^{1}H NMR spectroscopy was used to determine the conversion of adiponitrile in the hydrogenation reaction (Scheme 6.1). The NMR spectra for adiponitrile, 1,6-hexamethylenediamine, and for a crude product (adiponitrile and 1,6-hexamethylenediamine mixture) in $CDCl_3$ are provided in Figure A6.5 as an example. The peak at 2.42 ppm (label A on the spectrum) corresponds to the methylene groups adjacent to the nitrile functionality, and the peak at 1.84 ppm is for the methylene groups (B) central to the chain. After hydrogenation, the signal for the methylene groups neighboring the $–NH_2$ group (C) is shifted to 2.68 ppm. The ratio of the peak areas for the methylene groups adjacent to the terminal functionalities (2.68 ppm and 2.43 ppm) can thus be used to determine the conversion using Equation A6.1:

$$Conversion\ (mol\ \%) = \frac{Area\ (\mathrm{C})}{Area\ (\mathrm{C}) + Area\ (\mathrm{A})} \times 100 \qquad \text{(A6.1)}$$

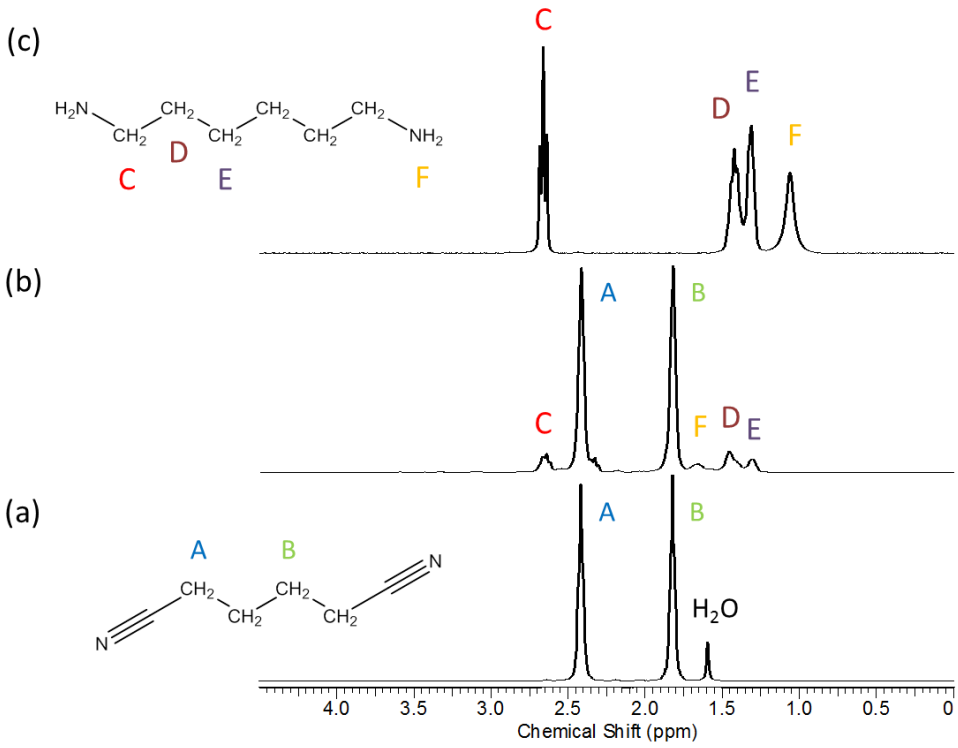

Figure A6.5 ^{1}H NMR (300 MHz) spectra in $CDCl_3$ for (a) adiponitrile (ADN), (b) the hydrogenation reaction mixture containing ADN and 1,6-hexamethylenediamine (HMD), and (c) HMD.

References

Chapter 1

1. Bell, A. T. *Science* **2003**, *299*, 1688–1691.
2. Schlögl, R.; Abd Hamid, S. B. *Angew. Chem. Int. Ed.* **2004**, *43*, 1628–1637.
3. Bronstein, L. M.; Sidorov, S. N.; Valetsky, P. M. *Russ. Chem. Rev.* **2004**, *73*, 501–515.
4. Shenhar, R.; Norsten, T. B.; Rotello, V. M. *Adv. Mater.* **2005**, *17*, 657–669.
5. Astruc, D. In *Nanoparticles and Catalysis*; Wiley-VCH: Weinheim, **2008**; p. 30.
6. Gubin, S. P. In *Magnetic Nanoparticles*; Wiley-VCH: Weinheim, **2009**; pp. 1–23.
7. Jia, C.-J.; Schüth, F. *Phys. Chem. Chem. Phys.* **2011**, *13*, 2457–2487.
8. Kreibig, U.; Bönnemann, H.; Hormes, J. In *Handbook of Surfaces and Interfaces of Materials*; Nalwa, H. S., Ed.; Academic Press: San Diego, **2001**; Vol. 3, pp. 1–85.
9. Nguon, O.; Gauthier, M.; Karanassios, V. *RSC Adv.* **2014**, *4*, 8978–8984.
10. Nguon, O.; Huang, S.; Gauthier, M.; Karanassios, V. *Proc. SPIE* **2014**, *9101*, 910106(1)–910106(7).

Chapter 2

1. Bhushan, B. In *Handbook of Nanotechnology*; Springer: Heidelberg, **2010**; pp. 1–13.
2. Feynman, R. P. *Eng. Sci.* **1960**, *23*, 22–36.
3. Blackman, J. A.; Binns, C. In *Handbook of Metal Physics - Metallic Nanoparticles*; Misra, P., Ed.; Elsevier: Amsterdam, **2009**; p. 2.
4. Schmid, G. *Nanoparticles -From Theory to Application*; 2nd ed.; Wiley-VCH: Weinheim, **2010**.
5. Corain, B.; Schmid, G.; Toshima, N. *Metal Nanoclusters in Catalysis and Materials Science - The Issue of Size Control*; Elsevier: Amsterdam, **2008**.
6. Serp, P.; Philippot, K. *Nanomaterials in Catalysis*; Wiley-VCH: Weinheim, **2013**.
7. Liz-Marzán, L. M.; Kamat, P. V *Nanoscale Materials*; Kluwer Academic: Dordrecht, **2004**.
8. Grunes, J.; Zhu, J.; Somorjai, G. A. *Chem. Commun.* **2003**, 2257–2260.
9. Schlögl, R.; Abd Hamid, S. B. *Angew. Chem. Int. Ed.* **2004**, *43*, 1628–1637.
10. Bell, A. T. *Science* **2003**, *299*, 1688–1691.
11. Polshettiwar, V.; Asefa, T. *Nanocatalysis - Synthesis and Applications*; John Wiley and Sons: Hoboken, **2013**.
12. Zecchina, A.; Bordiga, S.; Groppo, E. *Selective Nanocatalysts and Nanoscience*; Wiley-VCH: Weinheim, **2011**.
13. Toshima, N. In *Nanoscale Materials*; Liz-Marzán, L. M.; Prashant, K. V, Eds.; Kluwer Academic: Dordrecht, **2003**; pp. 92–94.
14. Astruc, D. *Nanoparticles and Catalysis*; Wiley-VCH: Weinheim, **2008**.
15. Heiz, U.; Landman, U. *Nanocatalysis*; Springer: Berlin, **2007**.
16. Zhou, B.; Han, S.; Raja, R.; Somorjai, G. A. *Nanotechnology in Catalysis*; Volume 3.; Springer: New York, **2007**; Vol. 3.
17. Zhou, B.; Hermans, S.; Somorjai, G. A. *Nanotechnology in Catalysis*; Volume 1.; Kluwer Academic: New York, **2004**.

18. Iwasawa, Y. *Tailored Metal Catalysts*; Reidel/Kluwer Academic: Dordrecht, **1986**.
19. Henry, C. R. In *Nanocatalysis*; Heiz, U.; Landman, U., Eds.; Springer: Berlin, **2007**; p. 245.
20. Philippot, K.; Serp, P. In *Nanomaterials in Catalysis*; Wiley-VCH: Weinheim, **2013**; pp. 1–15.
21. Philippot, K.; Serp, P. In *Nanomaterials in Catalysis*; Wiley-VCH: Weinheim, **2013**; pp. 1–54.
22. Heiz, U.; Landman, U. In *Nanocatalysis*; Springer: Berlin, **2007**; p. v.
23. Finke, R. G. In *Metal Nanoparticles - Synthesis, Characterization and Applications*; Feldheim, D. L.; Foss, C. A., Eds.; Marcel Dekker: New York, **2002**; pp. 17–54.
24. Mie, G. *Ann. Phys.* **1908**, *25*, 377–445.
25. Kelly, K.; Coronado, E.; Zhao, L. L.; Schatz, G. C. *J. Phys. Chem. B* **2003**, *107*, 668–677.
26. Parak, W. J.; Liberato, M.; Simmel, F. C.; Gerion, D.; Paul, A. In *Nanoparticles - From Theory to Application*; Schmid, G., Ed.; Wiley-VCH: Weinheim, **2010**; pp. 3–47.
27. Cao, G. *Nanostructures and Nanomaterials - Synthesis, Properties and Applications*; Imperial College Press: London, **2004**.
28. Bradley, J. S. In *Clusters and Colloids - From Theory to Applications*; Schmid, G., Ed.; VCH: Weinheim, **1994**; pp. 459–544.
29. Pomogailo, A. *Russ. Chem. Rev.* **1997**, *66*, 679–716.
30. Aiken III, J.; Finke, R. *J. Mol. Catal. A: Chem* **1999**, *145*, 1–44.
31. Toshima, N.; Yonezawa, T. *New J. Chem.* **1998**, *22*, 1179–1201.
32. Johnson, B. *Coord. Chem. Rev.* **1999**, *190-192*, 1269–1285.
33. Biffis, A.; Zecca, M.; Basato, M. *J. Mol. Catal. A: Chem* **2001**, *173*, 249–274.
34. Králik, M.; Biffis, A. *J. Mol. Catal. A: Chem* **2001**, *177*, 113–138.
35. Kreibig, U.; Bönnemann, H.; Hormes, J. In *Handbook of Surfaces and Interfaces of Materials*; Nalwa, H. S., Ed.; Academic Press: San Diego, **2001**; Vol. 3, pp. 1–85.
36. Roucoux, A.; Schulz, J.; Patin, H. *Chem. Rev.* **2002**, *102*, 3757–3778.

37. Toshima, N. In *Nanoscale Materials*; Liz-Marzán, L. M.; Kamat, P. V, Eds.; Kluwer Academic: Dordrecht, **2003**; pp. 79–96.
38. Philippot, K.; Chaudret, B. *Comptes Rendus Chim.* **2003**, *6*, 1019–1034.
39. Nagabhushana, K. S.; Bönnemann, H. In *Nanotechnology in Catalysis*; Zhou, B.; Hermans, S.; Somorjai, G. A., Eds.; Springer Science and Buisness: New York, **2004**; p. 51.
40. Bönnemann, H.; Nagabhushana, K. S. In *Encyclopedia of Nanoscience and Nanotechnology*; Nalwa, H. S., Ed.; American Scientific, **2004**; Vol. 1, pp. 777–813.
41. Cushing, B. L.; Kolesnichenko, V. L.; O'Connor, C. J. *Chem. Rev.* **2004**, *104*, 3893–3946.
42. Wang, Q.; Ostafin, A. E. In *Encyclopedia of Nanoscience and Nanotechnology*; Nalwa, H. S., Ed.; American Scientific, **2004**; Vol. 5, pp. 475–503.
43. Cao, G. In *Nanostructures and Nanomaterials - Synthesis, Properties and Applications*; Imperial College Press: London, **2004**; pp. 51–109.
44. Burda, C.; Chen, X.; Narayanan, R.; El-Sayed, M. A. *Chem. Rev.* **2005**, *105*, 1025–1102.
45. Richards, R.; Bönnemann, H. In *Nanofabrication Towards Biomedical Applications: Techniques, Tools, Applications, and Impact*; Kumar, C. S. S. R.; Hormes, J.; Leuschner, C., Eds.; Wiley-VCH: Weinheim, **2005**; p. 18.
46. Durán Pachón, L.; Rothenberg, G. *Appl. Organomet. Chem.* **2008**, *22*, 288–299.
47. Bönnemann, H.; Nagabhushana, K. S. In *Metal Nanoclusters in Catalysis and Materials Science*; Corain, B.; Schmid, G.; Toshima, N., Eds.; Elsevier: Amsterdam, **2008**; pp. 21–48.
48. Bönnemann, H.; Nagabhushana, K. S.; Richards, R. M. In *Nanoparticles and Catalysis*; Astruc, D., Ed.; Wiley-VCH: Weinheim, **2008**; pp. 49–91.
49. Kolesnichenko, V. L. In *Magnetic Nanoparticles*; Gubin, S. P., Ed.; Wiley-VCH: Weinheim, **2009**; pp. 25–58.
50. Semagina, N.; Kiwi-Minsker, L. *Catal. Rev.* **2009**, *51*, 147–217.

51. Yu, C.-H.; Tam, K.; Tsang, E. S. C. In *Handbook of Metal Physics - Metallic Nanoparticles*; Misra, P.; Blackman, J. A., Eds.; Elsevier: Amsterdam, **2009**; pp. 113–141.
52. Schmid, G.; Krylova, G.; Bodnarchuk, M. I.; Tromsdorf, U. I.; Shevchenko, E. V; Talapin, D. V; Weller, H. In *Nanoparticles - From Theory to Application*; Schmid, G., Ed.; Wiley-VCH: Weinheim, **2010**; pp. 214–310.
53. Zhang, W.; Wang, D.; Yan, R. In *Selective Nanocatalysts and Nanoscience: Concepts for Heterogeneous and Homogeneous Catalysis*; Zecchina, A.; Bordiga, S.; Groppo, E., Eds.; Wiley-VCH: Weinheim, **2011**; pp. 29–71.
54. Jia, C.-J.; Schüth, F. *Phys. Chem. Chem. Phys.* **2011**, *13*, 2457–2487.
55. Lu, K. In *Nanoparticulate Materials - Synthesis, Characterization and Processing*; John Wiley & Sons: Hoboken, **2013**; pp. 24–127.
56. Sreeprasad, T. S.; Pradeed, T. In *Springer Handbook of Nanomaterials*; Vajtai, R., Ed.; Springer: Heidelberg, **2013**; pp. 303–388.
57. Beck, A.; Horváth, A.; Sárkány, A.; Guczi, L. In *Nanotechnology in Catalysis*; Zhou, B.; Hermans, S.; Somorjai, G. A., Eds.; Springer Science and Buisness: New York, **2004**; Vol. 1, pp. 83–110.
58. Cao, G. In *Nanostructures and Nanomaterials - Synthesis, Properties and Applications*; Imperial College Press: London, **2004**; pp. 277–328.
59. Baker, C. C.; Pradhan, A.; Shah, S. I. In *Encyclopedia of Nanoscience and Nanotechnology*; Nalwa, H. S., Ed.; American Scientific, **2004**; Vol. 5, pp. 449–473.
60. Astruc, D. In *Nanoparticles and Catalysis*; Wiley-VCH: Weinheim, **2008**; p. 30.
61. Serp, P.; Philippot, K. In *Nanomaterials in Catalysis*; Wiley-VCH: Weinheim, **2013**; pp. xiii–xvi.
62. Berzelius, J. *R. Swedish Acad. Sci.* **1835**, 245.
63. Satterfield, C. N. *Heterogeneous Catalysis in Practice*; 2nd ed.; McGraw-Hill: New York, **1991**; p. 6.
64. Augustine, R. L. *Heterogeneous Catalysis for the Synthetic Chemist*; 1st ed.; Marcel Dekker: New York, **1996**; p. 7.

65. Satterfield, C. N. *Heterogeneous Catalysis in Practice*; 2nd ed.; McGraw-Hill: New York, **1991**; p. 17.
66. Bartholomew, C. H. *Appl. Catal., A* **2001**, *212*, 17–60.
67. Noyori, R. *Angew. Chem. Int. Ed.* **2002**, *41*, 2008–2022.
68. Somorjai, G.; Borodko, Y. *Cat. Lett.* **2001**, *76*, 1–5.
69. Kolasinski, K. W. *Surface Science - Foundation of Catalysis and Nanoscience*; 3rd ed.; John Wiley & Sons: Chichester, **2012**; pp. 2–3.
70. Boudart, M. *AIChE J.* **1972**, *18*, 465–478.
71. Rothenberg, G. *Catalysis - Concepts and Green Applications*; Wiley-VCH: Weinheim, **2008**; p. 15.
72. Chandler, B.; Gilbertson, J. *Top. Organomet. Chem.* **2006**, *20*, 97–120.
73. Murugan, E.; Rangasamy, R. *J. Polym. Sci. Part A: Polym. Chem.* **2010**, *48*, 2525–2532.
74. Conlon, D. A.; Pipik, B.; Ferdinand, S.; LeBlond, C. R.; Sowa, J. R. J.; Izzo, B.; Collins, P.; Ho, G.-J.; Williams, J. M.; Shi, Y.-J.; Sun, Y. *Adv. Synth. Catal.* **2003**, *345*, 931–935.
75. Astruc, D.; Lu, F.; Aranzaes, J. R. *Angew. Chem. Int. Ed.* **2005**, *44*, 7852–7872.
76. Vasylyev, M. V; Maayan, G.; Hovav, Y.; Haimov, A.; Neumann, R. *Org. Lett.* **2006**, *8*, 5445–5448.
77. Schmid, G.; Lehnert, A.; Kreibig, U.; Adamczyk, Z.; Belouschek, P. *Zeitschrift für Anal. Chemie* **1990**, *45*, 989–994.
78. Aiken III, J. D.; Lin, Y.; Finke, R. G. *J. Mol. Catal. A: Chem* **1996**, *114*, 29–51.
79. Laine, R. *J. Mol. Catal.* **1982**, *14*, 137–169.
80. Crabtree, R. H. *Chem. Rev.* **2012**, *112*, 1536–1554.
81. Bradley, J. *J. Am. Chem. Soc.* **1979**, *101*, 7419–7421.
82. Hagen, C.; Vieille-Petit, L.; Laurenczy, G.; Süss-Fink, G.; Finke, R. G. *Organometallics* **2005**, *24*, 1819–1831.

83. Bayram, E.; Linehan, J. C.; Fulton, J. L.; Roberts, J. A. S.; Szymczak, N. K.; Smurthwaite, T. D.; Özkar, S.; Balasubramanian, M.; Finke, R. G. *J. Am. Chem. Soc.* **2011**, *133*, 18889–18902.
84. Lin, Y.; Finke, R. *Inorg. Chem.* **1994**, *33*, 4891–4910.
85. De Vries, J. In *Selective Nanocatalysts and Nanoscience: Concepts for Heterogeneous and Homogeneous Catalysis*; Zecchina, A.; Bordiga, S.; Groppo, E., Eds.; Wiley-VCH: Weinheim, **2011**; pp. 73–103.
86. Rösch, N.; Pacchioni, G. In *Clusters and Colloids - From Theory to Applications*; Schmid, G., Ed.; VCH: Weinheim, **1994**; p. 5.
87. Schmid, G. *Nanoparticles - From Theory to Application*; 2nd ed.; Wiley-VCH: Weinheim, **2010**; p. 215.
88. Chow, J.; Watson, J. *Aerosol Air Qual. Res.* **2007**, *7*, 121–173.
89. Pelzer, K.; Candy, J.-P.; Godard, G.; Basset, J.-M. In *Nanoparticles and Catalysis*; Astruc, D., Ed.; Wiley-VCH: Weinheim, **2008**; p. 578.
90. Kung, H. H.; Kung, M. C. In *Nanotechnology in Catalysis*; Zhou, B.; Han, S.; Raja, R.; Somorjai, G. A., Eds.; Springer: New York, **2007**; p. 1.
91. Philippot, K.; Serp, P. In *Nanomaterials in Catalysis*; Wiley-VCH: Weinheim, **2013**; p. 2.
92. Castleman, A. W.; Khanna, S. N. *J. Phys. Chem. C* **2009**, *113*, 2664–2675.
93. Bradley, J. S. In *Clusters and Colloids - From Theory to Applications*; Schmid, G., Ed.; VCH: Weinheim, **1994**; p. 492.
94. Klasovsky, F.; Claus, P. In *Metal Nanoclusters in Catalysis and Materials Science: The Issue of Size Control*; Corain, B.; Schmid, G.; Toshima, N., Eds.; Elsevier: Amsterdam, **2008**; pp. 167–168.
95. Toshima, N. In *Nanoscale Materials*; Liz-Marzán, L. M.; Kamat, P. V, Eds.; Kluwer Academic: Dordrecht, **2003**; pp. 86–87.
96. Sachtler, W. M. H. *Catal. Rev. Sci. Eng.* **1976**, *14*, 193–210.
97. Leofanti, G.; Padovan, M.; Tozzola, G.; Venturelli, B. *Catal. Today* **1998**, *41*, 207–219.

98. Richards, R. M. In *Nanoscale Materials in Chemistry*; Klabunde, K. J.; Richards, R. M., Eds.; John Wiley and Sons: Hoboken, **2009**; pp. 6–8.
99. Bond, G. *Surf. Sci.* **1985**, *156*, 966–981.
100. Van Hardeveld, R.; Hartog, F. *Surf. Sci.* **1969**, *15*, 189–230.
101. Molnár, Á.; Sárkány, A.; Varga, M. *J. Mol. Catal. A: Chem* **2001**, *173*, 185–221.
102. Uzio, D.; Berhault, G. *Catal. Rev. - Sci. Eng.* **2010**, *52*, 106–131.
103. Laskar, M.; Skrabalak, S. E. *ACS Catal.* **2014**, *4*, 1120–1128.
104. Li, Y.; Boone, E.; El-Sayed, M. A. *Langmuir* **2002**, *18*, 4921–4925.
105. Veisz, B.; Király, Z.; Tóth, L.; Pécz, B. *Chem. Mater.* **2002**, *4*, 2882–2888.
106. Montejano-Carrizales, J. M.; Aguilera-Granja, F.; Morán-López, J. L. *Nanostructured Mater.* **1997**, *8*, 269–287.
107. Zhang, Q.; Deng, W.; Wang, Y. *Chem. Commun.* **2011**, *47*, 9275–9292.
108. Burch, R. In *Catalysis*; Bond, G. C.; Webb, G., Eds.; The Royal Society of Chemistry: London, **1985**; Vol. 7, pp. 149–196.
109. Richards, R. M. In *Nanoscale Materials in Chemistry*; Klabunde, K. J.; Richards, R. M., Eds.; John Wiley and Sons: Hoboken, **2009**; pp. 4–6.
110. Blech, K.; Homberger, M.; Simon, U. In *Nanoparticles - From Theory to Application*; Schmid, G., Ed.; Wiley-VCH: Weinheim, **2010**; pp. 402–403.
111. Johnston, R. *Atomic and Molecular Clusters*; 1st ed.; Taylor and Francis: New York, **2002**; p. 133.
112. Boudart, M.; Aldag, A.; Benson, J.; Dougharty, N. A.; Girvin Harkins, C. *J. Catal.* **1966**, *6*, 92–99.
113. Boudart, M. *Adv. Catal. Relat. Subj.* **1969**, *20*, 153–166.
114. Boudart, M. *Chem. Rev.* **1995**, *95*, 661–666.
115. Bond, G. C. *Chem. Soc. Rev.* **1991**, *20*, 441–475.
116. Van Santen, R. A. *Acc. Chem. Res.* **2009**, *42*, 57–66.
117. Garin, F.; Légaré, P. In *Nanoparticles and Catalysis*; Astruc, D., Ed.; Wiley-VCH: Weinheim, **2008**; p. 531.
118. Zhang, H.; Jin, M.; Xiong, Y.; Lim, B.; Xia, Y. *Acc. Chem. Res.* **2013**, *46*, 1783–1794.

119. Xiong, Y.; Xia, Y. *Adv. Mater.* **2007**, *19*, 3385–3391.
120. Tao, A. R.; Habas, S.; Yang, P. *Small* **2008**, *4*, 310–325.
121. Lim, B.; Jiang, M.; Tao, J.; Camargo, P. H. C.; Zhu, Y.; Xia, Y. *Adv. Funct. Mater.* **2009**, *19*, 189–200.
122. Peng, Z.; Yang, H. *Nano Today* **2009**, *4*, 143–164.
123. Xia, Y.; Xiong, Y.; Lim, B.; Skrabalak, S. E. *Angew. Chem. Int. Ed.* **2009**, *48*, 60–103.
124. Niu, W.; Xu, G. *Nano Today* **2011**, *6*, 265–285.
125. Zhou, Z.-Y.; Tian, N.; Li, J.-T.; Broadwell, I.; Sun, S.-G. *Chem. Soc. Rev.* **2011**, *40*, 4167–4185.
126. Chen, M.; Wu, B.; Yang, J.; Zheng, N. *Adv. Mater.* **2012**, *24*, 862–879.
127. Xiong, Y.; McLellan, J. M.; Yin, Y.; Xia, Y. *Angew. Chem. Int. Ed.* **2007**, *46*, 790–794.
128. Lim, B.; Xiong, Y.; Xia, Y. *Angew. Chem. Int. Ed.* **2007**, *46*, 9279–9282.
129. Huang, X.; Tang, S.; Zhang, H.; Zhou, Z.; Zheng, N. *J. Am. Chem. Soc.* **2009**, *131*, 13916–13917.
130. Niu, Z.; Peng, Q.; Gong, M.; Rong, H.; Li, Y. *Angew. Chem. Int. Ed.* **2011**, *50*, 6315–6319.
131. Niu, W.; Zhang, L.; Xu, G. *ACS Nano* **2010**, *4*, 1987–1996.
132. Zhou, Z.-Y.; Tian, N.; Huang, Z.-Z.; Chen, D.-J.; Sun, S.-G. *Faraday Discuss.* **2008**, *140*, 81–92.
133. Tian, N.; Zhou, Z.-Y.; Sun, S.-G. *Chem. Commun.* **2009**, 1502–1504.
134. Xiong, Y.; McLellan, J. M.; Chen, J.; Yin, Y.; Li, Z.-Y.; Xia, Y. *J. Am. Chem. Soc.* **2005**, *127*, 17118–17127.
135. Narayanan, R.; El-Sayed, M. A. *Nano Lett.* **2004**, *4*, 1343–1348.
136. Narayanan, R.; El-Sayed, M. A. *Langmuir* **2005**, *21*, 2027–2033.
137. Jin, M.; Zhang, H.; Xie, Z.; Xia, Y. *Angew. Chem. Int. Ed.* **2011**, *50*, 7850–7854.
138. Chen, Y.-H.; Hung, H.-H.; Huang, M. H. *J. Am. Chem. Soc.* **2009**, *131*, 9114–9121.

139. Toshima, N.; Yan, H.; Shiraishi, Y. In *Metal Nanoclusters in Catalysis and Materials Science science: The Issue of Size Control*; Corain, B.; Schmid, G.; Toshima, N., Eds.; Elsevier: Amsterdam, **2008**; pp. 49–75.
140. Scott, R. W. J.; Wilson, O. M.; Oh, S.-K.; Kenik, E. A.; Crooks, R. M. *J. Am. Chem. Soc.* **2004**, *126*, 15583–15591.
141. Venkatesan, P.; Santhanalakshmi, J. *J. Mol. Catal. A: Chem* **2010**, *326*, 99–106.
142. Kim, M.-R.; Choi, S.-H. *J. Nanomater.* **2009**, *2009*, 1–7.
143. Kim, S.-J.; Oh, S.-D.; Lee, S.; Choi, S.-H. *J. Ind. Eng. Chem.* **2008**, *14*, 449–456.
144. Blaser, H.-U.; Indolese, A.; Schnyder, A.; Steiner, H.; Studer, M. *J. Mol. Catal. A: Chem* **2001**, *173*, 3–18.
145. Bäumer, M.; Freund, H. *Prog. Surf. Sci.* **1999**, *61*, 127–198.
146. Djakovitch, L.; Klaus, K.; de Vries, J. G. In *Nanoparticles and Catalysis*; Astruc, D., Ed.; Wiley-VCH: Weinheim, **2008**; pp. 303–348.
147. Köhler, K.; Heidenreich, R. G.; Soomro, S. S.; Pröckl, S. S. *Adv. Synth. Catal.* **2008**, *350*, 2930–2936.
148. Siamaki, A. R.; Khder, A. E. R. S.; Abdelsayed, V.; El-Shall, M. S.; Gupton, B. F. *J. Catal.* **2011**, *279*, 1–11.
149. Cornelio, B.; Rance, G. A.; Laronze-Cochard, M.; Fontana, A.; Sapi, J.; Khlobystov, A. N. *J. Mater. Chem. A* **2013**, *1*, 8737–8744.
150. Biffis, A.; Sperotto, E. *Langmuir* **2003**, *19*, 9548–9550.
151. Cho, J. K.; Najman, R.; Dean, T. W.; Ichihara, O.; Muller, C.; Bradley, M. *J. Am. Chem. Soc.* **2006**, *128*, 6276–6277.
152. Ogasawara, S.; Kato, S. *J. Am. Chem. Soc.* **2010**, *132*, 4608–4613.
153. Ohtaka, A.; Teratani, T.; Fujii, R.; Ikeshita, K.; Kawashima, T.; Tatsumi, K.; Shimomura, O.; Nomura, R. *J. Org. Chem.* **2011**, *76*, 4052–4060.
154. Astruc, D. *Tetrahedron: Asymmetry* **2010**, *21*, 1041–1054.
155. Budarin, V. L.; Clark, J. H.; Luque, R.; Macquarrie, D. J.; White, R. J. *Green Chem.* **2008**, *10*, 382–387.

156. Søbjerg, L. S.; Lindhardt, A. T.; Skrydstrup, T.; Finster, K.; Meyer, R. L. *Colloids Surf. B. Biointerfaces* **2011**, *85*, 373–378.
157. Parker, H. L.; Rylott, E. L.; Hunt, A. J.; Dodson, J. R.; Taylor, A. F.; Bruce, N. C.; Clark, J. H. *PLoS One* **2014**, *9*, e87192.
158. Gates, B. C. *Chem. Rev.* **1995**, *95*, 511–522.
159. Henry, C. *Surf. Sci. Rep.* **1998**, *31*, 231–325.
160. Binns, C. *Surf. Sci. Rep.* **2001**, *44*, 1–49.
161. Toebes, M. L.; van Dillen, J. A.; de Jong, K. P. *J. Mol. Catal. A: Chem* **2001**, *173*, 75–98.
162. Pacchioni, G; Giordano, L; Ferrari, A. M.; Abbet, S.; Heiz, U. In *Theoretical Aspects of Heterogeneous Catalysis*; Nascimento, C., Ed.; Kluwer Academic: Dordrecht, **2001**; 183–198.
163. a) Haruta, M.; Kobayashi, T.; Sano, H.; Yamada, N. *Chem. Lett.* **1987**, *16*, 405–408. b) Haruta, M.; Yamada, N.; Kobayashi, T.; Iijima, S. *J. Catal.* **1989**, *115*, 301–309.
164. Haruta, M.; Tsubota, S.; Kobayashi, T.; Kageyama, H.; Genet, M. J.; Delmon, B. *J. Catal.* **1993**, *144*, 175–192.
165. Faraday, M. *Phil. Trans. Roy. Soc.* **1857**, *147*, 145–181.
166. Yan, N.; Xiao, C.; Kou, Y. *Coord. Chem. Rev.* **2010**, *254*, 1179–1218.
167. Astruc, D. In *Nanoparticles and Catalysis*; Wiley-VCH: Weinheim, **2008**; pp. 1–48.
168. Cao, G. *Nanostructures and nanomaterials - Synthesis, Properties and Applications*; Imperial College Press: London, **2004**; p. 8.
169. Doppiu, S.; Langlais, V.; Sort, J.; Suriñach, S.; Baró, M. D.; Zhang, Y.; Hadjipanayis, G.; Nogués, J. *Chem. Mater.* **2004**, *16*, 5664–5669.
170. Gaffet, E.; Tachikart, M.; El Kedim, O.; Rahouadj, R. *Mater. Charact.* **1996**, *36*, 185–190.
171. Frank, M.; Bäumer, M. *Phys. Chem. Chem. Phys.* **2000**, *2*, 3723–3737.
172. Gao, P. X.; Ding, Y.; Wang, Z. L. *Nano Lett.* **2003**, *3*, 1315–1320.
173. Guczi, L.; Horváth, D.; Pászti, Z.; Tóth, L.; Horváth, Z. E.; Karacs, A.; Petõ, G. *J. Phys. Chem. B* **2000**, *104*, 3183–3193.

174. Eppler, A.; Rupprechter, G.; Guczi, L.; Somorjai, G. A. *J. Phys. Chem. B* **1997**, *101*, 9973–9977.
175. Narita, I.; Oku, T. *Diam. Relat. Mater.* **2002**, *11*, 949–952.
176. Kim, B.; Lee, G.; Park, H.; Kim, N. *Nanostructured Mater.* **1999**, *12*, 637–640.
177. Srikanth, H.; Hajndl, R.; Chirinos, C.; Sanders, J.; Sampath, A.; Sudarshan, T. S. *Appl. Phys. Lett.* **2001**, *79*, 3503–3505.
178. Smyth, J. F.; Schultz, S.; Fredkin, D. R.; Kern, D. P.; Rishton, S. A.; Schmid, H.; Cali, M.; Koehler, T. R. *J. Appl. Phys.* **1991**, *69*, 5262–5266.
179. Shearwood, C.; Blundell, S. J.; Baird, M. J.; Bland, J. A. C.; Gester, M.; Ahmed, H.; Hughes, H. P. *J. Appl. Phys.* **1994**, *75*, 5249–5256.
180. Huang, Y.-Z.; Cockayne, D. J. H.; Ana-Vanessa, J.; Cowburn, R. P.; Wang, S.-G.; Ward, R. C. C. *Nanotechnology* **2008**, *19*, 015303.
181. Pető, G.; Molnár, G. L.; Pászti, Z.; Geszti, O.; Beck, A.; Guczi, L. *Metarials Sci. Eng. C* **2002**, *19*, 95–99.
182. Heyderman, L. J.; Solak, H. H.; David, C.; Atkinson, D.; Cowburn, R. P.; Nolting, F. *Appl. Phys. Lett.* **2004**, *85*, 4989–4991.
183. Luo, Y.; Misra, V. *Nanotechnology* **2006**, *17*, 4909–4911.
184. Savas, T. A.; Farhoud, M.; Smith, H. I.; Hwang, M.; Ross, C. A. *J. Appl. Phys.* **1999**, *85*, 6160–6162.
185. Rampino, L.; Nord, F. *J. Am. Chem. Soc.* **1941**, *63*, 2745–2749.
186. Tsutsumi, K.; Funaki, Y.; Hirokawa, Y.; Hashimoto, T. *Langmuir* **1999**, *15*, 5200–5203.
187. Bradley, J. S.; Hill, E. W.; Behal, S.; Klein, C.; Chaudret, B.; Duteil, A. *Chem. Mater.* **1992**, *4*, 1234–1239.
188. Ornelas, C.; Salmon, L.; Ruiz Aranzaes, J.; Astruc, D. *Chem. Commun.* **2007**, *3*, 4946–4948.
189. Mayer, B. R. *Mater. Sci. Eng. C* **1998**, *6*, 155–166.
190. Ye, Q.; Wang, X.; Hu, H.; Wang, D.; Li, S.; Zhou, F. *J. Phys. Chem. C* **2009**, *113*, 7677–7683.

191. Antonietti, M.; Wenz, E.; Bronstein, L. M.; Seregina, M. V *Adv. Mater.* **1995**, *7*, 1000–1005.
192. Li, Y.; El-Sayed, M. A. *J. Phys. Chem. B* **2001**, *105*, 8938–8943.
193. Duteil, A.; Quéau, R.; Chaudret, B.; Mazel, R.; Roucau, C.; Bradley, J. S. *Chem. Mater.* **1993**, *5*, 341–347.
194. Bronstein, L. M.; Sidorov, S. N.; Gourkova, A. Y.; Valetsky, P. M.; Hartmann, J.; Breulmann, M.; Cölfen, H.; Antonietti, M. *Inorganica Chim. Acta* **1998**, *280*, 348–354.
195. Mecking, S.; Thomann, R.; Frey, H.; Sunder, A. *Macromolecules* **2000**, *33*, 3958–3960.
196. Hatakeyama, Y.; Umetsu, M.; Ohara, S.; Kawadai, F.; Takami, S.; Naka, T.; Adschiri, T. *Adv. Mater.* **2008**, *20*, 1122–1128.
197. Metin, Ö.; Durap, F.; Aydemir, M.; Özkar, S. *J. Mol. Catal. A: Chem* **2011**, *337*, 39–44.
198. Mayer, A.; Mark, J. *Colloid Polym. Sci.* **1997**, *275*, 333–340.
199. Toshima, N.; Shiraishi, Y.; Teranishi, T.; Miyake, M.; Tominaga, T.; Watanabe, H.; Brijoux, W.; Bönnemann, H.; Schmid, G. *Appl. Organomet. Chem.* **2001**, *15*, 178–196.
200. Shifrina, Z. B.; Rajadurai, M. S.; Firsova, N. V.; Bronstein, L. M.; Huang, X.; Rusanov, A. L.; Muellen, K. *Macromolecules* **2005**, *38*, 9920–9932.
201. Sawoo, S.; Srimani, D.; Dutta, P.; Lahiri, R.; Sarkar, A. *Tetrahedron* **2009**, *65*, 4367–4374.
202. Teranishi, T.; Miyake, M. *Chem. Mater.* **1998**, *10*, 594–600.
203. Hirai, H.; Chawanya, H.; Toshima, N. *React. Polym.* **1985**, *3*, 127–141.
204. Sanji, T.; Ogawa, Y.; Nakatsuka, Y.; Tanaka, M.; Sakurai, H. *Chem. Lett.* **2003**, *32*, 980–981.
205. Piao, Y.; Jang, Y.; Shokouhimehr, M.; Lee, I. S.; Hyeon, T. *Small* **2007**, *3*, 255–260.
206. Chauhan, B. P. S.; Rathore, J. S.; Chauhan, M.; Krawicz, A. *J. Am. Chem. Soc.* **2003**, *125*, 2876–2877.

207. Tanaka, T.; Ohyama, J.; Teramura, K.; Hitomi, Y. *Catal. Today* **2012**, *183*, 108–118.
208. Becker, R.; Döring, W. *Ann. Phys.* **1935**, *24*, 719–752.
209. LaMer, V.; Dinegar, R. *J. Am. Chem. Soc.* **1950**, *72*, 4847–4854.
210. Derjaguin, B.; Landau, L. *Acta Physicochim. URSS* **1941**, *14*, 633–662.
211. Verwey, E.; Overbeek, J. *Theory of the Stability of Lyophobic Colloids*; Elsevier: Amsterdam, **1948**.
212. Elimelech, M.; Gregory, J.; Jia, X.; Williams, R. A. In *Particles Deposition and Aggregation - Measurement, Modelling and Simulation*; Butterworth-Heinemann: Woburn, **1995**; pp. 33–67.
213. Israelachvili, J. N. In *Intermolecular and Surface Forces*; Academic Press: Burlington, **2011**; pp. 253–289.
214. Hamaker, H. *Physica* **1937**, *4*, 1058–1072.
215. Feke, D.; Prabhu, N.; Mann, J.; Mann III, J. *J. Phys. Chem.* **1984**, *88*, 5735–5739.
216. Widegren, J. A.; Finke, R. G. *J. Mol. Catal. A: Chem* **2003**, *198*, 317–341.
217. Feigin, R.; Napper, D. *J. Colloid Interface Sci.* **1980**, *75*, 525–541.
218. Israelachvili, J. N. In *Intermolecular and Surface Forces*; Academic Press: Burlington, **2011**; pp. 381–413.
219. Mayer, A. *Polym. Adv. Technol.* **2001**, *12*, 96–106.
220. Bradley, J. S. In *Clusters and Colloids*; Schmid, G., Ed.; Wiley-VCH: Weinheim, **1994**; p. 466.
221. Sato, T.; Ruch, R. In *Stabilization of Colloidal Dispersions by Polymer Adsorption, Surfactant Science Series*; Marcel Dekker: New York, **1980**; pp. 65–119.
222. De Gennes, P. G. *Macromolecules* **1981**, *14*, 1637–1644.
223. Li, F.; Pincet, F. *Langmuir* **2007**, *23*, 12541–12548.
224. Zsigmondy, R. *Zeitschrift für Anal. Chemie* **1901**, *40*, 697–719.
225. Thiele, H.; von Levern, H. S. *J. Colloid Sci.* **1965**, *20*, 679–694.
226. Domènech, B.; Bastos-Arrieta, J.; Alonso, A.; Macanás, J.; Muñoz, M.; Muraviev, D. N. In *Ion Exchange Technologies*; Kilislioğlu, A., Ed.; InTech, **2012**; pp. 35–72.
227. Hirai, H.; Nakao, Y.; Toshima, N.; Adachi, K. *Chem. Lett.* **1976**, *9*, 905–910.

228. Hirai, H.; Nakao, Y.; Toshima, N. *J. Macromol. Sci. Part A - Chem. Pure Appl. Chem.* **1978**, *12*, 1117–1141.
229. Hirai, H. *J. Macromol. Sci. Part A - Chem. Pure Appl. Chem.* **1979**, *13*, 633–649.
230. Hirai, H.; Nakao, Y.; Toshima, N. *J. Macromol. Sci. Part A - Chem. Pure Appl. Chem.* **1979**, *13*, 727–750.
231. Hirai, H.; Ohtaki, M.; Komiyama, M. *Chem. Lett.* **1987**, *127*, 149–152.
232. Rampino, L.; Kavanagh, K.; Nord, F. *Proc. Natl. Acad. Sci.* **1943**, *29*, 246–256.
233. Smith, T.; Wychick, D. *J. Phys. Chem.* **1980**, *84*, 1621–1629.
234. Elimelech, M.; Gregory, J.; Jia, X.; Williams, R. A. In *Particles Deposition and Aggregation - Measurement, Modelling and Simulation*; Butterworth-Heinemann: Woburn, **1995**; pp. 54–56.
235. Toshima, N. In *Nanoscale Materials*; Liz-Marzán, L. M.; Kamat, P. V, Eds.; Kluwer Academic: Dordrecht, **2003**; p. 82.
236. Boutonnet, M.; Kizling, J.; Touroude, R.; Maire, G.; Stenius *Appl. Catal.* **1986**, *20*, 163–177.
237. Klingelhöfer, S.; Heitz, W.; Greiner, A.; Oestreich, S.; Förster, S.; Antonietti, M. *J. Am. Chem. Soc.* **1997**, *119*, 10116–10120.
238. Toshima, N.; Shiraishi, Y.; Teranishi, T. *J. Mol. Catal. A: Chem* **2001**, *177*, 139–147.
239. Ohtaki, M.; Komiyama, M.; Hirai, H.; Toshima, N. *Macromolecules* **1991**, *24*, 5567–5572.
240. Cookson, J. *Platin. Met. Rev.* **2012**, *56*, 83–98.
241. Astruc, D. *Inorg. Chem.* **2007**, *46*, 1884–1894.
242. Hirai, H.; Chawanya, H.; Toshima, N. *Die Makromol. Chemie, Rapid Commun.* **1981**, *2*, 99–103.
243. Mayer, A. B. R.; Mark, J. E.; Hausner, S. H. *J. Appl. Polym. Sci.* **1998**, *70*, 1209–1219.
244. Zhao, M.; Crooks, R. M. *Angew. Chem. Int. Ed.* **1999**, *38*, 364–366.
245. Hou, Z.; Theyssen, N.; Brinkmann, A.; Leitner, W. *Angew. Chem. Int. Ed.* **2005**, *44*, 1346–1349.

246. Léger, B.; Nowicki, A.; Roucoux, A.; Rolland, J.-P. *J. Mol. Catal. A: Chem* **2007**, *266*, 221–225.
247. Gniewek, A.; Ziółkowski, J.; Trzeciak, A.; Kępiński, L. *J. Catal.* **2006**, *239*, 272–281.
248. Beller, M.; Fischer, H.; Kühlein, K.; Reisinger, C.-P.; Herrmann, W. A. *J. Organomet. Chem.* **1996**, *520*, 257–259.
249. Yeung, L. K.; Crooks, R. M. *Nano Lett.* **2001**, *1*, 14–17.
250. Meier, M. A. R.; Filali, M.; Gohy, J.-F.; Schubert, U. S. *J. Mater. Chem.* **2006**, *16*, 3001.
251. Astruc, D.; Ornelas, C.; Diallo, A. K.; Ruiz, J. *Molecules* **2010**, *15*, 4947–60.
252. Balanta, A.; Godard, C.; Claver, C. *Chem. Soc. Rev.* **2011**, *40*, 4973–4985.
253. Polshettiwar, V.; Decottignies, A.; Len, C.; Fihri, A. *ChemSusChem* **2010**, *3*, 502–522.
254. Horinouchi, S.; Yamanoi, Y.; Yonezawa, T.; Mouri, T.; Nishihara, H. *Langmuir* **2006**, *22*, 1880–1884.
255. Mubeen, S.; Zhang, T.; Yoo, B.; Deshusses, M. A.; Myung, N. V. *J. Phys. Chem. C* **2007**, *111*, 6321–6327.
256. Beletskaya, I.; Kashin, A.; Litvinov, A.; Tyurin, V. S.; Valetsky, P. M.; van Koten, G. *Organometallics* **2006**, *25*, 154–158.
257. Narayanan, R.; El-Sayed, M. A. *Top. Catal.* **2008**, *47*, 15–21.
258. Corain, B.; Kralik, M. *J. Mol. Catal. A: Chem* **2001**, *173*, 99–115.
259. Li, L.; Zhao, H.; Wang, J.; Wang, R. *ACS Nano* **2014**, *8*, 5352–5364.
260. Pachfule, P.; Panda, M. K.; Kandambeth, S.; Shivaprasad, S. M.; Díaz, D. D.; Banerjee, R. *J. Mater. Chem. A* **2014**, *2*, 7944–7952.
261. Liang, Q.; Liu, J.; Wei, Y.; Zhao, Z.; MacLachlan, M. J. *Chem. Commun.* **2013**, *49*, 8928–8930.
262. Zhou, Y.; Xiang, Z.; Cao, D.; Liu, C.-J. *Chem. Commun.* **2013**, *49*, 5633–5635.
263. Itoh, H.; Maeda, H.; Yamada, S.; Hori, Y. *ChemCatChem* **2012**, *4*, 1737–1740.
264. Richter, J.; Seidel, R.; Kirsch, R.; Mertig, M.; Pompe, W.; Plaschke, J.; Schackert, K. *Adv. Mater.* **2000**, *12*, 507–510.

265. Sajiki, H.; Ikawa, T.; Yamada, H.; Tsubouchi, K.; Hirota, K. *Tetrahedron Lett.* **2003**, *44*, 171–174.
266. Sathishkumar, M.; Sneha, K.; Kwak, I. S.; Mao, J.; Tripathy, S. J.; Yun, Y.-S. *J. Hazard. Mater.* **2009**, *171*, 400–404.
267. Whilton, N. T.; Berton, B.; Bronstein, L.; Hentze, H.-P.; Antonietti, M. *Adv. Mater.* **1999**, *11*, 1014–1018.
268. Biffis, A. *J. Mol. Catal. A: Chem* **2001**, *165*, 303–307.
269. Biffis, A.; Minati, L. *J. Catal.* **2005**, *236*, 405–409.
270. Liu, Y.; Khemtong, C.; Hu, J. *Chem. Commun.* **2004**, 398–399.
271. Mayer, A.; Mark, J. *Polymer* **2000**, *41*, 1627–1631.
272. Wei, G.; Wen, F.; Zhang, X.; Zhang, W.; Jiang, X.; Zheng, P.; Shi, L. *J. Colloid Interface Sci.* **2007**, *316*, 53–58.
273. Wei, G.; Zhang, W.; Wen, F.; Wang, Y.; Zhang, M. *J. Phys. Chem. C* **2008**, *112*, 10827–10832.
274. Telkar, M. M.; Rode, C. V.; Chaudhari, R. V.; Joshi, S. S.; Nalawade, A. M. *Appl. Catal., A* **2004**, *273*, 11–19.
275. Kavanagh, K.; Nord, F. *J. Am. Chem. Soc.* **1943**, *65*, 2121–2125.
276. Coulter, M. M.; Dinglasan, J. A.; Goh, J. B.; Nair, S.; Anderson, D. J.; Dong, V. M. *Chem. Sci.* **2010**, *1*, 772–775.
277. Ornelas, C.; Diallo, A. K.; Ruiz, J.; Astruc, D. *Adv. Synth. Catal.* **2009**, *351*, 2147–2154.
278. Mayer, A. B. R.; Mark, J. E. *Macromol. Reports* **1996**, *A33*, 451–459.
279. Bronstein, L.; Chernyshov, D.; Timofeeva, G. I.; Dubrovina, L. V; Valetsky, P. M.; Obolonkova, E. S.; Khokhlov, A. R. *Langmuir* **2000**, *16*, 3626–3632.
280. Okumura, A.; Tsutsumi, K.; Hashimoto, T. *Polym. J.* **2000**, *32*, 520–523.
281. Semagina, N. V; Bykov, A. V; Sulman, E. M.; Matveeva, V. G.; Sidorov, S. N.; Dubrovina, L. V; Valetsky, P. M.; Kiselyova, O. I.; Khokhlov, A. R.; Stein, B.; Bronstein, L. M. *J. Mol. Catal. A: Chem* **2004**, *208*, 273–284.
282. Nakamura, Y.; Hirai, H. *Chem. Lett.* **1976**, *5*, 1197–1202.

283. Favier, I.; Gómez, M.; Muller, G.; Picurelli, D.; Nowicki, A.; Roucoux, A.; Bou, J. *J. Appl. Polym. Sci.* **2007**, *105*, 2772–2782.
284. Antonietti, M.; Förster, S.; Hartmann, J.; Oestreich, S. *Macromolecules* **1996**, *29*, 3800–3806.
285. Bosman, A. W.; Vestberg, R.; Heumann, A.; Fréchet, J. M. J.; Hawker, C. J. *J. Am. Chem. Soc.* **2003**, *125*, 715–728.
286. Dockendorff, J. M. Arborescent copolymers: Synthesis, Properties and Metallic Nanoparticle Templating, Ph.D. Thesis, University of Waterloo, Waterloo, **2011**, pp. 116–169.
287. Dockendorff, J. M. Arborescent Copolymers: Synthesis, Properties and Metallic Nanoparticle Templating, Ph.D. Thesis, University of Waterloo, Waterloo, **2011**, pp. 224–317.
288. Gopidas, K. R.; Whitesell, J. K.; Fox, M. A. *Nano Lett.* **2003**, *3*, 1757–1760.
289. Wu, L.; Li, B.-L.; Huang, Y.-Y.; Zhou, H.-F.; He, Y.-M.; Fan, Q.-H. *Org. Lett.* **2006**, *8*, 3605–3608.
290. Mei, Y.; Lu, Y.; Polzer, F.; Ballauff, M.; Drechsler, M. *Chem. Mater.* **2007**, *19*, 1062–1069.
291. Li, D.; Dunlap, J. R.; Zhao, B. *Langmuir* **2008**, *24*, 5911–5918.
292. Chauhan, B. P. S.; Rathore, J. S.; Bandoo, T. *J. Am. Chem. Soc.* **2004**, *126*, 8493–8500.
293. Underhill, R.; Liu, G. *Chem. Mater.* **2000**, *12*, 2082–2091.
294. Underhill, R. S.; Liu, G. *Chem. Mater.* **2000**, *12*, 3633–3641.
295. Zhang, J.; Wang, X.; Fu, Y.; Han, Y.; Cheng, J.; Zhang, Y.; Li, W. *Langmuir* **2013**, *29*, 14345–14350.
296. Khan, M.; Khan, M.; Kuniyil, M.; Adil, S. F.; Al-Warthan, A.; Alkhathlan, H. Z.; Tremel, W.; Tahir, M. N.; Siddiqui, M. R. H. *Dalt. Trans.* **2014**, *43*, 9026–9031.
297. Wang, Y.; Ouyang, G.; Zhang, J.; Wang, Z. *Chem. Commun.* **2010**, *46*, 7912–7914.
298. Coppage, R.; Slocik, J. M.; Sethi, M.; Pacardo, D. B.; Naik, R. R.; Knecht, M. R. *Angew. Chemie* **2010**, *122*, 3855–3858.

299. Li, W.; Fu, Y.; Wang, X.; Zhang, J. *Cat. Lett.* **2013**, *143*, 578–586.
300. Rampino, L.; Nord, F. *J. Am. Chem. Soc.* **1941**, *63*, 3268–3268.
301. Nakamura, Y.; Hirai, H. *Chem. Lett.* **1976**, *5*, 165–168.
302. Liu, Y.; Cheng, S.; Wen, X.; Hu, J. *Langmuir* **2002**, *18*, 10500–10502.
303. Papp, S.; Szücs, A.; Dékány, I. *Appl. Clay Sci.* **2001**, *19*, 155–172.
304. Antonietti, M.; Heinz, S. *Nachrichten aus Chemie, Tech. und Lab.* **1992**, *40*, 308–314.
305. Meier, M. A. R.; Gohy, J.-F.; Fustin, C.-A.; Schubert, U. S. *J. Am. Chem. Soc.* **2004**, *126*, 11517–11521.
306. Zhao, M.; Sun, L.; Crooks, R. *J. Am. Chem. Soc.* **1998**, *120*, 4877–4878.
307. Balogh, L.; Tomalia, D. *J. Am. Chem. Soc.* **1998**, *120*, 7355–7356.
308. Astruc, D.; Chardac, F. *Chem. Rev.* **2001**, *101*, 2991–3023.
309. Crooks, R. M.; Zhao, M.; Sun, L.; Chechik, V.; Yeung, L. K. *Acc. Chem. Res.* **2001**, *34*, 181–90.
310. Crooks, R.; Lemon III, B.; Sun, L.; Yeung, L.; Zhao, M. *Top. Curr. Chem.* **2001**, *212*, 81–135.
311. van Heerbeek, R.; Kamer, P. C. J.; van Leeuwen, P. W. N. M.; Reek, J. N. H. *Chem. Rev.* **2002**, *102*, 3717–3756.
312. Niu, Y.; Crooks, R. M. *Comptes Rendus Chim.* **2003**, *6*, 1049–1059.
313. Scott, R. W. J.; Wilson, O. M.; Crooks, R. M. *J. Phys. Chem. B* **2005**, *109*, 692–704.
314. Astruc, D.; Berger, A.; Chandler, B.; Daniel, M.-C.; Gade, L.; Gilbertson, J.; Haag, R.; Hajji, C.; Kassube, J.; Klein Gebbink, R.; van Koten, G.; van Leeuwen, P.; Reek, J.; Ribaudo, F.; Ruiz, J. *Top. Organomet. Chem.* **2006**, *20*, 1–189.
315. Andrés, R.; de Jesús, E.; Flores, J. C. *New J. Chem.* **2007**, *31*, 1161–1191.
316. Astruc, D.; Boisselier, E.; Ornelas, C. *Chem. Rev.* **2010**, *110*, 1857–959.
317. Bronstein, L. M.; Shifrina, Z. B. *Chem. Rev.* **2011**, *111*, 5301–5344.
318. Myers, V. S.; Weir, M. G.; Carino, E. V.; Yancey, D. F.; Pande, S.; Crooks, R. M. *Chem. Sci.* **2011**, *2*, 1632–1646.
319. Wang, D.; Astruc, D. *Coord. Chem. Rev.* **2013**, *257*, 2317–2334.

320. Huang, W. In *Current Trends of Surface Science and Catalysis*; Park, J. Y., Ed.; Springer Science and Buisness: New York, **2014**; pp. 65–91.
321. Scott, R. W. J.; Ye, H.; Henriquez, R. R.; Crooks, R. M. *Chem. Mater.* **2003**, *15*, 3873–3878.
322. Yeung, L. K.; Lee Jr., C. T.; Johnston, K. P.; Crooks, R. M. *Chem. Commun.* **2001**, 2290–2291.
323. Hult, A.; Johansson, M.; Malmström, E. *Adv. Polym. Sci.* **1999**, *143*, 1–34.
324. Kee, R. A.; Gauthier, M.; Tomalia, D. A. In *Dendrimers and Other Dendritic Polymers*; Fréchet, J. M. J.; Tomalia, D. A., Eds.; John Wiley and Sons: New York, **2001**; pp. 209–236.
325. Sunder, A.; Krämer, M.; Hanselmann, R.; Mülhaupt, R.; Frey, H. *Angew. Chem. Int. Ed.* **1999**, *38*, 3552–3555.
326. Gauthier, M.; Li, J.; Dockendorff, J. *Macromolecules* **2003**, *36*, 2642–2648.
327. Dockendorff, J.; Gauthier, M. *J. Polym. Sci. Part A: Polym. Chem.* **2014**, *52*, 1075–1085.
328. Dockendorff, J.; Gauthier, M.; Mourran, A.; Möller, M. *Macromolecules* **2008**, *41*, 6621–6623.
329. Fihri, A.; Bouhrara, M.; Nekoueishahraki, B.; Basset, J.-M.; Polshettiwar, V. *Chem. Soc. Rev.* **2011**, *40*, 5181–5203.
330. Molnár, Á. *Chem. Rev.* **2011**, *111*, 2251–2320.
331. Deraedt, C.; Astruc, D. *Acc. Chem. Res.* **2014**, *47*, 494–503.
332. Kotha, S.; Lahiri, K.; Kashinath, D. *Tetrahedron* **2002**, *58*, 9633–9695.
333. Miyaura, N.; Yanagi, T.; Suzuki, A. *Synth. Commun.* **1981**, *11*, 513–519.
334. Suzuki, A. In *Modern Arene Chemistry*; Astruc, D., Ed.; Wiley-VCH: Weinheim, **2002**; pp. 53–106.
335. Anastas, P.; Heine, L.; Williamson, T. In *Green Chemical Syntheses and Processes*; American Chemical Society: Washington, **2000**; pp. 1–6.
336. Polshettiwar, V.; Luque, R.; Fihri, A.; Zhu, H.; Bouhrara, M.; Basset, J.-M. *Chem. Rev.* **2011**, *111*, 3036–3075.

337. Lamblin, M.; Nassar-Hardy, L.; Hierso, J.-C.; Fouquet, E.; Felpin, F.-X. *Adv. Synth. Catal.* **2010**, *352*, 33–79.
338. Beletskaya, I. P.; Kashin, A. N.; Khotina, I. A.; Khokhlov, A. R. *Synlett* **2008**, *10*, 1547–1552.
339. Keller, M.; Hameau, A.; Spataro, G.; Ladeira, S.; Caminade, A.-M.; Majoral, J.-P.; Ouali, A. *Green Chem.* **2012**, *14*, 2807–2815.
340. Reetz, M.; Breinbauer, R.; Wanninger, K. *Tetrahedron Lett.* **1996**, *37*, 4499–4502.
341. a) Narayanan, R.; El-Sayed, M. A. *J. Am. Chem. Soc.* **2003**, *125*, 8340–8347.
b) Li, Y.; Hong, X.; Collard, D. M.; El-Sayed, M. A. *Org. Lett.* **2000**, *2*, 2385–2388.
342. Ohtaka, A.; Tamaki, Y.; Igawa, Y.; Egami, K.; Shimomura, O.; Nomura, R. *Tetrahedron* **2010**, *66*, 5642–5646.
343. Narayanan, R.; El-Sayed, M. A. *J. Phys. Chem. B* **2004**, *108*, 8572–8580.
344. Pittelkow, M.; Moth-Poulsen, K.; Boas, U.; Christensen, J. B. *Langmuir* **2003**, *19*, 7682–7684.
345. Wu, L.; Li, Z.-W.; Zhang, F.; He, Y.-M.; Fan, Q.-H. *Adv. Synth. Catal.* **2008**, *350*, 846–862.
346. Beletskaya, I. P.; Cheprakov, A. V. *Chem. Rev.* **2000**, *100*, 3009–3066.
347. de Vries, A. H. M.; Mulders, J. M. C. A.; Mommers, J. H. M.; Henderickx, H. J. W.; de Vries, J. G. *Org. Lett.* **2003**, *5*, 3285–3288.
348. de Vries, J. G.; de Vries, A. H. M. *European J. Org. Chem.* **2003**, *2003*, 799–811.
349. Diallo, A. K.; Ornelas, C.; Salmon, L.; Ruiz Aranzaes, J.; Astruc, D. *Angew. Chem. Int. Ed.* **2007**, *46*, 8644–8648.
350. Hu, J.; Liu, Y. *Langmuir* **2005**, *21*, 2121–2123.
351. Ornelas, C.; Ruiz, J.; Salmon, L.; Astruc, D. *Adv. Synth. Catal.* **2008**, *350*, 837–845.
352. Deraedt, C.; Salmon, L.; Etienne, L.; Ruiz, J.; Astruc, D. *Chem. Commun.* **2013**, *49*, 8169–8171.
353. De Broglie, L. Recherches sur la Théorie des Quanta, Ph.D. Thesis, Paris, **1924**.
354. De Broglie, L. *Ann. Phys.* **1925**, *10*, 22–128.

355. Blackman, J. A.; Binns, C. In *Handbook of Metal Physics - Metallic Nanoparticles*; Misra, P., Ed.; Elsevier: Amsterdam, **2009**; p. 4.
356. Graham, T. *Phil. Trans. Roy. Soc.* **1861**, *151*, 183–224.
357. McNaught, A. D.; Wilkinson, A. Colloidal. *IUPAC. Compend. Chem. Terminol.* **2006**.
358. Lin, Y.; Finke, R. G. *J. Am. Chem. Soc.* **1994**, *116*, 8335–8353.

Chapter 3

1. Astruc, D.; Lu, F.; Aranzaes, J. R. *Angew. Chem. Int. Ed.* **2005**, *44*, 7852–7872.
2. Parak, W. J.; Liberato, M.; Simmel, F. C.; Gerion, D.; Paul, A. In *Nanoparticles - From Theory to Application*; Schmid, G., Ed.; Wiley-VCH: Weinheim, **2010**; pp. 3–47.
3. Philippot, K.; Serp, P. In *Nanomaterials in Catalysis*; Wiley-VCH: Weinheim, **2013**; pp. 1–54.
4. Heiz, U.; Landman, U. *Nanocatalysis*; Springer: Berlin, **2007**.
5. Niu, Y.; Crooks, R. M. *Comptes Rendus Chim.* **2003**, *6*, 1049–1059.
6. Scott, R. W. J.; Wilson, O. M.; Crooks, R. M. *J. Phys. Chem. B* **2005**, *109*, 692–704.
7. Astruc, D. *Inorg. Chem.* **2007**, *46*, 1884–1894.
8. Andrés, R.; de Jesús, E.; Flores, J. C. *New J. Chem.* **2007**, *31*, 1161–1191.
9. Astruc, D. *Tetrahedron: Asymmetry* **2010**, *21*, 1041–1054.
10. Wang, D.; Astruc, D. *Coord. Chem. Rev.* **2013**, *257*, 2317–2334.
11. Bronstein, L. M.; Shifrina, Z. B. *Chem. Rev.* **2011**, *111*, 5301–5344.
12. Reetz, M. T.; Lohmer, G.; Schwickardi, R. *Angew. Chem. Int. Ed.* **1997**, *36*, 1526–1529.
13. Kleij, A. W.; Gossage, R. A.; Klein Gebbink, R. J. M.; Brinkmann, N.; Reijerse, E. J.; Kragl, U.; Lutz, M.; Spek, A. L.; van Koten, G. *Angew. Chem. Int. Ed.* **2000**, *122*, 12112–12124.
14. Zhao, M.; Crooks, R. M. *Angew. Chem. Int. Ed.* **1999**, *38*, 364–366.
15. Yeung, L. K.; Crooks, R. M. *Nano Lett.* **2001**, *1*, 14–17.
16. Li, Y.; El-Sayed, M. A. *J. Phys. Chem. B* **2001**, *105*, 8938–8943.
17. Scott, R. W. J.; Ye, H.; Henriquez, R. R.; Crooks, R. M. *Chem. Mater.* **2003**, *15*, 3873–3878.
18. Chechik, V.; Zhao, M.; Crooks, R. M. *J. Am. Chem. Soc.* **1999**, *121*, 4910–4911.
19. Narayanan, R.; El-Sayed, M. A. *J. Phys. Chem. B* **2004**, *108*, 8572–8580.

20. Oh, S.; Niu, Y.; Crooks, R. M. *Langmuir* **2005**, *21*, 10209–10213.
21. Wu, L.; Li, B.-L.; Huang, Y.-Y.; Zhou, H.-F.; He, Y.-M.; Fan, Q.-H. *Org. Lett.* **2006**, *8*, 3605–3608.
22. Gauthier, M.; Möller, M. *Macromolecules* **1991**, *24*, 4548–4553.
23. Tomalia, D. A.; Hedstrand, D. M.; Ferritte, M. S. *Macromolecules* **1991**, *24*, 1435–1438.
24. Teertstra, S. J.; Gauthier, M. *Prog. Polym. Sci.* **2004**, *29*, 277–327.
25. Vivek, A. V; Babu, K.; Dhamodharan, R. *Macromolecules* **2009**, *42*, 2300–2303.
26. Tomalia, D. A.; Naylor, A. M.; Goddard, W. A. *Angew. Chem. Int. Ed.* **1990**, *29*, 138–175.
27. Kee, R. A.; Gauthier, M. *Macromolecules* **2002**, *35*, 6526–6532.
28. Gauthier, M.; Munam, A. *RSC Adv.* **2012**, *2*, 3100–3108.
29. Gauthier, M.; Li, J.; Dockendorff, J. *Macromolecules* **2003**, *36*, 2642–2648.
30. Dockendorff, J.; Gauthier, M. *J. Polym. Sci. Part A Polym. Chem.* **2014**, *52*, 1075–1085.
31. Njikang, G.; Gauthier, M.; Li, J. *Polymer* **2008**, *49*, 1276–1284.
32. Dockendorff, J.; Gauthier, M.; Mourran, A.; Möller, M. *Macromolecules* **2008**, *41*, 6621–6623.
33. Blaser, H.-U.; Indolese, A.; Schnyder, A.; Steiner, H.; Studer, M. *J. Mol. Catal. A: Chem* **2001**, *173*, 3–18.
34. Wang, Q.; Ostafin, A. E. In *Encyclopedia of Nanoscience and Nanotechnology*; Nalwa, H. S., Ed.; American Scientific, **2004**, Vol. 5, pp. 475–503.
35. Jia, C.-J.; Schüth, F. *Phys. Chem. Chem. Phys.* **2011**, *13*, 2457–2487.
36. Astruc, D. In *Nanoparticles and Catalysis*; Wiley-VCH: Weinheim, **2008**; p. 30.
37. Abràmoff, M. D.; Magalhães, P. J.; Ram, S. J. *Biophotonics Int.* **2004**, *11*, 36–42.
38. Koppel, D. E. *J. Chem. Phys.* **1972**, *57*, 4814–4820.
39. Provencher, W. *Comput. Phys. Commun.* **1982**, *27*, 213–227.
40. Provencher, W. *Comput. Phys. Commun.* **1982**, *27*, 229–242.
41. Njikang, G. N.; Cao, L.; Gauthier, M. *Macromol. Chem. Phys.* **2008**, *209*, 907–918.

42. Choi, S.; Briber, R. M.; Bauer, B. J.; Topp, A.; Gauthier, M.; Tichagwa, L. *Macromolecules* **1999**, *32*, 7879–7886.
43. Frank, R. S.; Merkle, G.; Gauthier, M. *Macromolecules* **1997**, *30*, 5397–5402.
44. Maiti, P. K.; Çağın, T.; Wang, G.; Goddard, W. A. *Macromolecules* **2004**, *37*, 6236–6254.
45. Li, J.; Gauthier, M. *Macromolecules* **2001**, *34*, 8918–8924.
46. Mencer, H. J.; Grubisic-Gallot, Z. *J. Liq. Chromatogr.* **1979**, *2*, 649–662.
47. Gauthier, M.; Li, W.; Tichagwa, L. *Polymer* **1997**, *38*, 6363–6370.
48. Yun, S. I.; Briber, R. M.; Kee, R. A.; Gauthier, M. *Polymer* **2003**, *44*, 6579–6587.
49. Beretta, S.; Lunelli, L.; Chirico, G.; Baldini, G. *Appl. Opt.* **1996**, *35*, 3763–70.
50. Frisken, B. J. *Appl. Opt.* **2001**, *40*, 4087–4091.
51. Njikang, G. N.; Gauthier, M.; Li, J. *Polymer* **2008**, *49*, 5474–5481.
52. Kiriy, A.; Gorodyska, G.; Minko, S.; Stamm, M.; Tsitsilianis, C. *Macromolecules* **2003**, *36*, 8704–8711.
53. Spatz, J. P.; Möller, M.; Noeske, M.; Behm, R. J.; Pietralla, M. *Macromolecules* **1997**, *30*, 3874–3880.
54. Li, Z.; Zhao, W.; Liu, Y.; Rafailovich, M. H.; Sokolov, J.; Khougaz, K.; Eisenberg, A.; Lennox, R. B.; Krausch, G. *J. Am. Chem. Soc.* **1996**, *118*, 10892–10893.
55. Sheiko, S. S. *Adv. Polym. Sci.* **2000**, *151*.
56. Raguzin, I.; Stoychev, G.; Stamm, M.; Ionov, L. *Soft Matter* **2013**, *9*, 359.
57. Sheiko, S. S.; Gauthier, M.; Möller, M. *Macromolecules* **1997**, *30*, 2343–2349.
58. Bates, F. S.; Fredrickson, G. H. *Annu. Rev. Phys. Chem.* **1990**, *41*, 525–57.
59. Bates, F. S. *Science* **1991**, *251*, 898–905.
60. Miller, R. L. In *Polymer Handbook*; Brandrup, J.; Immergut, E. H.; Grulke, E. A.; Abe, A.; Bloch, D. R., Eds.; John Wiley and Sons, **1999**; pp. VI–21.
61. Sheu, W. *J. Chem. Educ.* **2001**, *78*, 554–555.
62. Beck, A.; Horváth, A.; Sárkány, A.; Guczi, L. In *Nanotechnology in Catalysis*; Zhou, B.; Hermans, S.; Somorjai, G. A., Eds.; Springer Science and Buisness: New York, **2004**; Vol. 1, pp. 83–110.

63. Nguon, O.; Gauthier, M.; Karanassios, V. *RSC Adv.* **2014**, *4*, 8978–8984.
64. Wales, C. H.; Berger, J.; Blass, S.; Crooks, R. M.; Asherie, N. *Langmuir* **2011**, *27*, 4104–4109.
65. Choo, H.; He, B.; Liew, K. Y.; Liu, H.; Li, J. *J. Mol. Catal. A: Chem* **2006**, *244*, 217–228.
66. Ornelas, C.; Salmon, L.; Ruiz Aranzaes, J.; Astruc, D. *Chem. Commun.* **2007**, *3*, 4946–4948.
67. Napper, D. H. *Polymeric Stabilization of Colloidal Dispersions*; 1st Ed.; Academic Press: London, **1983**; p. 428.
68. Durand, J.; Teuma, E.; Gómez, M. *Eur. J. Inorg. Chem.* **2008**, *2008*, 3577–3586.
69. Zhang, H.; Jin, M.; Xiong, Y.; Lim, B.; Xia, Y. *Acc. Chem. Res.* **2013**, *46*, 1783–1794.
70. Li, Y.; Boone, E.; El-Sayed, M. A. *Langmuir* **2002**, *18*, 4921–4925.
71. Sun, Y.; Frenkel, A. I.; Isseroff, R.; Shonbrun, C.; Forman, M.; Shin, K.; Koga, T.; White, H.; Zhang, L.; Zhu, Y.; Rafailovich, M. H.; Sokolov, J. C. *Langmuir* **2006**, *22*, 807–816.
72. Mackay, A. L. *Acta Crystallogr.* **1962**, *15*, 916–918.
73. Benfield, R. E. *J. Chem. Soc. Faraday Trans.* **1992**, *88*, 1107–1110.
74. Vargaftik, M. N.; Zagorodnikov, V. P.; Stolyaroc, I. P.; Moiseev, I. I.; Likholobov, V. A.; Kochubey, D. I.; Chuvilin, A. L.; Zaikovsky, V. I.; Zamaraev, K. I.; Timofeevac, G. I. *J. Chem. Soc. Chem. Commun.* **1985**, 937–939.
75. Kubowicz, S.; Baussard, J.-F.; Lutz, J.-F.; Thünemann, A. F.; von Berlepsch, H.; Laschewsky, A. *Angew. Chem. Int. Ed.* **2005**, *44*, 5262–5265.
76. Gröschel, A. H.; Schacher, F. H.; Schmalz, H.; Borisov, O. V; Zhulina, E. B.; Walther, A.; Müller, A. H. E. *Nat. Commun.* **2012**, *3*, 1–10.
77. Mayer, B. R. *Mater. Sci. Eng. C* **1998**, *6*, 155–166.
78. Moughton, A. O.; Hillmyer, M. A.; Lodge, T. P. *Macromolecules* **2012**, *45*, 2–19.
79. Schacher, F.; Walther, A.; Ruppel, M.; Drechsler, M.; Müller, A. H. E. *Macromolecules* **2009**, *42*, 3540–3548.

80. Berlepsch, H. V; Böttcher, C.; Skrabania, K.; Laschewsky, A. *Chem. Commun.* **2009**, 2290–2292.
81. Gohy, J.-F.; Khousakoun, E.; Willet, N.; Varshney, S. K.; Jérôme, R. *Macromol. Rapid Commun.* **2004**, *25*, 1536–1539.
82. Schacher, F.; Walther, A.; Müller, A. H. E. *Langmuir* **2009**, *25*, 10962–10969.
83. Li, Z.; Hillmyer, M. A; Lodge, T. P. *Nano Lett.* **2006**, *6*, 1245–1249.
84. Li, Z.; Hillmyer, M. A; Lodge, T. P. *Langmuir* **2006**, *22*, 9409–9417.
85. Saito, N.; Liu, C.; Lodge, T. P.; Hillmyer, M. A. *ACS Nano* **2010**, *4*, 1907–1912.
86. Zhulina, E. B.; Borisov, O. V. *Macromolecules* **2012**, *45*, 4429–4440.
87. Spatz, J. P.; Sheiko, S.; Möller, M. *Macromolecules* **1996**, *29*, 3220–3226.
88. Antonietti, M.; Wenz, E.; Bronstein, L. M.; Seregina, M. V *Adv. Mater.* **1995**, *7*, 1000–1005.
89. Seregina, M. V; Bronstein, L. M.; Platonova, O. A.; Chernyshov, D. M.; Valetsky, P. M.; Hartmann, J.; Wenz, E.; Antonietti, M. *Chem. Mater.* **1997**, *9*, 923–931.
90. Jiang, X.; Wei, G.; Zhang, X.; Zhang, W.; Zheng, P.; Wen, F.; Shi, L. *J. Mol. Catal. A: Chem* **2007**, *277*, 102–106.
91. Bönnemann, H.; Nagabhushana, K. S. In *Encyclopedia of Nanoscience and Nanotechnology*; Nalwa, H. S., Ed.; American Scientific, **2004**, Vol. 1, pp. 777–813.
92. Leite, R.; Ribeiro, C. *Crystallization and Growth of Colloidal Nanocrystals*; Springer Science and Buisness: New York, NY, **2012**; p. 20.
93. Mössmer, S.; Spatz, J. P.; Möller, M.; Aberle, T.; Schmidt, J.; Burchard, W. *Macromolecules* **2000**, *33*, 4791–4798.
94. Worden, J. G.; Dai, Q.; Huo, Q. *Chem. Commun.* **2006**, 1536–1538.
95. Li, T.; Zhou, C.; Jiang, M. *Polym. Bull.* **1991**, *25*, 211–216.
96. Story, V. M.; McIntyre, D.; O'Mara, J. H. *J. Res. Natl. Bur. Stand. Sect. A Phys. Chem.* **1967**, *71A*, 169.
97. Zhang, H.; Wang, D.; Wang, Z.; Zhang, X. *Eur. Polym. J.* **2007**, *43*, 2784–2791.
98. Tixier, S.; Cooper, G.; Feng, R.; Brion, C. E. *J. Electron Spectros. Relat. Phenomena* **2002**, *123*, 185–197.

99. Partridge, R. H. *J. Chem. Phys.* **1967**, *47*, 4223.
100. Price, W. C.; Walsh, A. D. *Proc. R. Soc. A Math. Phys. Eng. Sci.* **1947**, *191*, 22–31.
101. Stephenson, T. A.; Morehouse, S. M.; Powell, A. R.; Heffer, J. P.; Wilkinson, G. *J. Chem. Soc.* **1965**.
102. Romm, I. P.; Malkov, A. A.; Lebedev, S. A.; Levashova, V. V.; Buslaeva, T. M. *Russ. J. Phys. Chem. A* **2011**, *85*, 248–253.
103. Creighton, J. A.; Eadon, D. G. *J. Chem. Soc. Faraday Trans.* **1991**, *87*, 3881–3891.
104. Redón, R.; García-Peña, N. G.; Ugalde-Saldivar, V. M.; García, J. J. *J. Mol. Catal. A: Chem* **2009**, *300*, 132–141.
105. Furlong, D. N.; Launikonis, A.; Sasse, W. H. F.; Sanders, J. V *J. Chem. Soc. Faraday Trans.* **1984**, *80*, 571–588.
106. Reetz, M. T.; Helbig, W.; Quaiser, S. A. In *Active Metals*; Fürstner, A., Ed.; VCH: Weinheim, **1996**; pp. 279–298.
107. Krogul, A.; Cedrowski, J.; Wiktorska, K.; Ozimiński, W. P.; Skupińska, J.; Litwinienko, G. *Dalton Trans.* **2012**, *41*, 658–66.
108. D'Souza, L.; Sampath, S. *Langmuir* **2000**, *16*, 8510–8517.
109. Fernandes, A. E.; Dirani, A.; D'Haese, C.; Deumer, G.; Guo, W.; Hensenne, P.; Nahra, F.; Laloyaux, X.; Haufroid, V.; Nysten, B.; Riant, O.; Jonas, A. M. *Chem. Eur. J.* **2012**, *18*, 16226–16233.
110. Amatore, C.; Jutand, A.; M'Barki, M. A. *Organometallics* **1992**, *11*, 3009–3013.
111. Zalesskiy, S. S.; Ananikov, V. P. *Organometallics* **2012**, *31*, 2302–2309.
112. Diallo, A. K.; Ornelas, C.; Salmon, L.; Ruiz Aranzaes, J.; Astruc, D. *Angew. Chem. Int. Ed.* **2007**, *46*, 8644–8648.
113. Biffis, A.; Zecca, M.; Basato, M. *J. Mol. Catal. A: Chem* **2001**, *173*, 249–274.
114. Djakovitch, L.; Wagner, M.; Hartung, C. G.; Beller, M.; Koehler, K. *J. Mol. Catal. A: Chem* **2004**, *219*, 121–130.
115. Phan, N. T. S.; Van der Sluys, M.; Jones, C. W. *Adv. Synth. Catal.* **2006**, *348*, 609–679.

116. Djakovitch, L.; Klaus, K.; Vries, J. G. De In *Nanoparticles and Catalysis*; Astruc, D., Ed.; Wiley-VCH: Weinheim, **2008**; pp. 303–348.
117. de Vries, J. G. *Dalton Trans.* **2006**, 421–429.
118. Durán Pachón, L.; Rothenberg, G. *Appl. Organomet. Chem.* **2008**, *22*, 288–299.

Chapter 4

1. Schmid, G. *Nanoparticles - From Theory to Application*; 2nd ed.; Wiley-VCH: Weinheim, **2010**.
2. Shenhar, R.; Norsten, T. B.; Rotello, V. M. *Adv. Mater.* **2005**, *17*, 657–669.
3. Faraday, M. *Phil. Trans. Roy. Soc.* **1857**, *147*, 145–181.
4. Bönnemann, H.; Nagabhushana, K. S. In *Metal Nanoclusters in Catalysis and Materials Science*; Corain, B.; Schmid, G.; Toshima, N., Eds.; Elsevier: Amsterdam, **2008**; pp. 21–48.
5. Hirai, H.; Nakao, Y.; Toshima, N.; Adachi, K. *Chem. Lett.* **1976**, *9*, 905–910.
6. Teranishi, T.; Miyake, M. *Chem. Mater.* **1998**, *10*, 594–600.
7. Bekturov, E. A.; Kudaibergenov, S. E.; Saltybaeva, S. S.; Sokolskii, D. V.; Zharmagambetova, A. K.; Anisimova, N. V. *React. Polym. Ion Exch. Sorbents* **1985**, *4*, 49–53.
8. Bekturov, E. A.; Kudaibergenov, S. E.; Sokolskii, D. V.; Zharmagametova, A. K.; Mukhamedzhanova, S. G.; Kuanyshev, A. S. *Makromol. Chem., Rapid Commun.* **1986**, *7*, 187–191.
9. Sokolskii, D. V.; Zharmagambetova, A. K.; Mukhamedzhanova, S. G.; Bekturov, E. A.; Kudaibergenov, S. E.; Mukhamedzhanova, E. A.; Bekturov, E. A. E. A.; Kudaibergenov, S. E. S. E. *React. Kinet. Catal. Lett.* **1987**, *33*, 387–392.
10. Hoogsteen, W.; Fokkink, L. G. J. *J. Colloid Interface Sci.* **1995**, *175*, 12–26.
11. Tsutsumi, K.; Funaki, Y.; Hirokawa, Y.; Hashimoto, T. *Langmuir* **1999**, *15*, 5200–5203.
12. Hashimoto, T.; Harada, M.; Sakamoto, N. *Macromolecules* **1999**, *32*, 6867–6870.
13. Semagina, N.; Joannet, E.; Parra, S.; Sulman, E.; Renken, A.; Kiwi-Minsker, L. *Appl. Catal., A* **2005**, *280*, 141–147.
14. Pathak, S.; Greci, M. T.; Kwong, R. C.; Mercado, K.; Prakash, G. K. S.; Olah, G. A.; Thompson, M. E. *Chem. Mater.* **2000**, *12*, 1985–1989.

15. Harada, M.; Ueji, M.; Kimura, Y. *Colloids Surf., A* **2008**, *315*, 304–310.
16. Gauthier, M.; Li, J.; Dockendorff, J. *Macromolecules* **2003**, *36*, 2642–2648.
17. Gauthier, M.; Munam, A. *RSC Adv.* **2012**, *2*, 3100–3108.
18. Dockendorff, J. M. Arborescent Copolymers: Synthesis, Properties and Metallic Nanoparticle Templating, Ph.D. Thesis, University of Waterloo, Waterloo, **2011**.
19. Nguon, O.; Gauthier, M. *Manuscript in preparation*.
20. Astruc, D. In *Nanoparticles and Catalysis*; Wiley-VCH: Weinheim, **2008**; p. 30.
21. Jia, C.-J.; Schüth, F. *Phys. Chem. Chem. Phys.* **2011**, *13*, 2457–2487.
22. Wang, Q.; Ostafin, A. E. Metal Nanoparticles in Catalysis. *Encycl. Nanosci. Nanotechnol.* **2004**, *5*, 475–503.
23. Blaser, H.-U.; Indolese, A.; Schnyder, A.; Steiner, H.; Studer, M. *J. Mol. Catal. A: Chem* **2001**, *173*, 3–18.
24. Balanta, A.; Godard, C.; Claver, C. *Chem. Soc. Rev.* **2011**, *40*, 4973–4985.
25. Fihri, A.; Bouhrara, M.; Nekoueishahraki, B.; Basset, J.-M.; Polshettiwar, V. *Chem. Soc. Rev.* **2011**, *40*, 5181–5203.
26. Molnár, Á. *Chem. Rev.* **2011**, *111*, 2251–2320.
27. Biffis, A.; Zecca, M.; Basato, M. *J. Mol. Catal. A: Chem* **2001**, *173*, 249–274.
28. Kleist, W.; Pröckl, S. S.; Köhler, K. *Cat. Lett.* **2008**, *125*, 197–200.
29. Choudary, B. M.; Madhi, S.; Chowdari, N. S.; Kantam, M. L.; Sreedhar, B. *J. Am. Chem. Soc.* **2002**, *124*, 14127–14136.
30. Astruc, D. *Tetrahedron: Asymmetry* **2010**, *21*, 1041–1054.
31. Marvin, K. A.; Johnson, J. A.; Rodenbusch, S. E.; Gong, L.; Vanden Bout, D. A.; Stevenson, K. J. *Anal. Chem.* **2012**, *84*, 5154–5158.
32. Liao, W.; Chen, Y.; Wang, J. S.; Yak, H. K.; Wai, C. M. *Ind. Eng. Chem. Res.* **2007**, *46*, 5089–5093.
33. Huang, S.-M.; He, B.-L. *React. Polym.* **1994**, *23*, 1–9.
34. Wu, Y.; Wang, D.; Zhao, P.; Niu, Z.; Peng, Q.; Li, Y. *Inorg. Chem.* **2011**, *50*, 2046–2048.
35. Pachulski, A.; Schödel, R.; Claus, P. *Appl. Catal., A* **2011**, *400*, 14–24.

36. Zhao, F.; Shirai, M.; Arai, M. *J. Mol. Catal. A: Chem* **2000**, *154*, 39–44.
37. Durap, F.; Metin, Ö.; Aydemir, M.; Özkar, S. *Appl. Organomet. Chem.* **2009**, *23*, 498–503.
38. Ohtaka, A.; Teratani, T.; Fujii, R.; Ikeshita, K.; Kawashima, T.; Tatsumi, K.; Shimomura, O.; Nomura, R. *J. Org. Chem.* **2011**, *76*, 4052–4060.
39. He, Y.; Cai, C. *Cat. Lett.* **2010**, *140*, 153–159.
40. Weagant, S.; Chen, V.; Karanassios, V. *Anal. Bioanal. Chem.* **2011**, *401*, 2865–2880.
41. Gibson, B.; Badiei, H. R.; Karanassios, V. *Spectrochim. Acta, Part B* **2006**, *61*, 753–758.
42. Karanassios, V.; Li, F. H.; Liu, B.; Salin, E. D. *J. Anal. At. Spectrom.* **1991**, *6*, 457–463.
43. Grindlay, G.; Maestre, S.; Gras, L.; Mora, J. *J. Anal. At. Spectrom.* **2006**, *21*, 1403–1411.
44. Weagant, S.; Karanassios, V. *Anal. Bioanal. Chem.* **2009**, *395*, 577–589.
45. Karanassios, V.; Johnson, K.; Smith, A. T. *Anal. Bioanal. Chem.* **2007**, *388*, 1595–1604.
46. Vanithakumari, S. C.; Nanda, K. K. *Phys. Lett. A* **2008**, *372*, 6930–6934.
47. Karanassios, V.; Grishko, V.; Reynolds, G. G. *J. Anal. At. Spectrom.* **1999**, *14*, 565–570.
48. Badiei, H. R.; Lai, B.; Karanassios, V. *Spectrochim. Acta, Part B* **2012**, *77*, 19–30.
49. Arvela, R. K.; Leadbeater, N. E.; Sangi, M. S.; Williams, V. A.; Granados, P.; Singer, R. D. *J. Org. Chem.* **2005**, *70*, 161–168.
50. Reetz, M. T.; Westermann, E.; Lohmer, R.; Lohmer, G. *Tetrahedron Lett.* **1998**, *39*, 8449–8452.
51. Beletskaya, I. P.; Cheprakov, A. V. *Chem. Rev.* **2000**, *100*, 3009–3066.
52. de Vries, A. H. M.; Mulders, J. M. C. A.; Mommers, J. H. M.; Henderickx, H. J. W.; de Vries, J. G. *Org. Lett.* **2003**, *5*, 3285–3288.
53. Bronstein, L. M.; Sidorov, S. N.; Valetsky, P. M.; Hartmann, J.; Cölfen, H.; Antonietti, M. *Langmuir* **1999**, *15*, 6256–6262.

54. Fernandes, A. E.; Dirani, A.; D'Haese, C.; Deumer, G.; Guo, W.; Hensenne, P.; Nahra, F.; Laloyaux, X.; Haufroid, V.; Nysten, B.; Riant, O.; Jonas, A. M. *Chem. Eur. J.* **2012**, *18*, 16226–16233.
55. Burton, P. D.; Boyle, T. J.; Datye, A. K. *J. Catal.* **2011**, *280*, 145–149.
56. Tait, C. D.; Janecky, D. R.; Rogers, P. S. Z. *Geochim. Cosmochim. Acta* **1991**, *55*, 1253–1264.
57. Elding, L. I. *Inorganica Chim. Acta* **1972**, *6*, 647–651.
58. Pankratov, A. N.; Borodulin, V. B.; Chaplygina, O. A. *Russ. J. Coord. Chem.* **2005**, *31*, 660–666.
59. Manning, T. J.; Grow, W. R. *Chem. Educator* **1997**, *2*, 1–19.

Chapter 5

1. Duncan, R. *Nat. Rev. Drug Discov.* **2003**, *2*, 347–360.
2. Elsabahy, M.; Wooley, K. *Chem. Soc. Rev.* **2012**, *41*, 2545–2561.
3. Kelly, J.; Mackenzie, W. M.; Sherrington, D. C.; Reiss, G. *Polymers* **1979**, *20*, 1048–1050.
4. Berlinova, I. *Die Makromol. Chemie* **1990**, *191*, 709–716.
5. Shenhar, R.; Norsten, T. B.; Rotello, V. M. *Adv. Mater.* **2005**, *17*, 657–669.
6. Otsuka, H.; Nagasaki, Y.; Kataoka, K. *Mater. Today* **2001**, *4*, 30–36.
7. Riess, G. *Prog. Polym. Sci.* **2003**, *28*, 1107–1170.
8. Kataoka, K.; Harada, A.; Nagasaki, Y. *Adv. Drug Deliv. Rev.* **2001**, *47*, 113–131.
9. Harada, A.; Kataoka, K. *Prog. Polym. Sci.* **2006**, *31*, 949–982.
10. Voets, I. K.; de Keizer, A.; Cohen Stuart, M. A. *Adv. Colloid Interface Sci.* **2009**, *147-148*, 300–318.
11. Harada, A.; Kataoka, K. *Macromolecules* **1995**, *28*, 5294–5299.
12. Harada, A.; Kataoka, K. *Science* **1999**, *283*, 65–67.
13. Liu, S.; Zhu, H.; Zhao, H.; Jiang, M.; Wu, C. *Langmuir* **2000**, *16*, 3712–3717.
14. Zhang, W.; Shi, L.; Gao, L.; An, Y.; Li, G.; Wu, K.; Lui, Z. *Macromolecules* **2005**, *38*, 899–903.
15. Zhang, W.; Shi, L.; An, Y.; Wu, K.; Gao, L.; Liu, Z.; Ma, R.; Meng, Q.; Zhao, C.; He, B. *Macromolecules* **2004**, *37*, 2924–2929.
16. Zhang, W.; Shi, L.; Miao, Z.-J.; Wu, K.; An, Y. *Macromol. Chem. Phys.* **2005**, *206*, 2354–2361.
17. Lefèvre, N.; Fustin, C.-A.; Varshney, S. K.; Gohy, J.-F. *Polymer* **2007**, *48*, 2306–2311.
18. Zhou, X.; Goh, S. H.; Lee, S. Y.; Tan, K. L. *Polymer* **1998**, *39*, 3631–3640.
19. Wang, Y.; Wei, G.; Wen, F.; Zhang, X.; Zhang, W.; Shi, L. *Eur. Polym. J.* **2008**, *44*, 1175–1182.

20. Huang, X.; Xiao, Y.; Lang, M. *J. Colloid Interface Sci.* **2011**, *364*, 92–99.
21. Li, G.; Guo, L.; Meng, Y.; Zhang, T. *Chem. Eng. J.* **2011**, *174*, 199–205.
22. Elsabahy, M.; Zhang, M.; Gan, S.-M.; Waldron, K. C.; Leroux, J.-C. *Soft Matter* **2008**, *4*, 294–302.
23. Herlambang, S.; Kumagai, M.; Nomoto, T.; Horie, S.; Fukushima, S.; Oba, M.; Miyazaki, K.; Morimoto, Y.; Nishiyama, N.; Kataoka, K. *J. Control. release* **2011**, *155*, 449–457.
24. Stapert, H. R.; Nishiyama, N.; Jiang, D.-L.; Aida, T.; Kataoka, K. *Langmuir* **2000**, *16*, 8182–8188.
25. Zhang, G.-D.; Harada, A.; Nishiyama, N.; Jiang, D.-L.; Koyama, H.; Aida, T.; Kataoka, K. *J. Control. Release* **2003**, *93*, 141–150.
26. Bayó-Puxan, N.; Dufresne, M.-H.; Felber, A. E.; Castagner, B.; Leroux, J.-C. *J. Control. release* **2011**, *156*, 118–127.
27. Nakamura, Y.; Hirai, H. *Chem. Lett.* **1976**, *5*, 1197–1202.
28. Ohtaka, A.; Tamaki, Y.; Igawa, Y.; Egami, K.; Shimomura, O.; Nomura, R. *Tetrahedron* **2010**, *66*, 5642–5646.
29. Cölfen, H. *Macromol. Rapid Commun.* **2001**, *22*, 219–252.
30. Taton, D.; Wilczewska, A.-Z.; Destarac, M. *Macromol. Rapid Commun.* **2001**, *22*, 1497–1503.
31. Kamachi, M.; Kurihara, M.; Stille, J. K. *Macromolecules* **1972**, *5*, 161–167.
32. Bastakoti, B. P.; Wu, K. C.-W.; Inoue, M.; Yusa, S.; Nakashima, K.; Yamauchi, Y. *Chem. Eur. J.* **2013**, *19*, 4812–4817.
33. Lin, M.; Xu, P.; Zhong, W. *J. Biomed. Mater. Res. B. Appl. Biomater.* **2012**, *100*, 1114–1120.
34. Andreopoulos, A. *Biomaterials* **1989**, *10*, 101–104.
35. Monleón Pradas, M.; Gómez Ribelles, J. L.; Serrano Aroca, A.; Gallego Ferrer, G.; Suay Antón, J.; Pissis, P. *Polymer* **2001**, *42*, 4667–4674.
36. Montheard, J.-P.; Chatzopoulos, M.; Chappard, D. *J. Macromol. Sci. Part C: Polym. Rev.* **1992**, *32*, 1–34.

37. Mun, G. A.; Nurkeeva, Z. S.; Akhmetkalieva, G. T.; Shmakov, S. N.; Khutoryanskiy, V. V.; Cheon Lee, S.; Park, K. *J. Polym. Sci. Part B: Polym. Phys.* **2006**, *44*, 195–204.
38. Lizotte, J. R.; Long, T. E. *Macromol. Chem. Phys.* **2004**, *205*, 692–698.
39. Mun, G. A.; Nurkeeva, Z. S.; Dergunov, S. A.; Nam, I. K.; Maimakov, T. P.; Shaikhutdinov, E. M.; Lee, S. C.; Park, K. *React. Funct. Polym.* **2008**, *68*, 389–395.
40. Chen, S.; Hu, T.; Tian, Y.; Chen, L.; Pojman, J. A. *J. Polym. Sci. Part A: Polym. Chem.* **2007**, *45*, 873–881.
41. Coca, S.; Jasieczek, C. B.; Beers, K. L.; Matyjaszewski, K. *J. Polym. Sci. Part A: Polym. Chem.* **1998**, *36*, 1417–1424.
42. Mühlebach, A.; Gaynor, S. G.; Matyjaszewski, K. *Macromolecules* **1998**, *31*, 6046–6052.
43. Vargün, E.; Usanmaz, A. *J. Polym. Sci. Part A: Polym. Chem.* **2005**, *43*, 3957–3965.
44. Dimitrov, P.; Iyer, P.; Bharadwaj, R.; Mallya, P.; Hogen-Esch, T. E. *Macromolecules* **2009**, *42*, 6873–6877.
45. Wang, Y.; Armitage, B. A.; Berry, G. C. *Macromolecules* **2005**, *38*, 5846–5848.
46. Lai, J. T.; Filla, D.; Shea, R. *Macromolecules* **2002**, *35*, 6754–6756.
47. Bian, K.; Cunningham, M. F. *Macromolecules* **2005**, *38*, 695–701.
48. Clément, B.; Trimaille, T.; Alluin, O.; Gigmes, D.; Mabrouk, K.; Féron, F.; Decherchi, P.; Marqueste, T.; Bertin, D. *Biomacromolecules* **2009**, *10*, 1436–1445.
49. Hoogenboom, R.; Popescu, D.; Steinhauer, W.; Keul, H.; Möller, M. *Macromol. Rapid Commun.* **2009**, *30*, 2042–2048.
50. Lu, Z.; Liu, G.; Duncan, S. *J. Memb. Sci.* **2003**, *221*, 113–122.
51. Qiu, X.; Liu, G. *Polymer* **2004**, *45*, 7203–7211.
52. Liu, G.; Yang, H.; Zhou, J.; Law, S.-J.; Jiang, Q.; Yang, G. *Biomacromolecules* **2005**, *6*, 1280–1288.
53. Zheng, R.; Liu, G.; Jao, T.-C. *Polymer* **2007**, *48*, 7049–7057.
54. Sanson, N.; Bouyer, F.; Gérardin, C.; In, M. *Phys. Chem. Chem. Phys.* **2004**, *6*, 1463–1466.

55. Sanson, N.; Bouyer, F.; Destarac, M.; In, M.; Gérardin, C. *Langmuir* **2012**, *28*, 3773–3782.
56. Kee, R. A.; Gauthier, M. *Macromolecules* **2002**, *35*, 6526–6532.
57. Gauthier, M.; Li, J.; Dockendorff, J. *Macromolecules* **2003**, *36*, 2642–2648.
58. Gauthier, M.; Munam, A. *RSC Adv.* **2012**, *2*, 3100–3108.
59. Teertstra, S. J.; Gauthier, M. *Prog. Polym. Sci.* **2004**, *29*, 277–327.
60. Njikang, G. N.; Gauthier, M.; Li, J. *Polymer* **2008**, *49*, 5474–5481.
61. Dockendorff, J.; Gauthier, M.; Mourran, A.; Möller, M. *Macromolecules* **2008**, *41*, 6621–6623.
62. Nguon, O.; Gauthier, M.; Karanassios, V. *RSC Adv.* **2014**, *4*, 8978–8984.
63. Yun, S. I; Gadd, G. E.; Lo, V.; Gauthier, M.; Munam, A. *Macromolecules* **2008**, *41*, 7166–7172.
64. Davis, K. A.; Matyjaszewski, K. *Macromolecules* **2000**, *33*, 4039–4047.
65. Mendrek, B.; Trzebicka, B. *Eur. Polym. J.* **2009**, *45*, 1979–1993.
66. Abràmoff, M. D.; Magalhães, P. J.; Ram, S. J. *Biophotonics Int.* **2004**, *11*, 36–42.
67. Haynes, W. In *CRC Handbook of Chemistry and Physics*; Haynes, W., Ed.; CRC Press/Taylor and Francis: Boca Raton, **2012**; pp. 5–128.
68. Fan, C. Laser-Based Measurements of Liquid Refractive Index, Concentration, and Temperature, M.Sc. Thesis, State University of New York at Stony Brook, **1998**, p. 30.
69. Kang, J.; Yoo, K.-P.; Kim, H.; Lee, H.; Yang, D. R.; Lee, C. S. *Int. J. Thermophys.* **2001**, *22*, 487–494.
70. Heller, W. *J. Phys. Chem.* **1965**, *69*, 1123–1129.
71. González, B.; Calvar, N.; Gómez, E.; Domínguez, Á. *J. Chem. Thermodyn.* **2007**, *39*, 1578–1588.
72. Koppel, D. E. *J. Chem. Phys.* **1972**, *57*, 4814–4820.
73. Frisken, B. *Appl. Opt.* **2001**, *40*, 4087–4091.
74. Morrison, I. D.; Grabowski, E. F.; Herb, C. A. *Langmuir* **1985**, *1*, 496–501.
75. Matyjaszewski, K.; Xia, J. *Chem. Rev.* **2001**, *101*, 2921–2990.

76. Cheng, G.; Simon, P. F. W.; Hartenstein, M.; Müller, A. H. E. *Macromol. Rapid Commun.* **2000**, *21*, 846–852.
77. Matsuzaki, K.; Uryu, T.; Ishida, A.; Ohki, T.; Takeuchi, M. *J. Polym. Sci. Part A: Polym. Chem.* **1967**, *5*, 2167–2177.
78. Bouyer, F.; Gérardin, C.; Fajula, F.; Putaux, J.-L.; Chopin, T. *Colloids Surf., A* **2003**, *217*, 179–184.
79. Finsy, R. *Adv. Colloid Interface Sci.* **1994**, *52*, 79–143.
80. Bloch, D. R. In *Polymer Handbook*; Brandrup, J.; Immergut, E. H.; Grulke, E. A., Eds.; Wiley: New York, **1999**; pp. VII–536.
81. Flory, P. In *Principles of Polymer Chemistry*; Cornell University Press: New York, **1953**; pp. 544–545.
82. Witono, J. R.; Marsman, J. H.; Noordergraaf, I.-W.; Heeres, H. J.; Janssen, L. P. B. M. *Carbohydr. Res.* **2013**, *370*, 38–45.
83. Dondos, A.; Papanagopoulos, D. *J. Polym. Sci. Part B: Polym. Phys.* **1996**, *34*, 1281–1288.
84. Tsitsilianis, C.; Kouli, O. *Macromol. Rapid Commun.* **1995**, *16*, 591–598.
85. Tsitsilianis, C.; Staikos, G.; Dondos, A. *Die Makromol. Chemie* **1990**, *191*, 2309–2318.
86. Bouzouia, F.; Djadoun, S. *J. Appl. Polym. Sci.* **2008**, *110*, 3574–3581.
87. Cesteros, L.; Meaurio, E.; Katime, I. *Macromolecules* **1993**, *26*, 2323–2330.
88. Bekturov, E.; Bimendina, L. *Adv. Polym. Sci.* **1981**, *41*, 99–147.
89. Tsuchida, E.; Abe, K. *Adv. Polym. Sci.* **1982**, *45*, 1–119.
90. Taft, R.; Kamlet, M. *J. Am. Chem. Soc.* **1976**, *98*, 2886–2894.
91. Wang, L.; Pearce, E.; Kwei, T. *J. Polym. Sci. Part B: Polym. Phys.* **1991**, *29*, 619–626.
92. Gregory, A.; Clarke, R. *Tables of the Complex Permittivity of Dielectric Reference Liquids at Frequencies Up to 5 GHz*; NPL Report, Teddington, Middlesex, **2012**; p. 87.
93. Matějíček, P.; Uchman, M.; Lokajová, J.; Štěpánek, M.; Procházka, K.; Špírková, M. *J. Phys. Chem. B* **2007**, *111*, 8394–8401.

94. Zhang, W.; Shi, L.; Gao, L.; An, Y.; Wu, K. *Macromol. Rapid Commun.* **2005**, *26*, 1341–1345.
95. Nyrkova, I. A.; Semenov, A. N. *Eur. Phys. J. E. Soft Matter* **2005**, *17*, 327–337.
96. Podzimek, S. *Light Scattering, Size Exclusion Chromatography and Asymmetric Flow Field Flow Fractionation*; 1st Ed.; John Wiley and Sons: Hoboken, **2011**; p. 81.
97. Topouza, D.; Orfanou, K.; Pispas, S. *J. Polym. Sci. Part A: Polym. Chem.* **2004**, *42*, 6230–6237.
98. Holappa, S.; Kantonen, L.; Andersson, T.; Winnik, F.; Tenhu, H. *Langmuir* **2005**, *21*, 11431–11438.
99. Hofs, B.; Voets, I. K.; de Keizer, A.; Cohen Stuart, M. A. *Phys. Chem. Chem. Phys.* **2006**, *8*, 4242–4251.
100. Choi, J.; Rubner, M. F. *Macromolecules* **2005**, *38*, 116–124.
101. Mun, G. A.; Khutoryanskiy, V. V; Akhmetkalieva, G. T.; Shmakov, S. N.; Dubolazov, A. V; Nurkeeva, Z. S.; Park, K. *Colloid Polym. Sci.* **2004**, *283*, 174–181.
102. Procházka, K.; Martin, T. J.; Webber, S. E.; Munk, P. *Macromolecules* **1996**, *29*, 6526–6530.
103. Matějíček, P.; Štěpánek, M.; Uchman, M.; Procházka, K.; Špírková, M. *Collect. Czechoslov. Chem. Commun.* **2006**, *71*, 723–738.
104. Röhlich, C.; Wirth, A. S.; Köhler, K. *Chem. Eur. J.* **2012**, *18*, 15485–15494.
105. Polshettiwar, V.; Decottignies, A.; Len, C.; Fihri, A. *ChemSusChem* **2010**, *3*, 502–522.
106. Uozumi, Y.; Danjo, H.; Hayashi, T. *J. Org. Chem.* **1999**, *64*, 3384–3388.
107. Meise, M.; Haag, R. *ChemSusChem* **2008**, *1*, 637–642.
108. Sawoo, S.; Srimani, D.; Dutta, P.; Lahiri, R.; Sarkar, A. *Tetrahedron* **2009**, *65*, 4367–4374.
109. Coulter, M. M.; Dinglasan, J. A.; Goh, J. B.; Nair, S.; Anderson, D. J.; Dong, V. M. *Chem. Sci.* **2010**, *1*, 772–775.

Appendix 5

1. Liu, G.; Yang, H.; Zhou, J.; Law, S.-J.; Jiang, Q.; Yang, G. *Biomacromolecules* **2005**, *6*, 1280–1288.
2. Matyjaszewski, K.; Xia, J. *Chem. Rev.* **2001**, *101*, 2921–2990.
3. Napper, D. H. In *Polymeric Stabilization of Colloidal Dispersions*; Academic Press: London, **1983**; p. 68.
4. Fort, R.; Polyzoidis, T. *Die Makromol. Chemie* **1977**, *178*, 3229–3235.
5. Napper, D. H. In *Polymeric Stabilization of Colloidal Dispersions*; Academic Press: London, **1983**; p. 64.
6. Burchard, W.; Schmidt, M.; Stockmayer, W. *Macromolecules* **1980**, *13*, 1265–1272.
7. Grulke, E. A. In *Polymer Handbook*; Brandrup, J.; Immergut, E. H.; Grulke, E. A., Eds.; Wiley: New York, **1999**; pp. VII/675–714.
8. Hildebrand, J. H.; Scott, R. L. *The Solubility of Nonelectrolytes*; Reinhold: New York, **1950**.
9. Scatchard, G. *Chem. Rev.* **1949**, *44*, 7–35.
10. Barton, A. *Chem. Rev.* **1975**, *75*, 731–753.
11. Hansen, C. M. The Three Dimensional Solubility Parameter and Solvent Diffusion Coefficient, Ph.D. Thesis, Technical University of Denmark, **1967**, p. 106.
12. Hansen, C. M. In *Hansen Solubility Parameters: A User's Handbook*; CRC Press: Boca Raton, **2000**; pp. 25–42.
13. Hansen, C. M. In *Hansen Solubility Parameters: A User's Handbook*; CRC Press: Boca Raton, **2000**; pp. 167–200.
14. Barton, A. F. M. *Handbook of Polymer-Liquid Interaction Parameters and Solublity Parameters*; 1st Ed.; CRC Press: Boca Raton, **1990**; p. 25.

Chapter 6

1. Schmid, G. *Nanoparticles - From Theory to Application*; 2nd ed.; Wiley-VCH: Weinheim, **2010**.
2. Lewis, L. N. *Chem. Rev.* **1993**, *93*, 2693–2730.
3. Johnson, B. *Coord. Chem. Rev.* **1999**, *190-192*, 1269–1285.
4. Bönnemann, H.; Nagabhushana, K. S. Chemical Synthesis of Nanoparticles. *Encycl. Nanosci. Nanotechnol.* **2004**, 777–813.
5. Burda, C.; Chen, X.; Narayanan, R.; El-Sayed, M. A. *Chem. Rev.* **2005**, *105*, 1025–1102.
6. Astruc, D. In *Nanoparticles and Catalysis*; Wiley-VCH: Weinheim, **2008**; p. 30.
7. Polshettiwar, V.; Varma, R. S. *Green Chem.* **2010**, *12*, 743–754.
8. Jia, C.-J.; Schüth, F. *Phys. Chem. Chem. Phys.* **2011**, *13*, 2457–2487.
9. Philippot, K.; Serp, P. In *Nanomaterials in Catalysis*; Wiley-VCH Verlag: Weinheim, **2013**; pp. 1–54.
10. Polshettiwar, V.; Baruwati, B.; Varma, R. S. *Green Chem.* **2009**, *11*, 127.
11. Ortega, D.; Kuznetsov, M. V.; Morozov, Y. G.; Belousova, O. V.; Parkin, I. P. *J. Alloys Compd.* **2013**, *579*, 495–501.
12. Reiss, G.; Hütten, A. *Nat. Mater.* **2005**, *4*, 725–726.
13. Sadek, A. Z.; Zhang, C.; Hu, Z.; Partridge, J. G.; McCulloch, D. G.; Wlodarski, W.; Kalantar-Zadeh, K. *J. Phys. Chem. C* **2010**, *114*, 238–242.
14. Gubin, S. P. In *Magnetic Nanoparticles*; Gubin, S. P., Ed.; Wiley-VCH: Weinheim, **2009**; pp. 1–23.
15. Lee, K.-B.; Park, S.; Mirkin, C. A *Angew. Chem. Int. Ed.* **2004**, *43*, 3048–3050.
16. Maity, D.; Mollick, M. M. R.; Mondal, D.; Bhowmick, B.; Neogi, S. K.; Banerjee, A.; Chattopadhyay, S.; Bandyopadhyay, S.; Chattopadhyay, D. *Carbohydr. Polym.* **2013**, *98*, 80–88.
17. Du, Y.; Chen, H.; Chen, R.; Xu, N. *Appl. Catal., A* **2004**, *277*, 259–264.

18. Telkar, M. M.; Rode, C. V.; Chaudhari, R. V.; Joshi, S. S.; Nalawade, A. M. *Appl. Catal., A* **2004**, *273*, 11–19.
19. Shen, W.; Wang, Y.; Shi, X.; Shah, N. *Energy and Fuels* **2007**, *21*, 3520–3529.
20. Fouad, O. A.; Abdel Halim, K. S.; Rashad, M. M. *Top. Catal.* **2008**, *47*, 61–65.
21. Kumar, A.; Kumar, S.; Saxena, A.; De, A.; Mozumdar, S. *Catal. Commun.* **2008**, *9*, 778–784.
22. Weber, A. P.; Seipenbusch, M.; Kasper, G. *J. Nanoparticle Res.* **2003**, *5*, 293–298.
23. Omata, K.; Mazaki, H.; Yagita, H.; Fujimoto, K. *Cat. Lett.* **1990**, *4*, 123–127.
24. Reetz, M. T.; Breinbauer, R.; Wedemann, P.; Binger, P. *Tetrahedron* **1998**, *54*, 1233–1240.
25. Wu, L.; Zhang, X.; Tao, Z. *Catal. Sci. Technol.* **2012**, *2*, 707–710.
26. Lipshutz, B. H.; Tasler, S.; Chrisman, W.; Spliethoff, B.; Tesche, B. *J. Org. Chem.* **2003**, *68*, 1177–89.
27. Lipshutz, B.; Blomgren, P. *J. Am. Chem. Soc.* **1999**, *121*, 5819–5820.
28. Zhang, W.; Qi, H.; Li, L.; Wang, X.; Chen, J.; Peng, K.; Wang, Z. *Green Chem.* **2009**, *11*, 1194–1200.
29. Park, J.; Kang, E.; Son, S. U.; Park, H. M.; Lee, M. K.; Kim, J.; Kim, K. W.; Noh, H.-J.; Park, J.-H.; Bae, C. J.; Park, J.-G.; Hyeon, T. *Adv. Mater.* **2005**, *17*, 429–434.
30. Zhao, J.; Jarvis, K.; Ferreira, P.; Manthiram, A. *J. Power Sources* **2011**, *196*, 4515–4523.
31. Fukui, T.; Ohara, S.; Naito, M.; Nogi, K. *Powder Technol.* **2003**, *132*, 52–56.
32. Paillet, M.; Jourdain, V.; Poncharal, P.; Sauvajol, J.; Zahab, A.; Meyer, J. C.; Roth, S.; Cordente, N.; Amiens, C.; Chaudret, B. *J. Phys. Chem. B* **2004**, *108*, 17112–17118.
33. Roy, A.; Srinivas, V.; Ram, S.; de Toro, J.; Mizutani, U. *Phys. Rev. B* **2005**, *71*, 184443(1–10).
34. Gavrin, A.; Chien, C. L. *J. Appl. Phys.* **1993**, *73*, 6949–6951.
35. Sakiyama, K.; Koga, K.; Seto, T.; Hirasawa, M.; Orii, T. *J. Phys. Chem. B* **2004**, *108*, 523–529.

36. Wang, W.-N.; Itoh, Y.; Lenggoro, I. W.; Okuyama, K. *Mater. Sci. Eng. B* **2004**, *111*, 69–76.
37. Doppiu, S.; Langlais, V.; Sort, J.; Suriñach, S.; Baró, M. D.; Zhang, Y.; Hadjipanayis, G.; Nogués, J. *Chem. Mater.* **2004**, *16*, 5664–5669.
38. Parada, C.; Morán, E. *Chem. Mater.* **2006**, *18*, 2719–2725.
39. Seipenbusch, M.; Weber, A. P.; Schiel, A.; Kasper, G. *J. Aerosol Sci.* **2003**, *34*, 1699–1709.
40. Moravec, P.; Smolik, J.; Keskinen, H.; Mäkelā, J. M.; Bakardjieva, S.; Levdansky, V. V *Mater. Sci. Appl.* **2011**, *2*, 258–264.
41. Sako, S.; Ohshima, K.; Sakai, M.; Bandow, S. *J. Vac. Sci. Technol. B Microelectron. Nanom. Struct.* **1997**, *15*, 1338–1342.
42. Reetz, M. T.; Helbig, W. *J. Am. Chem. Soc.* **1994**, *116*, 7401–7402.
43. Zach, M. P.; Penner, R. M. *Adv. Mater.* **2000**, *12*, 878–883.
44. Kim, K. H.; Lee, Y. B.; Choi, E. Y.; Park, H. C.; Park, S. S. *Mater. Chem. Phys.* **2004**, *86*, 420–424.
45. Fievet, F.; Lagier, J.; Blin, B.; Beaudoin, B.; Figlarz, M. *Solid State Ionics* **1989**, *32-33*, 198–205.
46. Couto, G. G.; Klein, J. J.; Schreiner, W. H.; Mosca, D. H.; de Oliveira, A. J. A.; Zarbin, A. J. G. *J. Colloid Interface Sci.* **2007**, *311*, 461–468.
47. Carroll, K. J.; Reveles, J. U.; Shultz, M. D.; Khanna, S. N.; Carpenter, E. E. *J. Phys. Chem. C* **2011**, *115*, 2656–2664.
48. Duteil, A.; Schmid, G.; Meyer-Zaika, W. *J. Chem. Soc. Chem. Commun.* **1995**, 31–32.
49. Hou, Y.; Gao, S. *J. Mater. Chem.* **2003**, *13*, 1510–1512.
50. Hou, Y.; Kondoh, H.; Ohta, T.; Gao, S. *Appl. Surf. Sci.* **2005**, *241*, 218–222.
51. Sidhaye, D. S.; Bala, T.; Srinath, S.; Srikanth, H.; Poddar, P.; Sastry, M.; Prasad, B. L. V. *J. Phys. Chem. C* **2009**, *113*, 3426–3429.
52. Estournès, C.; Lutz, T.; Happich, J.; Quaranta, P. W.; Guille, J. L. *J. Magn. Magn. Mater.* **1997**, *173*, 83–92.

53. Domínguez-Crespo, M.; Ramírez-Meneses, E.; Montiel-Palma, V.; Torres Huerta, A. M.; Dorantes Rosales, H. *Int. J. Hydrogen Energy* **2009**, *34*, 1664–1676.
54. Cordente, N.; Respaud, M.; Senocq, F.; Casanove, M.-J.; Amiens, C.; Chaudret, B. *Nano Lett.* **2001**, *1*, 565–568.
55. Ould Ely, T.; Amiens, C.; Chaudret, B. *Chem. Mater.* **1999**, *11*, 526–529.
56. Koltypin, Y.; Katabi, G.; Cao, X.; Prozorov, R.; Gedanken, A. *J. Non. Cryst. Solids* **1996**, *201*, 159–162.
57. Koltypin, Y.; Fernandez, A.; Rojas, C.; Campora, J.; Palma, P.; Prozorov, R.; Gedanken, A. *Chem. Mater.* **1999**, *11*, 1331–1335.
58. Chen, Y.; Peng, D.-L.; Lin, D.; Luo, X. *Nanotechnology* **2007**, *18*, 505703–505708.
59. Li, Y.; Cai, M.; Rogers, J.; Xu, Y.; Shen, W. *Mater. Lett.* **2006**, *60*, 750–753.
60. Zhang, D.; Dou, X.; Mao, H.; Ma, X.; Cai, S.; Liu, X.; Tong, Z. *CrystEngComm* **2013**, *15*, 6923–6927.
61. Rashid, M.; Raula, M.; Mandal, T. *J. Mater. Chem.* **2011**, *21*, 4904–4917.
62. Paserin, V.; Baksa, S.; Zaitsev, A.; Shu, J.; Shojai, F.; Nowosiadly, W. *J. Nanosci. Nanotechnol.* **2008**, *8*, 4049–4055.
63. Cárdenas, G.; Acuña, J. *Colloid Polym. Sci.* **2001**, *279*, 442–448.
64. Hu, Y.; Yu, Y.; Zhao, X.; Yang, H.; Feng, B.; Li, H.; Qiao, Y.; Hua, L.; Pan, Z.; Hou, Z. *Sci. China Chem.* **2010**, *53*, 1541–1548.
65. Gornostaeva, S. V.; Revina, A. A.; Belyakova, L. D.; Larionov, O. G. *Prot. Met.* **2008**, *44*, 372–375.
66. Xu, R.; Xie, T.; Zhao, Y.; Li, Y. *Nanotechnology* **2007**, *18*, 055602–055606.
67. Im, D. H.; Park, S. Y.; Hyun, S. H.; Lee, B. Y.; Kim, Y. H. *J. Mater. Sci.* **2004**, *39*, 3629–3633.
68. Liaw, B.-J.; Chiang, S.-J.; Tsai, C.-H.; Chen, Y.-Z. *Appl. Catal., A* **2005**, *284*, 239–246.
69. Toshima, N. In *Nanoscale Materials*; Liz-Marzán, L. M.; Kamat, P. V, Eds.; Kluwer Academic: Dordrecht, **2003**; pp. 79–96.

70. Umegaki, T.; Yan, J.-M.; Zhang, X.-B.; Shioyama, H.; Kuriyama, N.; Xu, Q. *Int. J.* **2009**, *34*, 3816–3822.
71. Bala, T.; Gunning, R. D.; Venkatesan, M.; Godsell, J. F.; Roy, S.; Ryan, K. M. *Nanotechnology* **2009**, *20*, 415603–415614.
72. Lu, J.; Chamberlin, D. *MRS Proc.* **2006**, *921*, 0921–T01–04 (1-6).
73. Pietruska, J. R.; Liu, X.; Smith, A.; McNeil, K.; Weston, P.; Zhitkovich, A.; Hurt, R.; Kane, A. B. *Toxicol. Sci.* **2011**, *124*, 138–148.
74. Kumar, R. K. *J. Fire Sci.* **1985**, *3*, 245–262.
75. Freidlin, L. K.; Sladkova, T. A.; Énglina, F. É. *Izv. Akad. Nauk SSSR, Seriya Khimicheskaya* **1965**, *7*, 1248–1253.
76. Zalipsky, S.; Gilon, C.; Zilkha, A. *Eur. Polym. J.* **1983**, *19*, 1177–1183.
77. Gauthier, M.; Frank, P. C. *React. Funct. Polym.* **1996**, *31*, 67–79.
78. Abràmoff, M. D.; Magalhães, P. J.; Ram, S. J. *Biophotonics Int.* **2004**, *11*, 36–42.
79. Mond, L.; Langer, C.; Quincke, F. *J. Chem. Soc. Trans.* **1890**, *57*, 749–753.
80. Brunauer, S.; Emmett, P.; Teller, E. *J. Am. Chem. Soc.* **1938**, *60*, 309–319.
81. Carpenter, R. Method and Apparatus for Forming Nano-particles. *US Pat. 7,282,167*.
82. Duch, M. W.; Allgeier, A. M. *Appl. Catal., A* **2007**, *318*, 190–198.
83. Allgeier, A. M.; Duch, M. W. In *Catalysis of Organic Reactions*; Ford, M. F., Ed.; Marcel Dekker: Basel, **2001**; pp. 229–239.
84. Deraz, N. M. *Curr. Appl. Phys.* **2012**, *12*, 928–934.
85. Gomez, S.; Peters, J. A.; Maschmeyer, T. *Adv. Synth. Catal.* **2002**, *344*, 1037–1057.
86. de Bellefon, C.; Fouilloux, P. *Catal. Rev. - Sci. Eng.* **1994**, *36*, 459–506.
87. Nishimura, S. In *Handbook of Heterogeneous Catalytic Hydrogenation for Organic Synthesis*; Nishimura, S., Ed.; Wiley-VCH: New York, NY, **2001**; pp. 254–285.
88. Lawrence, S. A. In *Amines: Synthesis, Properties and Applications*; Cambridge University Press: Cambridge, **2004**; p. 371.
89. Di Felice, R.; Bottino, A.; Capannelli, G.; Comite, A.; Di Felice, T. *Int. J. Chem. React. Eng.* **2005**, *3*, 1–11.

90. Oro, L. A.; Carmona, D.; Fraile, J. M. In *Metal-Catalysis in Industrial Organic Processes*; Chiusoli, G. P.; Maitlis, P. M., Eds.; The Royal Society of Chemistry: Cambridge, **2006**; pp. 79–113.
91. Freidlin, L. K.; Sladkova, T. A. *Izv. Akad. Nauk SSSR* **1962**, *2*, 336–341.
92. Matthieu, C.; Dietrich, E.; Delmas, H.; Jenck, J. *Chem. Eng. Sci.* **1992**, *47*, 2289–2294.
93. Balladur, V.; Fouilloux, P.; de Bellefon, C. *Appl. Catal., A* **1995**, *133*, 367–376.
94. Gavroy, D.; Joly-Vuillemin, C.; Cordier, G.; Fouilloux, P.; Delmas, H. *Catal. Today* **1995**, *24*, 103–109.
95. Joly-Vuillemin, C.; de Bellefon, C.; Delmas, H. *Chem. Eng. Sci.* **1996**, *51*, 2149–2158.
96. Tichit, D.; Durand, R.; Rolland, A.; Coq, B.; Lopez, J.; Marion, P. *J. Catal.* **2002**, *211*, 511–520.
97. Alini, S.; Bottino, A; Capannelli, G.; Carbone, R.; Comite, A; Vitulli, G. *J. Mol. Catal. A: Chem* **2003**, *206*, 363–370.
98. Serra, M.; Salagre, P.; Cesteros, Y.; Medina, F.; Sueiras, J. E. *J. Catal.* **2002**, *209*, 202–209.
99. Serra, M.; Salagre, P.; Cesteros, Y.; Medina, F.; Sueiras, J. E. *Appl. Catal., A* **2004**, *272*, 353–362.
100. Mignonac, G. *Comptes Rendus Chim.* **1920**, *171*, 114–117.
101. Braun, J.; Blessing, G.; Zobel, F. *Berichte der Dtsch. Chem. Gesellschaft* **1923**, *36*, 1988–2001.
102. Winans, C.; Adkins, H. *J. Am. Chem. Soc.* **1932**, *54*, 306–312.
103. Huang, Y.; Sachtler, W. M. H. *Appl. Catal., A* **1999**, *182*, 365–378.
104. Juday, R.; Adkins, H. *J. Am. Chem. Soc.* **1955**, *77*, 4559–4564.
105. Kindler, K.; Hesse, F. *Arch. des Pharm.* **1933**, *271*, 439–445.
106. Mares, F.; Galle, J.; Diamond, S.; Regina, F. *J. Catal.* **1988**, *112*, 145–156.
107. Marion, P.; Grenouillet, P.; Jenck, J.; Joucla, M. *Stud. Surf. Sci. Catal.* **1991**, *59*, 329–334.
108. Marion, P.; Joucla, M.; Taisne, C.; Jenck, J. *Stud. Surf. Sci. Catal.* **1993**, *78*, 291–298.

109. Huang, Y.; Sachtler, W. M. H. *J. Catal.* **1999**, *184*, 247–261.
110. Bartholomew, C. H. *Appl. Catal., A* **2001**, *212*, 17–60.
111. Van Santen, R. A. *Acc. Chem. Res.* **2009**, *42*, 57–66.
112. O'Keefe, W. K.; Jiang, M.; Ng, F. T. T.; Rempel, G. L. *Chem. Eng. Sci.* **2005**, *60*, 4131–4140.
113. Gandía, L.; Montes, M. *Appl. Catal., A* **1993**, *101*, L1–L6.
114. Mallory, G. O. In *Electroless Plating: Fundamental and Applications*; Mallory, G. O.; Hajdu, J. B., Eds.; American Electroplaters and Surface Finishers Society: Orlando, **1990**; p. 6.
115. Kajitani, M.; Watanabe, Y.; Iimura, Y.; Sugimori, A. *Bull. Chem. Soc. Jpn.* **1975**, *48*, 2848–2851.
116. Rablen, D. P.; Dodgen, H. W.; Hunt, J. P. *Inorg. Chem.* **1976**, *15*, 931–933.
117. Okewole, A. I.; Antunes, E.; Nyokong, T.; Tshentu, Z. R. *Miner. Eng.* **2013**, *54*, 88–93.
118. Watson, J. D.; Mod, W. A.; Teumac, F. N. Extraction Process for Ni, Cu, Cr and Co **1969**, *US Pat. 3,475,163*.
119. Hilgendorff, M.; Giersig, M. In *Nanoscale Materials*; Liz-Marzán, L. M.; Kamat, P. V., Eds.; Kluwer Academic: Boston, **2003**; pp. 337–340.
120. Elimelech, M.; Gregory, J.; Jia, X.; Williams, R. A. In *Particles Deposition and Aggregation - Measurement, Modelling and Simulation*; Butterworth-Heinemann: Woburn, **1995**; pp. 54–56.
121. Seebergh, J. E.; Berg, J. C. *Langmuir* **1994**, *10*, 454–463.
122. Wohlfarth, C. Permittivity (Dielectric Constant) of Liquids. *CRC Handb. Chem. Phys.* **2014**, (6)187–208.

Chapter 7

1. Nguon, O.; Gauthier, M.; Karanassios, V. *RSC Adv.* **2014**, *4*, 8978–8984.
2. Nguon, O.; Huang, S.; Gauthier, M.; Karanassios, V. *Proc. SPIE* **2014**, *9101*, 910106(1)–910106(7).
3. Bell, A. T. *Science* **2003**, *299*, 1688–1691.
4. Schlögl, R.; Abd Hamid, S. B. *Angew. Chem. Int. Ed.* **2004**, *43*, 1628–1637.
5. Bronstein, L. M.; Sidorov, S. N.; Valetsky, P. M. *Russ. Chem. Rev.* **2004**, *73*, 501–515.
6. Shenhar, R.; Norsten, T. B.; Rotello, V. M. *Adv. Mater.* **2005**, *17*, 657–669.
7. Wang, D.; Astruc, D. *Coord. Chem. Rev.* **2013**, *257*, 2317–2334.
8. Teertstra, S. J.; Gauthier, M. *Prog. Polym. Sci.* **2004**, *29*, 277–327.
9. Scott, R. W. J.; Wilson, O. M.; Oh, S.-K.; Kenik, E. A.; Crooks, R. M. *J. Am. Chem. Soc.* **2004**, *126*, 15583–15591.
10. Venkatesan, P.; Santhanalakshmi, J. *J. Mol. Catal. A: Chem* **2010**, *326*, 99–106.
11. Dockendorff, J.; Gauthier, M.; Mourran, A.; Möller, M. *Macromolecules* **2008**, *41*, 6621–6623.
12. Turkevich, J.; Kim, G. *Science* **1970**, *169*, 873–879.
13. Toshima, N.; Yonezawa, T. *New J. Chem.* **1998**, *22*, 1179–1201.
14. Deraedt, C.; Astruc, D. *Acc. Chem. Res.* **2014**, *47*, 494–503.
15. Dockendorff, J. M. Arborescent Copolymers: Synthesis, Properties and Metallic Nanoparticle Templating, Ph.D. Thesis, University of Waterloo, Waterloo, **2011**, pp. 224–317.
16. Zhang, H.; Jin, M.; Xiong, Y.; Lim, B.; Xia, Y. *Acc. Chem. Res.* **2013**, *46*, 1783–1794.
17. Smith, T.; Wychick, D. *J. Phys. Chem.* **1980**, *84*, 1621–1629.
18. Sheiko, S. S.; Gauthier, M.; Möller, M. *Macromolecules* **1997**, *30*, 2343–2349.
19. Hamley, I. W. *Prog. Polym. Sci.* **2009**, *34*, 1161–1210.
20. Massey, J.; Power, K. N.; Manners, I.; Winnik, M. A. *J. Am. Chem. Soc.* **1998**, *120*, 9533–9540.

21. Wang, H.; Winnik, M. A.; Manners, I. *Macromolecules* **2007**, *40*, 3784–3789.
22. Wang, X.; Guerin, G.; Wang, H.; Wang, Y.; Manners, I.; Winnik, M. A. *Science* **2007**, *317*, 644–647.
23. Aridi, T. N. Arborescent Polymers from "Click" Chemistry and Other Methods, Ph.D. Thesis, University of Waterloo, **2013**.
24. Molev, G.; Lu, Y.; Kim, K.; Majdalani, I.; Guerin, G.; Petrov, S.; Walker, G.; Manners, I.; Winnik, M. A. *Macromolecules* **2014**, *47*, 2604–2615.
25. Mannelli, I.; Marco, M.-P. *Anal. Bioanal. Chem.* **2010**, *398*, 2451–2469.
26. Lin, W.; Hou, Y.; Lu, Y.; Abdelrahman, A. I.; Cao, P.; Zhao, G.; Tong, L.; Qian, J.; Baranov, V.; Nitz, M.; Winnik, M. A. *Langmuir* **2014**, *30*, 3142–3153.
27. Bandura, D. R.; Baranov, V. I.; Ornatsky, O. I.; Antonov, A.; Kinach, R.; Lou, X.; Pavlov, S.; Vorobiev, S.; Dick, J. E.; Tanner, S. D. *Anal. Chem.* **2009**, *81*, 6813–6822.